8-21-2018 10:00 AM

Microinjection Molding of Carbon Filled Polymer Composites

Shengtai Zhou
The University of Western Ontario

Supervisor
Andrew N. Hrymak
The University of Western Ontario Co-Supervisor
Musa R. Kamal (McGill University)
The University of Western Ontario

Graduate Program in Chemical and Biochemical Engineering
A thesis submitted in partial fulfillment of the requirements for the degree in Doctor of Philosophy

Recommended Citation

Zhou, Shengtai, "Microinjection Molding of Carbon Filled Polymer Composites" (2018). *Electronic Thesis and Dissertation Repository*. 5579.
https://ir.lib.uwo.ca/etd/5579

Abstract

There has been increasing demand for microparts in the areas of electronics, automotive, biomedical and micro-electro-mechanical systems. Microinjection molding (μIM) is becoming an important technology to fabricate miniature products or components to satisfy the ever-increasing needs of the above industries. Polymers and polymeric composites are ubiquitously adopted as molding materials due to their weight advantage, good processability and excellent resistance to corrosion.

Earlier studies have been primarily focused on the μIM of unfilled thermoplastics; however, microparts with multi-functionalities, such as electrical, thermal and mechanical properties are always accommodated by using multi-functional filler loaded polymer composites. Recently, μIM of carbon nanotubes (CNT) filled polymer composites has received much attention due to its commercialization potential. However, a comprehensive study is necessary to understand the properties of carbon filled micromoldings. Thus, it is important to understand the effects of the extreme shearing and cooling conditions which are common features of μIM, due to the very high molding temperatures and molding pressures as well as injection velocities involved and the very large surface area to volume ratio of microparts. These characteristics of the μIM process significantly determine the microstructure of the parts, thereby affecting the properties of final micromoldings.

In the present research, the influence of process parameters (i.e. melt temperature, mold temperature, backpressure and injection velocity), the types of carbon fillers (i.e. CNT, carbon black, graphite nanoplatelets and graphite) and the host polymer matrices (i.e. polypropylene, polystyrene, polyamide 6 and polycarbonate), the adoption of CNT filled immiscible polymer blends, and the hybrid carbon fillers loading on the electrical and morphological properties of carbon-containing microparts was systematically investigated. To this end, a rectangular mold insert which has three consecutive zones with step decreases in thickness along the melt flow direction was used to explore the effect of abrupt changes in mold geometry on the distribution of carbon fillers within subsequent moldings. To facilitate characterizations, the microparts were divided into three sections based on part thickness, namely thick section, middle section

and thin section. The volume electrical conductivity for each section of carbon filled microparts was measured using a two-probe method, which was correlated with the development of internal microstructure, as characterized by morphology observations. Therefore, the study was carried out according to the sequence described below:

Firstly, the effect of process parameters (i.e. melt temperature, mold temperature, backpressure and injection velocity) on the properties of 10 wt% CNT filled polypropylene (PP) composites was explored by employing the design of experiments method. The distribution of maximum shear rates along the melt flow direction was simulated via Moldflow (Autodesk), and the state of distribution of CNT within each section of the microparts was examined using a high-resolution scanning electron microscope (SEM). The melting and crystallization behavior of microparts molded from unfilled PP and PP/CNT 10 wt% composites at different sampling positions along the flow direction was studied using differential scanning calorimetry (DSC). Results showed that there is no significant difference between the melting behavior for sections taken from both microparts. However, the crystallization process of unfilled PP taken from different regions of the microparts is temperature dependent (i.e. sections taken from high shear regions crystallize first), and such behavior is not significant for CNT-containing counterparts. In addition, the crystallization of PP was significantly accelerated with the presence of CNT. For example, the crystallization temperature for sections taken from the PP/CNT 10 wt% microparts is at least 8^{o}C higher than respective sections taken from pure PP microparts.

Secondly, the influence of host polymer matrix selection and the loading concentration of CNT on the electrical and morphological properties of nanotubes-containing microparts was studied by adopting various polymer matrices based on their polarity and crystallinity. The adopted host polymers were PP, polystyrene (PS), polycarbonate (PC) and polyamide 6 (PA6), respectively. Results suggested that the choice of host polymer(s) could significantly influence the microstructure development within the microparts, thereby affecting the electrical conductivity. Additionally, the percolation threshold of polymer/CNT microparts shifted to higher filler concentrations, when compared with that observed for the compression molded counterparts. Furthermore, the thermal stability of PP/CNT and PC/CNT composites, as well as subsequent microparts, was studied using thermogravimetric analysis (TGA). Moreover, the melting and crystallization behavior of CNT filled PP and PA6 counterparts were evaluated using DSC.

Thirdly, the concept of selective localization of CNT in immiscible polymer blends was studied by adopting poly(lactic acid)/poly[(butylene succinate)-co-adipate] (PLA/PBSA) blend as the host matrix. The weight ratio of PLA to PBSA is 70:30 and the concentration of CNT is fixed at 5 wt%. Four different types of compounding procedures were employed to study the effect of compounding sequence of various components on the electrical conductivity of subsequent microparts. Results indicated that the electrical conductivity of PLA/PBSA/CNT microparts is invariably higher than that of CNT loaded mono-PLA counterparts, regardless of the component blending sequence. The prevailing high shearing conditions in µIM led to the coalescence of CNT-enriched PBSA domains, which is beneficial to the formation of conductive pathways along the flow direction, as confirmed by SEM observations. The thermal properties of CNT-containing blends and sections of associated microparts were characterized using TGA and DSC, respectively.

Fourthly, the influence of different types of carbon fillers on the electrical and morphological properties of microparts was carried out by adopting PP as the model host matrix. Different types of carbon fillers such as CNT, high structure carbon black (CB), graphite nanoplatelets (GNP) and graphite (i.e. synthetic graphite and low temperature expandable graphite) were employed as the conductive fillers. Results suggested that the evolution of microstructure is strongly dependent on the type of carbon filler used in µIM, which is crucial to the enhancement of electrical conductivity for resulting microparts. For example, the utilization of high structure CB and CNT is beneficial to the formation of conductive pathways within the molded samples. In addition, the adoption of large size low temperature expandable graphite (LTEG) is essential to the formation of intact conductive network, thereby enhancing the electrical conductivity moldings for subsequent moldings.

Lastly, the influence of hybrid carbon filler (i.e. CB and CNT) loading on the electrical and morphological properties of microparts was studied by systematically changing the weight ratio of CB to CNT in the PS matrix. A series of polymer composites with three different filler concentrations (i.e. 3, 5 and 10 wt%) at various weight ratios of CNT/CB (100/0, 30/70, 50/50, 70/30, 0/100) were prepared by melt blending, then followed by µIM under a defined set of processing conditions. Results showed flow-induced orientation of the carbon fillers increased with increasing shearing effect along the melt flow direction. High structure CB is found to be more effective than CNT in terms of enhancing the electrical conductivity. This was attributed

to the good distribution of CB particles in PS and their ability to form conductive pathways via self-assembly. Furthermore, it was found that an annealing treatment is advantageous for enhancing the electrical conductivity of CNT-containing microparts, whereas the electrical conductivity of only CB filled counterparts decreased.

Keywords

Microinjection molding; Polymer composites; Carbon fillers; Immiscible blends; Hybrid fillers; Electrical conductivity; Microstructure; Thermal analysis.

Co-Authorship Statement

Seven peer-reviewed journal papers, two conference papers and one book chapter have been generated which were incorporated into the thesis. The extent of collaboration of co-authors is listed below.

Journal papers:

1. S. Zhou, A.N. Hrymak, and M.R. Kamal. Electrical and morphological properties of microinjection molded polystyrene/multi-walled carbon nanotubes nanocomposites. *Polymer Engineering and Science*, 2016, 56(10), 1182-1190.
2. S. Zhou, A.N. Hrymak, and M.R. Kamal. Electrical and morphological properties of microinjection molded polypropylene/carbon nanocomposites. *Journal of Applied Polymer Science*, 2017, 134(43), 45462.
3. S. Zhou, A.N. Hrymak, and M.R. Kamal. Electrical, morphological and thermal properties of polyamide 6/multi-walled carbon nanotubes nanocomposites. *Composites Part A: Applied Science and Manufacturing*, 2017, 103, 84-95.
4. S. Zhou, A.N. Hrymak, and M.R. Kamal. Microinjection molding of polypropylene/multi-walled carbon nanotube nanocomposites: the influence of process parameters. *Polymer Engineering and Science*, 2018, 58(S1), E226-E234.
5. S. Zhou, A.N. Hrymak, and M.R. Kamal. Microinjection molding of multi-walled carbon nanotubes (CNT)-filled polycarbonate nanocomposites and comparison with electrical and morphological properties of various other CNT filled thermoplastic micromoldings. *Polymers for Advanced Technologies*, 2018, 29(6), 1753-1764.
6. S. Zhou, A.N. Hrymak, and M.R. Kamal. Properties of microinjection-molded multi-walled carbon nanotubes-filled poly(lactic acid)/poly[(butylene succinate)-co-adipate] blend nanocomposites. *Journal of Materials Science*, 2018, 53(12), 9013-9025.

7. S. Zhou, A.N. Hrymak, and M.R. Kamal. Electrical, morphological and thermal properties of microinjection molded polypropylene/multi-walled carbon nanotubes nanocomposites. *International Polymer Processing*, 2018, 33(4), 514-524.

For the journal papers listed above, S. Zhou conceived the research ideas with the guidance of Dr. Hrymak and Dr. Kamal, S. Zhou conducted all experiments and characterizations as well as wrote draft papers and made corrections thereafter. Dr. Hrymak and Dr. Kamal provided supervision and support for the research as well as feedback for all drafted papers.

Conference Papers:

1. S. Zhou, A.N. Hrymak, and M.R. Kamal. Microinjection molding: Influence of the molding parameters on the electrical conductivity of polypropylene filled with multi-walled carbon nanotubes. SPE ANTEC®-Indianapolis (USA), 2016, 1167-1171.

2. S. Zhou, A.N. Hrymak, and M.R. Kamal. Microinjection molding of polypropylene/graphite composites. SPE ANTEC®-Orlando (USA), 2018.

For the conference papers listed above, S. Zhou conceived the research ideas with the guidance of Dr. Hrymak and Dr. Kamal, S. Zhou conducted all experiments and characterizations as well as wrote draft papers and made corrections thereafter. Dr. Hrymak and Dr. Kamal provided supervision and support for the research as well as feedback for all drafted papers.

Book Chapter:

1. S. Zhou, A.N. Hrymak, and M.R. Kamal. Book chapter of "Microinjection molding of filler loaded polymer nanocomposites" in the book of '*Processing of Nanocomposite Polymers*' edited by Professor Samuel Kenig (Israel), 2018.

For the book chapter listed above, S. Zhou did the literature review and wrote the draft version as well as made a few corrections thereafter, based on the comments and feedback from Dr. Hrymak and Dr. Kamal. Dr. Hrymak initiated the preparation of the book chapter, wrote the abstract, provided suggestions for structure organization and reviewed several draft versions. Dr. Kamal provided suggestions for structure organization and reviewed several draft versions.

Acknowledgments

In the first place, I would like to express my sincerest gratitude and thanks to my supervisors, Prof. Andrew N. Hrymak and Prof. Musa R. Kamal for their continuous guidance, wisdom and extensive support throughout the completion of current project. I am inspired by their attitudes and insightful thoughts to life and research. I would also like to thank my advisory committee members, Prof. Paul Charpentier, Prof. Wankei Wan and Prof. John R. de Bruyn, for their time, invaluable advice and experimental support for this research. The comments and suggestions from my thesis examination board, Prof. Uttandaraman Sundararaj (Chemical and Petroleum Engineering, University of Calgary), Prof. Giovanni Fanchini, Prof. Paul Charpentier and Prof. Amin Rizkalla are also greatly appreciated.

The research was financially supported by the Natural Sciences and Engineering Research Council of Canada (NSERC), the Network for Innovative Plastic Materials and Manufacturing Processes (NIPMMP) and the China Scholarship Council (CSC). We are grateful for the above-mentioned sponsors which were essential to the completion of this research project.

The thesis would be impossible without the generous help and support from my colleagues and friends. Particularly, I would like to thank Mr. Normand Nardini (Industrial Materials Institute of National Research Council of Canada) for his training to operate the Battenfeld Microsystem 50 machine. I want to acknowledge Mr. Ian Vinkenvleugel (University Machine Services, the University of Western Ontario) for his assistance in swapping mold inserts for the Battenfeld machine and providing micrometer for shrinkage measurements. I would also like to thank Dr. Victor Tan, Dr. Amin Mirzadeh, Dr. Wissam K. Abdallah, and Dr. Fatma Mahrous Mohamed (Department of Chemical Engineering, McGill University) for their friendship, time and assistance during my stay in Montréal at McGill University. The generous help from my colleagues and friends at the University of Western Ontario is also greatly appreciated. I would like to take this opportunity to express my thanks to the former and current group members for their support and encouragement. My special thanks go to Fate Hashemi (Department of Chemical and Biochemical Engineering), Dr. Gleb Meirson (Fraunhofer Project Centre for Composites Research @ Western), Nuwansiri Nirosh Getangama (Department of Physics and Astronomy) and Keller George (Department of Chemical and Biochemical Engineering) for their time, experimental help and support.

The technical team from Surface Science Western, Mr. Brad Kobe, Ms. Rebecca Sarazen, and Ms. Heather Bloomfield for the image analysis and Ms. Mary Jane Walzak for Raman analysis, is greatly acknowledged for their high skills, time and patience. Also, I would like to thank Dr. Richard Gardiner and Ms. Karen Nygard (Biotron Integrated Microscopy, the University of Western Ontario) for providing training on transmission electron microscopy and suggestions on sample preparation.

Last but not least, I would like to acknowledge my family for their support, understanding and encouragement. Their unconditional love, support and understanding have always been a great source of strength for me to carry out my research here in London, Canada. I want to thank my girlfriend, Huiyang Yu, who has been a consistent source of love, comfort and encouragement. Without all of you in my heart, this thesis would not be possible. I will carry with me all your blessings and support into my future career.

The difficult is what takes a little time; the impossible is what takes a little longer.

---Fridtjof Nansen

Table of Contents

List of Tables

List of Figures

List of Symbols

p_c	Percolation threshold
T_g	Glass transition temperature
Ω	Ohm (resistance unit)
σ	Volume electrical conductivity
S	Siemens
χ_c	Crystallinity
T_{onset}	Onset crystallization temperature
T_c	Peak crystallization temperature
T_{cc}	Cold crystallization temperature
T_m	Melting temperature
T_d	Initial decomposition temperature
T_{max}	Maximum weight loss temperature
wt%	Weight percent
vol%	Volume percent
G'	Storage modulus
G''	Loss modulus
η*	Complex viscosity

List of Abbreviations

MEMS	Micro-electro-mechanical system
µIM	Microinjection molding
CIM	Conventional injection molding
CPC	Conductive polymer composite
EMI	Electromagnetic interference
ESD	Electrostatic dissipation
0D	Zero-dimensional
1D	One-dimensional
2D	Two-dimensional
3D	Three-dimensional
VGCF	Vapor-grown carbon fiber
TRGO	Thermally reduced graphite oxide
RGO	Reduced graphene oxide
SWCNT	Single-walled carbon nanotube
MWCNT	Multi-walled carbon nanotubes
CNT	Carbon nanotubes
CB	Carbon black
CF	Carbon fiber
GO	Graphene oxide

EG	Expandable graphite
LTEG	Low temperature expandable graphite
SG	Synthetic graphite
GNP	Graphite nanoplatelet
GIC	Graphite intercalated compound
PS	Polystyrene
PP	Polypropylene
PC	Polycarbonate
PU	Polyurethane
PI	Polyimide
PCL	Polycaprolactone
POM	Polyoxymethylene or polyacetal
PA6	Polyamide 6
PA12	Polyamide 12
PA66	Polyamide 6,6
PEI	Polyetherimide
EVA	Ethylene-vinyl acetate
PLA	Poly(lactic acid)
LDPE	Low-density polyethylene
LDPE	High-density polyethylene

ABS	Acrylonitrile butadiene styrene
PET	Poly(ethylene terephthalate)
UHMWPE	Ultra-high molecular weight polyethylene
PMMA	Poly(methyl methacrylate)
PBSA	Poly[(butylene succinate)-co-adipate]
PVDF	Poly(vinylidene fluoride)
DSC	Differential scanning calorimetry
TGA	Thermogravimetric analysis
OM	Optical microscopy
SEM	Scanning electron microscopy
TEM	Transmission electron microscopy

Chapter 1

1 Introduction

1.1 Motivation

Polymers and polymer-based composites have become an important factor in our daily life due to their low density, ease of processability and resistance to corrosive environments, when compared with metals and other materials. Injection molding has been traditionally geared to mass fabrication of products in several industrial sectors, such as automotive and electronics among others. Currently, a trend of miniaturization of components in various sectors has triggered a thriving market for fabricating minute products. In addition, the advances in microsystems and micro-electro-mechanical systems (MEMS) require development of suitable micro-molding technologies [1]. In this scenario, several micro-processing technologies, such as microinjection molding (µIM), hot embossing, injection-compression molding and thermoforming have been developed [2]. Among them, µIM has been widely employed at large scale production thanks to its short cycle times, full-automation ability, accurate replication and dimensional control [3].

Conventionally, microparts should satisfy at least one of the following features [4]:

- ✓ Part weight is several milligrams, and in some cases even a few micrograms;
- ✓ Part dimensions are within the order of micrometer range (for example, micro filters and diffraction gratings);
- ✓ Tolerances of part dimensions are within the order of micrometer range (such as microfluidic cells, optical components and some biomedical devices).

Recently, a considerable number of studies have been carried out to evaluate the products molded from unfilled thermoplastics by µIM [5–10]. However, in the case of applications which require microparts that fulfill multi-functional properties, such as combinations of electrical, thermal and mechanical properties, are commonly accommodated by using polymeric composites. Thus, the micromolding of filler-containing polymer composites is receiving increasing attention following recent progress in μIM of unfilled thermoplastic polymers [11–14].

Conductive polymers and conductive polymer composites (CPCs) have a variety of practical applications, such as sensors, electromagnetic interference (EMI) shielding and electrostatic dissipation (ESD) protection, depending on the levels of electrical conductivity [15–17]. Although conductive polymers can be synthesized by either chemical or electrochemical methods, the yield from the above-mentioned polymerization process is quite small [18,19]. In addition, conductive polymers generally demonstrate poor mechanical properties and processability [19,20]. Therefore, their applications have been limited to the areas of biomedical, biosensor and tissue engineering [19,21,22]. As a result, CPCs have promising applications in the antistatic, EMI shielding, thermal management, fuel cells, sensing and other areas [16,23–26].

Traditionally, the addition of highly conductive fillers into insulating polymers has been regarded as an effective way to improve overall thermal and electrical performance. Thus, metallic particles [27–30] and carbonaceous fillers [31–34] are commonly adopted thanks to their intrinsically high thermal and electrical conductivities. The major drawback associated with the use of metallic fillers is possible oxidation of metal elements into metal oxides which could, to some degree, limit the enhancement of electrical and thermal conductivities of subsequent composites [35]. In addition, the density of metallic particles loaded polymer composites increases simultaneously with increasing filler concentrations. For example, Ramezani Kakroodi et al. [30] reported that the addition of 50 vol% iron particles in maleated polyethylene (MPE) led to a density of 4.08 g/cm^3 for subsequent composite due to the high density of iron (7.20 g/cm^3). Therefore, carbon-based fillers are considered as a class of promising multi-functional additives thanks to their intrinsically high thermal and electrical conductivities, lightweight, and natural abundance [36].

Basically, insulating polymers will become conductive when the added functional fillers attain a three-dimensional (3D) structure within the host polymers. As a result, electrical conductivity of subsequent composites would change significantly with a slight alteration of filler concentration. The characteristic filler concentration at which transition from the insulating polymers to conductive composites occurs is recognized as the percolation threshold, p_c. The CPCs can be fabricated by using *in situ* polymerization, solution mixing or melt blending [16,37,38]. Melt blending technique has been widely adopted due to attractive energy and environmental considerations as well as compatibility with current industrial processing techniques, such as extrusion and injection molding processes [39].

1.2 Carbonaceous fillers

Carbon, the sixth element in the periodic table, has been known since prehistoric time [40]. The family of carbon contains several types of allotropic forms, such as diamond, graphite, fullerenes, amorphous carbon and carbon nanotubes [41], depending on the organization and arrangement of carbon atoms, as displayed in Figure 1.1. Consequently, the properties of carbon allotropes vary significantly.

For example, diamond which consists of sp^3 hybridized carbon atoms, has been applied in industrial cutting and polishing tools as well as gemstones owing to its extreme hardness and very high optical transparency [40,42]. However, graphite, a naturally abundant material, can be seen as stacks of graphene nanosheets which are weakly bonded by Van der Waals forces [34]. Graphene consists of a single layered structure with honeycombed sp^2 hybridized carbons, which imparts graphene superior electrical and thermal conductivities [43–46]. As a result, graphite has been considered as an excellent cost-effective candidate for enhancing the thermal and electrical conductivities of polymers [26,37,47]. To enhance the electrical conductivity of insulating polymers, the most commonly adopted carbon fillers are carbon black (CB), graphene, carbon nanotubes (CNT) and graphite of various forms, such as flake graphite (FG) and expandable graphite (EG). Thus, the properties of each type of carbon fillers will be discussed in the following part.

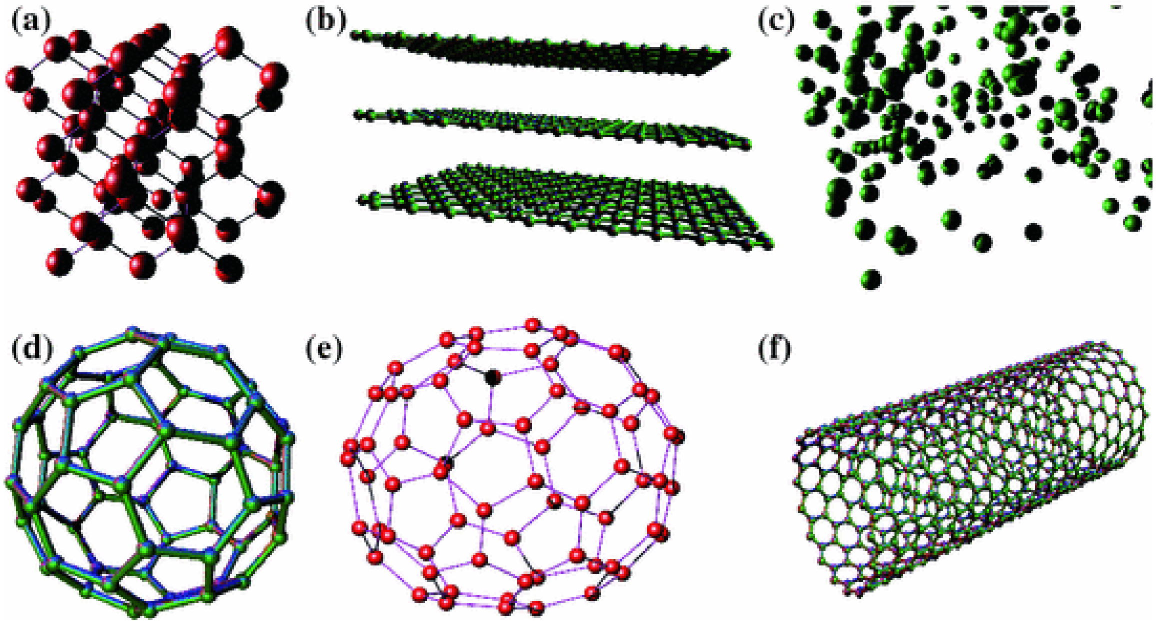

Figure 1.1 Allotropes of carbon. (a) Diamond. The carbon atoms are bonded together in a tetrahedral lattice arrangement. The carbon atoms are *sp*^{3} hybridized. (b) Graphite. The carbon atoms are bonded together in sheets of a hexagonal lattice. The Van der Waals force bonds all sheets together. The carbon atoms are *sp*^{2} hybridized. (c) Amorphous carbon. The carbon atoms are randomly arranged. (d) Spherical fullerene, C60. The carbon atoms of C60 are bonded together in pentagons and hexagons. (e) Ellipsoidal fullerene, C70. The carbon atoms are bonded together in an ellipsoidal formation. (f) Tubular fullerene, single-walled carbon nanotube (SWCNT). The carbon atoms are in a tubular formation [40].

1.2.1 Carbon black (CB)

CB is a broad term, which encompasses furnace black, thermal black, lamp black, channel black and acetylene black, depending on their manufacturing methods [48]. According to Kühner and Voll [49], the production process for CB can be classified into two categories: *(1)* Incomplete combustion, i.e. the thermal-oxidative decomposition, is the most important process for manufacturing CB. For example, at least 98% CB consumed worldwide was prepared by incomplete combustion. *(2)* Thermal decomposition of hydrocarbons, i.e. the thermal decomposition of hydrocarbons in the absence of oxygen, comprises only a small portion of overall production in comparison with the incomplete combustion process.

The major consumption for CB is by the tire industry to enhance the tear strength and the wear properties of tires [50]. In addition, CB is widely adopted as a conductive filler, an ultraviolet light stabilizer, an antioxidant, a pigment or colorant [51–57]. For example, Huang [48] reported that CBs with large surface area are suitable as conductive particles. Also, the particle size (surface area), structure and surface chemistry of CBs are critical for enhancing the electrical conductivity of polymer composites.

Balberg [58] pointed out that the p_c of CB filled polymer composites is strongly related to the structure of CB and the molding conditions. For example, Huang [48] found that the utilization of CB with higher structure, larger surface area and lower volatile content leads to higher electrical conductivity of subsequent polymer composites. However, this will in turn result in higher melt viscosity, which will impair their processability at very high CB loading concentrations.

1.2.2 Graphene

Graphene has received enormous research attention since the seminal work reported by Novoselov et al. [59]. Graphene is recognized as a 2D carbon filler with a one-atom-thick planar sheet of sp^2 bonded carbon atoms that are densely packed in a honeycomb crystal lattice [60], which can be seen as the building material of other carbon materials, as shown in Figure 1.2. The typical planar structure endows graphene with exceptional thermal, electrical and mechanical performance [43–46]. Therefore, graphene has been extensively studied as a prospective nanofiller to fabricate multi-functional polymer composites [61,62], which have a wide range of potential applications in several industrial sectors, such as lightweight structural materials, sensors, electronics, and thermal interface materials [63].

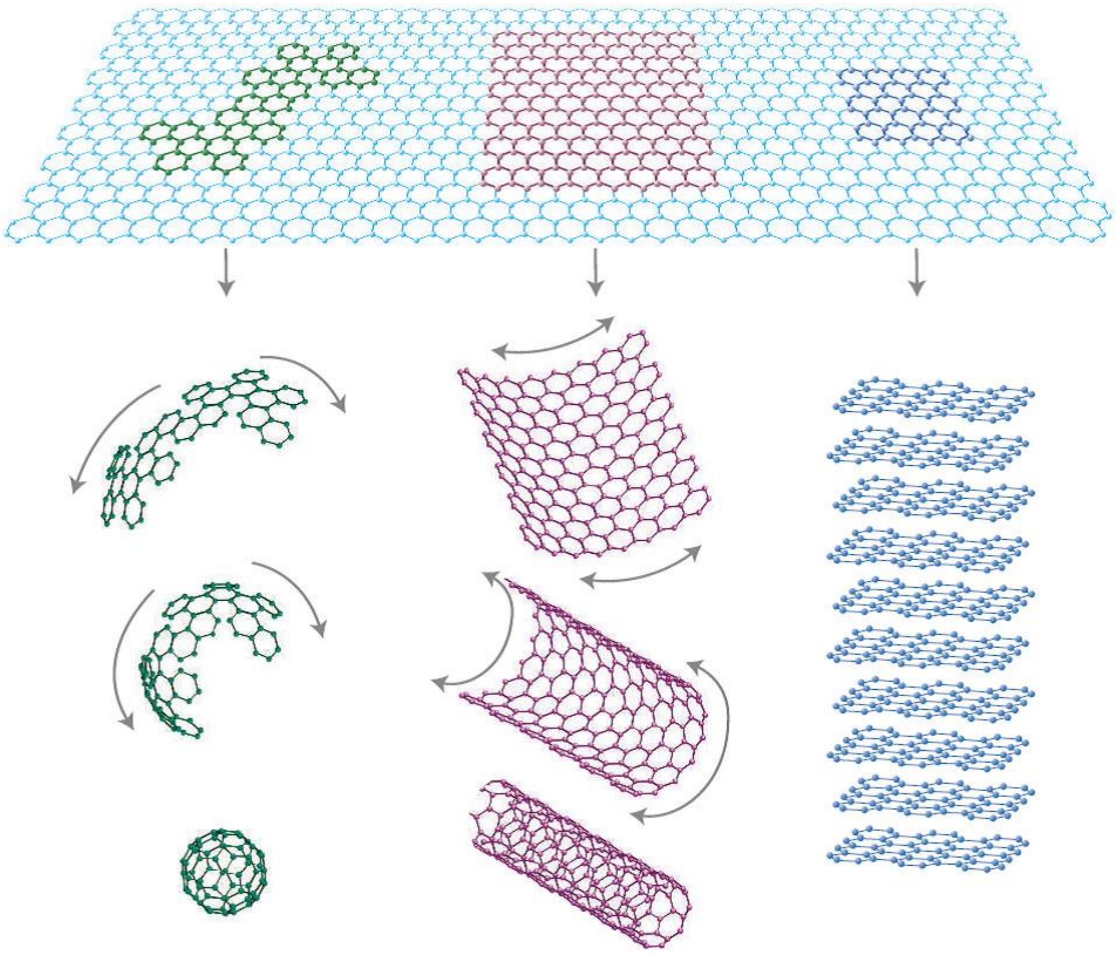

Figure 1.2 Graphene, a 2D starting structure, can be wrapped up into 0D buckyballs, rolled into 1D nanotubes and stacked into 3D graphite [64].

Stankovich et al. [61] reported that the p_c of polystyrene (PS)/graphene composites is about 0.1 vol% which can be attributed to the extremely high aspect ratio of graphene nanosheets, very high surface area (~2600 m^2/g) and uniform dispersion in the host matrix. Ramanathan et al. [65] found that there is a remarkable increase of the glass transition temperature (T_g) for poly(methyl methacrylate) (PMMA) at 0.05 wt% graphene. Rheology measurements indicated that a percolated structure was attained at identical filler concentration, which is responsible for the marked improvement of mechanical properties. This is undoubtedly attributed to the good dispersion of graphene nanosheets and strong interfacial interaction with the host matrix. Fang et al. [66] reported that the tensile strength and Young's modulus of PS/graphene composites increased 70% and 57%, respectively, when compared with the unfilled polymer matrix, with the addition of merely 0.9 wt% graphene nanosheets.

The single layer graphene also exhibits exceptional thermal conductivity (~5300 W/mK) [45]. For example, Yu et al. [67] reported that the thermal conductivity of polyvinylidene fluoride (PVDF)/graphene composites was almost double that of pure PVDF at 0.5 wt% graphene. Unlike the remarkable increase of electrical conductivity in the vicinity of p_c, the enhancement of thermal conductivity is not as drastic as that of electrical conductivity. This could be attributed to the smaller difference ($\sim 5.3\times10^4$) in the thermal conductivity between unfilled polymers (0.1-0.3 W/mK [32]) and graphene [45] when compared with electrical conductivity which has a difference up to 6×10^{18} [68]. In addition, the phonon mismatch between the filler-polymer and/or filler-filler interfaces leads to high thermal resistance, thereby hindering overall enhancement of thermal conductivity [68].

Although graphene nanosheets are capable of offering unrivaled mechanical, electrical and thermal properties, the preparation of high quality graphene is rather lengthy and costly which hinders its large scale application [62,69,70]. In addition, the major challenge for the preparation of graphene filled polymer composites is to obtain uniform dispersion and distribution of nanofillers within the host matrix while still maintaining the integrity of single layered nanosheet [63]. To best transfer the exceptional electrical conductivity and mechanical properties of graphene nanosheets to the host polymers, the resultant polymer composites were either prepared by solution mixing or the *in situ* polymerization process [60,71,72], which is not compatible with current industrial processing practice, such as extrusion and/or injection molding. However, much more graphene is typically needed to achieve the desired performance of composites prepared by melt blending. For example, Gaikwad et al. [73] reported that the p_c for melt processed samples is about 7 wt%, which was attributed to the reduction of the aspect ratio of graphene flakes induced by the high shear forces involved in the melt blending processes.

1.2.3 Carbon nanotubes (CNT)

The studies concerning CNT have surged since the pioneering work reported by Iijima in 1991 [74]. Nanotubes are ideally regarded as the rolled-up structure of graphene nanosheets (as given in Figure 1.2), which are capped by half of a fullerene at each end [75]. CNTs could be classified into single-walled carbon nanotube (SWCNT) and multi-walled carbon nanotubes (MWCNT), depending on the number of concentric graphene cylinders [76]. The properties of CNT could be determined by the diameter of nanotubes and helicity of carbon atoms in the nanotube shell [77]. For example, CNT can be either metallic or semi-conductive. The atomic models of SWCNT structure are shown in Figure 1.3. Grobert [75] pointed out that, for typical diameters, the armchair and one-third of all zigzag nanotubes are metallic whereas the rest are semi-conductive.

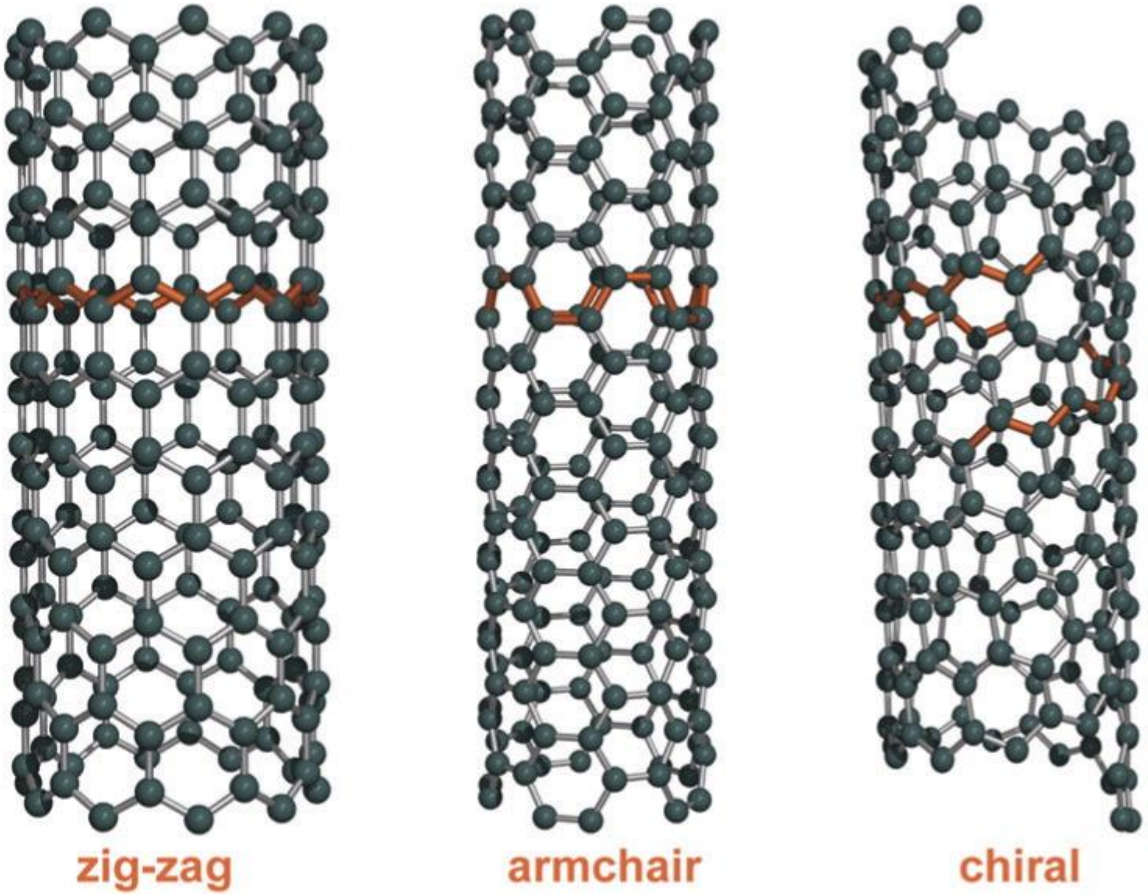

Figure 1.3 The models of SWCNT structure [75].

CNT has been recurrently employed as an excellent additive to enhance the properties of metals [78,79], ceramics [80], wood [81] and polymers [38,82–85], thanks to its high aspect ratio (>1000), electrical and thermal conductivities, and exceptional mechanical properties [77,86–88]. For example, Ma et al. [89] found that the addition of CNT can significantly improve the electrical conductivity of resultant composites, which was attributed to the higher aspect ratio and intrinsically higher electrical conductivity of CNT.

However, the expected merits of incorporating CNT into the polymer matrices are always constrained due to the poor interfacial interaction between CNT and host polymers [90], the quality of CNT dispersion in the host matrices [84], and the processing techniques [85,87]. Thus, a variety of surface modification techniques have been developed to improve the interfacial interactions between the polymer matrix and CNT [91–94]. Velasco-Santos et al. [94] reported that the chemical modification of CNT could efficiently improve the mechanical transfer from the polymer matrix to nanotubes. For example, both the storage modulus (G') and T_g of PMMA/CNT composites were increased by 1135% and about 40^oC with the addition of 1 wt% functionalized CNT when compared with their counterparts with unmodified CNT. In addition, a layer of PS surrounding CNT could be formed by *in situ* polymerization [92], as displayed in Figure 1.4(b). Thus, the presence of the PS layer leads to an improved dispersion of CNT in the PS, which can significantly enhance the mechanical properties of resultant composites.

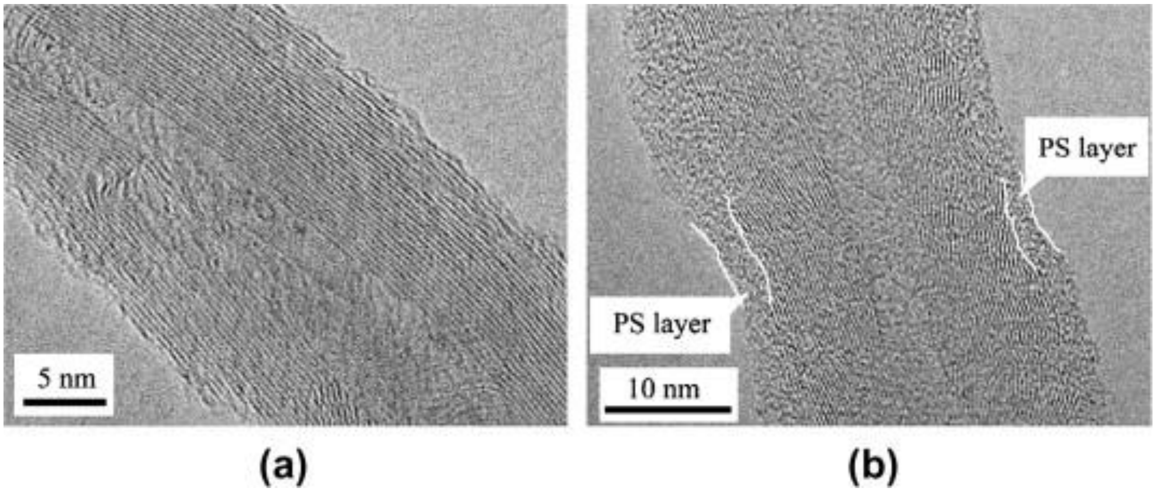

Figure 1.4 TEM of (a) purified CNT and (b) functionalized CNT [92].

Although the improved dispersion of modified nanotubes is beneficial to the enhancement of mechanical properties of corresponding polymer composites, it would be detrimental to the enhancement of electrical conductivity owing to the destruction of surface integrity of nanotubes and the presence of insulating polymer layers due to the modification treatment

[95–97]. Moreover, the p_c of CNT filled polymer composites can be significantly affected by varying the aspect ratio and the state of distribution of nanotubes within the host matrix [98].

The electrical conductivity of CNT-containing composites could also be influenced by the employed processing techniques which may affect the distribution and orientation of added fillers. Du et al. [99] reported that the electrical conductivity of CNT-containing polymer composites is affected by the filler concentration and the state of CNT orientation as well. Torres-Giner et al. [100] reported that the p_c occurs at 3 wt% for polypropylene (PP)/CNT composites obtained by the conventional injection molding (CIM). However, Abbasi et al. [101] found that the p_c is about 4 wt% for micro-injection molded PP/CNT composites. Thus, the slight discrepancy between these p_c values could be attributed to the prevailing higher shear rates in µIM, which favors the orientation of CNT along the flow direction.

1.2.4 Graphite and graphite derivatives

Graphite, which can be considered as stacks of 2D graphene nanosheets with sp^2 hybridized carbon atoms, has been extensively used as a cost-effective filler to enhance the thermal, electrical and mechanical properties of polymer composites [26,34,37,102]. The adjacent graphene nanosheets in graphite, bonded by Van der Waals forces, are separated from each other by 0.335 nm, thereby rendering the lubricating nature of graphite [37]. As a result, graphite has been adopted to improve the lubrication of metallic composites [103–105].

As single layered graphene nanosheets are the building materials for graphite, it can thus be used to enhance the electrical and thermal conductivities as well as mechanical properties of polymers. However, a relatively high loading concentration (>30 wt%) of FG is required for the formation of a conductive network within the polymer matrix. Recently, Zhou et al. [34,47,102] reported that the *in situ* expansion of low temperature expandable graphite (LTEG) during melt blending is essential for the enhancement of the thermal and electrical conductivities of subsequent blends.

Expandable graphite (EG) is a type of graphite intercalated compounds (GICs) which can be prepared by the intercalation of a variety of inserting agents under strong oxidation conditions [106,107]. EG can be rapidly exfoliated, to some extent, hundreds of times over its initial volume when subjected to thermal shock, forming a worm-like structure, as depicted in Figure 1.5. For example, Zheng and Wong [108] found that the p_c for PMMA/EG (1 wt%) composites is much lower than that of PMMA/FG (3.5 wt%) and PMMA/CB (8 wt%) counterparts. The exfoliation of EG makes it easier to form 3D conductive pathways, which is crucial to the overall enhancement of electrical and thermal conductivities of subsequent composites [109]. An informative review on the mechanical and electrical properties of graphite loaded polymer composites was reported by Sengupta et al. [37].

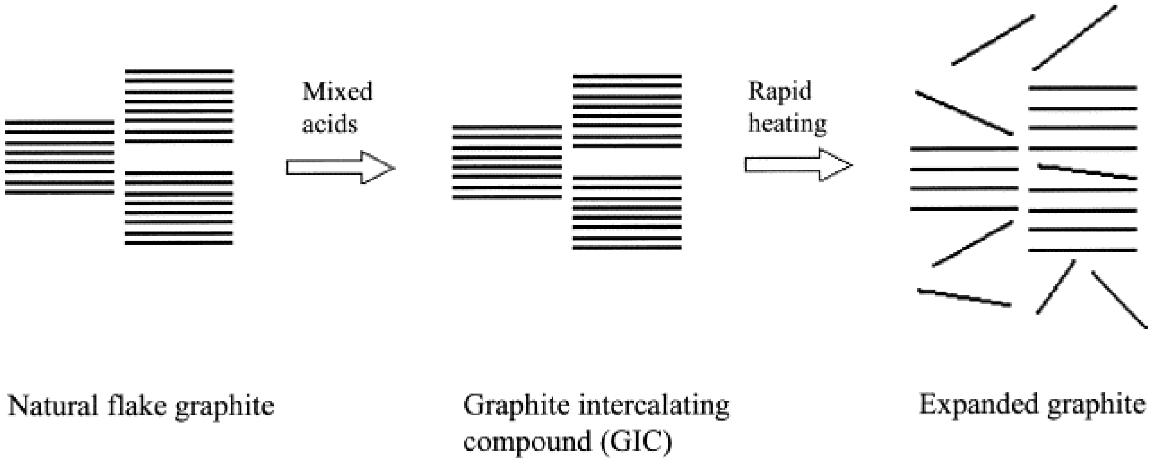

Figure 1.5 A schematic showing the preparation of EG from natural flake graphite [108].

1.3 Processing of carbon filled polymer composites

The incorporation of fillers into polymer matrices has been recognized as an efficient and versatile way to satisfy the increasing demands for high performance materials in the areas of automotive, electronics, aerospace, stimuli-responsive shape memory and other application [110,111]. The adopted fillers could either be organic or inorganic materials [112]. Basically, the selection of fillers is based on their ability to endow the polymer matrix with certain functional and/or mechanical performance. For example, carbon-based fillers are normally adopted to enhance the electrical, thermal conductivity and mechanical properties thanks to their lightweight, good dispersibility, and intrinsically high thermal and/or electrical conductivity [16,32,37,60,84,113]. Fibril-like structured fillers, such as glass fiber (GF), carbon fiber (CF) and CNT, cellulose as well as wood fiber, have been introduced to enhance the mechanical performance of polymer matrices [16,84,114–116]. Thus, several processing techniques such as *in situ* polymerization in the presence of fillers, solution mixing, coating and melt blending have been developed to fabricate polymer composites. Herein, the applications and limitations for each method will be discussed in the following part.

1.3.1 In situ polymerization

Basically, the *in situ* polymerization method requires the functional fillers to be swollen or well dispersed within the liquid monomers. The polymerization process can be initiated either by the introduction of heat or radiation, or by the addition of suitable initiators under certain settings [110]. Afterwards, the polymerization reaction occurs in the presence of functional fillers. In this scenario, the fillers would undergo very good dispersion and therefore, the properties of polymer composites could be significantly enhanced at a relatively low filler concentration [117]. For example, Park et al. [118] reported that the electrical conductivity of polyimide (PI) composites became about ten orders of magnitude higher than that of unfilled matrix with the addition of only 0.1 vol% SWCNT. Similarly, Jiang et al. [119] reported that p_c of PI/CNT is about 0.15 vol%, which is attributed to the uniform dispersion of conductive fillers when prepared by *in situ* polymerization.

Coleman et al. [84] also pointed out that there is a possibility of incorporating high loading fractions of functional fillers and achieving improved miscibility with the polymer matrix by adopting *in situ* polymerization process. In addition, they proposed that this technique is particularly useful for the preparation of insoluble or thermally unstable polymers, which are difficult to obtain using solution mixing or melt mixing method.

According to Sengupta et al. [37], the limitation of this technique is that it is difficult to operate at industrial scale to fabricate polymer composites since a large amount of electrical energy is required to disperse fillers during mixing. In addition, the technique requires highly purified monomers, initiators (if any) and added fillers to minimize the influence of impurities [120]. Furthermore, the *in situ* polymerization is often carried out under an inert atmosphere and the resultant products normally require post-treatments to remove eventual traces of unreacted monomers. As a result, the *in situ* polymerization is mainly adopted at the laboratory scale [121–124].

1.3.2 Solution mixing

The solution mixing method involves the dispersion of fillers in either a solvent or a polymer solution with the help of external agitation or sonication. The viscosity of polymer solutions is kept low to allow possible uniform mixing of fillers with the polymer chains, which is crucial to the enhancement of mechanical [125] and other properties [126] of polymer composites. Afterwards, the mixture is precipitated by mixing with a non-solvent [127] or the adopted solvent is fully evaporated [128] to obtain filler-containing polymer composites.

The prerequisite for the solution mixing method is that the polymer of interest should be soluble in the solvent which is essential to the achievement of uniform blending of fillers with polymer chains. However, the choice of solvents is always based on the solubility of polymers [84]. Moreover, the resultant products always require post-treatments to remove remaining traces of solvent [129]. In addition, it is not preferable to operate such process at large scales since the handling of large amounts of organic solvents poses potential or direct threat to human health and environment [37]. Furthermore, sonication is always introduced to achieve good dispersion of fillers in the solution, which could be detrimental to the structure of the nanofillers with high aspect ratios. For example, Li et al. [98] found that there is a significant length reduction of CNT after sonication treatment.

1.3.3 Coating method

Kalaitzidou et al. [130] proposed that the coating of polymer particles with nanofillers is an effective technique to fabricate polymer composites. In their study, the coating of PP powder with graphite nanoplatelets (GNP) in the presence of isopropyl alcohol (IPA) was conducted at room temperature. In simpler terms, GNP was initially dispersed in IPA with the help of sonication. Afterwards, PP powder was added to the above mixture under the sonication treatment. Finally, IPA was evaporated which led to the complete coverage of PP particles with GNP. The obtained composites could be subject to conventional molding practice, such as compression molding and injection molding. The advantage of this process is that the introduction of sonication could break down the GNP agglomerates which is beneficial to achieve homogenous dispersion of GNP in the solution, and this is crucial to the efficient coating of polymer powders with GNP. Moreover, IPA could also be recovered by simply filtration process which is considered environmental friendly when compared with solution mixing. They also found that samples prepared by the coating and subsequent compression or injection molding processes exhibited superior mechanical and electrical properties in comparison with their melt blended and subsequently molded counterparts, which is ascribed to the fact that the plate-like structure of GNP could be well maintained. Furthermore, the dispersion quality of GNP in PP is improved by using the coating method.

A similar coating approach has been adopted by researchers to fabricate graphene loaded polymer composites [131–133]. For example, Hu et al. [131] used a two-step approach to prepare graphene filled ultra-high molecular weight polyethylene (UHMWPE) composites. Firstly, UHMWPE powders were coated with graphene oxide (GO) under sonication in the presence of water/ethanol solution. Subsequently, the GO coated polymer powders were treated with hydrazine hydrate solutions to reduce GO to graphene. Then, samples were prepared by compression molding. They found that the p_c could occur at about 0.028 vol% graphene, which is attributed to the excellent dispersion of fillers by adopting the coating method.

1.3.4 Melt blending

Melt blending is a versatile and viable method to prepare thermoplastic polymers and composites. The standard polymer pellets could be transformed to viscous melts when the set temperature is higher than that of the melting temperature (T_m) or T_g, depending on the types of polymer matrices employed. Meanwhile, the nanofillers could be dispersed within the polymer melts by shear mixing. This technique is widely adopted at the industrial scale due to its high production efficiency and ease of implementation. As a result, a variety of processing techniques have been developed, such as single- or twin-screw extrusion, batch mixing and two-roll milling, etc.

The dispersion of fillers in polymer matrices is influenced by the intrinsic properties of the fillers and the polymer matrices, the volume fraction of fillers, the adopted processing parameters and the molding techniques, etc. For example, Müller et al. [134] reported that the dispersibility of CNT in PP could be optimized based on the intrinsic properties of CNT and the feeding position in a twin-screw extruder. Their results indicated that the more compact CNT agglomerates (Baytubes® C150P) should be added into the hopper along with the polymer pellets whereas it is suggested that the more loosely packed nanotubes (Nanocyl™ NC7000) should be added through a side feeder to achieve a relatively uniform distribution.

Pötschke et al. [135] studied the effect of mixing conditions on the electrical conductivity of PC/CNT composites by using a micro-compounder (DACA instruments, Santa Barbara, CA, USA). They found that increasing mixing time leads to an improved distribution of CNT in polycarbonate (PC). Although the distribution of CNT improves with increasing screw speed, the length reduction of CNT becomes more severe when the concentration is above p_c, which is unfavorable for the enhancement of electrical conductivity. A similar finding was reported by Andrews et al. [136]. Simply put, better distribution and more severe CNT breakage happen simultaneously with an increase of mixing time and/or screw speed, which can be correlated with the mechanical energy input. As per Pötschke et al. [137], an adequate energy input is necessary to form conductive pathways within poly(caprolactone) (PCL)/CNT composites during melt compounding. For example, the samples showed the lowest electrical resistivity at the rotation speed, 75 rpm, which corresponds to a specific mechanical energy (SME), 0.47 kWh/kg, as shown in Figure 1.6. Alig et al. [138] reported that the formation of conductive network in CNT filled polymer melts could be affected by melt temperature, filler concentration, throughput, and the shearing and elongational force fields that are induced by the extruder.

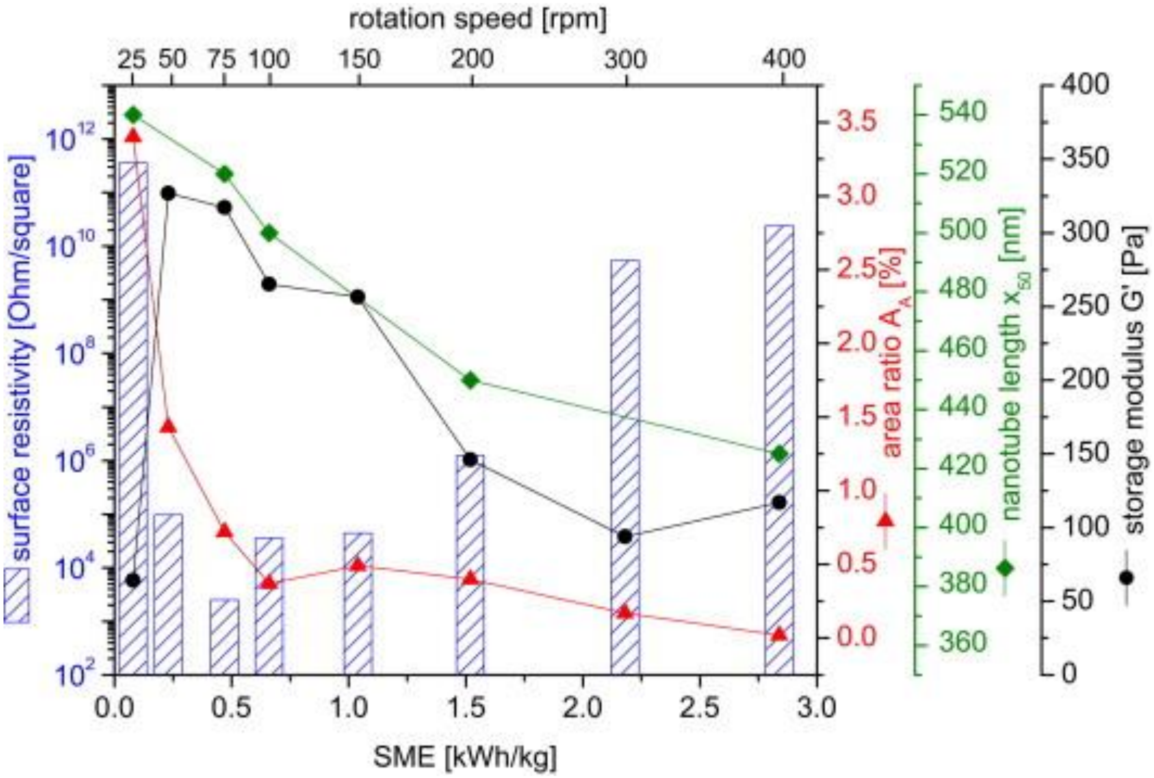

Figure 1.6 The surface resistivity, CNT agglomeration area ratio, CNT length and storage modulus (melt rheology) as a function of SME [137].

Jollands and Gupta [139] reported that the effect of operating parameters, such as mixing time, speed and temperature on the dispersion of fillers in batch mixing could be optimized by using the design of experiments method. Similarly, Pujari et al. [140] found that either increasing the mixing time or mixing speed leads to an improved distribution of CNT in PP when processed in a batch mixer. However, this would possibly lead to degradation of polymer chains. Similarly, Baiardo et al. [141] reported that the cellulosic fiber breakage became more severe with an increase of mixing speed or prolonged mixing time.

Tang et al. [39] reported that co-feeding the nanotubes with polymer pellets in a twin-screw extruder would be impractical because CNT tends to stick to the hopper walls, leading to an inaccurate CNT content in subsequent samples. Moreover, direct or indirect contact with CNT could potentially pose immediate or chronic health hazards to on-site workers and the environment [142,143]. Therefore, masterbatch dilution with pure polymers has been proposed as an effective approach to fabricate CNT-containing polymer composites. The masterbatch dilution method could be scaled to industrial quantities because fluffy CNT is bound to the polymers which is much easier to handle [144]. The leading companies for supplying CNT-containing masterbatches include Nanocyl S.A. (Sambreville, Belgium) and Hyperion Catalysis International Inc. (Cambridge, MA, USA).

Figure 1.7 displays the morphologies depicting of the distribution of CNT in extruded PS composites prepared via three different methods: masterbatch dilution (using masterbatch pellets from Hyperion Catalysis International), direct melt mixing of PS powders with CNT and direct melt mixing of PS pellets with CNT. All samples were prepared under the same conditions (i.e. 190^{o}C, 50 rpm and 10 min) and the concentration of CNT in PS was 3 wt%. Results revealed that direct mixing of PS pellets with the masterbatch pellets (i.e. PS/CNT 20 wt%) achieved the best filler distribution among these three different cases, regardless of the presence of small sized CNT agglomerates in corresponding extrudate. However, direct mixing of pristine CNT with pure polymer pellets led to the existence of large sized CNT agglomerates, which can be ascribed to the strong Van der Waals forces between individual CNTs.

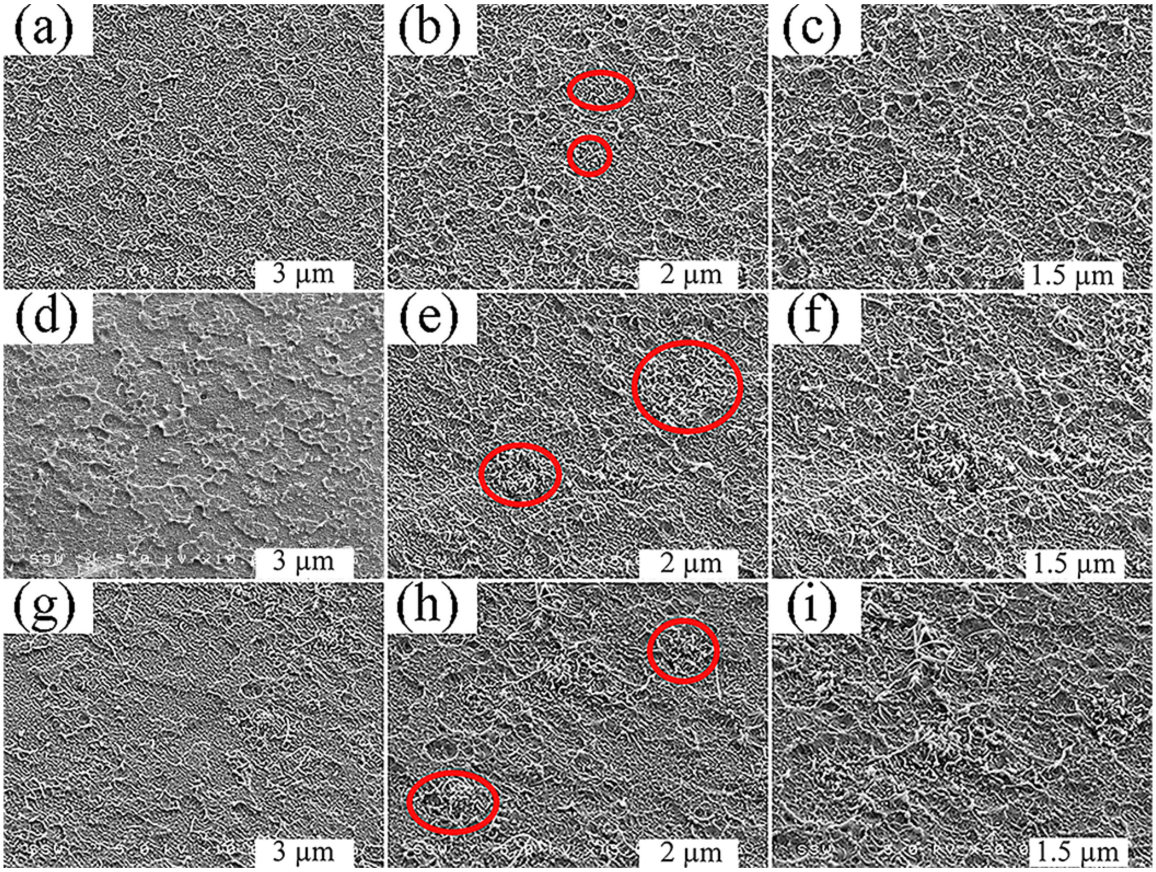

Figure 1.7 Extrudates prepared by (a-c) masterbatch dilution; (d-f) direct mixing of PS powders with pristine CNT; (g-i) direct mixing of PS pellets with pristine CNT. The examined samples were fractured in liquid nitrogen.

1.4 Properties of carbon filled polymer composites

The electrical, mechanical and thermal properties of carbon filled polymer composites are affected by the intrinsic properties of fillers and the interfacial interactions between fillers and host polymers as well as the quality of dispersion of the fillers within the host polymers. In addition, the processing techniques and the implemented processing conditions greatly influence the quality of distribution of fillers by virtue of the thermomechanical history experienced by both the matrix and the fillers during the molding process. Ultimately, the above factors influence the properties and behavior of resultant moldings. Furthermore, particularly for the injection molding process, the design of mold inserts could significantly affect the properties of the moldings. The following sub-sections focus on the properties of different carbon filled polymer composites which were fabricated by injection molding.

1.4.1 Electrical conductivity

There would be a significant increase of electrical conductivity when the conductive fillers attain an intact 3D structure within the host matrix, as shown in Figure 1.8. Therefore, the determination of electrical conductivity would, to a certain degree, reflect the dispersion of conductive particles within the polymer composites. As suggested above, the processing conditions, the choice of conductive fillers and the host polymer matrix as well as the geometry of mold design significantly influence the quality of filler distribution, thereby influencing the properties of resultant moldings [16,145–147]. For example, the electrical conductivity of compression molded samples is always higher than their injection molded counterparts [148]. Abbasi and co-workers [12,101] found that the p_c for injection molded polymer/CNT samples shifted to higher filler concentrations when compared with their compression molded counterparts, which was attributed to the anisotropic distribution of CNT in injection molded products, thereby impairing the random formation of conductive pathways.

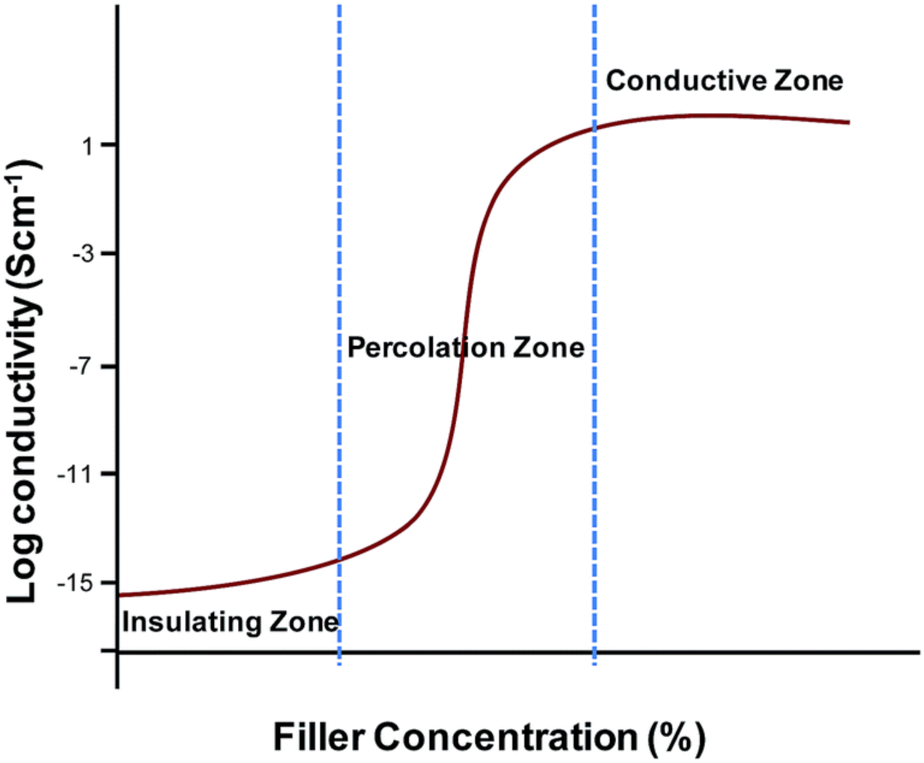

Figure 1.8 Electrical conductivity of polymer composites as a function of conductive filler concentration [19].

1.4.1.1 The influence of processing conditions

It has been reported that the electrical conductivity of injection molded products is strongly dependent on the processing conditions, because the conductive particles will be subject to the combined influence of shearing and elongational flow fields determined by various combinations of processing parameters [149,151,152].

Mahmoodi and co-workers [145] reported that the variation of processing conditions has a marked influence on the electrical conductivity of injection molded CNT-containing composites. Their results revealed that high T_m and low injection velocity are beneficial to the formation of interconnected conductive pathways. Moreover, Mahmoodi et al. [151] reported that the electrical conductivity of compression molded PS/CNT composites is higher than that of their injection molded counterparts at identical filler concentration. Also, the anisotropic thermal conductivity of injection molded samples with respect to the melt flow direction suggests that there is a preferential alignment of CNT along flow direction, which is detrimental to the construction of random conductive pathways within subsequent moldings. Wegrzyn et al. [149] studied the effects of injection velocity and T_m on the electrical conductivity of PC/ABS-CNT composites by injection molding. They found that both the surface and volume resistivities are dependent on injection velocity, while the filler distribution is related to T_m. Similarly, Villmow et al. [88] reported that injection velocity plays a dominant role in determining the electrical conductivity of injection molded PC/CNT composites, whereas the holding pressure and mold temperature show a trivial influence.

1.4.1.2 The influence of host matrix

The electrical conductivity of CNT filled polymer composites varies greatly with respect to the types of fillers employed, the choice of host polymers, the variation of processing conditions and the surface modification of fillers [38]. For example, Clingerman et al. [152] found that the distribution of carbon-based fillers varied with the type of host matrix. Based on their experiments, the polyamide 66 (PA66)/CF composites showed a higher electrical conductivity when compared with that of the PC-based counterparts at identical filler concentrations. Socher et al. [153] reported that the quality of CNT distribution could be affected by the viscosity of the polymers and the types of host polymer matrices. Simply put, the use of high viscosity polymers leads to better distribution and more severe length shortening of CNT. In addition, the CNT exhibits relatively unfavorable distribution in low density polyethylene (LDPE), when compared with polymer matrices with higher polarity such as polyamide 12 (PA12) and PC. Abbasi et al. [101] found that CNT exhibited better dispersion in PC than in PP. PC is a polar, amorphous polymer which has a strong affinity with CNT, thereby favoring the uniform dispersion of inorganic fillers. PP is a non-polar, semi-crystalline polymer which has poor interaction with CNT. Additionally, the presence of crystallites within PP would force CNTs to mainly disperse in the amorphous phase and result, to some extent, in the formation of CNT agglomerates in PP/CNT composites [101].

The idea of adopting immiscible polymer blends is often employed by researchers to obtain desired electrical and/or thermal conductivity at reduced filler loading concentrations. The selective localization of inclusion fillers in one continuous phase or at the interface of the polymer blends leads to a significant decrease of p_c for immiscible blends. For example, Zhou et al. [26] reported that the electrical and thermal conductivities of FG loaded PA6/PC immiscible polymer blends showed better conductive properties when compared with those of mono-PA6 counterparts at identical filler concentration (> 30 wt%). The above indicates that the intrinsic properties of host polymers would determine the state of distribution of inorganic fillers, thereby affecting the properties of resultant moldings.

1.4.1.3 The influence of filler type

High thermal and electrical conductive fillers are typically added into insulating polymers to make them suitable for replacing metal parts in the areas that require excellent electrical and thermal dissipation properties. Traditionally, carbon-based fillers are considered to be the most promising candidates for their intrinsically high electrical and thermal conductivities, lightweight, and most importantly, wide availability [47]. Therefore, CB, CF, graphite and CNT are commonly employed as conductive particles to enhance the electrical and thermal conductivities of insulating polymers. However, the electrical conductivity of carbon filler loaded polymer composites demonstrate different incremental improvement in conductivity depending on the types of fillers used [152].

For example, Jing et al. [154] reported that the distance between adjacent spherical fillers decreases greatly with decreasing particle size, which means the smaller the particle size of conductive particles, the lower the p_c for subsequent composites. In addition, fibril-like conductive fillers (especially those with high aspect ratios) are more efficient in enhancing the electrical conductivity of polymer composites [38]. Sohi and co-workers [155] reported that the p_c and electrical conductivity of polymer composites depend on the characteristics of conductive fillers, such as: intrinsic electrical conductivity, filler geometry and size, filler aspect ratio and the state of filler dispersion in the host polymer matrix. They found that the efficiency for carbon fillers to construct a conductive network in ethylene-vinyl acetate (EVA) obeys an order of CNT > CF > CB. Moreover, the electrical conductivity of polymer composites increases with an increase of filler aspect ratio and surface area [155–157]. Furthermore, the *in situ* expansion of EG is also crucial to the formation of conductive network, as reported by Luo et al. [102].

1.4.1.4 The influence of mold design

The geometrical factor of mold insert would affect the microstructure in injection molded products by altering the thermomechanical history that is experienced by the polymer melts. For example, Mahmoodi et al. [145] reported that the gate design would have an impact on the electrical conductivity of subsequent moldings, as exhibited in Figure 1.9. They found that using an edge gate (Cavity #1) leads to lower electrical conductivity along the melt flow direction and higher electrical conductivity across the transverse direction of the molded plates when compared with those obtained from samples molded with the fan gate (Cavity #2).

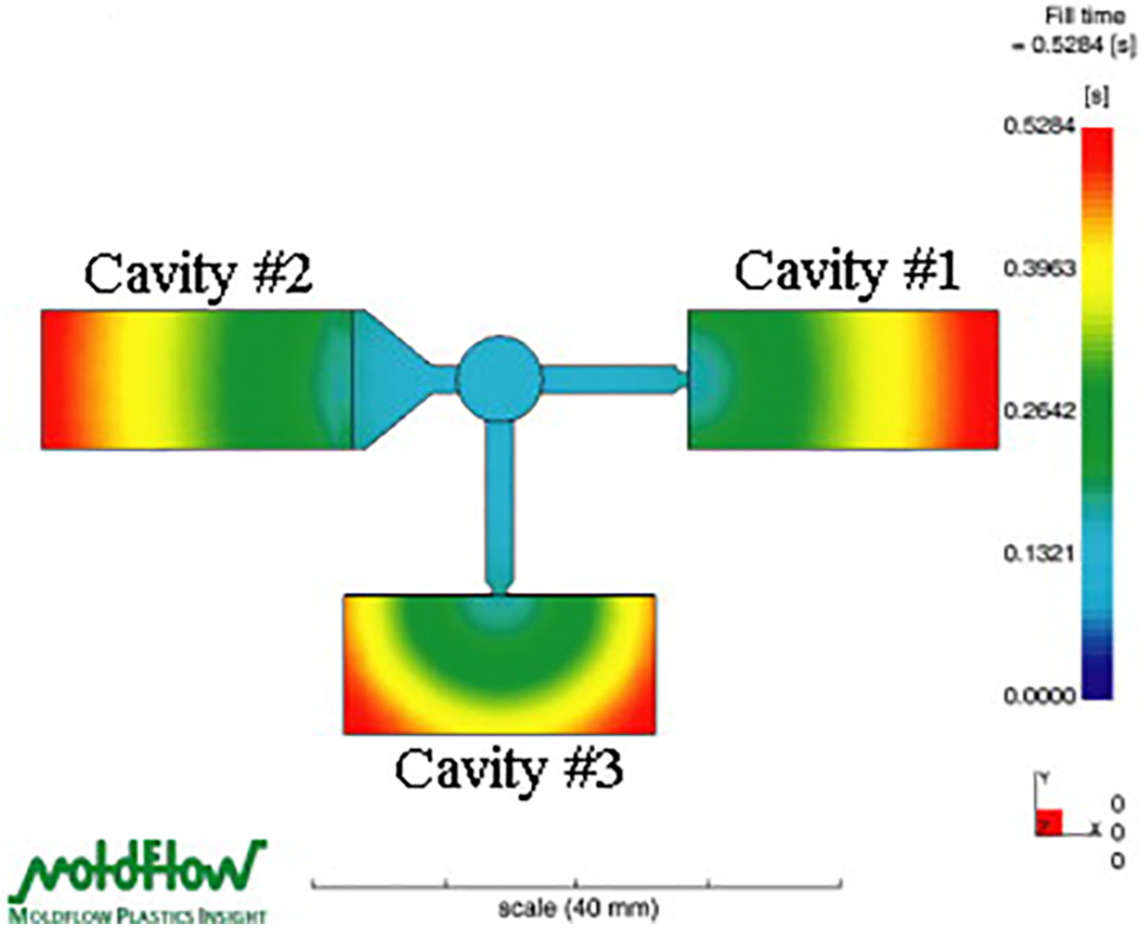

Figure 1.9 Filling simulation of the mold cavities using Moldflow™ software showing all mold cavities can be filled simultaneously. All mold cavities have a trapezoidal runner. Cavity #1: an edge gate; Cavity #2: a fan gate; Cavity #3: an edge gate, but the position of the gate was located at the longer edge of the rectangular cavity. Adapted from [145].

Similarly, Arjmand et al. [158] reported that the degree of orientation of conductive fillers significantly alters the electrical conductivity and the p_c of injection molded products. For example, the PC/CNT samples taken from different areas of the injection molded products were characterized by electrical conductivity measurements, as indicated in Figure 1.10. Results revealed that the p_c of CNT filled PC composites follows an order of Area (3) > Area (2) > Area (1) > compression molded samples, which is correlated with the state of orientation of CNT in different locations of the injection molded samples. In addition, Du et al. [159] reported that the electrical conductivity of aligned PMMA/SWCNT samples was nearly five orders of magnitude lower than that of less aligned counterparts at 2 wt% SWCNT.

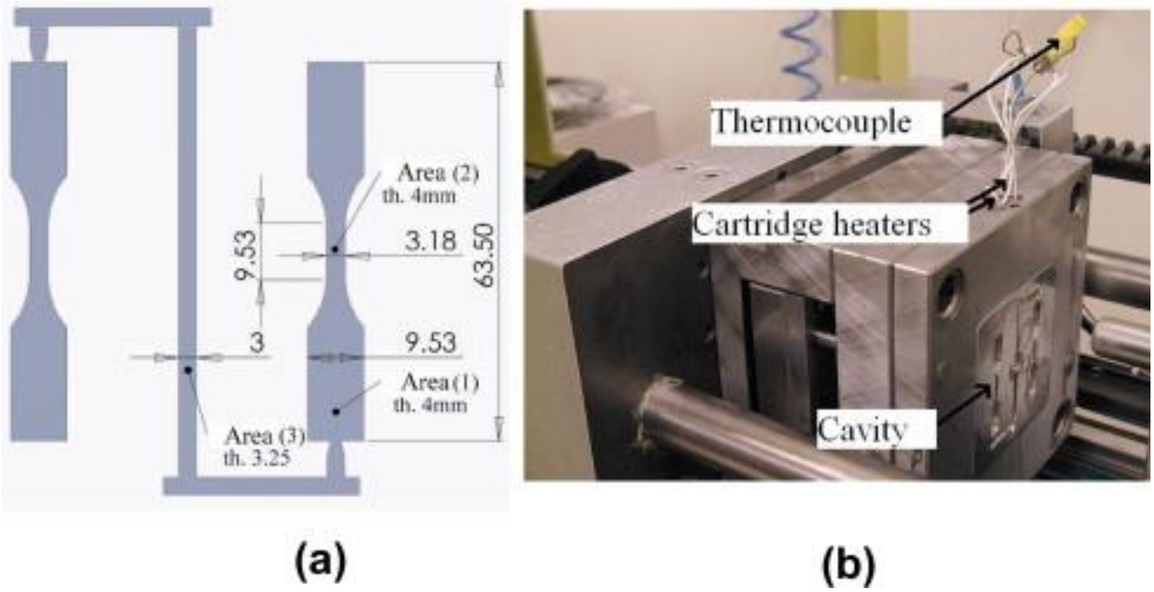

Figure 1.10 (a) The schematic of injection molded dog-bone samples. The three different areas studied in the specimens are indicated. (b) Experimental setup [158].

The shearing conditions within mold cavities could be altered significantly by varying the cavity thickness. For example, Enomoto et al. [160] reported that the electrical conductivity of PS/vapor-grown carbon fiber (PS/VGCF) composites increased with an increase of mold cavity thickness, which could be attributed to the difference between the degree of filler orientation within subsequent moldings. For example, the electrical conductivity of PS/VGCF 5.6 vol% composite with a sample thickness of 0.5 mm is 10^{-10} S/cm, whereas the corresponding value for a 2-mm thick counterpart is 10^{-4} S/cm, both prepared under the same set of molding conditions. Moreover, they [160] found that there is an interplay between the processing parameters and thickness of mold inserts. For example, a reduction of mold cavity thickness leads to a decrease of electrical conductivity of PS/VGCF samples, when a lower injection pressure was applied whereas such effect is insignificant in terms of the samples prepared under high injection pressure.

1.4.2 Thermal conductivity

Like electrical conductivity, the thermal conductivity of carbon filler-containing polymer composites increases with increasing filler concentration and the state of filler dispersion [161]. Wu and Drzal [161] found that GNP-containing samples prepared by coating method demonstrated higher electrical and thermal conductivities when compared with those melt compounded counterparts, which was ascribed to the formation of the percolated network. In addition, thermal conductivity of polymer composites is dependent on the size of fillers. Specifically, the larger the particle size, the higher the enhancement of overall thermal conductivity, which was ascribed to the lower interfacial thermal resistance (i.e. Kapitza resistance) that arises from the phonon mismatch at the interface between the added fillers and polymer matrix [162]. For example, thermal conductivity of CNT-containing polymer composites increases with the incorporation of longer CNTs with larger tubular diameter [163]. Unlike electrical conductivity, however, the enhancement of thermal conductivity is not only sensitive to the formation of conductive pathways, but also relies on the packing density of functional fillers [26]. Consequently, a modest increase of thermal conductivity is typically observed with an increase of filler concentrations.

Mahmoodi et al. [164] reported that injection molded PS/CNT composites demonstrated anisotropic thermal conductivity with respect to the melt flow direction. For example, the thermal conductivity measured along the flow direction is always higher than that obtained across the transverse direction, which is attributed to the preferred alignment of nanotubes along flow direction, arising from the influence of predominant shearing and elongational force fields along the melt flow direction. A similar trend was reported by Ha et al. [165] for injection molded liquid-crystal polymer (LCP)/graphite composites. They found that the in-plain thermal conductivity for samples with more aligned CNT is 0.402 W/mK which is nearly 20% higher than that obtained from less aligned counterparts when the CNT concentration is 5 wt% [164]. This suggests that the thermal conductivity of CNT filled polymer composites is affected significantly by the processing conditions in injection molding, which is related to the degree of orientation of nanotubes under specific molding conditions.

In general, a vast number of combinations of conductive fillers with thermoplastic polymers could be compounded and therefore applied for compression molding or injection molding process [166]. A comprehensive review regarding the use of carbonaceous fillers, particularly CNT, to produce polymer composites for the enhancement of thermal conductivity has been reported by Han and Fina [32].

1.4.3 Morphological properties

Morphology development of carbon filled polymer composites could be related to the intrinsic properties of the carbon fillers, their interfacial interactions with the host matrix and the processing techniques involved. For example, Hofmann et al. [167] studied the evolution of microstructure in different types of carbon fillers loaded PA12 composites. All samples having the same carbon filler concentration, i.e. 10 wt%, were prepared by injection molding under identical processing conditions. As given in Figure 1.11, thermally reduced graphite oxide (TRGO) achieves a uniform distribution within PA12, whereas a fraction of filler agglomerates was detected in MLG 350 (i.e. multilayered graphene) filled counterparts. The improved distribution of MLG 350 was attributed to the presence of functional groups, which is favorable for dispersing fillers within the host matrix. However, the existence of micro-size carbon assemblies in EG 60 (i.e. expandable graphite) loaded samples was due to an insufficient exfoliation of EG. In addition, both the CNT and CB have a relatively uniform distribution within PA12, albeit the presence of a scattering of small size agglomerates.

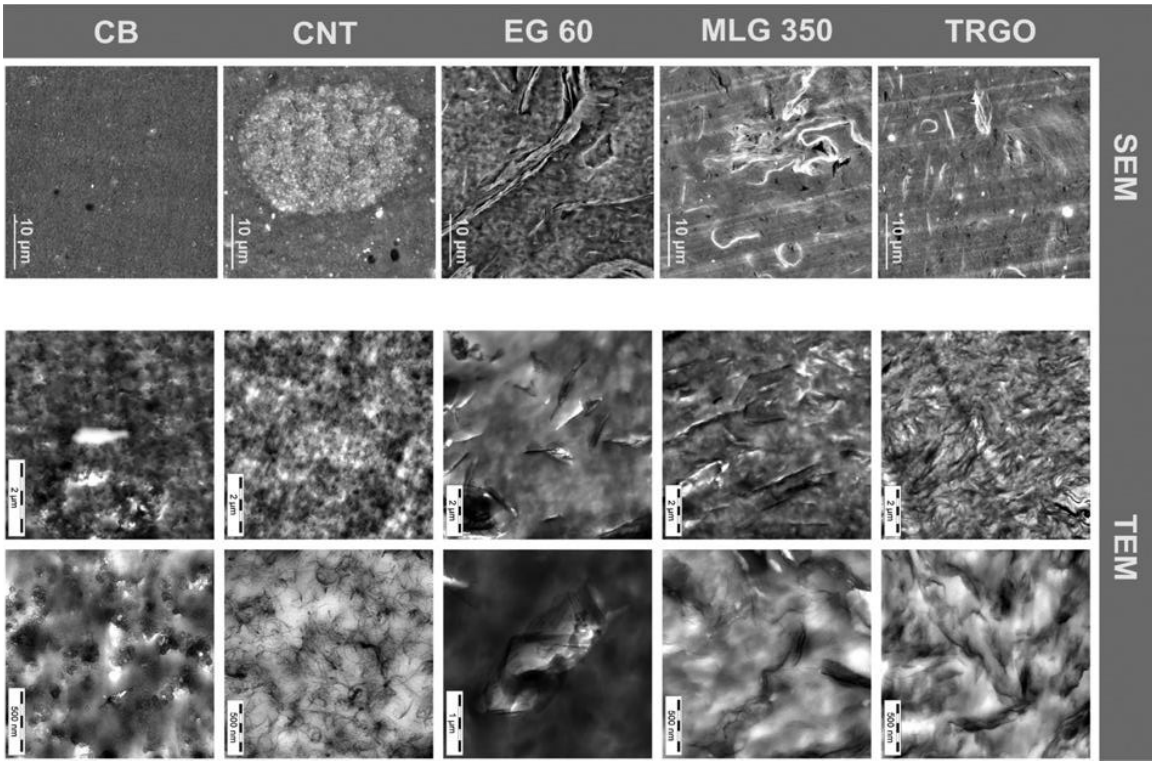

Figure 1.11 SEM and TEM images of different types of carbon fillers (10 wt%) filled PA12 composites. MLG 350 refers to multilayered graphene and EG 60 is a type of expandable graphite [167].

The shearing conditions during processing could affect the evolution of microstructure in injection molded samples. For example, the alignment of CNT in a polymer matrix could be altered by adjusting process parameters of injection molding by affecting the viscosity and the amount of shear stress exerted on the polymer melts [145]. As shown in Figure 1.12, sample A which was prepared under more severe shearing conditions, showed more CNT orientation. Sample B which experienced less shearing and thus showed a lower degree of CNT orientation, whereas a random state of dispersion of CNT was observed in Sample C which was prepared by compression molding [164].

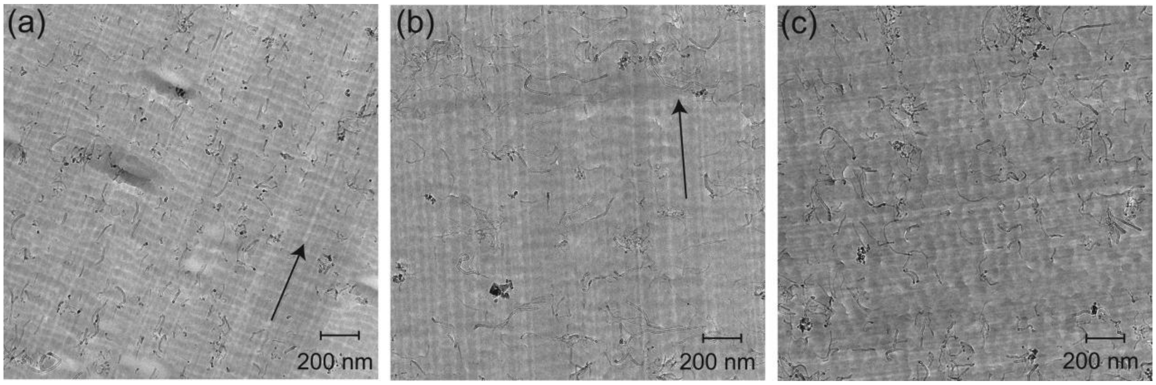

Figure 1.12 TEM micrographs from (a) specimen A, prepared under conditions of low T_m and high injection pressure; (b) specimen B, prepared under conditions of high T_m and low injection pressure; (c) specimen C, compression molded sample which features randomly dispersed CNTs. The concentration of CNT is 3.5 wt%. Black arrows indicate the flow direction of injection molded samples [164].

1.4.4 Mechanical properties

In addition to exceptional thermal and electrical conductivities of carbonaceous fillers, they possess excellent mechanical properties which have been widely employed as functional fillers to enhance the mechanical properties of polymer matrices. For example, polymer/carbon composites have been widely employed as structural materials in several industrial sectors, such as aerospace, sporting goods and automotive parts [85]. The typical properties of different types of carbonaceous fillers are tabulated in Table 1.1.

Table 1.1 Typical mechanical properties of different carbon fillers, i.e. MWCNT, graphite, graphene and VGCF [16,37,71,168].

Property	Unit	MWCNT	graphite	graphene	VGCF
Density	g/cm^3	1.75~1.8	2.26	2.2	2.0
Tensile strength	GPa	10-60	130	130	2.92~3
Tensile modulus	TPa	0.3~1	1	1	0.24~0.5

Stan et al. [169] reported that the mechanical properties, such as Young's modulus, tensile strength and yield strength, of PP/CNT composites improved with an increase of injection pressure, the weight fraction of nanotubes and strain rate whereas the yield strain and strain at break showed the opposite trend. Similarly, Bhuiyan et al. [170] reported that the tensile strength and Young's modulus increased with an increase of CNT concentration, which suggests a reinforcement effect by incorporated nanotubes.

Murariu et al. [171] reported that there is a simultaneous reduction of tensile strength and strain at break with a gradual incremental loading fraction of EG (see Figure 1.13), which was attributed to the aggregation of the added fillers and poor quality of dispersion of EG at high filler concentrations. However, Kanbur and Küçükyavus [148] found that the tensile strength and Young's modulus increased with an increasing loading fraction of CB in PP. In addition, the mechanical properties of injection molded PP/CB samples is superior to those of compression molded counterparts. The preferential alignment of polymer chains and added fillers along the flow direction [148] and the improved distribution of CB [172] in the injection molded articles are possible contributing factors.

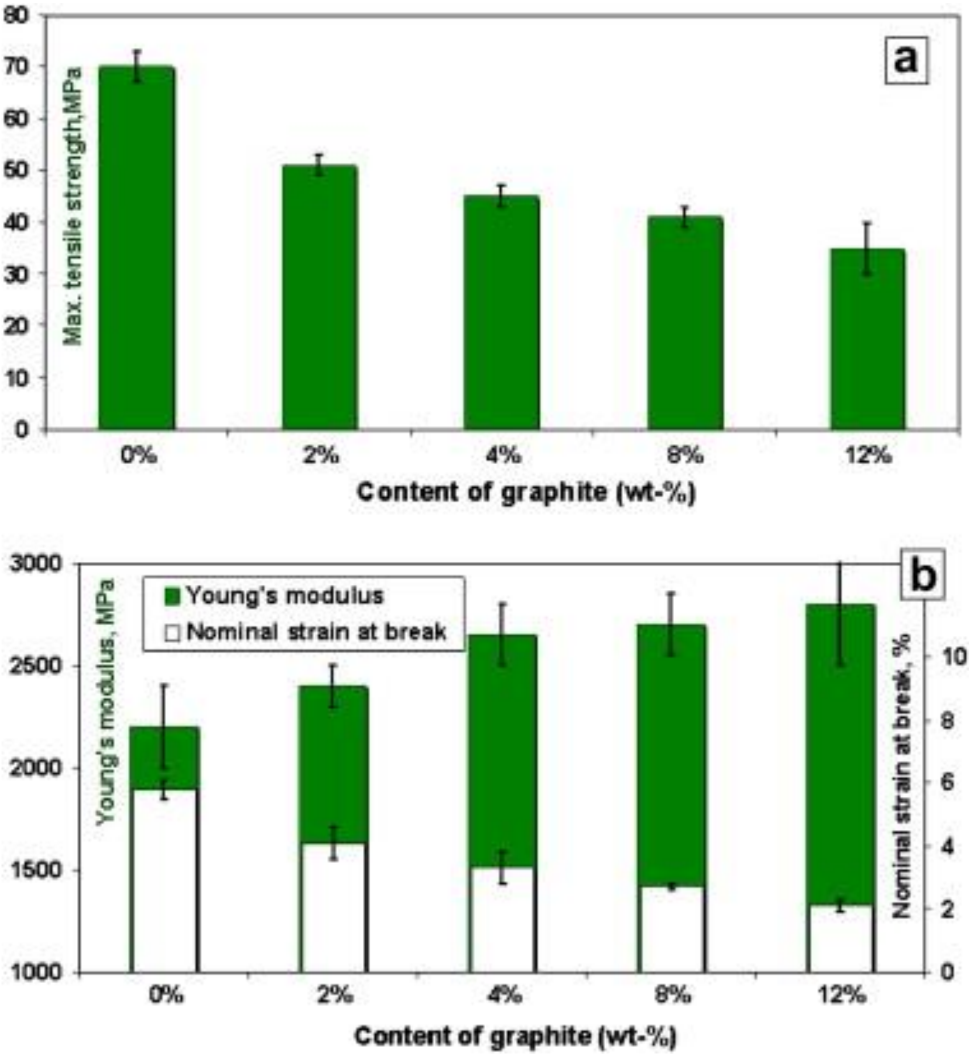

Figure 1.13 Evolution of (a) tensile strength, (b) Young's modulus and nominal strain at break for PLA composites with different contents of EG [171].

Ha et al. [165] also reported that the tensile modulus increased with an incremental loading fraction of graphite in LCP, which further revealed the reinforcement effect of inorganic fillers. In addition, the impact strength for sections taken from injection molded samples, i.e. gate end and far end, was studied as a function of graphite content in LCP. As shown in Figure 1.14(a), sections taken from the gate end exhibited better impact resistance when compared with those taken from the far end of the injection molded LCP/graphite samples. The favored alignment of graphite near the gate end is thought to be the contributing factor, as revealed by SEM observations in Figures 1.14(b) and (c) [165]. In addition, the coefficient of thermal expansion decreased with increasing filler content.

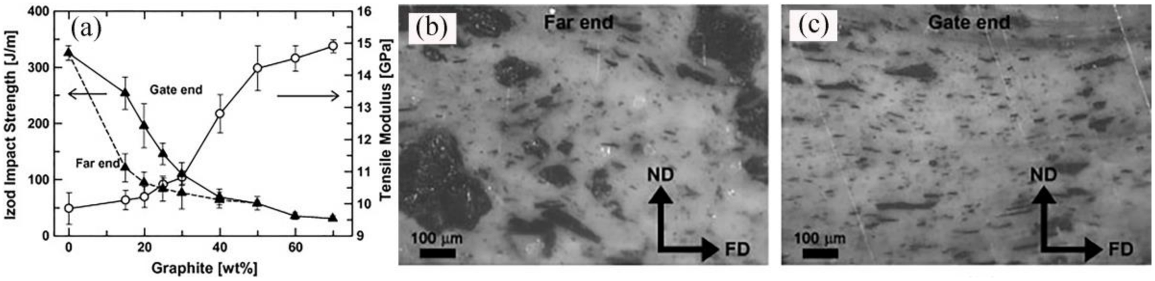

Figure 1.14 (a) The tensile modulus and impact strength of LCP/graphite composites, and (b) the morphology observations between sections taken from the far end and gate end of injection molded samples. Adapted from [165].

Furthermore, Karsli and Aytac [173] reported that the addition of compatibilizers or surface modification of incorporated fillers leads to better adhesion between fillers and the host polymer matrix, thereby resulting in a significant enhancement of mechanical properties of filler-containing polymer composites.

1.4.5 Crystallization properties

The presence of inorganic fillers would significantly accelerate the crystallization process of polymer chains by serving as a nucleating agent [174]. As given in Figure 1.15, Kazemi and co-workers [175] reported that the onset crystallization temperature (T_{onset}) and the peak crystallization temperature (T_c) significantly increased with the addition of CNT up to 5 wt%. For example, the T_c increased about 10^oC with the addition of 0.7 wt% CNT. In addition, both the T_{onset} and T_c increased gradually with an incremental loading fraction of CNT, indicating that the crystallization of macromolecular chains is related to the number of crystallization sites introduced by the added fillers. Also, they found that the crystallinity (χ_c) for PP increased when the loading concentration of CNT is at a low level (≤ 1 wt%), whereas the χ_c decreased with further increasing filler concentrations, which suggests that CNT plays two competing roles in the crystallization of PP [174,175]. In addition, Stan et al. [169] found that the χ_c of nanotubes filled PP decreased slightly with an increase of filler concentration, which was attributed to the formation of an interconnecting network within PP, thereby slowing down the crystal growth. However, the χ_c of injection molded samples increased slightly with CNT content [169], suggesting that the thermomechanical history experienced by polymer melts plays a significant role in determining the microstructure of resultant moldings. A thorough review on the effects of low dimensional carbon nanofillers (in particular, CNT and graphene) on polymer crystallization was reported by Xu et al. [174].

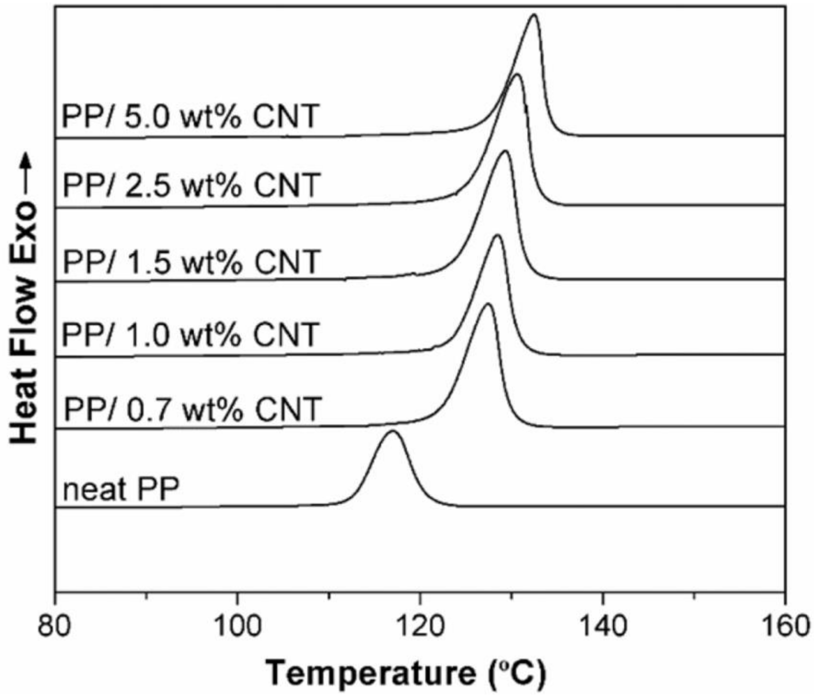

Figure 1.15 Cooling DSC thermograms of pure PP and PP/CNT composites [175].

1.4.6 Thermal stability

The thermal stability of thermoplastics and subsequent filler-containing composites could be traced by thermogravimetric analysis (TGA). Representative thermal analysis data such as decomposition temperature (T_d), the maximum decomposition temperature (T_{max}) and the char yield can be derived from the TGA thermographs. The T_d is often taken at the temperature with 5% weight loss whereas T_{max} is the peak value of first-order derivative of recorded weight loss thermographs [34].

The thermal stability of polymers could be affected by processing conditions, the testing environment and the molecular weight of polymers as well as the additives that are incorporated in host matrices such as thermal stabilizers or compatibilizers and functional fillers. For example, a chain scission effect might occur when the polymer melts are processed under high shearing conditions, thereby lowering the thermal stability of resultant polymers [176,177]. Also, the testing conditions, (i.e. the inert or air atmosphere [178], the heating rate [179], etc,) may play a role in determining the thermal stability. In addition, Adam et al. [180] found that the degradation of PC is greatly affected by the molecular weight. The degradation of PC chains becomes more severe with the use of PC which has lower macromolecular weight. Jang and Wilkie [181] found that the presence of phosphate enhanced the thermal stability whereas the thermal stability of carbon filled polymer composites could be affected by the intrinsic properties of carbon fillers [182–185]. Jakab and Omastová [185] found that CB with higher volatile content can initiate the decomposition of PP chains whereas CB with lower volatile content enhances the thermal stability. Kashiwagi et al. [186] pointed out that the flammability of PMMA/CNT composites could be effectively suppressed by the formation of a jammed filler structure.

1.5 Microinjection molding

To address the ever-increasing need for microparts, several micro-processing technologies, such as microinjection molding (µIM), hot embossing, injection-compression molding and thermoforming have been developed [2]. Among these techniques, the hot embossing and µIM methods have been proposed as the most industrially viable processes to fabricate microparts [187]. Basically, the hot embossing method involves several steps: (1) a mold (tool) which bears microstructure features is pre-heated; (2) the pre-heated mold is brought into contact with a semi-finished polymer part; (3) the whole tool and part are cooled down and the part is removed from the mold [187]. However, hot embossing is mostly adopted at laboratory scale due to the long cycle times involved [2]. Since hot embossing is characteristic of low melt flow velocity, low pressure and low cooling rate, it is thus appropriate for fabricating complex or high aspect ratio (>2) objects [187]. As a result, it is ideal for producing precise components that can be used in optical application where the molded components require high precision and quality [188]. Thus, µIM can be scaled to large quantities due to its high production efficiency and accurate dimensional control.

1.5.1 Development of microinjection molding technology

The µIM process was developed in the late 1980s and was accommodated with modified conventional injection molding (CIM) machines [189]. However, the production of microparts using these adapted machines led to significant waste of polymer melts (over 90%) and long cycle times [190]. In addition, material degradation during different processing stages (see Figure 1.17) and inaccurate control of metering size severely limited precise replication of microparts [187]. Thereafter, research attention was paid to the invention of special µIM machines which could minimize material waste, limit possible degradation of polymer melts and above all, fulfill the molding of precision microparts.

To this end, a smaller barrel and screw diameter (less than 20 mm) is typically adopted since only a small fraction of polymer melts is sufficient for the fabrication of microparts [187]. For example, the diameter of injection plunger for Battenfeld Microsystem 50 is 5 mm. As a result, the metering size of polymer melts increases about 23 mg of PMMA when the injection plunger moves forward 1 mm, which is less than the weight of a standard PMMA pellet (~28 mg) [191]. A vivid example is displayed in Figure 1.16. The gear wheel weighs 0.008 g, i.e. 8 mg [192].

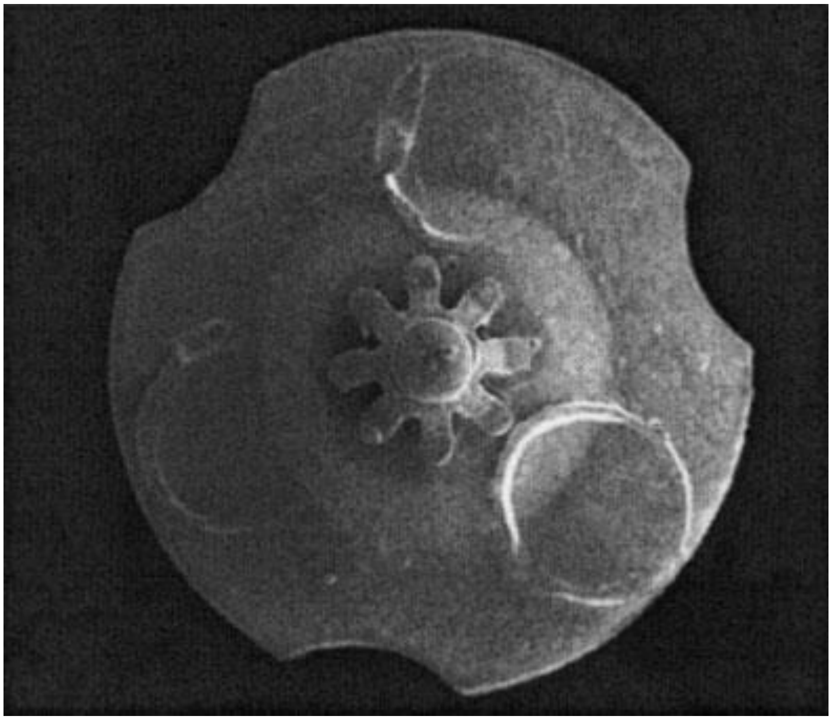

Figure 1.16 SEM image of a POM microgear [192].

The plunger injection system, which adopts separate screw melting, metering and injection units has been widely implemented by machine manufacturers, such as the Battenfeld, Boy

Machines and so forth. Based on literature [1], some commercially available µIM machines and their characteristics are tabulated in Table 1.2.

Table 1.2 Some commercially available µIM machines and their characteristics [1].

Manufacturer	Model	Clamping force (kN)	Injection capacity (cm^3)	Injection pressure (bar)	S or P diameter[(a)] (mm)	Injection speed (mm/s)
APM	SM-5EJ	50	1.2	3000	S14	800
Arburg	220 S	150	15	2500	S15/S8	112
Babyplast	Babyplast 6/10P	62.5	4	265	P10	-
Boy	XS	100	4.5	3130	S12	-
Desma	FormicaPlast	10	0.15	3000	P6/P3	500
Fanuc	Roboshot S2000-I 5A	50	6	2000	S14	300
Lawton	Sesame Nanomolder	13.6	0.082	3500	P10	1200
Nissei	AU3E	30	1.4	2500	S14/P8	300
Rondol	High Force 5	50	4.5	1600	S20	-
Sodick	LP10EH2	100	2	1970	S14/P8	1500
Sumitomo (SHI) Demag	SE18DUZ	170	6.2	2230	S14	500
Toshiba	EC5-A	48	5.6	2000	S14	150
Wittmann-Battenfeld	Micropower 5	50	1.2	3000	S14/P5	750

Note: (a) A/B = Plasticization unit/injection unit; S denotes screw and P refers to piston.

1.5.2 General characteristics of the microinjection molding process

μIM is becoming a key technology to fabricate microparts thanks to its short cycle times, full-automation ability and relatively accurate dimensional control, which can be scaled at large quantities [1]. Like CIM, μIM adopts similiar processing stages (Figure 1.17) which include: plasticization of polymer pellets, metering of polymer melts, injecting of polymer melts into mold cavities, packing, cooling, and finally demolding [1]. However, μIM is not simply a scaled down version of CIM because it involves higher injection velocities and higher molding temperatures and pressures. These are normally adopted to avoid potential short shots during the mold filling process since microparts exhibit very high surface area to volume ratios (up to 10^3-10^6/m) [193], which pose certain challenges for a typical molding process. Consequently, very high shear rates and large thermal gradients are common characteristics of μIM. For example, Jiang et al. [13] pointed out that shear rates as high as 10^6/s are not rare in μIM, which are at least two orders of magnitude higher than those typically encountered in CIM.

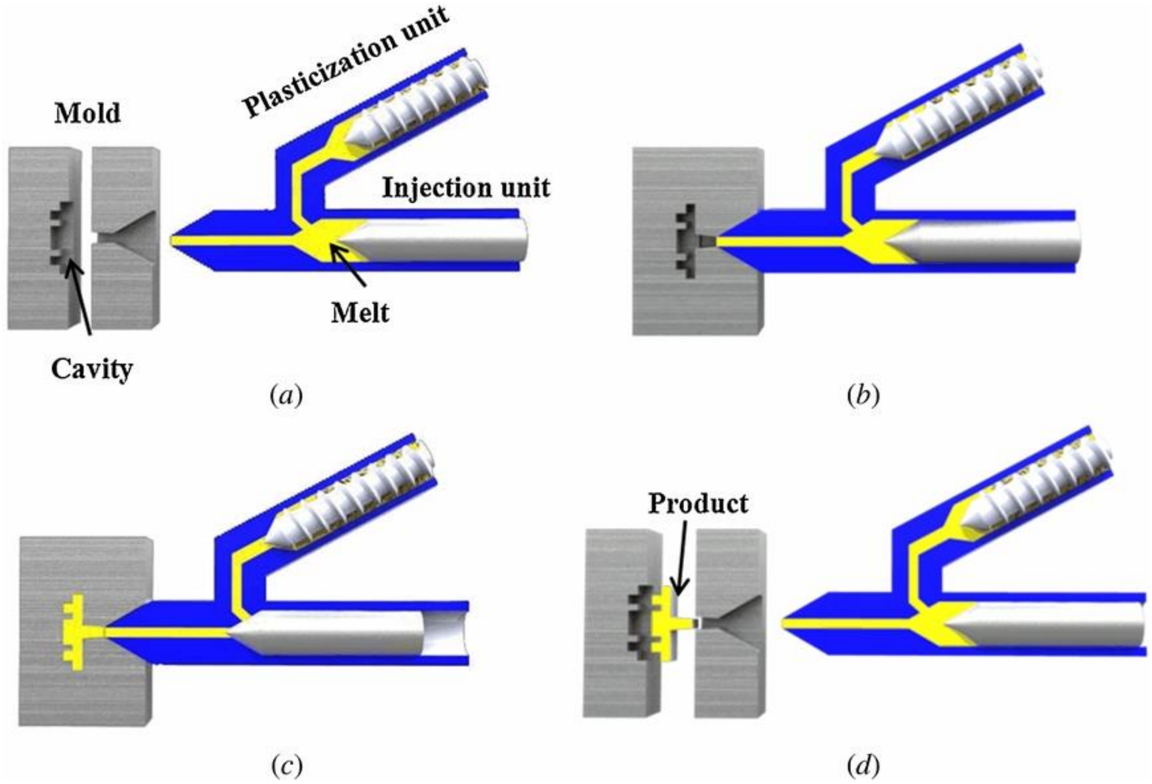

Figure 1.17 Different stages of μIM process: (a) plasticization of polymer pellets, (b) mold closing, (c) injection, packing and cooling, and (d) demolding and re-plasticization [1].

In addition, the cooling effect becomes accentuated in µIM. According to Pan et al. [194], the cooling time for the average temperature of polymer melts to approach the mold temperature during solidification stage is reduced significantly with deceasing thickness of microparts. For example, the cooling time for CIM macroparts (thickness: 1.5 mm) is nearly 60 times longer than that of µIM counterparts (thickness: 0.2 mm), under a defined set of molding conditions. As a result, the thermomechanical history differs greatly between CIM and µIM, which affects the development of microstructure in subsequent moldings. Ding et al. [195] found that there is an *in situ* nano-fibrillization effect of dispersed PCL phase in the PLA/PCL blend microparts, which was induced by prevailing high shearing and fast cooling effects in µIM, whereas only micro fibrils were detected in CIM macroparts.

1.5.3 Special considerations in the microinjection molding process

For the past few decades, great progress has been witnessed with respect to µIM of unfilled and/or filler-containing thermoplastic polymers. Rapid cooling of polymer melts would be anticipated since very high surface area to volume ratio is the common feature for samples with micro/nano-scale features, such as microneedles, microgears and microfluidic chips [193]. Thus, the mold temperature is always set to a temperature close to or higher than the T_g or softening temperature of the polymer melts to prevent early freezing during the mold filling process. For example, the strategy is commonly considered in an attempt to fabricate components with a wall thickness less than 20 µm and/or a flow length-to-wall thickness higher than 10:1 [196]. However, safe removal of microparts requires sufficient stiffness and hardness [196].

To facilitate melt filling and accurate replication of high aspect ratio features, a system called "*variotherm system*" which allows a hot mold during the injection stage and a cold mold during the cooling stage was adopted [197]. However, the long cycle times (four to five minutes) of a *variotherm system* [196] reduce the production efficiency of µIM. For example, Xie and Ziegmann [198] found that it took about 200 and 288 s during the mold heating and cooling processes by switching the mold temperatures between 40 and 180^{o}C. Although the *variotherm system* was developed several decades ago and it demonstrates advantages with increasing flow length, improving the replication of minute features, there are still some challenges which significantly restrict its wide application in industry [197]. A detailed discussion of the *variotherm system* and its potential application in μIM was reported by Su et al. [197].

The intrinsic properties of thermoplastic polymers affect the quality of microparts. Gornik [199] found that PC tends to solidify faster than PS during the mold filling process, which might be attributed to the different intrinsic properties of polymer melts, such as the melt viscosity and thermal conductivity. Consequently, higher mold temperature and injection pressure are needed to aid the rapid filling of the mold.

To better duplicate the micro-features, a thorough investigation of the influence of molding parameters would be of great importance. Therefore, the design of experiments method has been adopted by researchers to understand the influence of machine variables (i.e. process parameters) such as melt temperature, mold temperature, injection velocity, holding time, holding pressure, and backpressure, etc. For example, Zhang et al. [8] reported that the quality of microfeature replication could be significantly affected by the flow direction and molding process parameters. In addition, Chu et al. [7] reported that the injection velocity showed the highest influence during the mold filling process, and the effects of melting temperature and mold temperature varied with respect to molding materials and machine settings.

1.6 Simulation of the microinjection molding process

Numerical simulation has been adopted to predict the mold filling behavior and shear rate distribution in μIM process. However, the size-dependent viscosity of polymer melts (i.e. the viscosity of polymer melts decreases with a reduction of the micro-channel size [200]), wall slip effect and surface tension (especially when the channel size is less than 1 μm [201]), as well as heat transfer between the mold surface and polymer melts could have a significant effect on the melt behavior due to extremely high shear rates and high molding temperatures [1,201–203]. Thus, Chien et al. [202] proposed that prevalent simulation software packages, which are typically developed for CIM, cannot be precisely transferred to simulate or predict the mold filling process without considering the above-mentioned factors. However, obtaining rheological properties of polymer melts under the conditions of μIM is presently infeasible due to the lack of suitable equipment for the very high shearing and cooling effects involved [202]. As a result, current simulation software packages are still adapted for μIM process. For example, Moldflow (Autodesk) [189,204], C-MOLD (AC Technology) [205], Moldex3D (CoreTech System Co., Ltd) [206,207] and finite element analysis [6,208–210] have been employed to assess the mold filling behavior during the μIM process.

Zhang et al. [211] adopted Moldflow software to simulate the mold filling process of a dumbbell micropart. They found that there is an increase of shear rate around the edge with decreasing thickness of the gate, which leads to an increase of local temperature arising from shear heating. Kamal et al. [212] systematically studied the morphology development of POM microparts along the melt flow direction. They reported that the spherulitic core becomes thicker and the skin layer thickness becomes thinner which was quantitatively supported by simulated temperature distribution along the flowing path (using Moldflow).

Su et al. [206] validated the accuracy of simulation of thin-wall micromolding by adopting Moldex3D software. Acceptable agreement was obtained between simulated and measured processing data. However, the actual flow rate was faster than that predicted by simulation which was attributed to the wall slip effect due to the high shear rate involved. They also found that the actaul flow rate of polymer melts and the heat transfer coefficients during the mold filling process had an influence on the simulation results. As a result, these factors need to be determined and considered for accurate prediction of μIM. Moreover, El-Otmani et al. [209] simulated the melt filling behavior of a microgear by using the finite element simulation method. A good agreement between the simulation results and experimental results was found regarding the presence of non-symmetrical distribution of flow front.

1.7 Characterization of microinjection molded products

Normally, the microparts are very tiny in size or very small in weight. Therefore, classical mechanical and dynamic-mechanical analysis cannot be directly applied to determine the properties of microparts. For example, proper clamping of the microparts for mechanical testing is a challenge due to the size constraints or possible slippage [187]. To attempt to address potential slippage of the microparts and ensure sample alignment for mechanical testing, customized sample holders have to be invented [211]. Alternatively, new micro-tensile testing devices, which are specifically designed to accommodate microparts could be employed to evaluate the mechanical properties [213]. In addition, the nanoindentation measurements have been employed to evaluate the mechanical properties such as modulus of elasticity and hardness of microparts [192].

Morphology observation is a straightforward technique, which could provide sufficient details about the micro- and/or nano-structure of microparts. Therefore, scanning electron microscopy (SEM), optical microscopy (OM) and transmission electron microscopy (TEM) are common techniques which can be used to elucidate the structure of microparts. For example, Ding and co-workers [195] reported that the PLA/PCL microparts showed better mechanical properties such as the tensile strength, Young's modulus and strain at break when compared with their CIM counterparts. This is attributed to the presence of dispersed PCL nanofibrils and their preferred orientation in PLA, as revealed by SEM. A summary of testing techniques, which mainly focuses on the measurement of mechanical properties, is available [213].

Thermal properties such as the melting and crystallization behavior can be traced by differential scanning calorimetry (DSC), whereas the thermal stability of microparts can be evaluated by TGA. These techniques are applicable to the characterization of microparts since only a small portion (several mg) of materials is sufficient for thermal measurements.

To the best of our knowledge, the determination of thermal conductivity for micromoldings is currently infeasible due to a lack of suitable commercial testing equipment. However, the miniature size of microparts would become a limiting factor for detecting the thermal conductivity by adopting conventional measurement techniques, such as hot-disk method [97,214–218], laser flash method [219–223] and transient hot-wire technique [224–227]. Thus, suitable techniques need to be invented or developed for accurate determination of the thermal conductivity of microparts.

1.8 Microinjection molding of carbon filled polymer composites

1.8.1 Electrical conductivity

Normally, most polymers are thermally and electrically insulating materials, which hinder their potential application in the areas that require certain conductive properties, such as EMI shielding, ESD protection and thermal dissipation [16,32]. Insulating polymers will become conductive when the incorporated conductive fillers attain a 3D network structure within the host polymer matrices. The electrical conductivity of polymer composites is determined by the intrinsic properties of conductive fillers, the geometric factors of the conductive fillers (i.e. size, shape and aspect ratio), filler dispersion and their interfacial interactions with the polymer matrix [155,156,228] as well as processing methods [101].

1.8.1.1 The effect of carbon filler type

Hofmann et al. [167] reported that the electrical conductivity of insulating polymers can be greatly enhanced with the addition of carbon-based fillers and the trend of electrical conductivity enhancement varies with the types of carbon fillers employed. For example, functionalized graphene loaded polymer composites showed lower p_c and slightly higher electrical conductivity when compared with that of CNT-, CB- or EG-filled counterparts. In a recent study, Santos et al. [229] pointed out that samples containing large size GNP particles demonstrated higher electrical conductivity.

1.8.1.2 The effect of polymer matrix

Abbasi et al. [101] studied the electrical conductivity of CNT filled PP and PC composites in µIM, respectively. The electrical conductivity of PP/CNT microparts is approximately one order of magnitude higher than that of PC/CNT counterparts, which is attributed to the fact that PP is a semi-crystalline polymer and the formation of PP crystals would expel the dispersion of CNT in the amorphous region. The existence of CNT-rich amorphous phase is beneficial to the enhancement of electrical conductivity as per the concept of double p_c phenomenon [101].

1.8.1.3 The effect of surface modification of conductive fillers

Ferreira et al. [95] investigated the state of dispersion of pristine and functionalized CNT (i.e. p-CNT and f-CNT) in PA6. The CNTs were functionalized based on the 1,3-dipolar cycloaddition reaction of azomethine yields using N-benzyloxycarbonyl glycine and formaldehyde, as reported by Paiva and co-workers [230]. Their results revealed improved dispersion of f-CNT in subsequent microparts when compared with that of p-CNT filled counterparts. However, PA6/p-CNT samples showed higher electrical conductivity when compared with samples containing f-CNT. The phenomenon was attributed to the development of a PA6/f-CNT interphase, which acts as an insulating barrier, thereby impeding the enhancement of electrical conductivity. The result is consitent with the findings reported by Bose et al. [231]. For example, Bose et al. reported that the p_c for f-CNT filled PA6/ABS blends is about 3-4 wt%, which is slightly higher than that of unmodified CNT loaded counterparts (~1-2 wt%).

1.8.1.4 The effect of molding conditions

The processing conditions, such as molding temperatures, injection velocity and molding pressures, are of significant importance in determining microstructure in injection molding [38]. Kamal et al. [212] found that a five-layer skin core structure could be formed in POM microparts (see Figure 1.18), in comparison with commonly reported three-layer structure in CIM macroparts. They also found that the injection velocity shows the highest impact on the development of microstructure, followed by mold temperature. The variation of skin-core structure would greatly influence the properties of microparts. Zhang et al. [193] reported that the modulus and hardness of the skin layer are higher than the core layer. In addition, the Young’s modulus and strain at break as well as yield stress increase with an increase of skin ratio [193]. The development of microstructure was correlated with the variation of process parameters, such as mold temperature, injection velocity and holding pressure [193]. Zhao et al. [232] reported that the metering size and holding pressure/time as well as their interaction could significantly affect the quality of microparts. Song and co-workers [233] found that the filling capability would be greatly reduced with a reduction of part thickness in ultra-thin wall injection molding process. Sha et al. [234] reported that increasing the melting temperature (T_m), mold temperature and injection velocity would generally improve the replication qualities of molded micro-features.

In addition, Jiang et al. [13] reported that increasing injection velocity would enhance the electrical conductivity of POM/CNT microparts whereas an adverse effect was found by Fei et al. [235], which supports that host polymer selection would affect the construction of conductive pathways within the microparts. The above indicates that the chosen molding parameters would significantly influence the development of conductive pathways within the microparts, thereby affecting the properties of subsequent moldings.

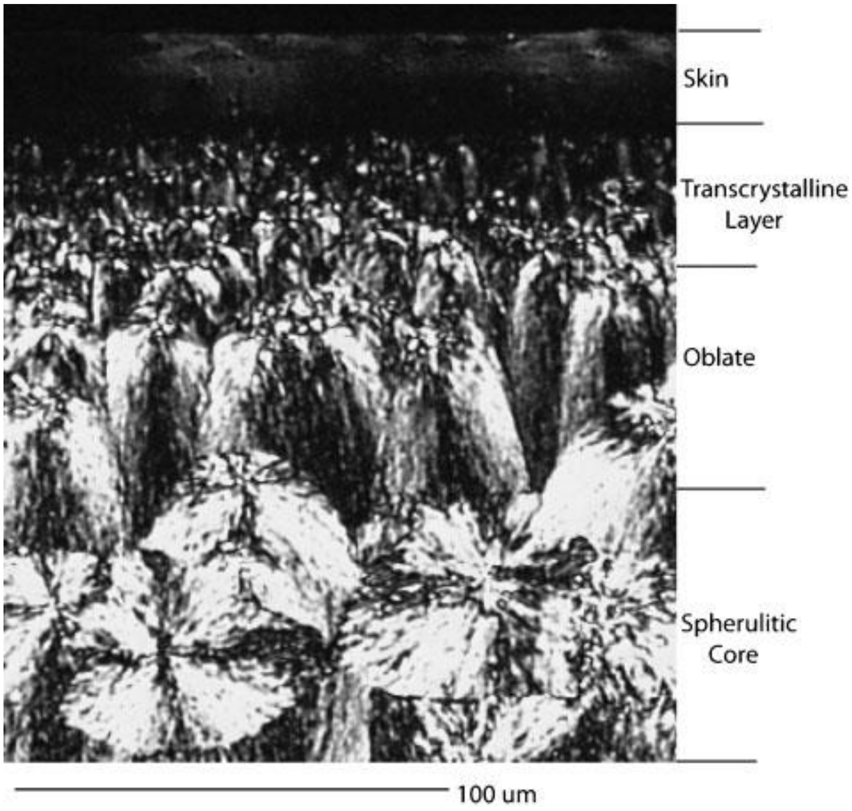

Figure 1.18 Five morphological zones in a POM micropart, observed across the transverse direction. Adapted from [212].

1.8.2 Morphological properties

It has been mentioned in *Section 1.5* that μIM involves extreme shearing conditions and large thermal gradients which could significantly determine the microstructure, especially for filler-containing counterparts. For example, Jiang et al. [13] found that the distribution of CNT showed a hierarchical structure across the transverse direction of CNT filled POM microparts, as shown in Figure 1.19. There is a strong orientation of CNT in the shear layer of microparts whereas the degree of filler orientation becomes less in the core layer, which could be attributed to the difference of shearing effect between the shear layer and the core layer of microparts. However, such phenomenon is not obvious in CIM macroparts since skin layer occupies a negligible fraction of total thickness. In addition, large size spherulite structures are observed in CIM macroparts, whereas highly oriented shish-kebab structures are present along the flow direction (Figure 1.20), which is due to the marked difference of shearing effect between different molding processes, i.e. CIM and μIM [12,13].

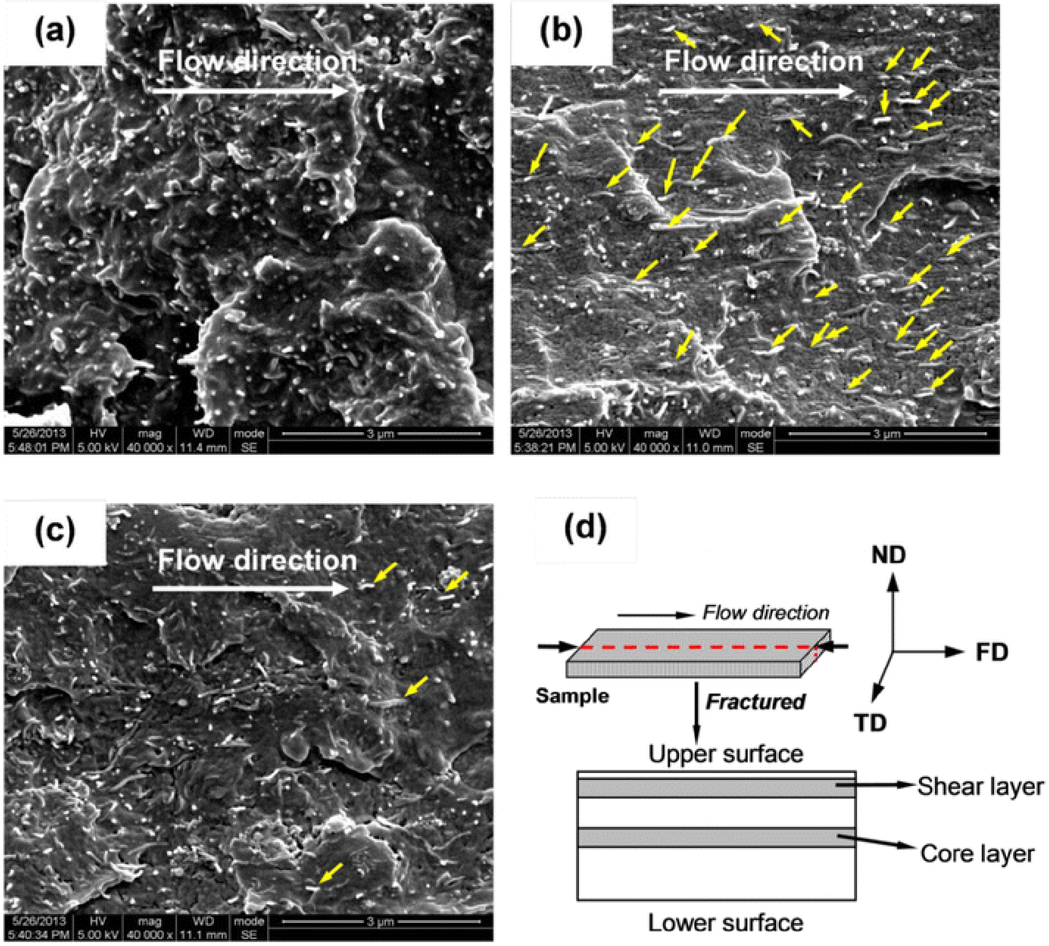

Figure 1.19 SEM images of cryo-fractured surface of (a) a CIM macropart and (b-c) a micropart. For example, (b) shows the shear layer of a micropart; (c) shows the core layer of a micropart; (d) shows the preparation of fractured surface along the ND-FD plane in liquid nitrogen. FD: flow direction, TD: transverse direction, ND: normal direction [13].

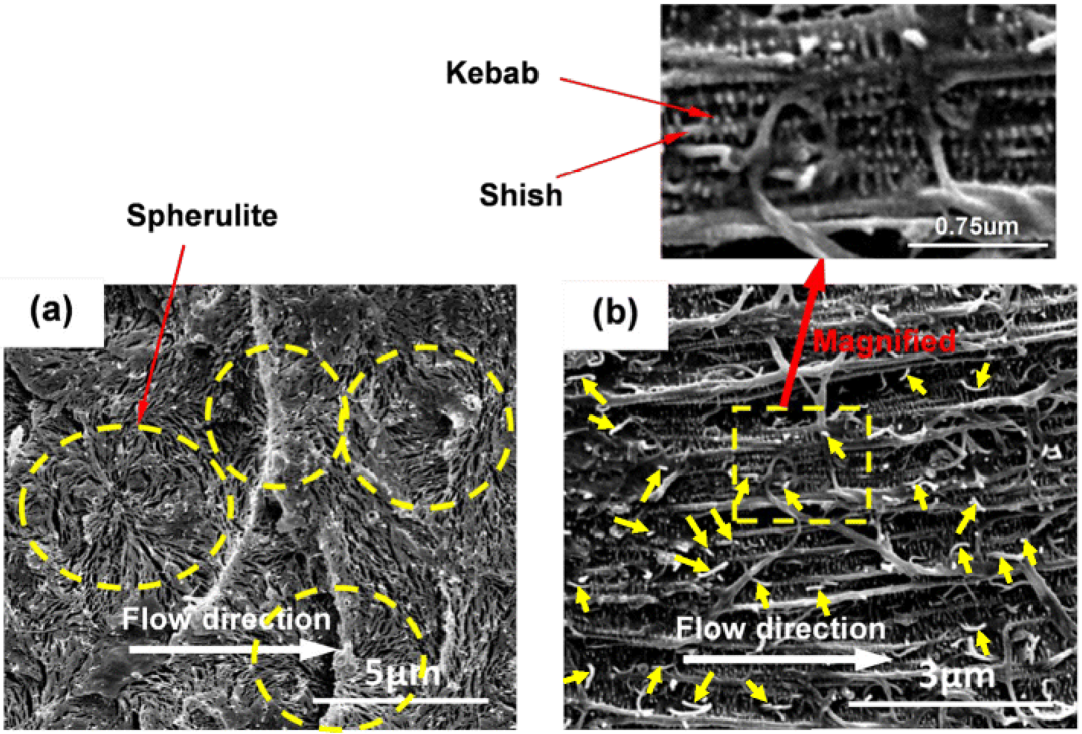

Figure 1.20 SEM images of the etched fractured surface of (a) macropart, and (b) micropart of a POM/CNT 5 wt% nanocomposite in flow direction [13].

Ferreira et al. [95] reported that an improved distribution of CNT in PA6 was achieved by using chemically modified CNT, which was ascribed to the better interfacial interactions between functionalized fillers and the host matrix. Furthermore, samples prepared by µIM showed improved filler distribution, which suggests that the very high shearing conditions would facilitate the dispersion of nanotubes [236].

1.8.3 Mechanical properties

The addition of carbon fillers would greatly affect the mechanical properties of subsequent moldings. For example, Heinrich et al. [237] systematically investigated the influence of T_m and injection velocity on the mechanical properties of PP/CNT microparts. Their results showed that both the Young's modulus and yield stress of PP/CNT microparts decreased with an increase of T_m from 240 to 300^{o}C. However, injection velocity showed a similar but less profound impact on the mechanical properties of the microparts. Wang et al. [238] reported that the mechanical properties, such as yield stress, Young’s modulus and storage modulus, of PCL/reduced graphene oxide (PCL/RGO) microparts was enhanced with an increase of filler concentration up to 1 wt%. The substantial increase of mechanical properties was attributed to the intrinsically high mechanical strength of RGO and the enhanced crystallization and orientation of PCL/RGO composites. However, Zhong and Isayev [239] found that the tensile strength gradually decreased with increasing fraction of graphite in polyetherimide (PEI), which could be correlated with the existence of graphite agglomerates, as corroborated by OM observations. Hofmann and co-workers [167] found that the Young’s modulus of PA12 was significantly enhanced with the addition of TRGO, in comparison with CNT or CB loaded counterparts, which was ascribed to the improved dispersion of functionalized graphene within the host matrix.

Abbasi et al. [101] studied the effect of filler concentration on the mechanical properties of PC/CNT and PP/CNT composites in µIM. Their results indicated that the strain at break decreases significantly with the addition of CNT, which is attributed to the existence of CNT agglomerates in subsequent moldings. The CNT content showed modest impact on the tensile strength, which was attributed to the poor interfacial interactions between CNT and the host polymer matrix.

Aside from the influence of molecular structure of polymer matrix and characteristics of fillers, the properties of injection molded microparts are strongly dependent on the evolution of microstructure. For example, Liou and Young [240] found that the filling efficiency of reinforcements in the microfeatures is greatly affected by the size of added particles and microfeatures as well as filler content. Thus, the variation of filling behavior with respect to filler size has a significant impact on the local mechanical properties of microfeatures.

1.8.4 Crystallization properties

The crystallization behavior for polymer composites and subsequent moldings could be traced by DSC. For example, Jiang et al. [13] reported that there are two melting peaks for POM/CNT microparts in comparison with that of CIM counterparts, which was attributed to the presence of various crystal morphologies of POM. For example, only spherulite structure is present in CIM macroparts whereas a typical shish-kebab structure is observed in microinjection molded counterparts, as depicted in Figure 1.20. The presence of highly aligned shish-kebab structure was ascribed to the prevailing high shear rate existing in the shear layer of the microparts. They also found that the peak intensity of secondary shoulder peak increases with CNT concentration, which suggests that the formation of shish-kebab structure was related to the number of aligned CNT structures along the melt flow direction. In addition, either increasing the injection velocity or mold temperature is beneficial to the formation of shish-kebab structure, which is related to the enhancement of flow induced crystallization of polymer chains [13].

1.9 Original contribution of the work

There has been increasing research interest from both the academic and industrial spheres with respect to the micromolding of functional components which is always accommodated by molding multi-functional fillers loaded polymer composites. Carbon-based fillers, such as CNT, CB, graphene and graphite, etc., have been widely adopted as functional fillers to enhance the electrical and thermal conductivities as well as the mechanical properties of thermoplastic polymers thanks to their lightweight, exceptional electron transport behavior and good dispersibility within the host polymers.

Presently, microinjection molding (μIM) of CNT loaded polymer composites is receiving attention due to its capability to effectively enhance the overall electrical and thermal conductivities as well as mechanical properties. To the best of our knowledge, there is no comprehensive study with respect to the influence of process parameters, the types of polymer matrices and carbon fillers, the utilization of immiscible polymer blends and hybrid filler loading on the electrical and morphological properties of carbon filled microparts. To attempt to address this knowledge gap, a rectangular mold insert which has three consecutive zones with decreasing cavity thickness along the melt flow direction was employed in this study. The adoption of the three-step mold insert allows us to evaluate the properties of samples which have undergone different thermomechanical histories. Thus, the research was carried out as follows:

- In this study, the influence of machine variables (i.e. process parameters) such as melt temperature, mold temperature, backpressure and injection velocity on the electrical conductivity of PP/CNT 10 wt% microparts was systematically studied by adopting the design of experiments (DOE) method.

- Different types of polymer matrices which have different intrinsic properties such as polarity and crystallinity were adopted as host polymer matrices for CNT. The selected polymer matrices are PP, PS, PA6 and PC, respectively. A comparison of the electrical conductivity and microstructure for CNT filled polymers was studied.
- The efficacy of adopting immiscible polymer blends (PLA/PBSA) on the properties of CNT filled blend composites was studied. In addition, the blending sequence for different components of immiscible blend composites (i.e. PLA, PBSA and CNT) was investigated.
- Different types of carbon fillers such as CNT, CB, GNP, and graphite were adopted as conductive fillers in PP. The influence of filler type on the electrical conductivity and morphological properties of corresponding microparts was studied.
- The effect of hybrid filler loadings (i.e. CNT and CB) on the electrical conductivity and morphological properties of PS microparts was studied. In addition, the effect of annealing on the electrical conductivity of microparts was studied in detail.
- A mold insert which has a uniform thickness (0.85 mm) along the flow direction as that of the thick section of the three-stepped mold insert was adopted to fabricate PP/CNT microparts under the same processing conditions. The properties of plaque microparts were compared with those of three-step counterparts.

1.10 Organization of the thesis

The research methodology will appear in Chapter 2. Chapter 3 gives a breakdown of main findings of the present research. Chapter 4 elaborates the experimental part which provides detailed information for sample preparation and subsequent characterizations. The main achievements of the present research will be exhibited in Chapter 5. The conclusions are placed in Chapter 6, followed by the recommendations for future research in Chapter 7.

Chapter 2

2 Research methodology

As mentioned in Chapter 1 *Section 1.3*, melt blending is commonly adopted to fabricate filler-containing polymer composites because it is environmental friendly (solvent free) and compatible with current industrial practice when compared with *in situ* polymerization and solution mixing. Thus, the melt blending method was employed in the present study to fabricate carbon filled polymer composites which were subjected to compression molding and microinjection molding processes. In this chapter, a brief description of the adopted research methodologies is given below.

2.1 Preparation of carbon filled composites

Two different processing strategies were adopted to prepare different carbon filled polymer composites and subsequent moldings. The preparation procedure is illustrated below.

- **Masterbatch dilution approach**

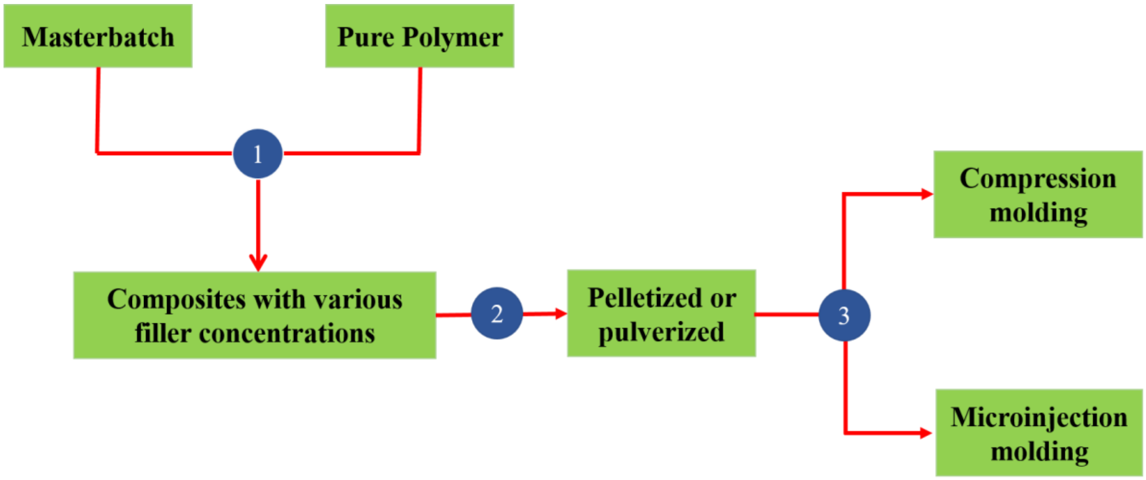

Figure 2.1 Preparation (masterbatch dilution) of carbon filled polymer composites and subsequent moldings.

The processing conditions are subject to the types of polymer matrices employed. Therefore, detailed processing conditions will be provided in Chapter 4. Three main steps are involved during the sample preparation. Briefly stated, the first step is the melt dilution of a commercially available masterbatch. All experiments were performed by employing a laboratory scale twin-screw mixer or a batch mixer, under a defined set of processing conditions. Afterwards, the obtained composites were either pelletized or pulverized to obtain suitable size particles for subsequent µIM or compression molding. The original polymer in the masterbatch will not significantly affect the properties of prepared polymer composites because only a small quantity of masterbatch is required [12].

- **Direct melt mixing approach**

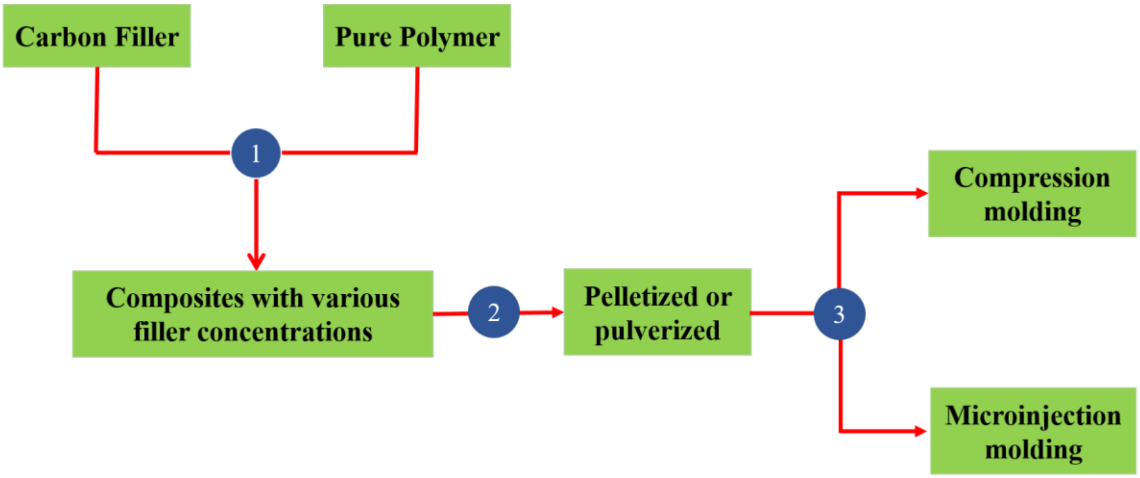

Figure 2.2 Preparation (direct mixing) of carbon filled polymer composites and subsequent moldings.

Similarly, the processing conditions are subject to the types of polymer matrices employed. The detailed processing conditions for each system will be provided in Chapter 4. Three main steps are involved during sample preparation. Briefly stated, the first step is melt mixing of polymer pellets with different types of carbon fillers. All experiments were performed by adopting a laboratory scale twin-screw mixer or a batch mixer, under a defined set of processing conditions. Then, the resultant composites were either pelletized or pulverized to make suitable size particles for subsequent µIM or compression molding.

2.2 Design of experiments

The design of experiments (DOE) method was employed to elucidate the effects of process parameters on the electrical and dimensional properties of PP/CNT 10 wt% composite. The selected process parameters were melt temperature, mold temperature, backpressure and injection velocity, which are the key machine variables for the injection molding process [7,88,147,149]. The levels of molding conditions and applied experimental design will be tabulated in *Section 4.4*. The obtained results will be analyzed using a statistical software, Minitab 17 (USA).

Chapter 3

3 Thesis structure

The achievements of the present research will be displayed in Chapter 5, which contains five sub-sections. Each sub-section of Chapter 5 includes the main findings (i.e. results and discussion) which either were published or will be submitted to a scientific journal. The organization of Chapter 5 and the rest parts of the thesis are presented below.

➢ **Chapter 5**

- ***Section 5.1*** discusses the influence of process parameters such as melt temperature, mold temperature, backpressure and injection velocity on the properties of PP/CNT 10 wt% composites in μIM, by using the design of experiments method. In addition, the microstructure development and crystallization behavior of the microparts are explored. Part of this section was published in the journal of "Polymer Engineering & Science" (S. Zhou, A.N. Hrymak, and M.R. Kamal, 2018; 58(S1), E226-E234) and a conference paper (SPE ANTEC® 2016 Indianapolis, 1167-1171).
- ***Section 5.2*** reports the influence of host matrix on the electrical and morphological properties of subsequent microparts. Experimental results are explained in terms of theoretical interfacial interaction calculations. The employed polymers are PP, PS, PA6 and PC. CNT is adopted as the conductive filler. In addition, the effect of filler concentration on the properties of corresponding moldings are detailed. Content of this section was published in the following journals: "Polymers for Advanced Technologies" (S. Zhou, A.N. Hrymak, and M.R. Kamal, 2018; 29(6): 1753-1764), "Composites Part A: Applied Science and Manufacturing" (S. Zhou, A.N. Hrymak, and M.R. Kamal, 2017; 103: 84-95), "Polymer Engineering & Science" (S. Zhou, A.N Hrymak, and M.R. Kamal, 2016; 56(10): 1082-1190) and "International Polymer Processing" (S. Zhou, A.N. Hrymak, and M.R. Kamal, 2018; 33(4): 514-524).
- ***Section 5.3*** explores the effect of compounding sequence of components of PLA, PBSA and CNT on the electrical conductivity of PLA/PBSA/CNT microparts; in addition, the microstructure evolution and thermal properties of PLA/PBSA/CNT

microparts are studied in detail. This section was reported in the journal of "Journal of Materials Science" (S. Zhou, A.N. Hrymak, and M.R. Kamal, 2018; 53(12): 9013-9025).

- ***Section 5.4*** systematically investigates the effect of different types of carbon fillers, such as CNT, CB, GNP, SG and LTEG on the properties of PP composites obtained via μIM. The electrical and morphological properties of subsequent microparts are explored in detail. Part of this section was reported in the journal of "Journal of Applied Polymer Science" (S. Zhou, A.N. Hrymak, and M.R. Kamal, 2017; 134(43): 45462), "International Polymer Processing" (S. Zhou, A.N. Hrymak, and M.R. Kamal, 2018; 33(4): 514-524) and a conference paper (SPE ANTEC® 2018 Orlando). Additionally, part of this section may be included in a manuscript submitted to a journal in the future.
- ***Section 5.5*** reports the influence of hybrid filler loading of CB and CNT in PS, and the impact of annealing on the electrical conductivity and morphological properties of different carbon filled PS microparts. This section will be submitted to a journal.

➢ **Chapter 6** is the conclusion section which covers all aspects of findings achieved in this research.

➢ **Chapter 7** points out the recommendations for future studies.

➢ **Appendix section** discusses the effect of mold geometry on the properties of CNT-containing PP microparts in μIM by adopting different types of mold inserts. A mold insert which has uniform thickness (0.85 mm) along the flow direction was adopted to fabricate microparts. The electrical conductivity and morphological properties of subsequent plaque microparts were compared with those of three-step counterparts. Part of this section may be included in a manuscript submitted to a journal in the future.

Chapter 4

4 Experimental: materials, equipment & characterizations

Experimental aspects relating to the present study are described in this chapter.

4.1 Materials

Masterbatches:

Four types of CNT-containing masterbatches were used in this study, which are listed in Table 4.1. They were kindly donated by Hyperion Catalysis International Inc. (Cambridge, MA, USA) and all information on relevant grades was obtained from the company's website (http://hyperioncatalysis.com/technology2.htm). According to the supplier, the proprietary nanotubes, FIBRIL^{TM}, were vapor grown with a length over 10 μm and an outside diameter about 10 nm. The FIBRL^{TM} nanotubes have a density of 1.75 g/cm^3 [241] and a surface area of about 178 m^2/g [242].

Table 4.1 Grades of CNT-containing masterbatches from Hyperion Catalysis International.

Base resin	Grade name	CNT concentration (wt%)
PP	MB3020-01	20
PS	MB2020-00	20
PC	MB6015-00	15
PA6	MB4020-00	20

Polymer resins:

Isotactic polypropylene (PP, average Mw: ~250,000; average Mn: ~67,000) was purchased from Sigma Aldrich (Oakville, Canada). The polymer has a density of 0.9 g/cm^3 and a melt flow index of 12 g/10 min (230^{o}C @ 2.16 kg load).

Polystyrene (PS) was supplied by Tabriz Petrochemical Company with a commercial grade of GPPS 1540. According to the supplier, GPPS 1540 is an easy flowing polymer which is suitable for extrusion or injection molding applications. The polymer has a density of 1.04 g/cm^3 and the melt flow index is 11 g/10 min (200^{o}C @ 5 kg load).

Polycarbonate (PC), under a trademark of Panlite® K-1300, was obtained from Teijin Chemicals Ltd. (Japan). The density of PC is 1.20 g/cm^3. PC is hygroscopic and must be dried thoroughly prior to melt processing. Thus, pure PC and related composites were dried under vacuum at 120^{o}C for 5 h.

Polyamide 6 (PA6), under a trademark of Ultramid® B3S, was kindly provided by BASF Corporation, North America. According to the supplier, the PA6 is an easy flowing, finely crystalline injection molding grade which is suitable for thin-walled products. It has a density of 1.13 g/cm^3 and melt volume-flow index of 160 cm^3/10 min (275^{o}C @ 5 kg load). Prior to processing, PA6 and related composites were dried under vacuum at 85 °C for 8 h.

Poly(lactic acid) (PLA), under a tradename of 4032D was obtained from Natureworks LLC (USA) and Poly[(butylene succinate)-co-adipate] (PBSA), under a trademark of Bionolle 3001M was supplied by Showa High Polymer (Japan). Some characteristic properties of PLA and PBSA are available in Table 4.2. To remove eventual traces of moisture, both the PLA and PBSA were dried under vacuum at 60°C for 12 h prior to melt compounding.

Table 4.2 Some characteristics properties of PLA and PBSA [243].

Properties	PLA (4032D)	PBSA (3001M)	ASTM method
Density (g/cm^3)	1.24	1.23	D792
T_g (^{o}C)	55-60	-45	D3418
Melt flow index (g/10 min) @ 210^{o}C/2.16 kg load	7	1.4	D1238
T_m (^{o}C)	155-170	94	D3418

Carbonaceous fillers:

Five types of carbon fillers were employed as conductive additives in this research. The relevant grade and properties of each filler are listed in Table 4.3. The morphologies of CB and GNP were characterized by SEM. Prior to morphology observations, CB and GNP were dispersed in acetone. Figure 4.1(a) indicates that the primary CB particles have a typical spherical shape and a great tendency to form a ‘string-bead’ like structure due to the strong Van der Walls forces. The mean particle size is in a range from 30 to 50 nm. Figure 4.1(b) reveals that GNP has a plate-like structure and the mean particle size is approximately 15 µm.

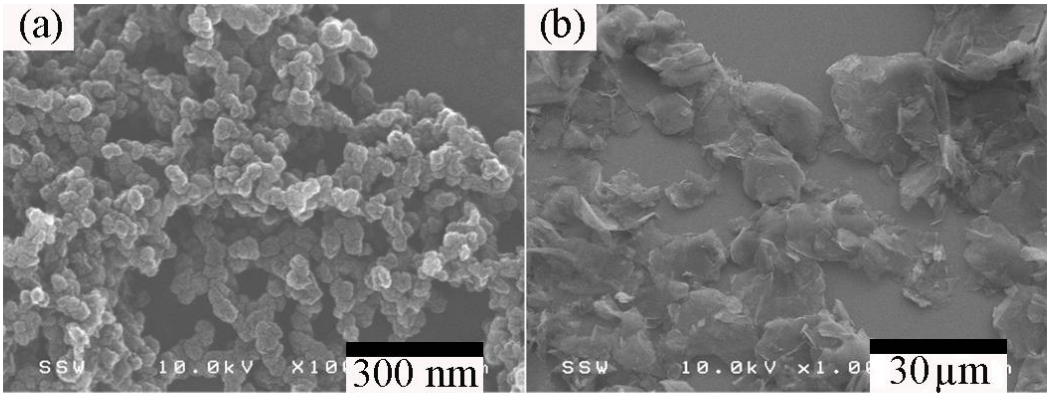

Figure 4.1 The images of (a) CB and (b) GNP.

The morphologies of synthetic graphite (SG) and low temperature expandable graphite (LTEG) are displayed in Figure 4.2. According to Rew et al. [244], the average particle size of SG is about 20 µm and the resistivity is 0.047 Ω cm. According to the supplier, the initial expanding temperature of LTEG is in the vicinity of 150°C (as corroborated by Wu et al. [109]) and the overall expansion ratio is about 230 mL/g. In addition, LTEG exhibits a mean particle size of nearly 180 µm with a density of 2.20 g/cm^3.

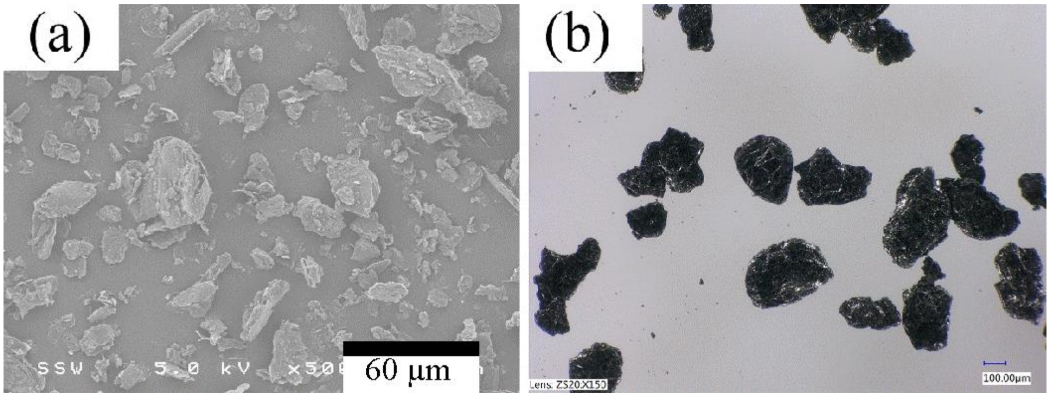

Figure 4.2 The images of (a) pristine SG, and (b) LTEG.

Table 4.3 Relevant grade and properties of carbon fillers.

Filler	Manufacturer	Grade	Density (g/cm^3)	Surface area (m^2/g)
CB	Akzo Nobel Polymer Chemicals LLC. (Chicago, IL, USA)	Ketjenblack® EC-600JD	1.80	~1400
GNP	XG Sciences Inc. (Lansing, MI, USA)	xGnP® Grade M	2.20	120~150
CNT	Chengdu Organic Chemicals Co. Ltd., (China)	TNIM2	2.10	230
SG	Asbury Graphite Mills Inc. (Asbury, NJ, USA)	A99	2.23	8
LTEG	Shijiazhuang ADT Carbonic Material Factory (China)	ADT KP801	2.20	N/A

The above-mentioned characteristic data were taken from the datasheets provided by the suppliers. N/A: Not applicable.

The industrial grade multi-walled carbon nanotubes (CNT, Grade: TNIM2) was purchased from Chengdu Organic Chemicals Co. Ltd. (China). The morphology of pristine CNT is displayed in Figure 4.3. The nanotubes are clearly entangled together. According to the supplier, the CNT, with length in the range of 30–50 µm, was fabricated by chemical vapor deposition (CVD) method. The outer diameter and inner diameter of the CNT are 8-15 and 3-6 nm, respectively.

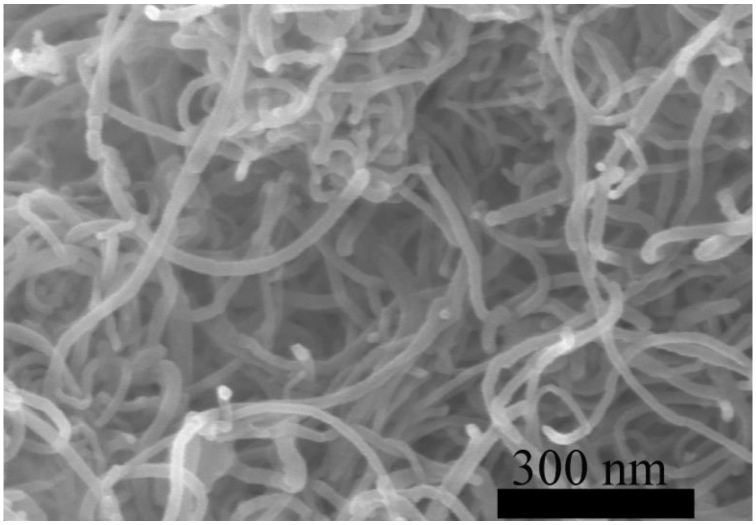

Figure 4.3 SEM image of as-received multi-walled carbon nanotubes, CNT.

4.2 Preparation of carbon filled microparts

All carbon filled polymer composites were prepared by melt blending using either a laboratory scale twin-screw mixer or an internal batch mixer. The detailed preparation procedure for all samples is given below.

i. For samples used in *Section 5.1*.

The adopted material in this section is PP/CNT 10 wt% composite. Samples were prepared by melt dilution of CNT-containing masterbatch (PP/20 wt%) from Hyperion Catalysis International with pure PP, under the operating conditions of 60 rpm and 190^{o}C for 10 min by using a laboratory scale co-rotating twin-screw mixer (Haake Minilab Rheomix CTW5, USA).

ii. For samples used in *Section 5.2*.

In this section, different types of polymer matrices were used during sample preparation. The processing conditions for each sample are tabulated in Table 4.4. All samples were prepared by the melt dilution of masterbatches from Hyperion Catalysis International with corresponding pure polymer matrix, as elaborated in *Section 4.1* Table 4.1. The PA6 and PC are hygroscopic materials. Therefore, PA6 and PC as well as corresponding CNT-containing masterbatch pellets were dried thoroughly prior to melt processing.

Table 4.4 Processing conditions for CNT-containing polymer composites.

Sample	Equipment type (laboratory scale)	Conditions
PP/CNT 10 wt%	Internal batch mixer (C.W. Brabender Instruments)	50 rpm/190ºC/10 min
PS/CNT 10 wt%	Twin-screw mixer (Haake Minilab Rheomix CTW5)	60 rpm/200°C/10 min
PA6/CNT 10 wt%	Twin-screw mixer (Haake Minilab Rheomix CTW5)	60 rpm/240ºC/10 min
PC/CNT 10 wt%	Internal batch mixer (Haake Rheomix OS)	50 rpm/260°C/10 min

iii. For samples used in *Section 5.3*.

The PLA/PBSA immiscible blend with a mass ratio of 7:3 was prepared simultaneously in a Brabender batch mixer (C.W. Brabender Instruments, Inc., South Hackensack, NJ, USA), operating at 190ºC and 60 rpm for 5 min. PLA/PBSA/CNT blends, PLA and PBSA had a constant mass ratio of 7:3, and the incorporated CNT was kept at 5 wt% for the whole system, which could be identified as PLA(66.5 wt%)/PBSA(28.5 wt%)/CNT(5 wt%).

Different compounding procedures were adopted to prepare PLA/PBSA/CNT composites. *Sample 1*: PLA was firstly compounded with CNT for 5 min at the above-mentioned conditions, then PBSA was added to the PLA/CNT blend and mixed for another 5 min. *Sample 2*: PBSA was firstly compounded with CNT for 5 min, then PLA was added and compounded for another 5 min at the same conditions. *Sample 3*: PLA and PBSA were pre-mixed for 5 min, then CNT was added and compounded for another 5 min. *Sample 4*: PLA, PBSA and CNT were simultaneously added into the batch mixer and compounded at the previous conditions for 10 min. In comparison with PLA/PBSA/CNT immiscible blends, pure PLA and PLA/CNT 5 wt% blends were processed at the same conditions. All blends were crushed into small particles for μIM.

iv. For samples used in *Section 5.4*.

The Brabender batch mixer (C.W. Brabender Instruments), equipped with two counter-rotating blades, was used to prepare carbon fillers loaded PP composites. The concentration of carbon-based fillers (such as CB, GNP and CNT) was in a range from 0.5 to 15 wt%.

The compounding was carried out at 50 rpm and 190^{o}C for 10 min, and the obtained blends were crushed and used for µIM. Similar to previously mentioned systems, CNT-containing PP composites were prepared by melt dilution of PP/CNT 20 wt% masterbatch. To differentiate and express each system clearly, the obtained blends were named as follows: CB0.5 indicates the concentration of CB in PP/CB composites is 0.5 wt%, and GNP0.5 and CNT0.5 indicate that the concentration of GNP and CNT is 0.5 wt%, respectively. The PP/SG composites with filler concentrations of 10, 20, 30, 40 and 50 wt% were fabricated under the same conditions of 190°C and 50 rpm for 10 min, using Brabender. Similarly, a blend of PP composite with 30 wt% LTEG was prepared under the same conditions.

v. For samples used in *Section 5.5*.

The Brabender batch mixer (C.W. Brabender Instruments) was employed to fabricate different carbon fillers loaded polymer composites. The concentration of total carbon fillers in PS is fixed at 3, 5 and 10 wt%, respectively. However, the weight ratio of CNT to CB was systematically altered at various combinations (100/0, 30/70, 50/50, 70/30 and 0/100). Melt blending was carried out at 200^{o}C and 50 rpm for 10 min. The obtained samples were named as *x*-PS/CNT*y*0/CB*z*0, where *x* is the weight fraction of total carbon fillers, *y* and *z* are the weight ratio of CNT and CB in the total carbon fillers. To put it simply, 3 wt%-PS/CNT30/CB70 represents the samples with 3 wt% total carbon fillers and the weight ratio of CNT to CB is 3:7, i.e. PS(97 wt%)/CNT(0.9 wt%)/CB(2.1 wt%).

4.3 Equipment and mold inserts

All samples prepared in *Section 4.2* were subject to µIM in a Battenfeld Microsystem 50 (Wittmann Battenfeld GmbH, Austria), as displayed in Figure 4.4. The all-electric molding machine features a plunger injection system, which consists of a screw plasticization unit, a metering unit, and an injection unit [7]. The maximum clamping force and injection velocity are 50 kN and 760 mm/s, respectively. As given in Figure 4.4(b), an extrusion screw with a diameter of 14 mm was mounted at an angle of 45 degrees to the direction of the injection piston. Then, a pre-set volume of polymer melt was transferred to the metering unit which allows accurate replication of products. Then, a certain amount of polymer melt was delivered into the injection unit and was pushed forward into the mold insert with the advancement of the injection piston. The diameter of the injection piston is 4.89 mm.

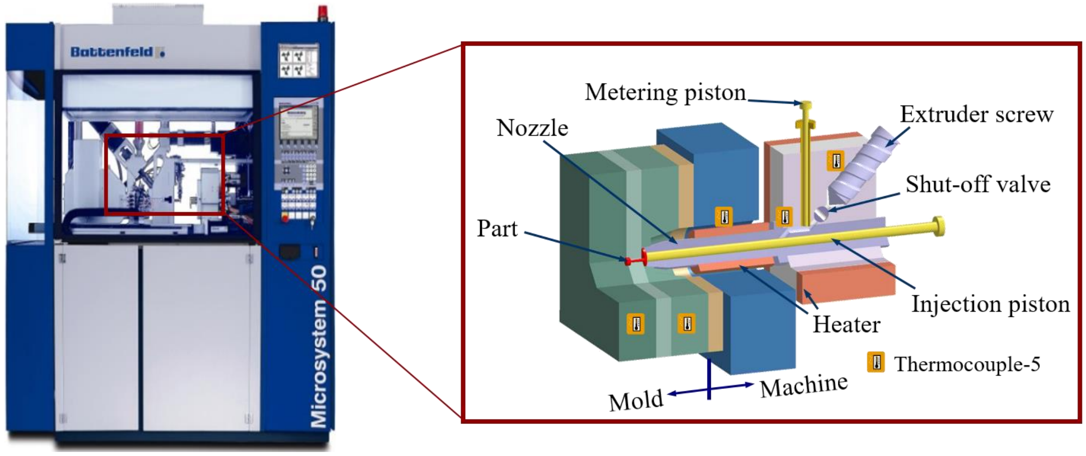

Figure 4.4 Image of a Battenfeld Microsystem 50 machine and the schematic layout of the plasticization unit, metering unit and injection unit. Adapted from Battenfeld: http://www.battenfeld.ru/fileadmin/templates/docs/imm/microsystem_presentation.pdf.

A mold insert which has three consecutive zones with decreasing thickness along the flow direction [245] was adopted, as depicted in Figure 4.5 (b). The dimensional details for each section of the microparts are tabulated in Table 4.5. The adoption of the three-step mold insert allows us to investigate the properties of samples which have experienced different thermomechanical histories under various shearing and cooling conditions.

Table 4.5 Dimensional details for each section of the three-step microparts.

Designation	Length (mm)	Width (mm)	Thickness (mm)
Thick section	5.00	2.40	0.85
Middle section	5.00	2.40	0.50
Thin section	4.80	2.40	0.20

4.4 Processing conditions of carbon filled microparts

The processing conditions for microparts varied with the materials of interest. Therefore, the detailed processing conditions for each set of microparts are provided below.

I. For microparts in *Section 5.1*.

As mentioned in *Section 1.4*, the properties of injection molded parts can be significantly affected by adjusting the process parameters. To elucidate the effect of process parameters such as melt temperature, mold temperature, backpressure and injection velocity on the properties of PP/CNT microparts, a 2^4 factorial design was employed because 2^k factorial design requires the smallest number of runs when a few influential factors are to be studied. The levels of molding conditions and the applied experimental design are given below.

Table 4.6 Experimental design showing the 2-level 4-factor full factorial design.

Exp.	T_melt (ºC)	T_mold (ºC)	Back_Press (bar)	Inj_Vel (mm/s)
1	220	60	50	100
2	220	60	50	500
3	220	60	100	500
4	220	60	100	100
5	220	100	50	100
6	220	100	50	500
7	220	100	100	500
8	220	100	100	100
9	260	100	50	100
10	260	100	50	500
11	260	100	100	500
12	260	100	100	100
13	260	60	100	100
14	260	60	100	500
15	260	60	50	500
16	260	60	50	100

II. For microparts in *Section 5.2*.

In this study, four different types of polymer composites were employed. The melt and mold temperatures for each type of the polymer composites were given in Table 4.6. The injection velocity for all experiments was 300 mm/s. The CNT filled PA6 and PC composites were dried thoroughly under vacuum to remove traces of moisture prior to melt processing.

Table 4.7 Processing conditions of polymer/CNT microparts.

Microparts	PP/CNT	PS/CNT	PA6/CNT	PC/CNT
Melt temperature (°C)	260	260	260	300
Mold temperature (°C)	100	80	80	100

III. For microparts in *Section 5.3*.

The experiments were carried out at a melt temperature of 180°C and a mold temperature of 55°C. The injection velocity was 300 mm/s. Prior to molding, all samples were dried under vacuum at 60°C for at least 12 h.

IV. For microparts in *Section 5.4*.

The melt temperature and mold temperature were 260 and 100°C, respectively. The injection velocity was 300 mm/s.

V. For microparts in *Section 5.5*.

The melt temperature and mold temperature were 260 and 80°C, respectively. The injection velocity was 100 mm/s.

4.5 Characterization

The characterization techniques for the microparts are displayed as follows. To facilitate characterization, all microparts were divided into three sections at the transition areas based on part thickness, as given in Figure 4.5(b). The properties of each section were determined with respect to the flow direction, which will be detailed in Chapter 5.

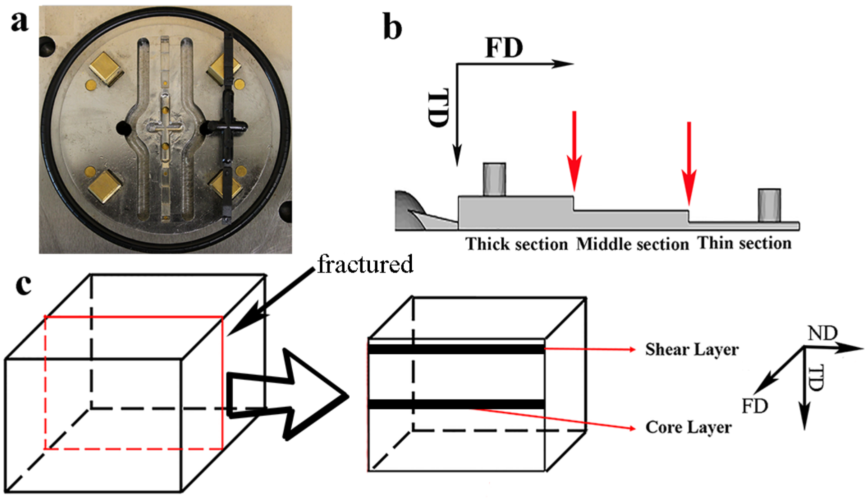

Figure 4.5 (a) Images of the mold insert and a final micropart; (b) three-step configurations of the microparts, red arrows indicate the boundary of each section; (c) sampling positions of each section for morphology observations.

4.5.1 Electrical conductivity

The direct current (DC) electrical resistance (*R*, Ω) of each sample was measured across the transverse direction (TD) and parallel to flow direction (FD), respectively (see Figure 4.5b). The *R* was determined using a two-probe method. In this method, the cut section from the microparts was placed between two copper electrodes, and applied pressure was used to minimize the contact resistance between the copper electrodes and surfaces of the sample. The *R* of each sample was measured by a Keithley 6514 electrometer (USA). The electrometer was calibrated using a known standard resistance. Afterwards, the electrical conductivity (σ, S/cm) for each sample was calculated with Eq. (1):

$$\sigma = \frac{1}{\rho} = \frac{L}{AR} \tag{1}$$

where L (cm) is the distance between the copper electrodes, and A (cm^2) is the contact area between the sample and copper electrodes. Five specimens were characterized for each measurement.

4.5.2 Dimensional stability

The dimensional stability (i.e., shrinkage) of the thick section across TD of PP and PP/CNT microparts was determined by a micrometer (Mitutoyo, Japan). It was calculated using Eq. (2).

$$Shrinkage = \frac{d_m - d}{d_m} \times 100\% \qquad (2)$$

where d_m is the reference dimension (i.e. the thickness of the mold cavity) and d is the measured thickness of microparts. All microparts were sealed in plastic bags at room temperature for approximately six months after molding. For each case, the average thickness was calculated as the arithmetic mean of five specimens.

4.5.3 Morphological properties

Morphology observation is a direct method to probe the microstructure of filler-containing polymer composites and subsequent moldings. The samples for SEM observations were either cryo-fractured in liquid nitrogen or sectioned with a microtome, which will be detailed in sections of Chapter 5. Afterwards, the examined surface was sputter coated with a thin layer of platinum or gold prior to observations. The morphology was taken from the core layer or shear layer of each section of microparts, as depicted in Figure 4.5(c). In addition, all carbon filled PP samples were subject to chemical etching treatment to remove the amorphous phase of PP, according to Park et al. [246]. All samples were etched in a mixture of H_2SO_4(64.7 wt%)/H_3PO_4(32.3 wt%)/$KMnO_4$(3 wt%) for 7h.

4.5.4 Differential scanning calorimetry (DSC)

The melting and crystallization behavior of polymers and carbon filled polymer composites as well as each section of corresponding microparts were characterized using a differential scanning calorimeter. All samples were characterized under a pre-set temperature profile.

- For PP and related moldings in *Section 5.1*.

The thermal behavior of PP and PP/CNT microparts were investigated using a differential scanning calorimeter (Perkin-Elmer DSC Model 1) under nitrogen atmosphere. Thin slices taken from different sections of the microparts were cut across the TD. The measurement which consists of a heating phase followed by a cooling phase was performed between 0 and 200°C at a heating rate of 20°C/min. The crystallinity (χ_c) was calculated with Eq. (3).

$$\chi_c = \frac{\Delta H_m}{\Delta H^{calc}} \tag{3}$$

where ΔH_m is the observed melting enthalpy of PP and ΔH^{calc} is the product of melting enthalpy for 100% crystalline PP and its mass ratio in the composite. The melting enthalpy of 100% crystalline PP is 207 J/g [247].

- For PP and related moldings in *Section 5.2*.

The melting and crystallization behavior of pure PP, diluted PP/CNT composites and each section of corresponding microparts were traced by a differential scanning calorimeter (Q200, TA Instruments). The experiment was carried out under nitrogen with a gas flow rate of 50 mL/min. Firstly, the sample was scanned from 30 to 220^{o}C at a heating rate of 10^{o}C/min. The sample was immediately cooled at a rate of 5^{o}C/min to -30^{o}C. It was then scanned from -30 to 220^{o}C at a heating rate of 10^{o}C/min. The melting temperature (T_m) and peak crystallization temperature (T_c) were obtained from both the heating and cooling cycles, respectively. The χ_c of each sample obtained from both heating cycles was calculated with Eq. (3). The melting enthalpy of 100% crystalline PP is 207 J/g [247]. The results obtained from both heating cycles were compared in an attempt to evaluate the influence of processing history on the thermal behavior of each sample.

- For PA6 and related moldings in *Section 5.2*.

The melting and crystallization behavior of pure PA6, diluted PA6/CNT composites and each section of corresponding microparts were determined using a differential scanning calorimeter (Q2000, TA Instruments) under nitrogen with a gas flow rate of 50 mL/min. Thin slices taken from the middle of each section were cut across the TD. The test, which consists of a heating phase followed by a cooling phase, was carried out between 40 and

240°C at a heating rate of 10°C/min. The χ_c for each sample was calculated with Eq. (3). The melting enthalpy of 100% crystalline PA6 is 230 J/g [26].

- For PLA/PBSA blend and related moldings in *Section 5.3*.

The melting and crystallization behavior of respective sample was determined using a differential scanning calorimeter (Q200, TA Instruments). For microparts, the thick section is used for DSC measurements. The experiment was performed under nitrogen with a flow rate of 50 mL/min. The sample was scanned from 30 to 200°C at a heating rate of 10°C/min. The corresponding χ_c of PLA was calculated with Eq. (4) [248]:

$$\chi_c = \frac{\Delta H_m}{\Delta H^{calc}} \times 100\,\% = \frac{\left(\Delta H_m^* - \Delta H_{cc}\right)}{\Delta H^{calc}} \times 100\,\% \qquad (4)$$

where ΔH_m is the observed melting enthalpy of PLA. The ΔH^*_m is the endothermic enthalpy of melting and ΔH_{cc} is the exothermic enthalpy that is absorbed by crystals formed during the DSC heating scan, i.e. cold crystallization. ΔH^{calc} is the product of the melting enthalpy for 100% crystalline PLA and its mass fraction in the composites. The melting enthalpy of 100% crystalline PLA is 93.7 J/g [249].

4.5.5 Thermogravimetric analysis (TGA)

The thermal stability of each sample was determined by TGA (Q600, TA Instruments). Experiments were carried out under nitrogen at a constant gas flow rate of 60 mL/min with a heating rate of 10°C/min. The testing conditions for each sample were given in Table 4.7.

Table 4.8 The testing conditions of TGA.

Materials	Conditions
PP and related moldings	The relative mass loss was recorded from 50 to 650°C.
PC and related moldings	The relative mass loss was recorded from 50 to 800°C.
PLA/PBSA/CNT and related moldings	The relative mass loss was recorded from 50 to 650°C.

4.5.6 Simulation (Moldflow)

A commercial software package, Moldflow Synergy 16 (Autodesk), was used to estimate the maximum shear rate in μIM under the processing conditions [211]. The properties of CNT-containing polymer composites are not available in the database of software. In this scenario, a substitution could be chosen from the software database to perform simulation analysis [211,250]. Thus, relevant grades of pure polymers which have similar structure and properties were selected as the modeling materials, as detailed below. The simulation analysis was conducted with respect to PS, PP and PC.

- For the simulation of PP microparts.

A replacement of unfilled PP (Adstif HA740N, Basell Polyolefins North America), which has a similar structure as the pure PP used in the preparation of carbon filled PP composites, was selected.

- For the simulation of PC microparts.

The unfilled PC (Panlite® K-1300, Teijin, Japan) was selected from the software database for assessing the maximum shear rate in μIM.

- For the simulation of PS microparts.

A replacement of unfilled PS (GPPS 2282, Nova Chemicals) was selected to estimate the shear rate within microparts. The selected PS has similar properties to the pure PS that was used to dilute the masterbatch.

4.5.7 Dissolving experiments and transmission electron microscopy

The dissolving experiments, which show the state of CNT dispersion in a good solvent for the polymer matrix, are helpful to reflect the state of distribution that was achieved in the solid state [251]. Thus, in order to obtain a qualitative evaluation of CNT dispersion within PA6, the original PA6/CNT masterbatch, PA6/CNT 5 wt% extrudate and different sections taken from subsequent microparts were dissolved in formic acid for 1 h at 40°C. Small pieces of the PA6/CNT masterbatch, PA6/CNT 5 wt% extrudate and cut sections from subsequent microparts were immersed in about 50 mL formic acid with external stirring. These solutions were formulated to acquire an equivalent amount of CNT in each vial. The state of CNT dispersion in the PA6/formic acid solution was recorded in digital photos by a Canon camera (Japan). Furthermore, the PA6/CNT/formic acid solution was diluted with distilled water. Afterwards, the solution was sonicated (Branson B-220, USA) for 3 min at a power of 125 W. A drop of the above-mentioned solution was placed on a copper grid (400-mesh, Formvar Carbon Film, Electron Microscopy Sciences, USA). To observe the nanostructure of CNT, each sample was examined by transmission electron microscopy (TEM, Philips CM 10) at an acceleration voltage of 80 kV, after complete evaporation of the liquid phase. The diameter and length of CNT were measured manually with the help of an image analysis software (Image J).

4.5.8 Melt rheology

Melt rheology test was adopted to study the development of microstructure in compression molded PP/carbon composites. Pötschke et al. [252] pointed out that melt rheology analysis provides an alternative way to detect the percolated structure of PC/CNT composites. Thus, a dynamic rheology test was carried out using a rheometer (RSM II, Rheometrics) in the melt state. To keep the response in the linear viscoelastic region, the applied strain was set at 1%. Dynamic rheological tests were performed using a frequency sweep ranging from 0.1 to 100 rad/s at 190°C.

Chapter 5

5 Results and discussion

In this chapter, the properties of different carbon filled microparts are discussed in detail. The content for each section of Chapter 5 is briefly described below.

Section 5.1 describes the influence of processing conditions on the properties of CNT filled PP microparts, which was implemented by adjusting various process parameters, such as melt temperature, mold temperature, backpressure and injection velocity. These process parameters were selected because they were considered as the key machine variables for injection molding process. A PP/CNT 10 wt% composite was prepared by melt dilution of PP/CNT 20 wt% masterbatches supplied by Hyperion Catalysis International (USA). The design of experiments (DOE) method was employed to elucidate the effect of each process parameter on the properties of subsequent microparts.

Section 5.2 reports the influence of host polymer selection and filler concentration on the electrical, morphological and thermal properties of corresponding microparts. To this end, four different types of CNT-containing polymer composites (i.e. PP/CNT, PS/CNT, PC/CNT and PA6/CNT) were prepared by melt dilution of commercially available masterbatches from Hyperion Catalysis International. In this section, although different types of melt mixers were employed to prepare CNT-containing polymer composites, the obtained polymer blends were expected to have a relatively uniform filler distribution.

Section 5.3 focuses on the optimization of properties of CNT-containing microparts by adopting the immiscible polymer blends. The adopted polymers are PLA and PBSA. In the immiscible blends, the mass ratio of PLA to PBSA is 70:30 and the concentration of CNT is fixed at 5 wt%. Different blending procedures were adopted to study the influence of blending sequence of various components of immiscible polymer blends on the properties of molded microparts.

Section 5.4 describes the influence of different types of carbon fillers on the properties of molded microparts. The selected carbon materials are CNT, CB, GNP, SG and LTEG. PP was chosen as the host polymer for these carbon fillers. Additionally, the influence of shearing conditions on the electrical and morphological properties of molded samples was studied by employing two different types of processing methods, such as compression molding and microinjection molding.

Section 5.5 illustrates the effect of hybrid carbon filler loading and the annealing treatment on the properties of PS microparts. Herein, a series of hybrid carbon fillers (i.e. 3, 5, 10 wt%) loaded PS composites were fabricated by melt blending and the mass ratio of CNT to CB (0/100, 30/70, 50/50, 70/30 and 100/0) was systematically altered. Afterwards, the obtained composites were molded under a defined set of processing conditions using the Battenfeld micromolding machine.

5.1 The influence of process parameters

In this section, PP filled with 10 wt% CNT composites were prepared via masterbatch dilution and subjected to µIM under various processing conditions. The molding conditions were altered by systematically changing the selected process parameters, such as: melt temperature, mold temperature, backpressure and injection velocity. A mold insert with a three-step decrease in thickness along the flow direction was adopted. The effects of molding parameters on the electrical conductivity and dimensional stability of microparts were evaluated using the design of experiments method. The distribution of maximum shear rates along the flow direction was simulated via Moldflow, and the state of CNT distribution within microparts was examined by SEM. In addition, the thermal behavior of the microparts molded from unfilled PP and PP/CNT 10 wt% composites at different sampling positions along the flow direction was studied by DSC. Results showed that the crystallization process of unfilled PP taken from different regions of the microparts is temperature dependent, which was ascribed to the variations of shearing effects undergone by the polymer melts during µIM, while this effect was not significant for the CNT loaded systems.

5.1.1 Electrical conductivity

The electrical conductivity (σ) values for both the thick and middle sections of PP/CNT 10 wt% microparts measured across the transverse direction (TD) and along the melt flow direction (FD) are reported in Figures 5.1(a) and (b), respectively. The σ for the thin section of microparts is not reported because acceptable thin sections could not be successfully sectioned from the microparts using current cutting method. Figure 5.1 reveals that the values of σ for both the TD and FD change simultaneously with the variations in processing conditions as described in Table 4.6, which suggests that the state of distribution of CNT within microparts becomes different with the adjustment of process parameters, such as melt temperature (T_melt), mold temperature (T_mold), backpressure (Back_Press) and injection velocity (Inj_Vel). The values of σ measured along the FD (Figure 5.1b) are invariably higher than those obtained across TD (Figure 5.1a) as per measurement sections, which indicates a role for the orientation of CNT along FD. Although obtaining a general relationship between the values of σ and the shearing conditions from Figure 5.1 is difficult, it is noted that the value of σ increases with increasing shearing conditions, which can be attributed to the influence of improved distribution of CNT in PP under high shearing conditions and the preferential alignment of nanotubes along the FD. For example, Li and Shimizu [236] reported that CNT shows better dispersion in a thermoplastic elastomer when processed at elevated shearing conditions. Thus, the improved distribution of CNT in subsequent microparts contributes to the increase of σ in both the TD and FD of each section, whereas the preferential orientation of CNT is likely to favor the formation of conductive pathways along the FD which results in the enhancement of σ in this specific direction. However, both effects are susceptible to the variations of process parameters, thereby affecting the microstructure of microparts. In addition, the shearing effect is expected to be higher in the middle section when compared with that of the thick section. Consequently, the FD σ of the middle section is generally higher than that of thick section counterpart, despite a few exceptions such as Case 1, Case 4 and Case 15.

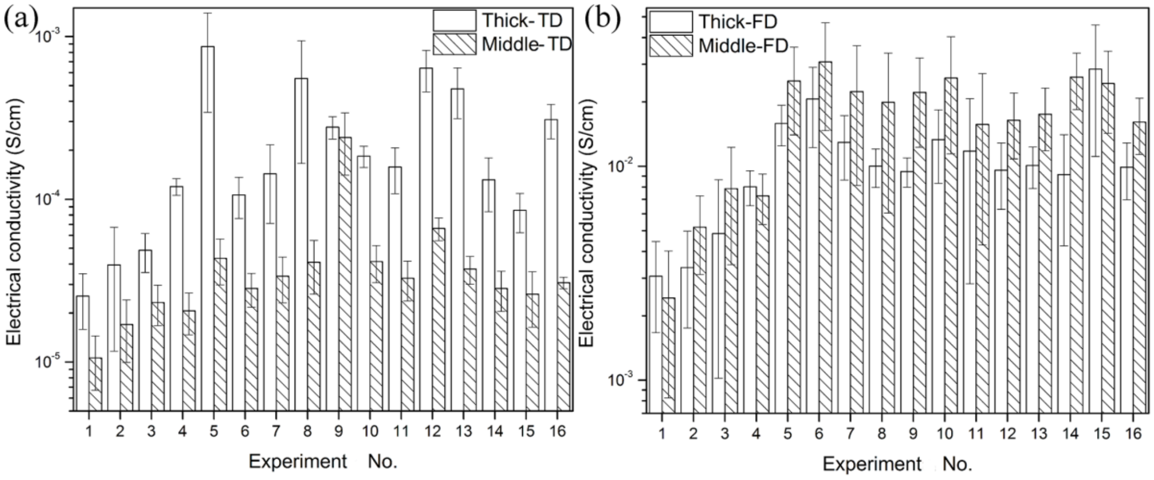

Figure 5.1 The σ measured across (a) TD and (b) FD of both the thick and middle section of PP/CNT 10 wt% microparts. Experiment numbers were defined in Table 4.6.

The level of influence of different process parameters on the σ of microparts was evaluated using a statistical software, Minitab 17 (USA). The main effect of process parameters on the σ across the TD for both the thick and middle sections are plotted in Figures 5.2(a) and (b), respectively. Figure 5.2(a) shows that the T_mold and Inj_Vel demonstrate significant influence on the σ of studied samples. Thus, based on the ranges examined, higher σ would be supported by higher T_mold (100^{o}C) and lower Inj_Vel (100 mm/s). From Figure 5.2(b), T_mold and Inj_Vel also have a significant impact on the σ measured across the TD of middle section. Additionally, T_melt has a marked effect on the σ measured across the TD of middle section. This indicates that polymer melts experience different shearing or thermal history in different sections of microparts when they are produced by µIM. For example, viscous heating [212] would become significant with an increase of shearing conditions from thick section to middle section, and the resulting high melt temperatures might promote the formation of conductive pathways within the microparts.

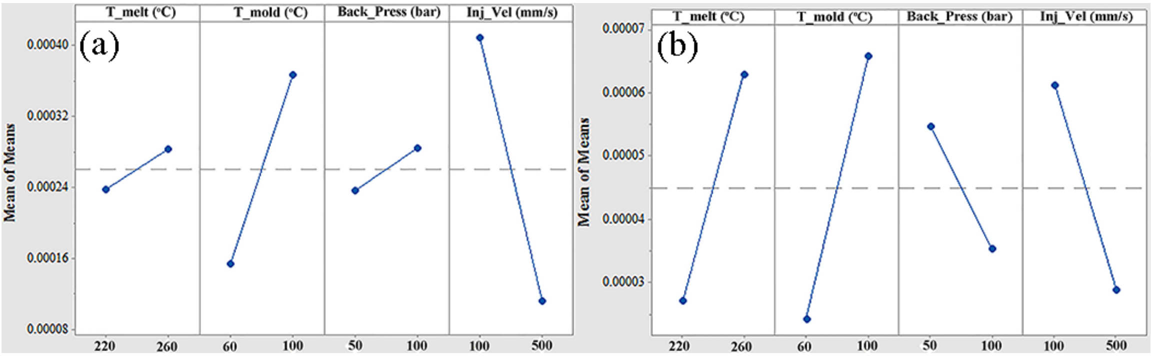

Figure 5.2 Main effect plots of the means of σ measured across the TD of the (a) thick and (b) middle sections.

Similarly, the main effect plots of σ measured in FD of both the thick and middle sections are given in Figures 5.3(a) and (b), respectively. Figure 5.3(a) reveals that T_melt, T_mold and Inj_Vel all have a significant, positive effect on the values of σ measured along FD. Back_Press is also a significant factor regarding the FD σ in the thick section, and higher σ is favored when Back_Press is low. It is expected that the viscosity of thermoplastic polymer melts decreases when they are processed at higher T_melt (260^{o}C). Meister and Drummer [253] reported that high T_mold would promote the mold filling of PP in µIM. Therefore, the degree of CNT orientation along the FD is enhanced, coupling with high Inj_Vel at 500 mm/s. Thus, the above factors increase the probability of CNT-CNT contact, which contributes to the enhancement of σ along the FD. In general, better distribution of fillers within the polymer melts could be achieved with an increase of Back_Press. The sizes of CNT agglomerates are, to some extent, reduced due to better mixing before polymer melts enter mold cavity, which might be detrimental to the enhancement of overall σ due to the improved filler dispersion. For example, Alig et al. [254] reported that the presence of CNT agglomerates is crucial to the enhancement of σ of polymer composites. Figure 5.3(b) indicates that a similar influencing trend is observed for the values of σ measured along the FD of middle section. However, T_mold shows the highest influencing effect, followed by T_melt, whereas the effect of other process parameters becomes less significant. It could be conjectured that the degree of orientation of polymer chains and CNT would be higher in the middle section than in the thick section arising from the sharp increase of shearing conditions [99,255]. Therefore, an increase of T_mold might promote the relaxation of polymer chains during µIM which is beneficial to the formation of random conductive pathways, thereby facilitating the increase of σ along the FD.

Combining the results of Figures 5.2 and 5.3, it is suggested that increasing both T_melt and T_mold generally raises the σ of microparts in both measurement directions, whereas an increase of Inj_Vel is advantageous to the enhancement of σ along FD and detrimental to the σ across TD. This can be related to the development of microstructure in µIM.

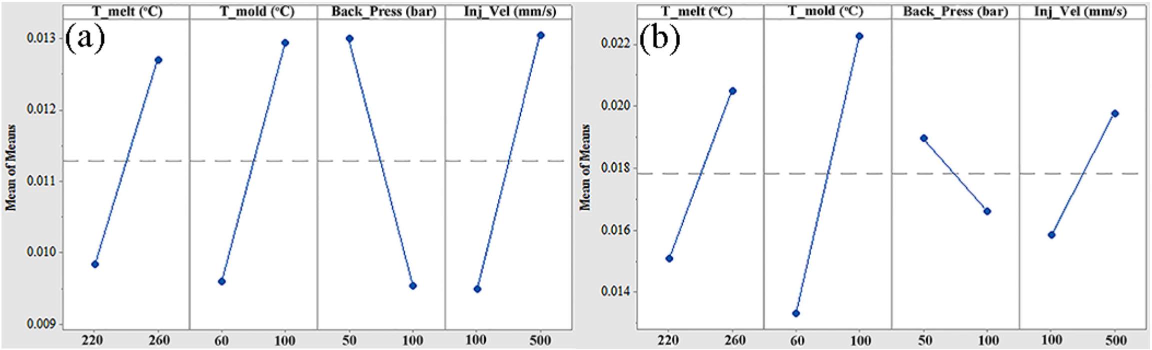

Figure 5.3 Main effect plots of the means of σ measured along the FD of the (a) thick and (b) middle sections.

5.1.2 Morphology

The above discussion suggests that high shearing conditions have a significant influence on the development of microstructure in microparts. Thus, Cases 11 and 14 were selected because higher shearing conditions are expected to prevail in those cases since the microparts were molded under conditions of higher T_melt and Inj_Vel. The morphology of the chemically etched surface which was taken from the core region of thick section is shown in Figure 5.4. Traces indicating the existence of CNT agglomerates (i.e. white spots/domains) are observed in Figure 5.4(a). This is mainly ascribed to the fact that PP is a semi-crystalline polymer. Therefore, the distribution of CNT within the PP crystallites is not favored and CNT is primarily distributed within the amorphous domains [101]. Figure 5.4(b) shows that the interconnected CNT network is constructed within PP which is crucial to the improvement of overall σ for as-molded products. Moreover, Figure 5.4(c) reveals that there is a preferential orientation of individual CNT or CNT bundles in one specific direction, i.e. flow direction. This is attributed to the combined effects of shearing and extensional force fields that are generated during the μIM process.

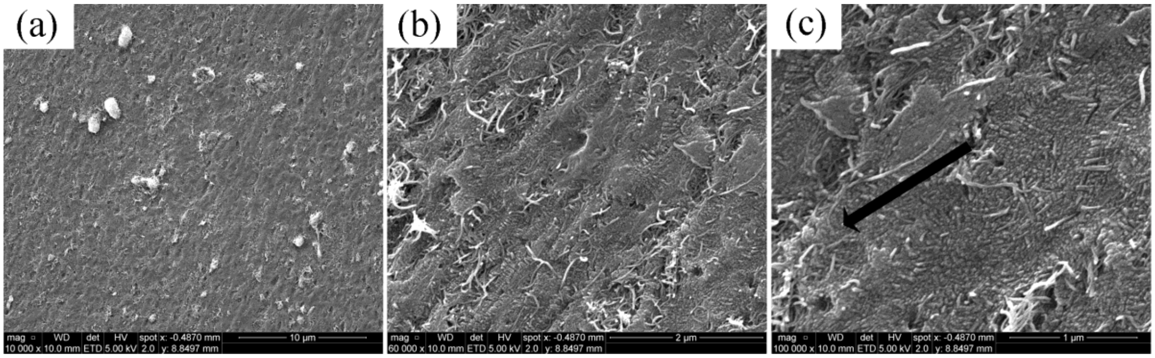

Figure 5.4 SEM images of chemically etched surface of the core region of the thick section molded under conditions of Case 14 at different magnifications: (a) ×10 k, (b) ×60 k and (c) ×100 k.

The development of internal microstructure observed from the etched surface of each section is presented in Figure 5.5. All samples were microtomed across the TD as per the cut section from the microparts. All images were captured from the core region of the microparts as indicated by the arrows. Results revealed that the distribution of CNT within PP is not uniform and CNT agglomerates with various sizes are detected in Figure 5.5(a), which is consistent with the result stated previously in Figure 5.4(a). As shown in Figure 5.5, CNT agglomerates are detected in the thick section (Figure 5.5a). The number of CNT agglomerates decreases in the middle section of micropart (Figure 5.5b), whereas nearly no CNT agglomerates could be observed in the thin section (Figure 5.5c). These differences are consistent with the variations of shearing conditions experienced by the polymer melts within different sections of microparts [236].

The simulation results for the distribution of maximum shear rates along the FD are also illustrated in Figure 5.5. The estimated (Moldflow) shear rate in the core layer of thick section is roughly 2.5×10^3/s (the average size of CNT agglomerates is about 0.59 μm), and the shear rate increases to nearly 6×10^3/s in the core layer of middle section (the average size of CNT agglomerates is approximately 0.32 μm) whereas the shear rate in their thin section counterpart is around 1.25×10^4/s (almost no agglomerates were observed). Please note that the simulation analysis was performed with pure PP; however, the results could qualitatively reflect the extent or variations of shearing effect present in different sections of PP/CNT microparts.

For the three-stepped microparts, an increase of effective shear rates is expected after the abrupt change of mold geometry amid different sections of the microparts arising from the 'contraction flow' of the advancing polymer melts. In addition, the extensional forces in different sections are quite significant in such rectangular mold cavities. Therefore, a higher degree of CNT orientation along FD is expected with an increase of shearing and extensional effects [256,257]. As a result, it is reasonable to attribute the development of microstructure in different sections of microparts to the variations of shearing conditions.

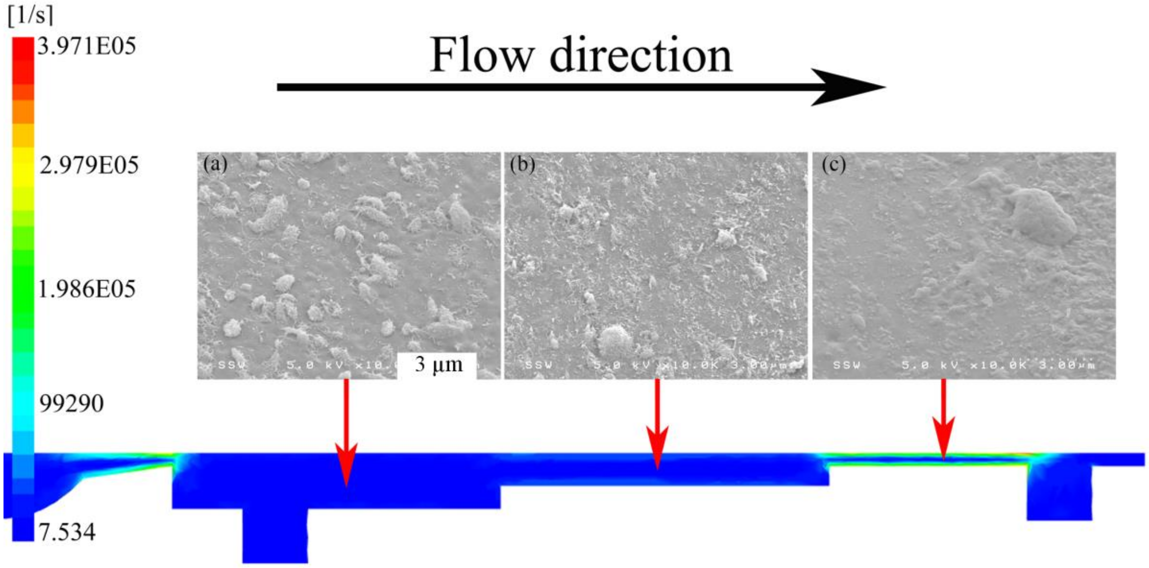

Figure 5.5 The distribution of maximum shear rates (Moldflow) and the development of microstructure along the flow direction for the (a) thick, (b) middle, and (c) thin sections of a micropart. The micropart was fabricated under conditions of Case 11.

5.1.3 Shrinkage analysis

The injection molded articles usually exhibit shrinkage arising from the orientation effect of polymer chains and as a result of the significant variations of pressure-volume-temperature (PVT) conditions during the process, especially for semi-crystalline polymers [258]. Jansen et al. [259] reported that the shrinkage of injection molded products is strongly dependent on the processing conditions. Thus, it is important to consider the dimensional stability of injection molded products, especially for intricate microparts which should meet precise size requirements.

Figure 5.6(a) shows that microparts molded from unfilled PP exhibit the highest shrinkage. The orientation of polymer chains along the FD is responsible for this phenomenon [260]. Chu [258] pointed out that the molecular orientation is a result of combined effects of shearing and freezing. However, both effects are accentuated in μIM. Thus, the aligned structure could be easily frozen in the surface (skin) layer due to the fast cooling of polymer melts next to the mold wall. Since PP has a low thermal conductivity [32], the solidified skin layer acts as an insulating shield. As a result, the polymer chains in the core layer have more time to relax to their thermodynamically favored state, leading to the high shrinkage of pure PP microparts. However, the shrinkage is reduced substantially for CNT-containing microparts, which suggests that the addition of CNT enhances the dimensional stability of microparts. As shown in Figure 5.4(b), a 3D conductive network is typically established within the thick section at 10 wt% CNT. In this case, the physical network of CNT would restrict free motion of the polymer chains, which makes the dimensions of microparts more stable. In addition, there would be more retention of original dimensions of PP/CNT microparts due to the enhanced rigidity of polymer composites [261] when compared with that of pure PP. Furthermore, the addition of carbon-based fillers into polymer matrices not only increases the σ of resultant composites, but also the thermal conductivity is enhanced. Consequently, the higher thermal conductivity of CNT-containing PP composites facilitates heat conduction and the molded microparts could experience simultaneously fast cooling at the surface and in the core. Therefore, the relaxation of orientated structure is constrained, i.e. the shrinkage of as-molded microparts is reduced.

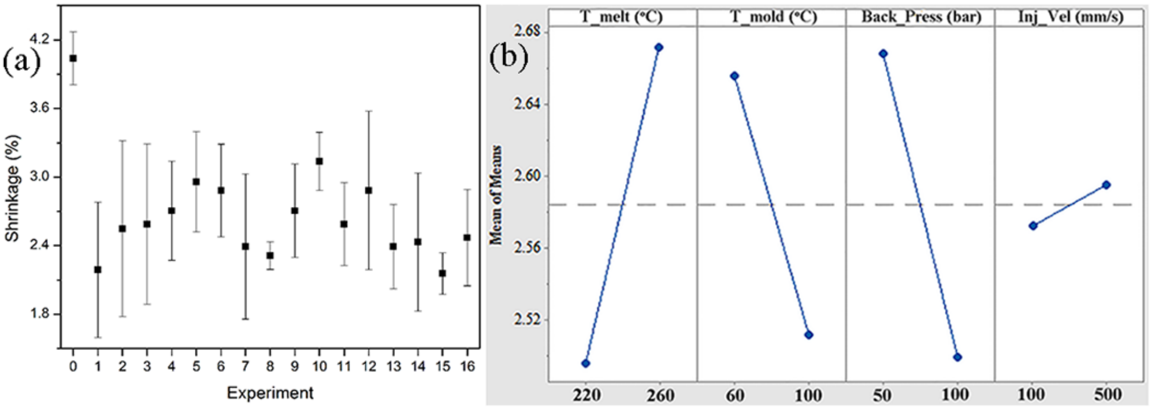

Figure 5.6 (a) Shrinkage of the thick section of microparts measured across the TD under various processing conditions. Case 0 refers to the µIM of unfilled PP; (b) the main effect plot of the means of shrinkage measured across the TD of thick section.

The influence of process parameters on the shrinkage of thick section across the TD is displayed in Figure 5.6(b) which shows that T_melt has the highest influence, then followed closely by Back_Press and T_mold. Increasing T_melt promotes the shrinkage of thick section in TD, which could be attributed to the increased mobility of polymer chains at elevated T_melt. The increased mobility of polymer chains facilitates the crystallization process, thereby increasing the shrinkage of subsequent moldings. Li et al. [262] reported that the shrinkage of polymer matrix could reduce the distance between adjacent CNT or CNT agglomerates, which contributes to the increase of σ of injection molded samples. Similar results were reported by Alig et al. [150] for PC/CNT composites. Although the increase of T_mold facilitates the motion of polymer chains, it could also promote the mold filling behavior of PP [253] which could, to some extent, enhance the dimensional stability of subsequent moldings. Increasing Back_Press is beneficial to the compact packing of polymer melts, which is helpful in reducing the shrinkage. Interestingly, the influence of Inj_Vel is minimal, which reflects that the shearing conditions are quite high even at a lower Inj_Vel (100 mm/s). Thus, a further increase of Inj_Vel has a trivial effect on the orientation of polymer chains along the FD. A similar effect was observed by Jansen et al. [259] in high density polyethylene (HDPE), for the injection molding process.

In general, µIM is a rapid molding process in which the mold filling could be completed within sub-second. Therefore, the concurrent shearing and cooling rates of polymer melts would be significantly higher in μIM when compared with those of CIM [193] due to their very high surface area to volume ratios. The average temperature ($T_{average}$) of polymer melts during solidification could be calculated based on the following equation [194]:

$$T_{average} = T\_mold + \frac{8}{\pi^2}(T\_melt - T\_mold) \cdot \exp(-\frac{\alpha\pi^2 t}{H^2})$$

where α is the thermal diffusivity and *H* is the thickness of the sample. Taking pure PP as an example, α is taken as 0.06 mm^2/s [194] and the values of *T_melt* and *T_mold* are 260 and 100^{o}C, respectively. Figure 5.7 reveals that there is a significant difference of cooling rates between different sections of microparts, and the cooling time drops quickly as the thickness of mold cavity is reduced. For instance, $T_{average}$ approaches *T_mold* at about 7 s for the thick section, followed by the middle section at 2.5 s and thin section at about 0.35 s. Additionally, corresponding values of samples with incorporated CNT are expected to be much lower due to their higher α. As a result, there would not be enough time for the relaxation of polymer chains in the microparts, and the flow-induced orientation of polymer chains could be adequately maintained [194].

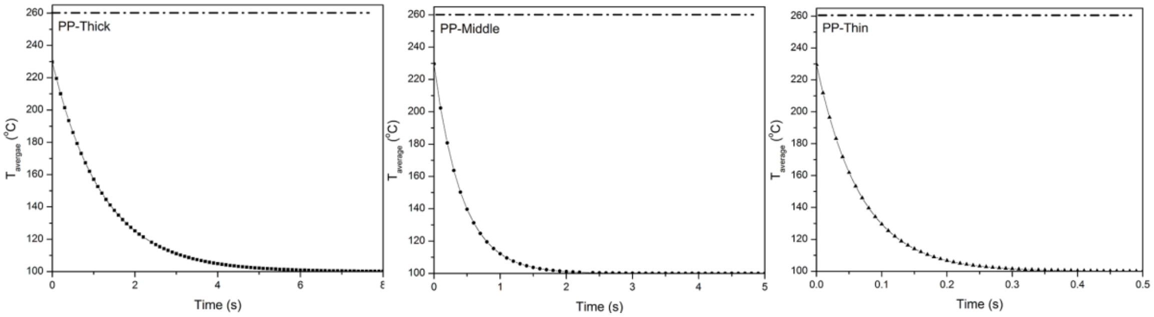

Figure 5.7 Temperature profiles in the thick section, middle section and thin section of pure PP microparts depending on the cooling time.

5.1.4 Differential scanning calorimetry (DSC)

As per *Section 4.5.4*, the thermal behavior of pure PP and PP/CNT microparts was studied using a differential scanning calorimeter (Perkin-Elmer DSC Model 1) under dry nitrogen. Figures 5.8(a) and (b) illustrate the thermal behavior of unfilled PP samples sectioned from different regions of the microparts along the flow path. It has been reported that PP has multiple crystalline forms, namely α (monoclinic), β (trigonal), γ (orthorhombic), and smectic mesophase [263]. Figure 5.8(a) shows that all samples exhibit similar melting behavior and the melting temperature (T_m) is found in the vicinity of 162°C, which is associated with the melting of α-crystals of PP [264]. In addition, a small melting peak is typically detected at around 170°C for the thick section of PP microparts, which might be attributed to the phase transformation of PP from β-form crystals to the α-form during the heating process. The recrystallization of polymer chains during the heating procedure in DSC measurement promotes the formation of thicker lamellae of α-crystals [265], thereby leading to the appearance of a much higher melting point. However, this could also be attributed to other influencing factors, e.g. the existence of impurities or other additives in the PP, since the second melting peak is only observed in the thick section and the melting peak is quite small when compared with the main melting peak which centers around 162°C. Therefore, a thorough investigation of the crystalline structure or microstructure might be helpful to elucidate this phenomenon.

Figure 5.5 shows that the average shear rate follows an order of gate region > thin section > middle section > thick section within the microparts. Then, it can be deduced from Figure 5.8(a) that the variation of shear rates has little influence on the crystal morphology within the microparts. Table 5.1 shows that the χ_c of each section for both pure PP microparts and PP/CNT 10 wt% microparts which were molded under conditions of Case 1 (which has the lowest shearing effect, as validated by Moldflow simulation) demonstrates similar trend as the simulated shear rates, indicative of flow-induced crystallization for the polymer matrix. In addition, the corresponding melting peaks for the thin section and gate region become narrower, suggesting a more homogeneous distribution of lamellae thickness. Furthermore, it is observed from Figure 5.8(b) and Table 5.1 that the crystallization of unfilled PP with respect to the sampling positions of micropart is shear rate dependent, or more specifically, temperature dependent. Samples taken from high shear regions, i.e. gate and thin sections crystalize first. In this scenario, the possible explanations could be: *(1)* the higher surface area to volume ratio of the thinner sections promotes the proliferation of nuclei during the crystallization process; *(2)* the variations of shearing conditions in different sections of the microparts contribute to the crystallization process, i.e. flow induced crystallization.

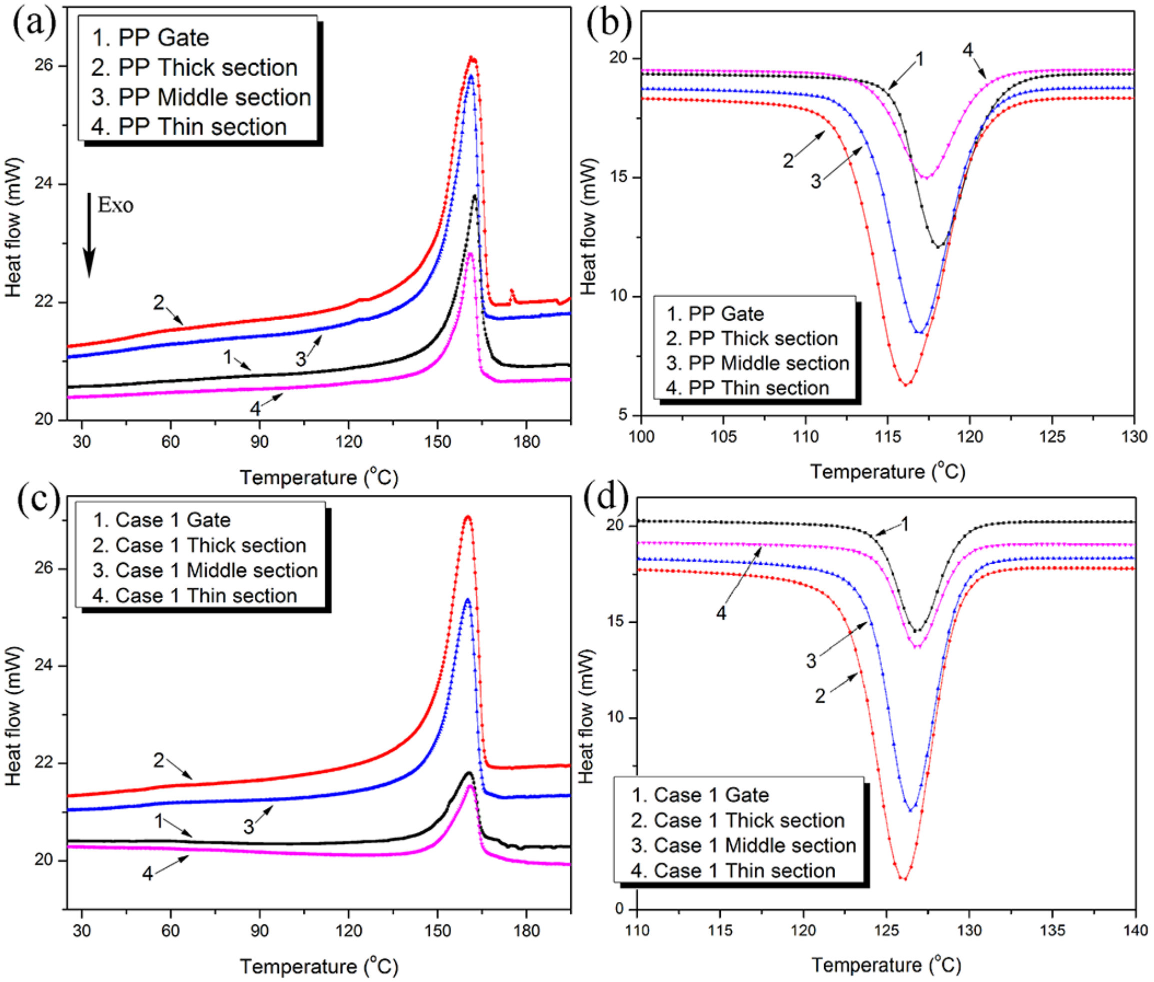

Figure 5.8 DSC (a) heating and (b) cooling curves obtained from microparts molded from unfilled PP; DSC (c) heating and (d) cooling curves obtained from microparts molded from PP/CNT 10 wt% composites under conditions of Case 1.

As to the microparts molded in Case 1, the thermal behavior of CNT filled microparts demonstrates differently when compared with that of unfilled system. Figure 5.8(c) shows that all samples exhibit nearly the same T_m (around 160°C) regardless of sampling positions along the FD. This finding is in agreement with the results reported for PP/CF composites [173] and PP/CNT composites [266]. In addition, there is a slight reduction of T_m for PP/CNT microparts when compared with their pure PP counterparts. This could be possibly attributed to the influence of the presence of CNT within polymer matrix. Irrespective of the significant shearing effect in µIM, the presence of CNT has a marked heterogeneous nucleation effect in PP/CNT systems which is reflected in Figure 5.8(d). As a result, the increased number of nucleation sites may lead to the formation of a large amount of small crystalline domains which are more susceptible to heat. In addition, Table 5.1 shows that the crystallization temperature (T_c) of CNT filled PP composites shifts to higher temperature regions when compared with those of unfilled PP. However, as compared with Figure 5.8(b), the temperature dependence of crystallization peaks diminishes for PP/CNT systems, which is ascribed to the fact that CNT plays a role of nucleating agent [267], which aids in the crystallization process of PP.

Table 5.1 The crystallization temperature (T_c) and crystallinity (χ_c) obtained for microparts molded from pure PP and PP/CNT 10 wt% composites with respect to different sampling positions.

Sample	Gate region		Thick section		Middle section		Thin section	
	T_c (ºC)	χ_c	T_c (ºC)	χ_c	T_c (ºC)	χ_c	T_c (ºC)	χ_c
unfilled PP	118.06	0.742	116.06	0.403	117.06	0.391	117.38	0.474
Case 1	126.73	0.602	126.17	0.393	126.45	0.389	126.72	0.490

5.1.5 Summary

PP/CNT 10 wt% composites were prepared via masterbatch dilution process, then followed by µIM under various processing conditions. The electrical conductivity measurements were carried out on the thick and middle sections of microparts with respect to melt flow direction. The effect of actual molding conditions on the electrical conductivity was analyzed. Results suggested that increasing backpressure does not significantly contribute to enhancing the electrical conductivity, but it could significantly enhance the dimensional stability of microparts. Higher melt temperature and mold temperature are beneficial to the formation of conductive pathways, thereby enhancing the electrical conductivity of resultant microparts. Increasing injection velocity has a detrimental effect on the electrical conductivity measured across the transverse direction, whereas the electrical conductivity along the melt flow direction is enhanced. The orientation of CNT along the flow direction is favored at elevated injection velocity, which would, to a certain degree, increase the probability of CNT-CNT contact, facilitating the enhancement of electrical conductivity along flow direction. Simulation results indicated that the distribution of maximum shear rates within microparts exhibits an increasing trend along the melt flow direction, i.e. thick section < middle section < thin section. SEM observations revealed that the distribution of CNT within PP is not uniform. The microstructure development along the flow direction was correlated with simulation results. Interestingly, the crystallization process of unfilled PP is shear rate (temperature) dependent which could be related to the very high shearing and extensional effects in µIM, and this phenomenon is absent from CNT loaded systems, indicating that the presence of CNT can alter the crystallization process of polymer chains, as indicated in Figure 5.8.

5.2 The influence of host polymer matrix and CNT loading concentrations

In this section, the effect of interfacial interactions between conductive filler, i.e. CNT, and different types of host polymers (i.e. PP, PS, PC and PA6) was studied in detail. Although the surface tension between CNT and each polymer can be estimated by measuring contact angle, the measurement process is quite lengthy and labor-intensive [268]. Therefore, the interfacial interaction between polymer and CNT was evaluated by theoretical calculation [269], which was commonly adopted to assess the interfacial tension between polymer and the incorporated fillers. In addition, the influence of filler concentration on the properties of polymer/CNT composites was thoroughly reported. To this end, a series of CNT-containing polymer composites were fabricated by melt dilution of commercially available masterbatches with respective pure polymer components using laboratory scale mixers. Subsequently, the obtained composites were processed by using a microinjection molding machine, i.e. Battenfeld Microsystem 50. A mold insert which has three consecutive zones with decreasing thickness along the flow direction was adopted to fabricate microparts. The microparts were mechanically divided into three sections, namely thick, middle and thin sections, based on part thickness. Morphology observations and electrical conductivity measurements were performed with each section of microparts to explore the evolution of microstructure. The electrical conductivity and microstructure of various thermoplastic microparts filled with CNT were compared. Results suggested that the selection of host polymers affects the distribution of CNT within subsequent moldings, which affects the electrical conductivity. The thermal stability of CNT-filled PC and PP composites as well as subsequent microparts were evaluated by TGA. Results showed that the thermal stability of PC/CNT moldings deteriorated upon the addition of CNT, whereas thermal stability of PP/CNT counterparts increased with increasing filler concentrations. In addition, the nanostructure of CNT after melt processing was investigated by TEM. The melting and crystallization behavior of PP/CNT and PA6/CNT composites as well as corresponding microparts were studied by DSC. Raman analysis was utilized to study the orientation and structural properties of CNT in microparts.

5.2.1 The effect of host matrix

5.2.1.1 Electrical conductivity

The average σ values measured for the thick and middle sections of different polymer/CNT microparts at a constant filler concentration, i.e. 10 wt%, are displayed in Figure 5.9. It is apparent that the average values of σ measured along the FD of the PC/CNT 10 wt% (PC-10), PA6/CNT 10 wt% (PA6-10), PS/CNT 10 wt% (PS-10) and PP/CNT 10 wt% (PP-10) microparts is invariably higher than that across the TD. However, the average FD σ for the thick section of PC-10 micropart is slightly lower than that measured across the TD. The above indicates that the host polymer selection has an influence on the σ of subsequent microparts. Moreover, the average TD σ for the thick section is always higher than that obtained from their middle section counterparts, whereas the average FD σ for the middle section is comparable to or slightly higher than that achieved for the thick section. This suggests a higher tendency for CNT alignment along the FD of the middle section caused by the higher shear rates in the thinner section. In addition to the existence of very high shear force fields in µIM, the extensional forces could be quite significant at the contraction regions which contribute to the preferential orientation of CNT in the melt filling direction. Moreover, the interfacial interactions between polymer matrix and CNT could play a part.

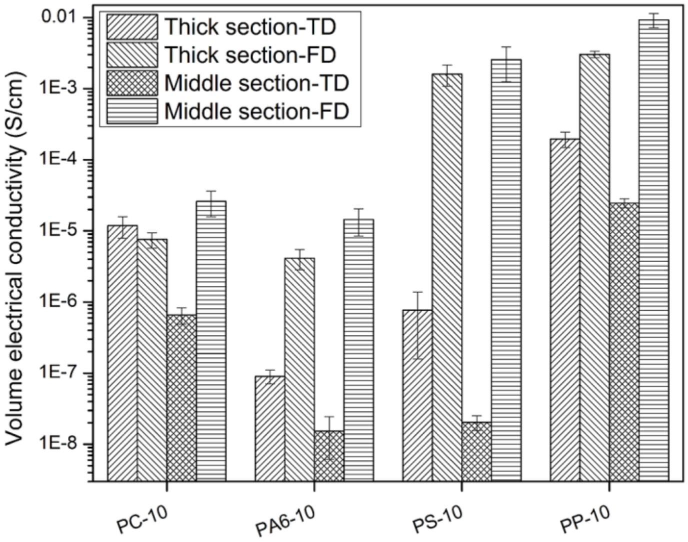

Figure 5.9 The comparison of electrical conductivity (σ) for different polymer systems with 10 wt% CNT with respect to the measurement sections and directions. FD-flow direction; TD-perpendicular to the melt flow direction, i.e. transverse direction.

The values of interfacial tension between different polymer matrices and CNT could be calculated using the geometric-mean equation which has been proposed for systems of a high-energy material, CNT, and a low-energy material, polymer matrix [269], as described below.

$$\gamma_{1-2} = \gamma_1 + \gamma_2 - 2(\gamma_1^p * \gamma_2^p)^{0.5} - 2(\gamma_1^d * \gamma_2^d)^{0.5} \qquad (5)$$

where γ_1 and γ_2 are the values of surface tension of component 1 and component 2, respectively. γ_1^p and γ_1^d are the polar and dispersive contribution of surface tension of component 1. The surface tension values for PA6, PP and PS at 260°C are taken from literature [270]. However, the values of surface tension of PC at 300°C are not available and they were extrapolated from literature values at 20°C [271] by taking the influence of temperature into account [272]. According to Pötschke et al. [272], the extrapolation of surface tension values towards the melt state are based on linear approximation and under assumption of temperature independence of polymer polarity. In addition, values of surface tension for CNT are taken from literature [268,273]. The above-mentioned data are listed in Table 5.2. The calculated interfacial intension values between different polymer/CNT pairs are displayed in Table 5.3.

Table 5.2 The surface tension values of PP, PS, PA6, PC and CNT.

Material	γ_i (mN/m)	γ_i^p (mN/m)	γ_i^d (mN/m)	Ref.
PP[a]	15.94	0.37	15.57	[270]
PS[a]	23.44	0.168	23.272	[270]
PA6[a]	36.42	13.2	23.22	[270]
PC[b]	23	4.37	18.63	N/A
CNT	27.8	10.2	17.6	[273]
	45.3	26.9	18.4	[268]

a. Data calculated at 260°C; b. data calculated from the surface tension values at 20°C, according to Pötschke et al. [272].

Table 5.3 shows that there is a noticeable disparity among the calculated interfacial tension values of different polymer/CNT pairs, when two different sets of surface tension values for CNT are used. Despite the difference of surface tension values for CNT, the general trend for resulting calculations is similar as the calculated values of interfacial tension for different polymer/CNT pairs obey the same order: PS/CNT > PP/CNT > PC/CNT > PA6/CNT. Moreover, Table 5.3 indicates that the polar polymers, such as PA6 and PC have lower interfacial tension with CNT, which means there is better wettability between the polymer matrix and CNT, implying better dispersion of CNT in corresponding polymer composites [95,97].

Interestingly, the calculated interfacial tension value for PS/CNT pair is higher than that of PP/CNT pair; however, the possible π-π interactions between sidewall of CNT and the pendant phenyl groups on PS chain backbones might enhance the interfacial interactions between PS and nanotubes [274], thereby leading to an improved dispersion of CNT in PS. Figure 5.9 reveals that the PP-10 microparts demonstrated the highest σ values for each section with respect to the measurement directions, when compared with other polymer systems. In this scenario, both the semi-crystalline nature of PP [101] and poor interfacial interactions between CNT and PP are likely contributing factors, which are beneficial to the formation of CNT agglomerates in PP, thereby enhancing the σ of subsequent moldings [101,150,275,276]. Moreover, an interphase layer of polymer matrix (such as PS, PC and PA6) surrounding CNT might be likely developed due to a better wettability between CNT and host polymers. Although the existence of interphase layer facilitates the distribution of CNT in corresponding polymer matrix, it would be detrimental to the enhancement of σ in subsequent moldings [97,277].

Table 5.3 Interfacial tensions between different pairs of polymer/CNT composites.

Pairs	Interfacial tension, mN/m (CNT [273])	Interfacial tension, mN/m (CNT [268])
PP/CNT	6.75	21.08
PS/CNT	8.15	23.1
PA6/CNT	0.582	2.69
PC/CNT	1.23	9.59

5.2.1.2 Morphology

The development of microstructure of the thick section in CNT filled various polymer matrices is displayed in Figure 5.10. Samples were fractured in liquid nitrogen across the TD. All images were taken from the core layer, as indicated in Figure 4.5. The distribution of nanotubes in each sample has been highlighted by black arrows or contours. Results indicate that CNT has a relatively uniform distribution in PC, PA6 and PS, which confirms the explanations in the previous section. However, despite the presence of individually dispersed CNT, CNT agglomerates could be clearly observed in the thick section of PP-10 microparts. It has been reported [150,275,276] that the existence of CNT agglomerates is beneficial to the enhancement of σ for polymer composites. This could explain the observation that the thick section of PP-10 microparts showed the highest σ values with respect to measurement directions when compared with the other polymeric systems, as displayed in Figure 5.9.

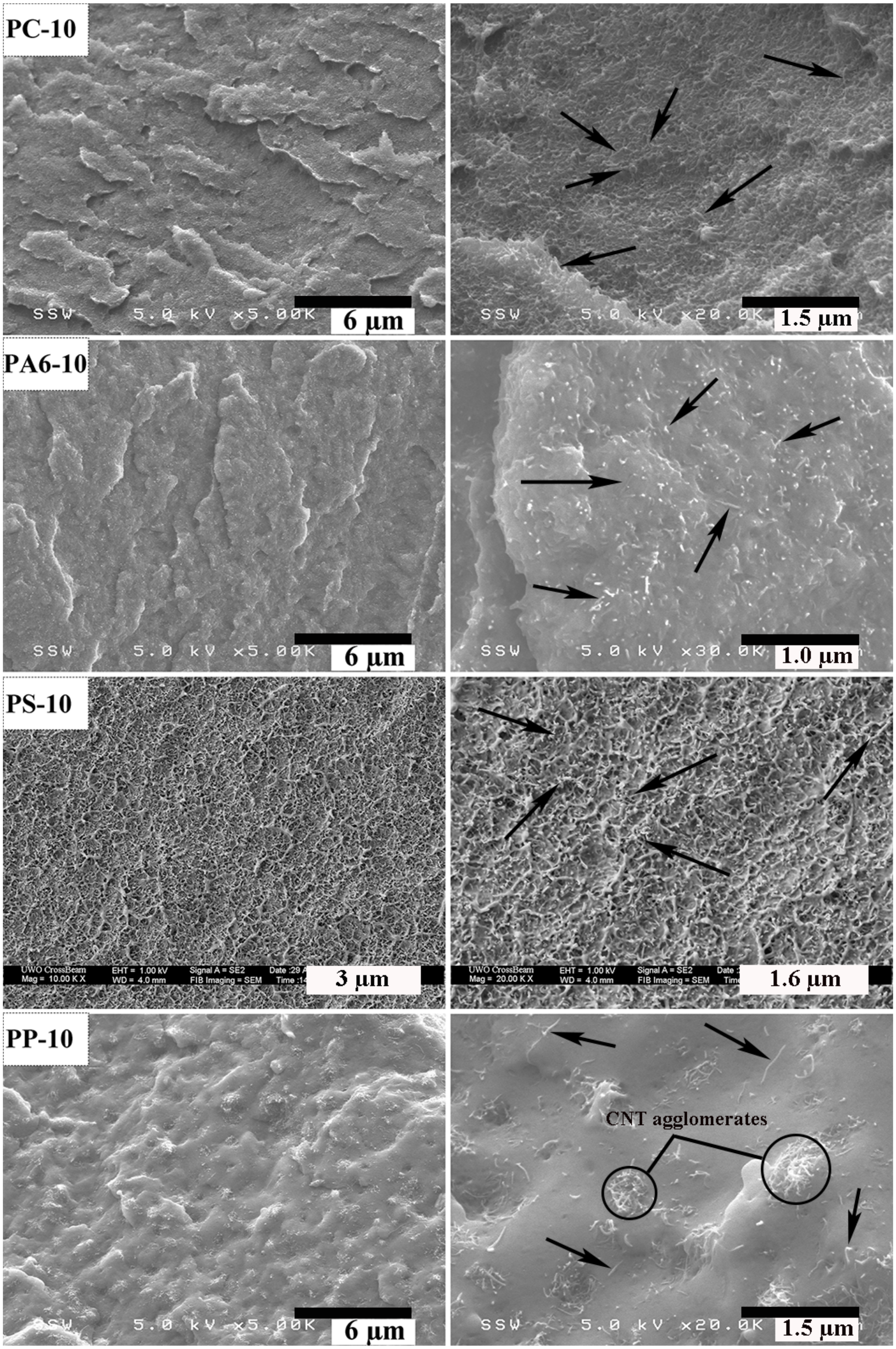

Figure 5.10 The morphology of the thick section of CNT filled various polymer systems.

5.2.2 The effect of CNT loading concentrations on the electrical and morphological properties of polymer/CNT microparts

5.2.2.1 The electrical conductivity and morphology of PS/CNT microparts

5.2.2.1.1 The effect of processing conditions on the electrical conductivity of PS/CNT microparts

The design of experiments (DOE) method was used to study the effect of machine variables (i.e. process parameters) on the properties of microparts. The selected process parameters were injection velocity and melt temperature, which are considered as key molding machine settings for injection molding process [88,149]. Thus, a two-level two-factor full factorial design was applied and tabulated in Table 5.4. The mold temperature was kept at 40°C. The weight fraction of CNT in the polymer composite used in the DOE design is fixed at 10%.

Table 5.4 The DOE design for µIM of PS/CNT 10 wt% composites.

Variables	Melt temperature (ºC)	Injection velocity (mm/s)
Case 1	240	550
Case 2	240	700
Case 3	260	550
Case 4	260	700

The log σ for each section of microparts is plotted as a function of measurement directions in Figure 5.11. The σ of microparts was measured in three perpendicular directions to determine anisotropy, i.e. the flow direction (FD), the transverse direction (TD) and the normal direction (ND), as depicted in Figure 5.11(a). Figure 5.11 demonstrates that melt temperature is the main factor that affects σ of PS/CNT microparts, which indicates that higher melt temperature is beneficial to the network formation by conductive fillers, thus improving the overall σ of resultant microparts. This finding is in agreement with the results reported by Lellinger et al. [278] for injection molded PC/CNT composites. This is mainly due to the fact that polymer chains are more flexible at higher melt temperature which makes them more responsive to shear force. However, Villmow et al. [88] found that the injection velocity plays a dominant role in determining the σ of CIM macroparts. This indicates that the processing history that prevails in µIM is different from that in CIM.

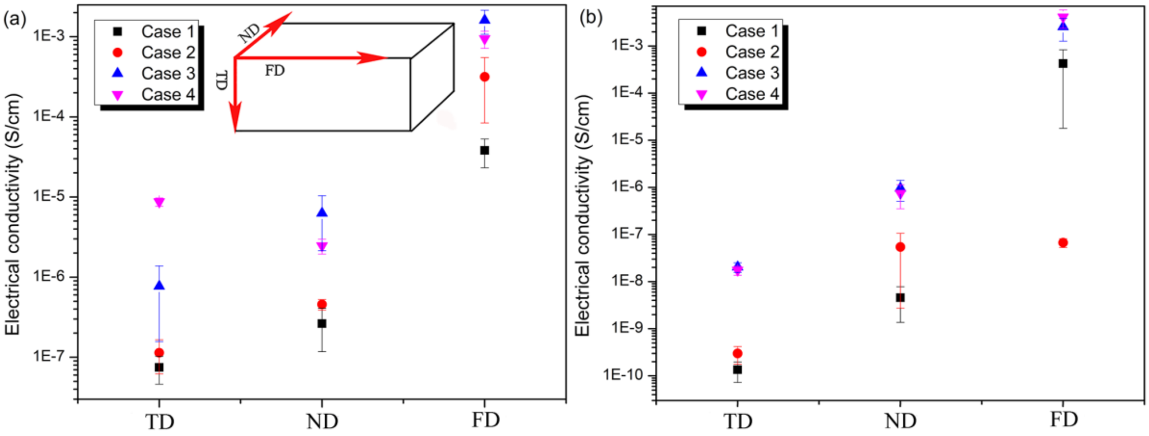

Figure 5.11 The σ measured through different directions of the (a) thick and (b) middle sections of PS/CNT microparts prepared under various processing conditions.

Figure 5.11(b) exhibits that the σ in the FD of the microparts prepared in Case 4 showed the highest value, which is nearly 5 orders of magnitude higher than that obtained from the microparts molded in Case 2. In this scenario, the result is explained by two factors: *(1)* in Case 4, both the melt temperature and injection velocity are higher which facilitate the orientation of CNT along the flow direction; *(2)* there is a sharp change of mold cavity thickness from 0.85 mm (thick section) to 0.50 mm (middle section). It is anticipated that the effective shear rate is much higher when the polymer melt flows from the thicker cavity into a thinner one, which was corroborated by the simulation results shown in Figure 5.12. In addition, the extensional forces are quite significant in the contraction regions between different sections of the microparts. Therefore, a strong CNT orientation in the thinner part of the microparts is expected when compared with that of its thicker counterpart.

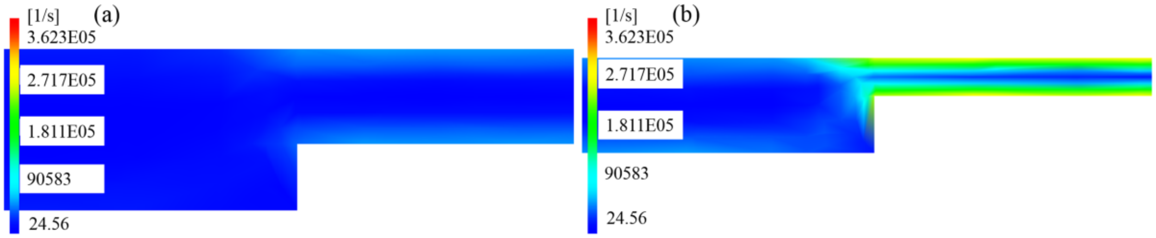

Figure 5.12 The simulated maximum shear rate distribution around the contraction areas: (a) from the thick to middle sections and (b) from the middle to thin sections, respectively.

5.2.2.1.2 The effect of CNT concentrations on the electrical conductivity of PS/CNT microparts

Like most polymers, PS is intrinsically an electrical insulator. It will become conductive when the conductive filler, i.e. CNT, dispersed within the host matrix attains sufficient contacts to form a percolated structure which assists the electron transportation. However, the configuration and quality of dispersion of conductive particles in injection molded host polymers, especially CNT with high aspect ratio, depend strongly on processing conditions [147]. Notably, shear rates as high as 10^6/s are not rare in µIM [13]. Therefore, the p_c of injection molded parts often shifts towards higher concentration of filler loadings when compared with other processing techniques, for example compression molding [12]. The log σ values are plotted against the weight fraction of CNT in Figure 5.13. The figures are plotted separately with respect to measurement directions relative to the mold filling (flow) direction. The microparts were prepared under the conditions of Case 3 (see Table 5.4).

Figure 5.13 illustrates that the σ for all studied samples increased with increasing loading fractions of CNT in the composites. Figure 5.13(a) indicates that the σ for the thick section measured across the TD is invariably higher than that observed for the middle section of micropart. Herein, it is proposed that there might be a shearing migration effect of CNT from the surface (skin) to the core region of the microparts during the injection molding process. It has been reported that higher migration of loading fillers occurs with an increase of shear rate [279,280]. Therefore, the corresponding σ obtained in the middle section is somewhat lower than that observed for the thick section counterpart. In addition, Figure 5.13(b) shows that the σ for both the thick and middle sections of microparts along the ND showed almost similar value up to a CNT loading of 7 wt%. This is mainly due to the fact that CNT is preferentially oriented along the FD during μIM. Therefore, it would be hard to construct enough conductive pathways by CNT in this specific direction at low filler concentrations. Similar trend was also observed for measurements along the FD up to a CNT loading of 10 wt%, as shown in Figure 5.13(c). It can be deduced from Figure 5.13 that the p_c for all studied directions falls in the region ranging from 5 to 7 wt%. In addition, Arjmand et al. [281] reported that the p_c for PS/CNT composites is about 5 wt% in CIM. Thus, the above indicates that percolated conductive structure is hard to build in injection molded samples, especially in μIM, which is consistent with the results reported by Abbasi et al [12].

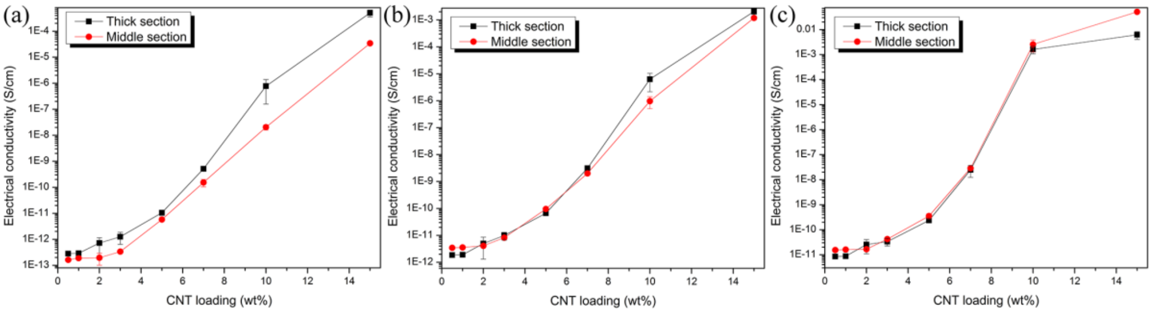

Figure 5.13 The σ measured across the (a) TD, (b) ND, and (c) FD on the thick and middle sections of PS/CNT microparts as a function of CNT content.

5.2.2.1.3 Morphology

The morphology of PS/CNT 10 wt% microparts along the FD is shown in Figure 5.14. All images were taken from the core region of each part which is marked by black arrows in Figure 5.14. Figure 5.14 indicates the formation of an interconnected network of CNT within PS in all graphs. Interestingly, a typical fiber distribution structure (labeled by red arrows in high magnification images) is observed along the FD, which suggests a preferential alignment of CNT in the FD owing to the strong shearing effect resulting from the combined effects of high injection velocity, high melt temperature and, most importantly, step decrease of the thickness of mold cavities. The diameter of individual CNT was measured from the SEM images with the software Image J and the detectable diameter of individual CNT observed in Figure 5.14 mainly lies in the range of 20-40 nm, which is higher than the technical data (approximately 10 nm) provided by the producer.

One possibility is that a thin layer of PS matrix surrounded the CNT after melt processing due to the possible π-π interaction [282] amid the sidewall of nanotubes and the polymer matrix. In addition, the σ for the middle section along the FD prepared in Case 4 is higher than that observed for the thick section, as indicated in Figure 5.11. Meanwhile, all samples experienced a simultaneous reduction of the σ measured through both the TD and ND for the middle section when compared with corresponding values obtained from thick section counterparts. The results reflect the higher degree of CNT orientation in the middle section due to a reduction of the mold cavity thickness along the flow direction, in agreement with the simulation results reported in Figure 5.12.

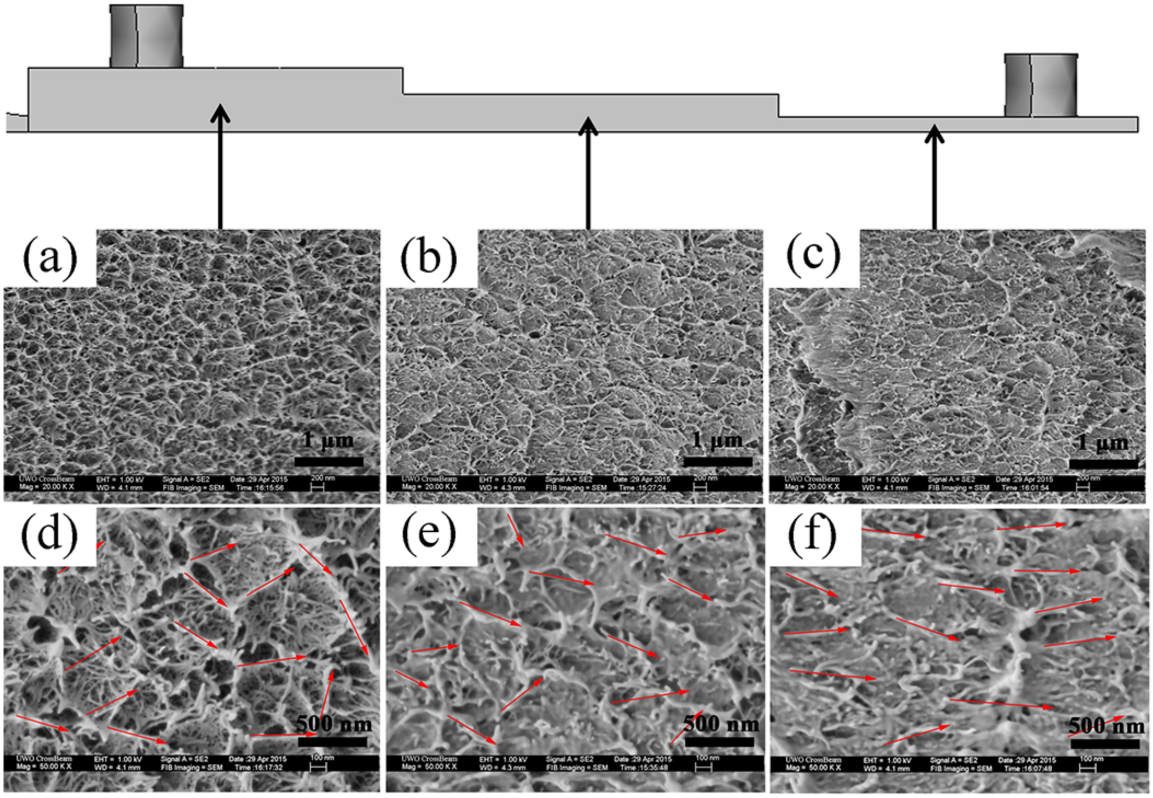

Figure 5.14 SEM images of cryo-fractured surface along the flow direction of microparts prepared in Case 4 with respect to measurement sections: (a, d) thick section; (b, e) middle section, and (c, f) thin section.

Normally, a typical ‘skin-core’ structure is expected in injection molded articles due to the high shear force and fast solidification of polymer melt close to the cold surface of mold wall, thus filler orientation is observed in the skin region [88]. For example, Jiang et al.

[13] reported that CNT is preferentially aligned along the flow direction in the shear layer (i.e. skin layer) rather than the core region of the microinjection molded parts.

The morphology of the cryo-fractured surface (perpendicular to flow direction) of the thick section for PS/CNT 10 wt% microparts prepared in Case 3 is presented in Figure 5.15. Figures 5.15(a) and (c) are taken from the middle of the thick section close to mold wall which is deemed as the skin layer, whereas (b) and (d) are taken from the core region correspondingly. Generally, the observable white dots in both photos are the ends of nanotubes. Figures 5.15(a) and (b) show that the CNT dispersed evenly within the host matrix and there are more white dots observed in the skin layer than in the core region, indicating that CNT is dominantly oriented in the skin layer along the flow direction. It can be seen from Figures 5.15(c) and (d) that the 3D conductive network is constructed by the interconnection of CNT within PS, facilitating the transport of electrons. In addition, there are more detectable CNT ends (i.e. white dots or protrudes) in Figures 5.15(c) than (d). Conversely, the diameter of CNT observed in Figure 5.15(d) is slightly higher than that in (c). This suggests that the very high shear deformation rate and stresses in the skin layer might overcome the interactions between the CNT particles and polymer matrix.

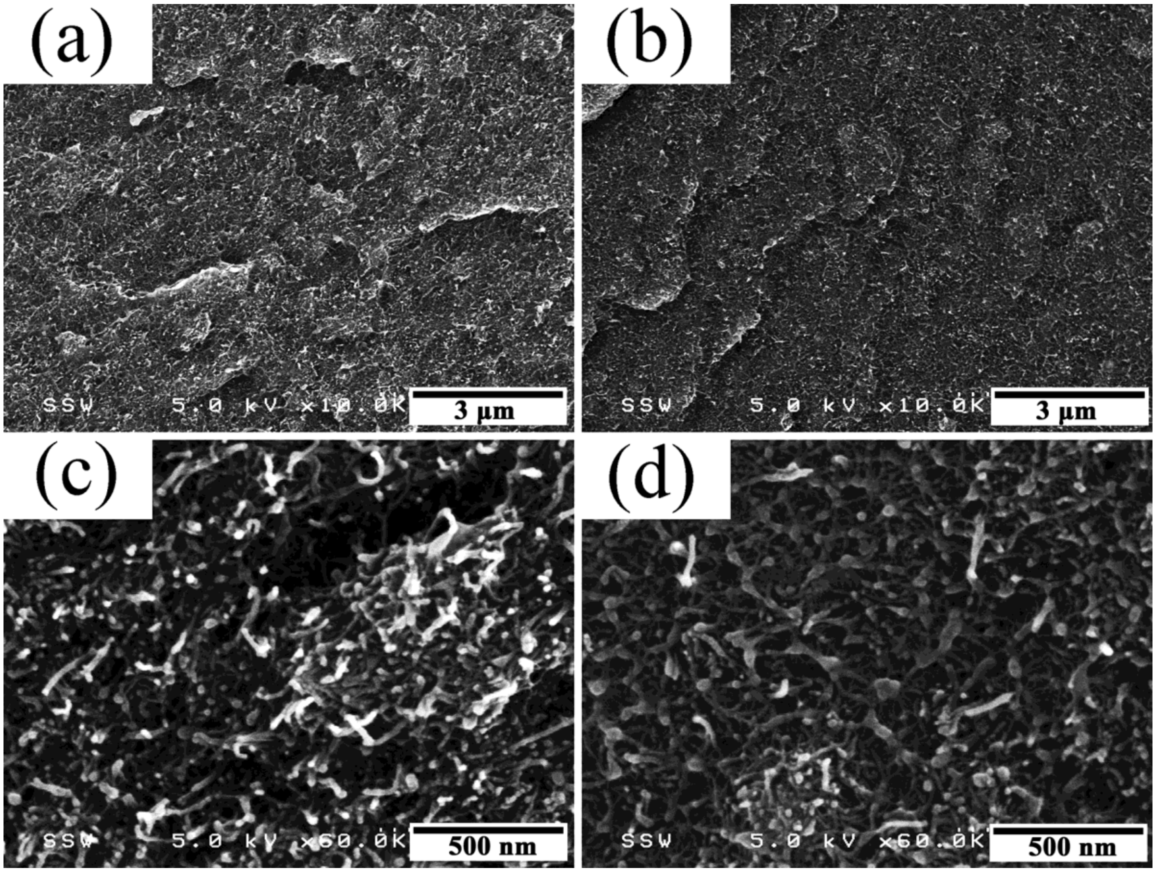

Figure 5.15 SEM images of the cross section of the microparts: (a, c) show the skin layer of thick section in different magnifications while (b, d) show the core layer of thick section in different magnifications.

5.2.2.2 The electrical conductivity and morphology of PA6/CNT microparts

5.2.2.2.1 The effect of CNT concentrations on the electrical conductivity of PA6/CNT microparts

The electrical resistivity (ρ) which is the reciprocal of the electrical conductivity (σ) for compression molded PA6/CNT samples and each section of corresponding microparts is reported in Figure 5.16. No ρ could be measured for the thin section of PA6/CNT 2 wt% (i.e. CNT2) microparts due to a lack of conductive pathways, as displayed in Figure 5.16(b). However, the ρ across the TD for both the thick and middle sections is almost two orders of magnitude higher than that measured along the FD, indicating a preferential orientation of CNT in the flow direction. In addition, there was a reduction of ρ in the middle section when compared with that of the thick section counterpart with respect to the measurement directions, which could be related to the improved dispersion of CNT in the polymer matrix (discussed in the following section). Although the formation of a conductive network seemed to be unlikely at such a lower CNT loading concentration (2 wt%), the improvement of σ in the FD could be explained by a hopping or tunneling mechanism [283]. In this case, physical contact between the added fillers is unnecessary as long as they are close enough to allow the passage of electrons [284,285]. As the orientation and dispersion of CNT are favored in PA6 with increasing shear rates, the average distance between individually dispersed CNT decreases in the middle section and the transport of electrons is therefore facilitated through ‘tunneling’ between adjacent CNTs [283,286].

Figure 5.16(c) shows that there was an increase of ρ measured in the TD and FD for CNT5 microparts from the thick to thin sections. However, like CNT2 microparts, the ρ measured along the FD was invariably lower than the value obtained from the compression molded samples (Figure 5.16a), which further confirmed a preferential alignment of CNT in the flow direction. An increase of ρ in the middle section of microparts could be related to the improved dispersion of CNT and the disentanglement of CNT aggregates arising from the increasing shear rates. For example, Ferreira et al. [95] pointed out that the p_c for PA6/CNT composites in μIM is 4-6 wt%. In the case of CNT5, the values of σ would be dominated by the formation of conductive network through physical interconnection amid dispersed CNTs and small CNT aggregates. Thus, the improved dispersion of the incorporated fillers in the middle section of corresponding microparts might be detrimental to the formation of conductive network [276,285], thereby lowering the σ in according section [285].

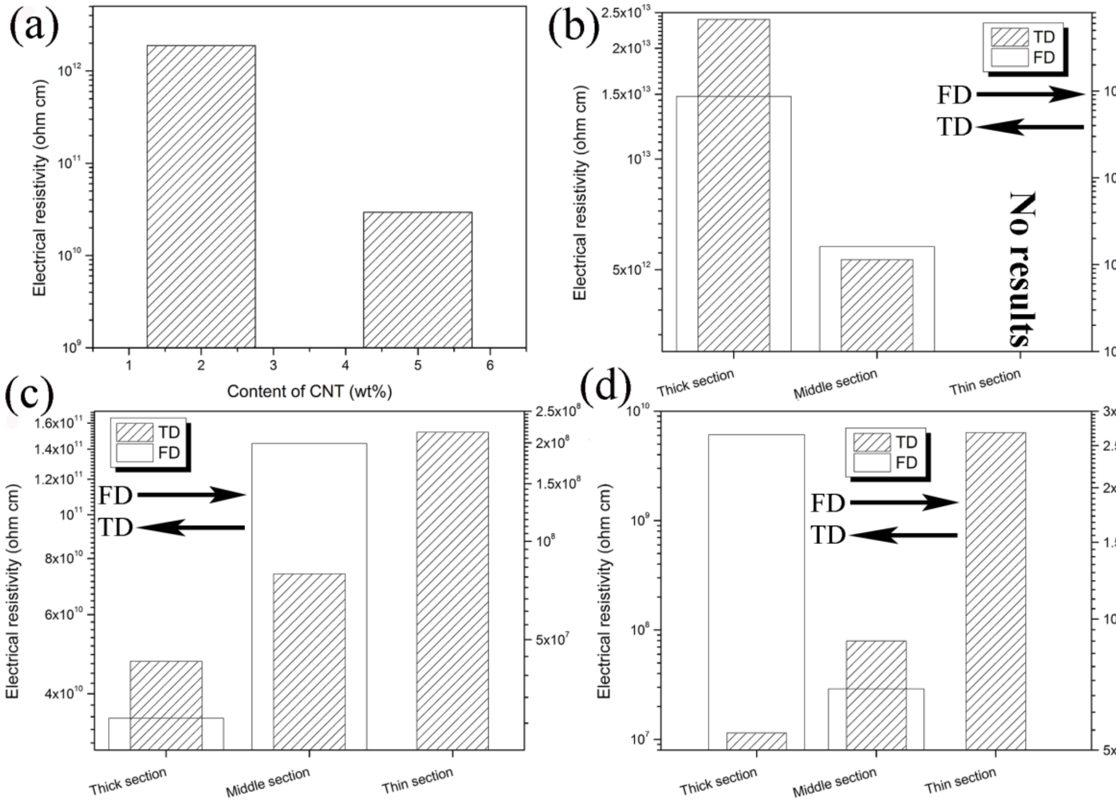

Figure 5.16 The electrical resistivity (ρ) of (a) compression molded PA6/CNT samples and sections of (b) CNT2 microparts, (c) CNT5 microparts and (d) CNT10 microparts.

The ρ measured across the TD for each section of CNT10 microparts exhibited a similar trend as reported for their CNT5 counterparts. However, the ρ measured in the FD for the middle section was lower than that for the thick section. Results suggest that sufficient conductive pathways could be formed within PA6 matrix at a CNT loading fraction of 10 wt%. The favored orientation of CNT along the FD tends to increase the probability of CNT-CNT contacts, thereby leading to an enhanced σ in the middle section when compared with that obtained from the thick section. Furthermore, Figures 5.16(c) and (d) reveal that the presence of very high shearing effect is unfavorable for the construction of conductive pathways within subsequent microparts because the thin section showed the highest ρ, regardless of CNT loading concentrations.

5.2.2.2.2 Morphology

The morphology of extrudates obtained from masterbatch dilution process was examined using SEM and the results are given in Figure 5.17. The bright dots (i.e. the end of CNT) and the fibril-like structure underneath the polymer surface, which are pointed out by red arrows, indicate the presence of CNT. In addition, the mean distance between individually dispersed CNT decreases with an increase of CNT concentration, which is favorable for the formation of 3D conductive pathways. In general, CNTs were uniformly dispersed within the extrudates, regardless of CNT concentrations, which further confirmed that the masterbatch dilution process is an effective method to fabricate polymeric composites containing CNT.

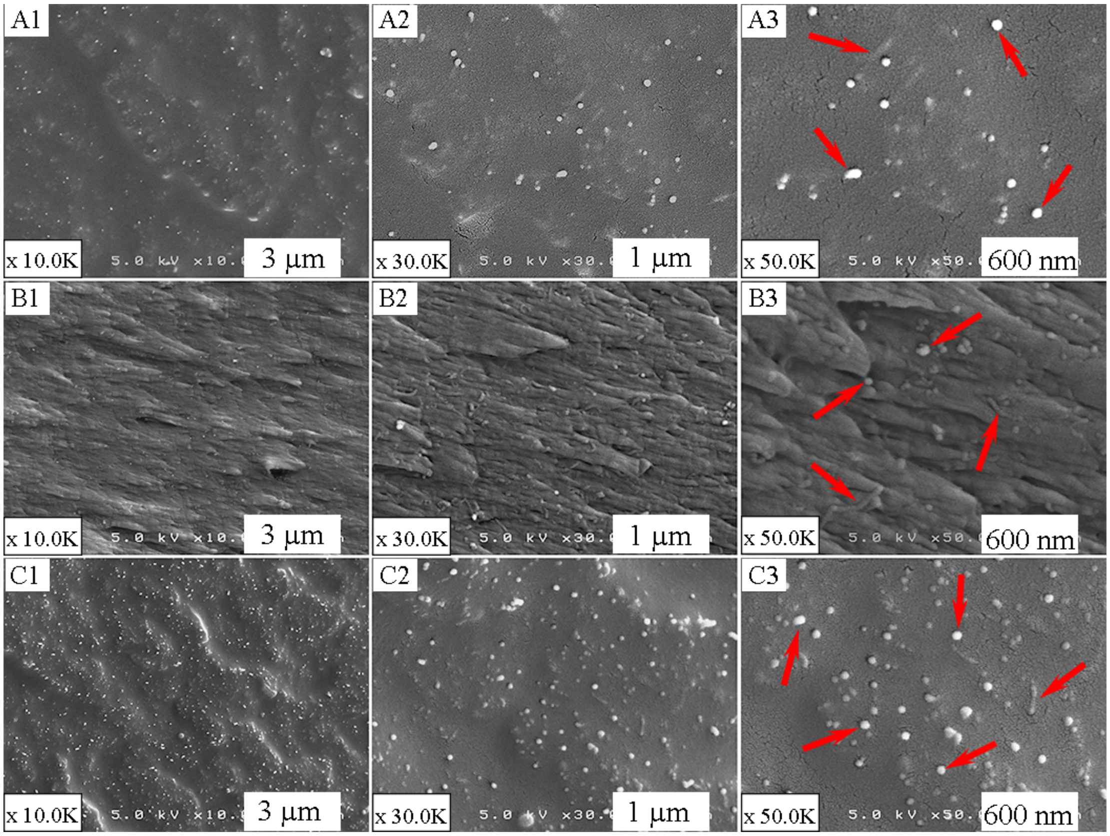

Figure 5.17 The morphology of cryo-fractured surface of diluted PA6/CNT extrudates: (A1-A3) 2 wt%, (B1-B3) 5 wt%, and (C1-C3) 10 wt%, respectively.

The development of internal microstructure within each section of PA6/CNT microparts, and the effect of CNT concentration on the morphology of subsequent microparts were evaluated using SEM as well. All samples for PA6/CNT microparts were fractured in liquid nitrogen across TD, i.e. perpendicular to the melt flow direction. Figure 5.18 shows that the microstructure of the thick section obtained from CNT5 microparts. Figures 5.18(a) and (b) were taken from the core layer of the thick section, whereas Figures 5.18(c) and (d) were taken from the shear layer which is close to the mold wall. Figures 5.18(a) and (c) suggest that CNTs are relatively uniformly distributed within the matrix since no obvious CNT aggregates were observed in either the core layer or shear layer. Interestingly, more bright dots could be observed in Figure 5.18(d) (shear layer) when compared with Figure 5.18(b) (core layer), suggesting that CNTs are preferentially aligned in the flow direction, which could be attributed to the influence of higher shearing effect that prevails in the shear layer. This is consistent with our previous observations for PS/CNT microparts. As a result, this would increase the probability of CNT-CNT contacts along the FD, thereby leading to a reduction of ρ in the FD when compared with that across the TD.

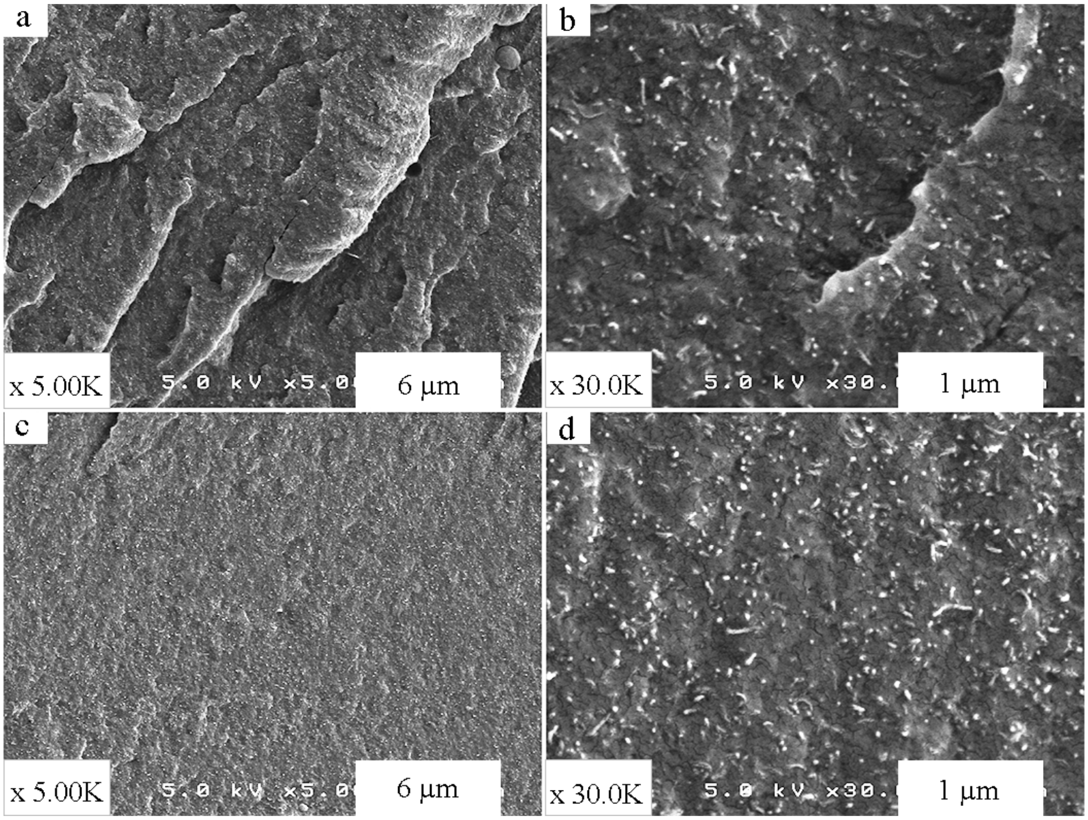

Figure 5.18 The morphology of thick section of CNT5 microparts taken from: (a, b) core layer; (c, d) shear layer.

Similarly, it could be deduced from Figures 5.19 and 5.20 that CNT achieved a relatively uniform distribution in both the middle and thin sections of CNT5 microparts, respectively. However, the number of detectable bright dots in corresponding layer of the middle (Figure 5.19d) and thin (Figure 5.20d) sections seemed to be smaller than that observed for the thick section (Figure 5.18d). As a result, it could be expected that this would lead to a higher ρ for both the middle and thin sections of microparts, indicating that the shearing conditions existed in different sections of the microparts play a pivotal role in determining the microstructure. Previous simulation analysis (see Figure 5.12) indicated that there is a significant increase of maximum shear rates with a simultaneous reduction of the thickness of mold cavities. Therefore, it seems to be reasonable to attribute the development of microstructure in each section to the variation of shearing conditions. Li and Shimizu [236] reported that the CNT could achieve a better dispersion in a polymer matrix when they were processed at elevated shearing conditions. Chen and co-workers [286] also reported similar findings in CNT filled PVDF composites. However, Pegel et al. [276] pointed out that although higher shear rates could provide suitable CNT dispersion in a host polymer matrix, secondary agglomeration of CNT was also prevented which is thought to be detrimental to the enhancement of σ of corresponding composites. In addition, the length reduction of CNT during the melt processing, especially under severe shearing conditions, could be another concern which would significantly devalue the σ of subsequent products [287].

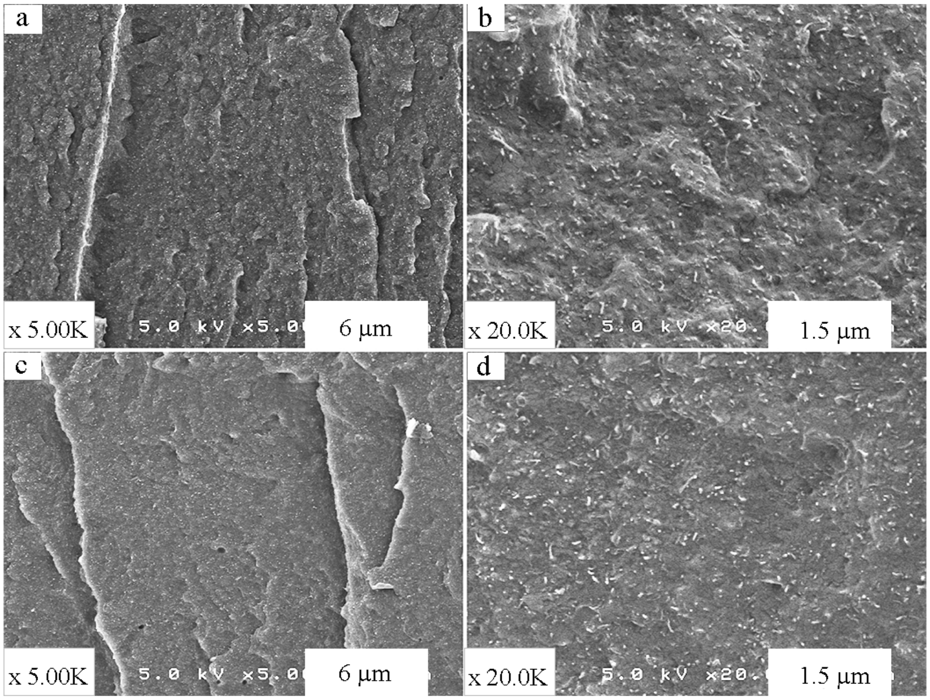

Figure 5.19 The morphology of middle section of CNT5 microparts taken from: (a, b) core layer; (c, d) shear layer.

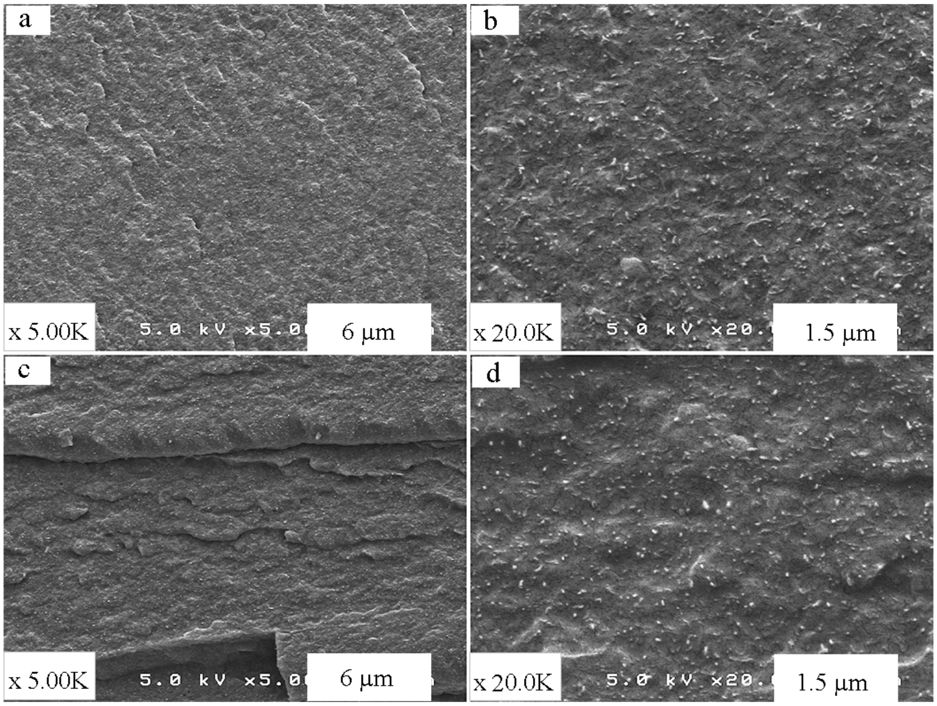

Figure 5.20 The morphology of thin section of CNT5 microparts taken from: (a, b) core layer; (c, d) shear layer.

Figure 5.21 displays the microstructure of the thick section of CNT2 microparts. The CNTs were uniformly dispersed in each layer, as no obvious CNT agglomeration can be observed. Moreover, it is hard for the CNTs to form intact 3D conductive pathways within PA6 due to the low loading fraction (i.e. 2 wt%). In addition, Figure 5.22 illustrates the morphology of the thick section of CNT10 microparts. As shown in Figures 5.22(b) and (d), there is no significant difference in the quality of CNT dispersion in each layer of the thick section at such a high filler concentration. Furthermore, a conductive network could be easily observed with the CNT particles entangled with each other, which is advantageous to the enhancement of σ.

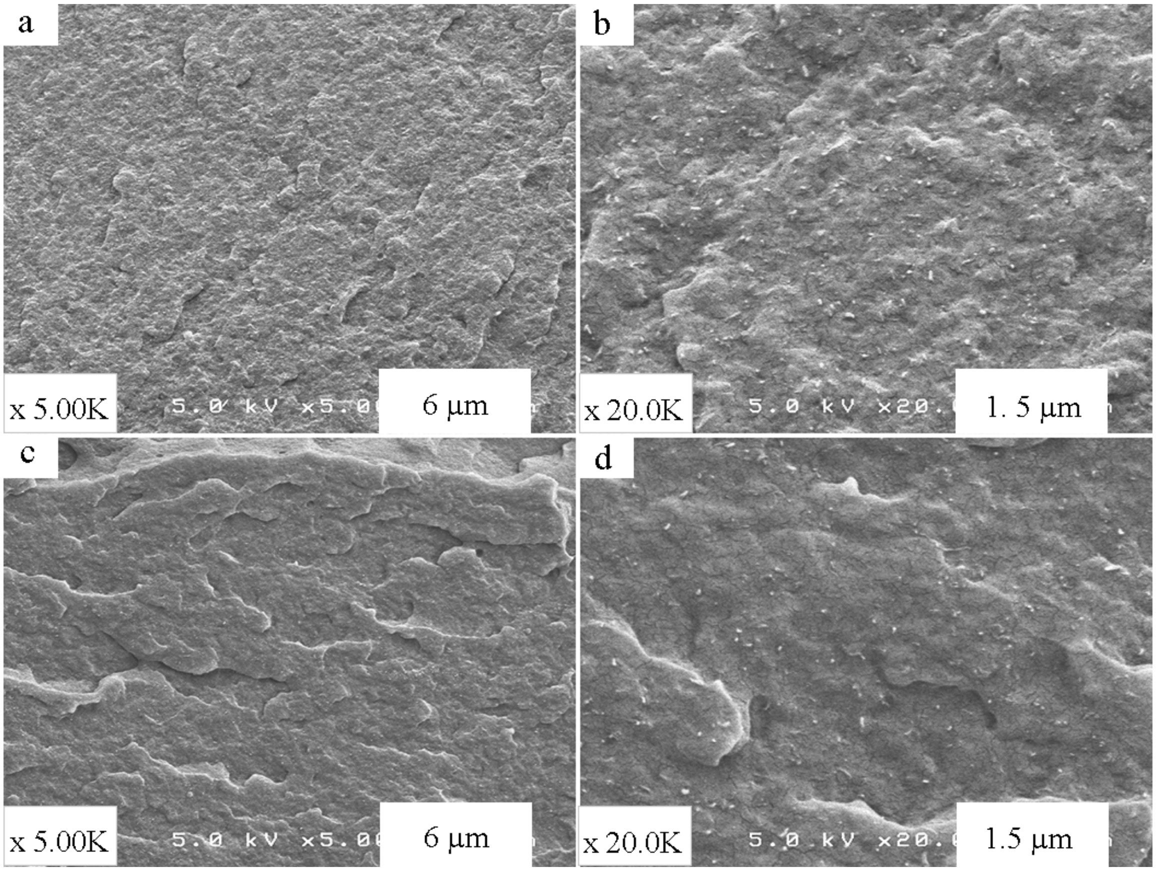

Figure 5.21 The morphology of thick section of CNT2 microparts taken from: (a, b) core layer; (c, d) shear layer.

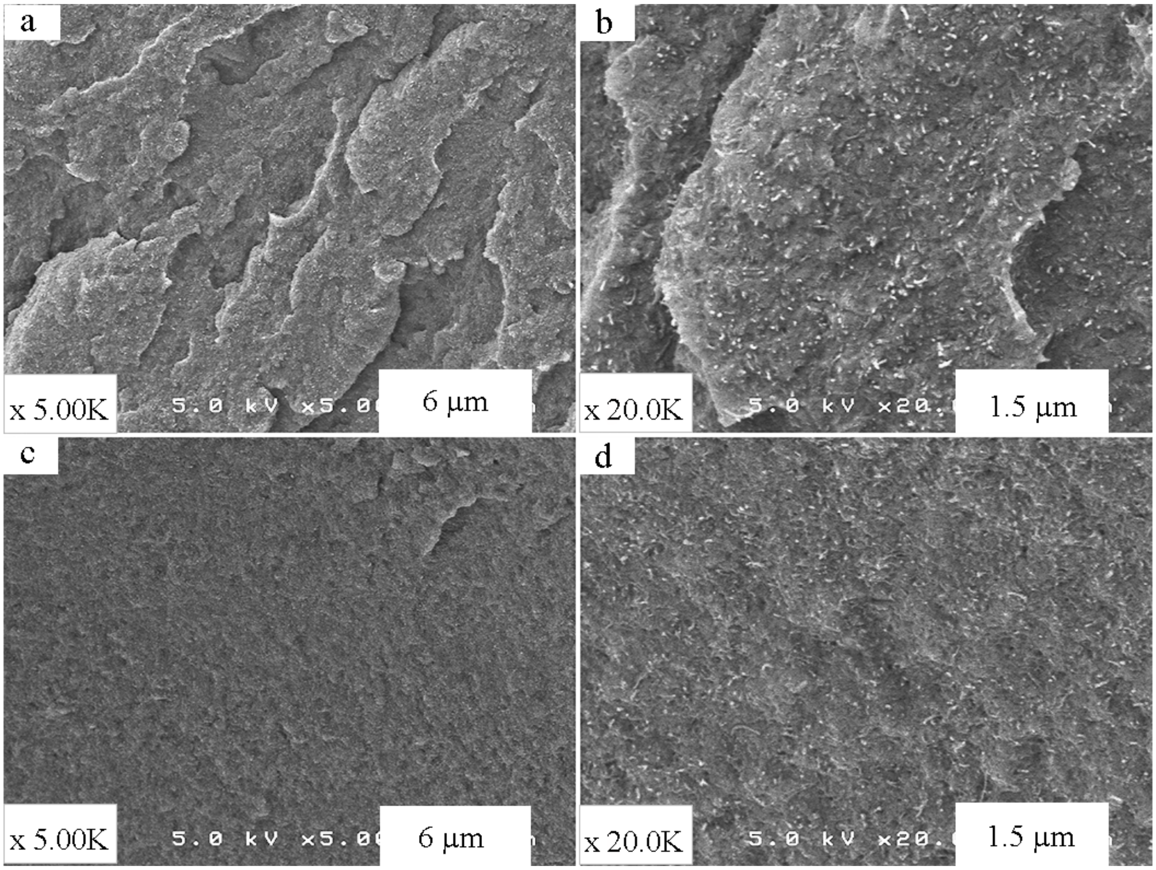

Figure 5.22 The morphology of thick section of CNT10 microparts taken from: (a, b) core layer; (c, d) shear layer.

5.2.2.3 The electrical conductivity and morphology of PC/CNT microparts

5.2.2.3.1 The effect of CNT concentrations on the electrical conductivity of PC/CNT microparts

Figure 5.23 displays the volume σ of PC/CNT microparts at different CNT concentrations with respect to measurement directions, i.e. TD and FD, for the thick and middle sections, respectively. In general, the σ increases with CNT concentration in corresponding PC/CNT microparts. The average values of σ for microparts with lower CNT concentrations (< 7 wt%) are not available because they are outside of the lower limit of the measurement scale for Keithley 6514 electrometer, indicating a higher filler concentration is required to attain sufficient conductive pathways within subsequent microparts. In contrast, Via et al. [288] reported that the p_c for CIM PC/CNT macroparts is about 1.7 wt% (1.2 vol%). Moreover, they reported that the σ reached 2.2×10^{-4} S/cm of PC/CNT 2 wt% macroparts [288] which is nearly 6 orders of magnitude higher than that obtained in µIM [101], indicating that the difference in shearing conditions plays a pivotal role in determining the microstructure of subsequent moldings.

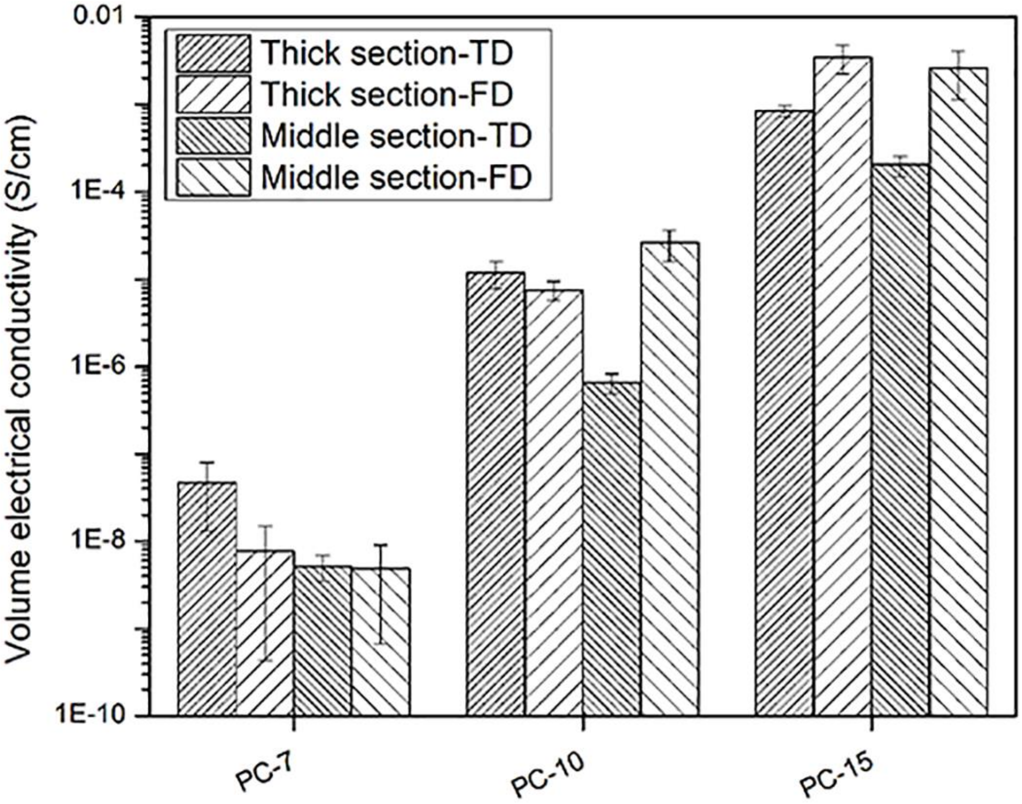

Figure 5.23 The σ of PC/CNT microparts with respect to the measurement directions as a function of filler content. PC-7 indicates PC/CNT 7 wt% composite.

5.2.2.3.2 Morphology

The morphology taken from different regions of the cross-section of both the thick and middle sections of PC/CNT 5 wt% (i.e. PC-5) microparts is illustrated in Figure 5.24. The sampling positions for SEM observations are pointed out by black arrows. Figure 5.24 indicates that there is no significant difference in the state of dispersion of CNT in both the shear layer (i.e. images at the left side) and core layer (right side) of corresponding sections. However, more white dots (i.e. the ends of nanotubes) seem to be detectable in the shear layer of the middle section, indicating that the higher shearing effect which prevails in the shear layer (as reflected by simulation analysis in the following section) contributes to the preferential orientation of CNT in the flow direction.

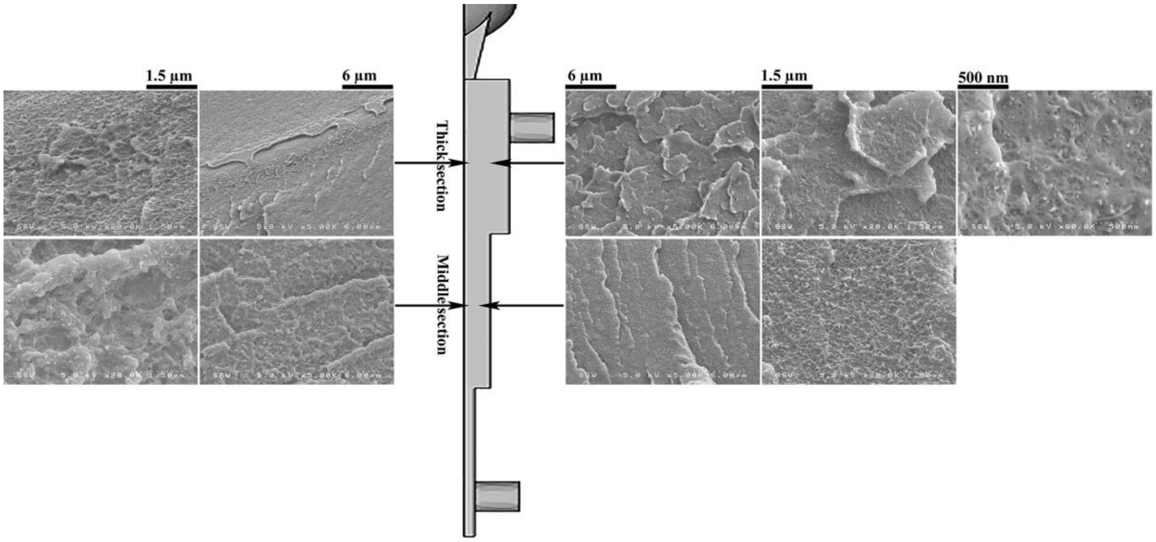

Figure 5.24 SEM images of the cross section of PC-5 microparts. Black arrows indicate the sampling positions for SEM observations.

5.2.2.3.3 Simulation (Moldflow)

The distribution of maximum shear rates as a function of distance across the thickness of each section is given in Figure 5.25. One can easily note that the maximum shear rate occurs in the vicinity of skin layer of the microparts. Eken et al. [256] reported that increasing shear rate would facilitate the orientation of CNT along the FD. Consequently, there would be a higher possibility of CNT-CNT contacts along FD, which contributes to the enhancement of σ. Simultaneously, the construction of intact 3D conductive pathways across the TD would be, to a certain degree, impaired which is unfavorable for the free passage of electrons in TD [275]. Moreover, it should be noted that the μIM cycle is very short, which results in rapid freezing of the generated structure which has little chance of returning to a random orientation. In this scenario, the σ of microparts measured in the TD would be significantly affected due to a lack of sufficient conductive pathways.

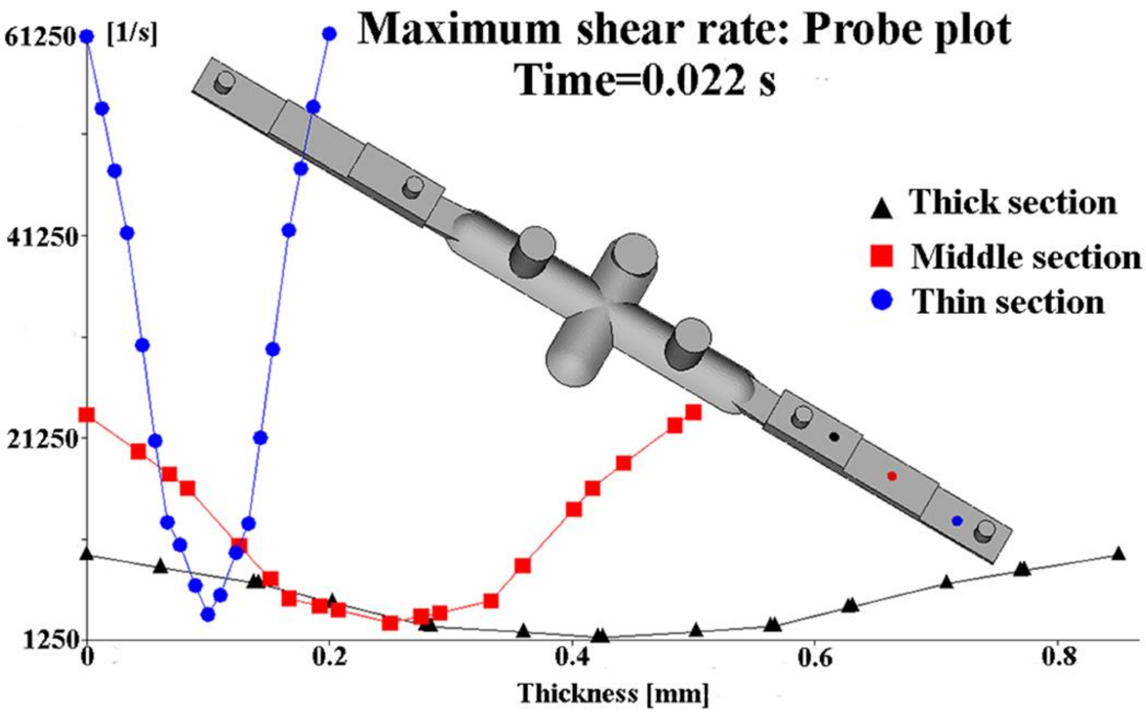

Figure 5.25 The probe plot of maximum shear rates as a function of distance across the TD of each section of pure PC microparts.

5.2.3 Differential scanning calorimetry (DSC)

Since PA6 and PP are semi-crystalline polymers, the melting and crystallization behavior for CNT filled PA6 and PP composites and subsequent moldings was studied using DSC.

5.2.3.1 Melting and crystallization behavior of PA6/CNT composites and subsequent moldings

As per *Section 4.5.4*, the melting and crystallization behavior of PA6 and diluted PA6/CNT extrudates as well as each section of the microparts were determined using a differential scanning calorimeter (DSC, Q2000, TA Instruments). The measurement, which consists of a heating phase followed by a cooling phase, was carried out between 40 and 240°C at a heating rate of 10°C/min. The typical thermal analysis data obtained from the DSC heating and cooling processes were listed in Table 5.5.

Table 5.5 The melting temperature (T_m), crystallinity (χ_c), crystallization temperatures (T_{c1}, T_{c2}) and onset crystallization temperature (T_{onset}) of pure PA6, PA6/CNT extrudates and different sections of corresponding microparts.

Samples	Melting process		Crystallization process		
	T_m (°C)	χ_c	T_{c1} (°C)	T_{c2} (°C)	T_{onset} (°C)
PA6	221.24	0.392	192.60	N/A	198.56
PA6 Thick section	220.30	0.419	191.76	N/A	196.19
PA6 Middle section	220.06	0.499	191.63	N/A	196.56
PA6 Thin section	217.98	0.417	191.31	N/A	196.03
CNT2 extrudate	220.99	0.301	194.25	206.19	215.92
CNT5 extrudate	219.66	0.321	193.13	207.85	218.83
CNT10 extrudate	221.53	0.335	196.00	209.35	218.66
CNT5 Thick section	221.88	0.340	195.99	210.08	220.31
CNT5 Middle section	217.66	0.342	193.15	208.67	219.25
CNT5 Thin section	217.38	0.317	192.68	209.69	217.93
CNT2 Middle section	217.10	0.369	193.69	206.54	214.94
CNT10 Middle section	217.51	0.328	194.56	209.84	220.24

Figures 5.26(a) and (b) display the DSC heating and cooling behavior, respectively, of pure PA6 and diluted PA6/CNT extrudates with various CNT fractions. Herein, CNT2 indicates the weight fraction of CNT in PA6 is 2 wt% and the same nomenclature applies to the other PA6 systems. It could be deduced from Figure 5.26 that the incorporation of CNT had little effect on the melting behavior of PA6. However, the crystallization process was greatly affected with the presence of CNT. For pure PA6, only a single crystallization peak (T_{c1}) was detected in the vicinity of 192°C. For PA6/CNT extrudates, as indicated in Figure

5.26(b) and Table 5.5, T_{c1} shifted to higher values when compared with that obtained from pure PA6. The T_{onset} increased significantly upon the incorporation of CNT, indicating that CNT played a role of nucleating agent. In addition, a second crystallization temperature (T_{c2}) was observed at higher temperatures for CNT-containing PA6 composites, and its position gradually shifted to high temperature region with an incremental loading fraction of CNT, which suggested that the appearance of second crystallization peak in PA6 could be related to the presence of CNT. Similar observations have been reported by Logakis et al. [289] and Krause et al. [290]. The appearance of the double crystallization peak in PA6/CNT composites could be explained by the formation of two different types of crystal morphologies or two-step crystallization due to the presence of one-dimensional filler, i.e. CNT, which has been detailed by Logakis et al. [289]. In the first case, the CNT surface may induce the crystallite growth in a manner that is perpendicular to the CNT axis, which leads to the development of trans-crystalline structure [95]. However, the polymer chains tend to form spherulites in the regions which are far away from the nanotubes [289]. Thus, the co-existence of two different types of crystals could possibly contribute to the appearance of double crystallization peak. In the other case, it was proposed that the presence of double crystallization peak could be related to the two-step crystallization of polymer chains. The incorporation of fillers in a polymer matrix would greatly accelerate the crystallization process of polymer chains [26]. Phang et al. [291] proposed that both the very high aspect ratio of CNT and high crystallization temperature are favorable for the formation of thermodynamically stable α-phase crystals. Both mechanisms suggest that the appearance and the intensity of the second crystallization peak could be related to the number of the incorporated CNTs.

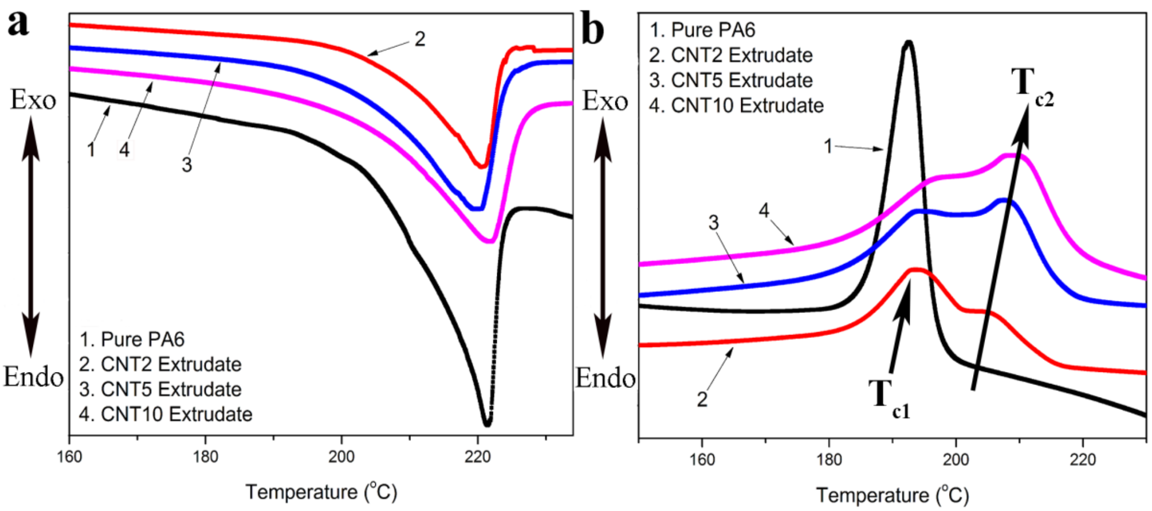

Figure 5.26 DSC (a) heating and (b) cooling curves obtained from pure PA6 and PA6/CNT extrudates with various filler concentrations.

Thermal behavior of pure PA6 and sections taken from corresponding microparts is given in Figure 5.27. As displayed in Figure 5.27 and Table 5.5, the T_m, T_{c1} and T_{onset} for each section of PA6 microparts decreased when compared with these values obtained from pure PA6. This could be attributed to the influence of thermomechanical history experienced by polymer melts in µIM which determines the microstructure during the injection molding process [292]. Kamal et al. [212] reported that a five-layer crystalline structure is observed in a POM micropart in comparison with commonly observed three-layer structure in CIM macroparts. Moreover, there would not be sufficient time allowed for polymer chains to form well-developed crystals during µIM due to the fast filling rate, large thermal gradients and short cycle times. Therefore, the slight downshift of T_m observed in sections of pure PA6 microparts (Table 5.5) indicates the existence of imperfections in resulting crystalline structures. However, a second melting peak (ca. 222.65°C) is noticeable for the middle section, suggesting that prevailing shearing conditions in the middle section might partially promote the formation of well-aligned structures. Table 5.5 reveals that although the T_m of different sections of PA6 microparts decreased when compared with that of pure PA6, a remarkable increase of χ_c was achieved for these sections. This could thus be attributed to the variation of shearing conditions in different sections of microparts. The higher shear rates facilitated the orientation of polymer chains along flow direction, leading to a higher

χ_c for sections that experienced relatively high shearing conditions. Moreover, the cooling effect becomes accentuated in different sections of PA6 microparts [193]. Under such circumstances, however, a relatively stable crystalline structure was hardly formed by the polymer chains, which in turn resulted in a reduction of T_m. Interestingly, the χ_c of thin section was comparable to that of thick section. However, the T_m of the thin section of pure PA6 micropart was at least $2^{o}C$ lower than that of thick section. Therefore, it appears that a combination of extremely high shear rates and fast cooling rates in the thin section is unfavorable for the formation of perfect crystallites, which leads to a reduction of T_m.

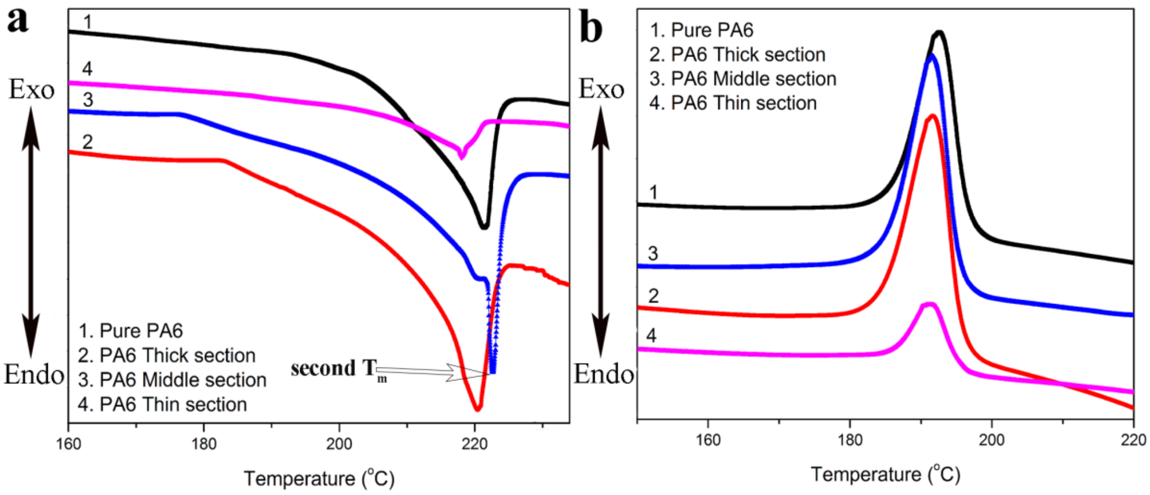

Figure 5.27 DSC (a) heating and (b) cooling curves obtained from pure PA6 and sections of pure PA6 microparts.

Figure 5.28 displays the thermal behavior of pure PA6 and different sections taken from PA6/CNT 5 wt% (abbreviated as CNT5) microparts. As shown in Figure 5.28(a), only a marginal difference of T_m was recorded, suggesting that the μIM process had little effect on the melting behavior of the microparts. Like PA6/CNT extrudates (Figure 5.26b), the presence of CNT in each section of corresponding microparts had a significant effect on the crystallization behavior and a double crystallization peak was typically observed as well. Compared with CNT5 extrudate, a slightly higher T_{c2} (Table 5.5) for each section of corresponding microparts might suggest a shear induced crystallization in μIM. However, the achieved χ_c for each section of CNT5 microparts was lower than that of corresponding sections of pure PA6 counterparts, suggesting that the presence of CNT might hinder the formation of ordered crystalline structure or domains, which resulted from the limited space and confinement effect that imposed on the polymer chains by CNT, irrespective of the heterogeneous nucleation effect induced by the incorporated fillers. The other possible explanation could be associated with the fact that the pure PA6 which was adopted to dilute the masterbatch is different from the original PA6 pellets that used in the masterbatch production. Therefore, the co-existence of two different types of PA6 polymer chains or the possible degradation of PA6 chains arising from the high shearing conditions might be reflected in the crystallization process, thereby leading to a relatively lower χ_c for diluted samples such as PA6/CNT extrudates and sections of corresponding microparts, as given in Table 5.5.

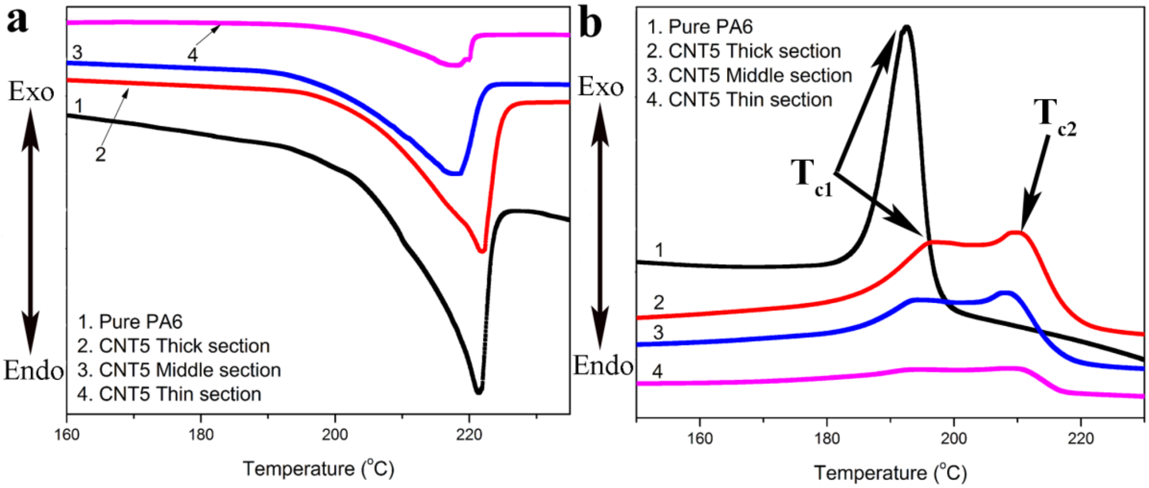

Figure 5.28 DSC (a) heating and (b) cooling curves obtained from pure PA6 and sections of CNT5 microparts.

The effect of CNT concentration on the thermal behavior of middle section of microparts as compared with pure PA6 is shown in Figure 5.29. Except for the middle section of pure PA6 microparts, Figure 5.29(a) and Table 5.5 reveal that there was an approximately 4°C reduction of T_m for the middle section of all microparts, regardless of CNT concentrations. This behavior may be explained by the consideration that the decrease of T_m is associated with the formation of imperfect crystals. Moreover, there was a reduction of χ_c with an incremental loading fraction of CNT, indicating a steric hindrance effect. In addition, aside from CNT10 micropart, the χ_c for the microparts is invariably higher than that observed in corresponding extrudates, which further supports the shear-induced crystallization effect in µIM. Thus, it could be concluded that the crystallization process is strongly influenced by the presence of CNT, while the employed molding conditions or thermomechanical history determines the microstructure of products.

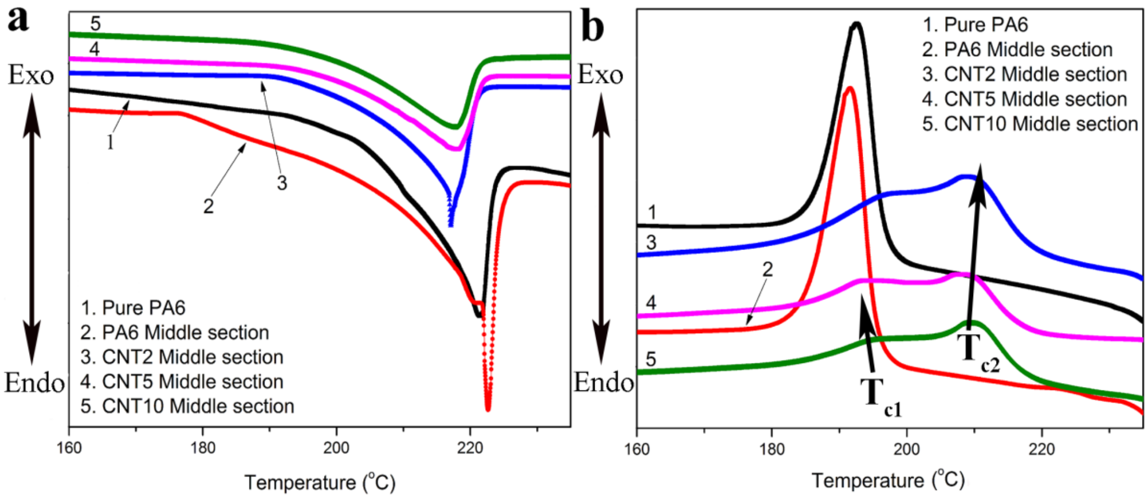

Figure 5.29 DSC (a) heating and (b) cooling curves obtained from pure PA6 and middle section of PA6/CNT microparts with various filler concentrations.

5.2.3.2 Melting and crystallization behavior of PP/CNT composites and subsequent moldings

As per *Section 4.5.4*, the melting and crystallization behavior of pure PP, diluted PP/CNT composites and each section of corresponding microparts was evaluated by a differential scanning calorimeter (Q200, TA Instruments). Figure 5.30 exhibits the thermal behavior of PP, PP/CNT blends and each section of subsequent microparts. For clarity, all displayed DSC curves were shifted vertically. Table 5.6 displays the characteristic data obtained from DSC heating and cooling curves. From Figures 5.30(a1) to (d1), there is a slight deviation of T_m for the PP/CNT blends when compared with that of pure PP, as displayed in Table 5.6. For example, a shoulder peak is detected for the PP/CNT composites in the vicinity of 160°C, which could be ascribed to the existence of small or imperfect α-crystals [293], as displayed in Figure 5.30(a1). Therefore, the addition of CNT might have an influence on the melting behavior of PP. Moreover, the T_c increased significantly upon the incorporation of CNT, as given in Figures 5.30(a2)-(d2). This is undoubtedly attributed to the heterogeneous nucleation effect of CNT [266,294,295]. As given in Table 5.6, there is a noticeable increase (nearly 12°C) of T_c for the PP/CNT 1 wt% (i.e. PP-1) blend and each section of subsequent microparts. In addition, the T_c increased with an incremental loading fraction of CNT in PP, revealing that the crystallization process of PP was associated with the number of crystallization sites that provided by CNT, which is consistent with the results reported by Kazemi et al. [175]. It is also illustrated in Table 5.6 that the addition of CNT greatly affects the χ_c of PP, irrespective of the heating cycles (i.e. Cycle 1 and Cycle 3). For example, increased χ_c is observed for PP/CNT composites with the addition of 1 wt% CNT, which suggests that CNT could offer crystallization sites for PP, thereby leading to an increase of χ_c. However, further increasing CNT concentrations leads to a slight reduction of χ_c for subsequent blends. In this scenario, the presence of a large number of CNTs may hinder the formation of stable crystalline domains, resulting from the limited space and confinement effect that imposed on polymer chains by the incorporated fillers [34]. In addition, the χ_c for each section of subsequent microparts obtained from Cycle 3 is always higher than that of respective section in Cycle 1. This suggests that the thermomechanical history undergone in the compounding and μIM processes might affect the development of microstructure in subsequent moldings or the relaxation of the oriented structure during Cycle 1 may affect the crystallization of PP in Cycle 2.

In general, the T_m (from Cycle 1) for each section of the PP microparts is slightly higher than their PP/CNT counterparts, which could be attributed to the flow-induced orientation of polymer chains. However, this effect vanishes in Cycle 3, confirming that the typical thermomechanical history experienced by polymer melts determines the microstructure of subsequent moldings. From Figures 5.30(a3) to (d3), it could be observed that the T_m for PP/CNT composites are slightly higher than that of pure PP, as displayed in Table 5.6. The results indicated that the incorporation of CNT may retard free motion of polymer chains during the melting process [296], thereby leading to an upshift of T_m to a higher temperature region. Additionally, the incorporated CNT plays a role of nucleation agent that accelerates the crystallization process of PP chains, which might, to some extent, facilitate the formation of stable PP crystals. Furthermore, the effect of thermomechanical history is also reflected in the melting behavior of PP/CNT microparts as there is a marked difference between the 1st (Cycle 1) and 2nd (Cycle 3) heating processes, as displayed in Figures 5.30.

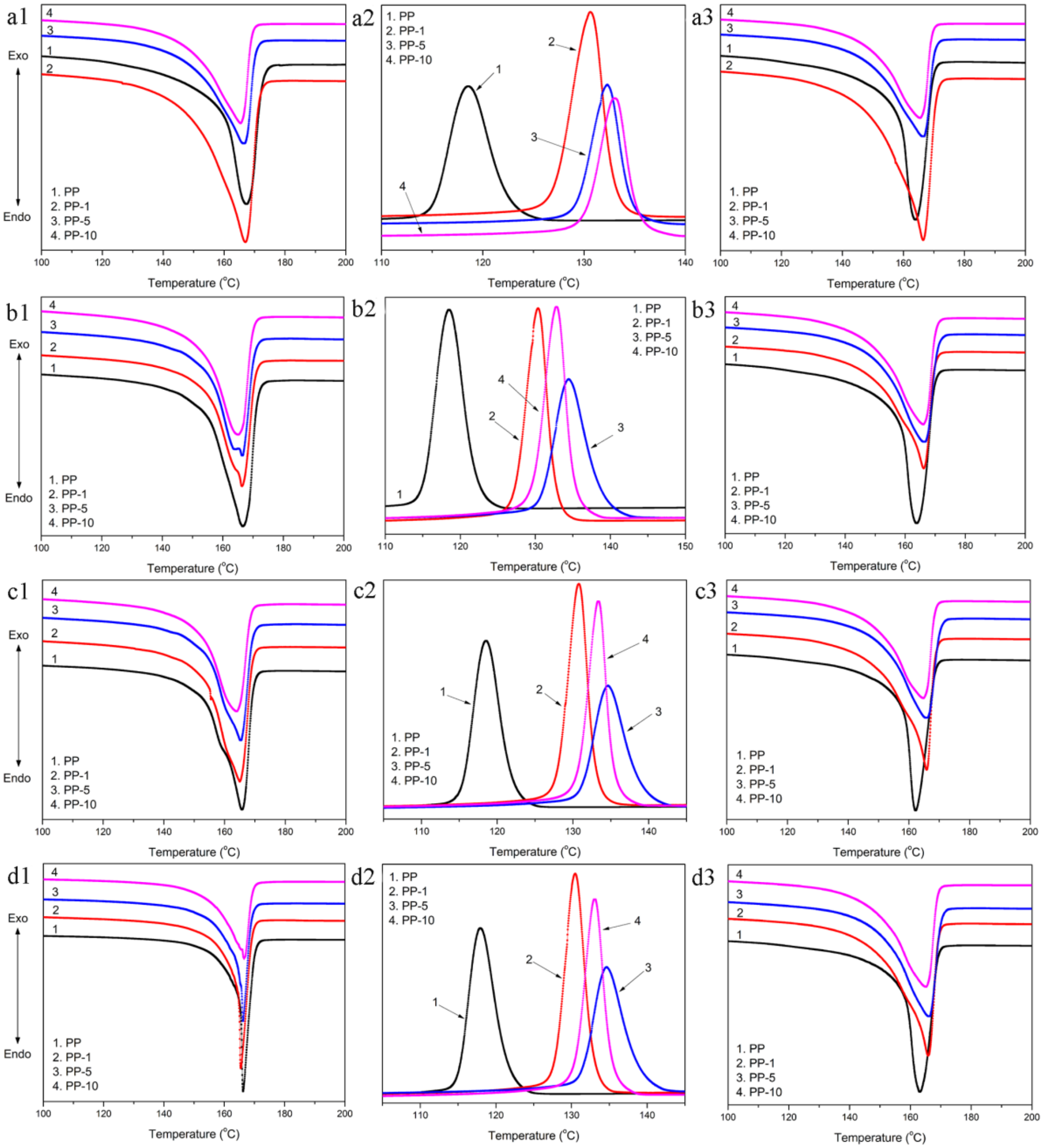

Figure 5.30 DSC curves of pure PP and PP/CNT composites with various filler concentrations. (a1-a3) PP and PP/CNT blends; (b1-b3) thick section; (c1-c3) middle section; (d1-d3) thin section of corresponding microparts. Herein, from left to right: 1-1st heating cycle; 2-cooling cycle and 3-2nd heating cycle of the DSC measurements.

Table 5.6 Characteristic data obtained from DSC curves. Cycle 1-1st heating process, Cycle 2-cooling process, and Cycle 3-2nd heating process.

Designation	T_m (ºC)		T_c (ºC)	χ_c	
	Cycle 1	Cycle 3	Cycle 2	Cycle 1	Cycle 3
PP	167.39	163.97	118.55	0.498	0.488
PP Thick section	166.56	163.83	118.49	0.459	0.483
PP Middle section	165.75	162.21	118.54	0.458	0.488
PP Thin section	166.25	163.13	117.96	0.426	0.468
PP-1	166.90	166.47	130.62	0.528	0.538
PP-1 Thick section	166.36	166.19	130.39	0.458	0.524
PP-1 Middle section	165.02	165.83	130.78	0.456	0.525
PP-1 Thin section	165.47	165.87	130.49	0.457	0.515
PP-5	166.52	166.46	132.31	0.504	0.521
PP-5 Thick section	166.42	166.29	134.46	0.359	0.419
PP-5 Middle section	165.32	165.71	134.65	0.352	0.421
PP-5 Thin section	166.19	166.04	134.63	0.368	0.422
PP-10	165.38	165.43	133.00	0.492	0.513
PP-10 Thick section	164.95	166.00	132.82	0.444	0.503
PP-10 Middle section	163.85	164.68	133.37	0.427	0.505
PP-10 Thin section	166.54	165.15	133.05	0.413	0.487

Results of *Section 5.2.3.2* were taken from the journal International Polymer Processing, 33(4), 514-524 (2018), by S. Zhou, A.N. Hrymak, Musa R. Kamal, © Carl Hanser Verlag GmbH & Co.KG, Muenchen. As per the permission obtained from the publisher.

5.2.4 Thermogravimetric analysis (TGA)

5.2.4.1 Thermal stability of PC/CNT composites and subsequent moldings

Figure 5.31 shows the weight loss and the first order derivative of weight loss thermograms as a function of temperature for pure PC, PC/CNT composites after melt mixing, and thick section of corresponding microparts. Representative thermal analysis data taken from these graphs for each sample are listed. The T_d is the temperature at 5% weight loss, while the T_{max} is taken from the peak value of each first-order derivative of weight loss thermograms. Results indicate that all samples decompose in a single step. The pure PC and PC thick section are quite stable until 450^{o}C with no more than 1.5% weight loss, leaving 24.8% and 23.9% in residue at 800^{o}C, respectively. In addition, Figure 5.31 shows that the T_d and T_{max} decrease when the concentration of CNT increases in PC. For example, significant reduction of both the T_d and T_{max} is observed for samples with only 1 wt% CNT when compared with those of pure PC. The char yield of PC at 800^{o}C (i.e. R_{800}) is simultaneously decreased with an increase of CNT concentration, as the CNT acted as inert fillers. This suggests that the thermal stability of PC/CNT composites and thick section of subsequent microparts deteriorates with the addition of CNT. Similar findings were reported by Schartel et al. [182] where they used the same CNT in a PC. On the one hand, the influence of melt processing such as possible reduction of molecular weight of PC [182,297,298] could be an influencing factor. Moreover, the residual catalyst used in nanotubes synthesis could be another factor [182]. However, Wang et al. [183] found that the addition of surface modified CNT could enhance the thermal stability of resultant PC/CNT composites, which was attributed to the improved dispersion of the surface functionalized CNT in PC and the barrier effect of interconnected CNT, thereby promoting the formation of a stable char layer during the pyrolysis process and improving thermal stability. Wu et al. [184] reported a slight improvement of the thermal stability of PC/CNT composites with an increase of CNT content prepared by melt mixing. They firstly treated the CNT with strong acid to graft carboxylic functional groups onto nanotubes, followed by further modification with cetyltrimethylammonium bromide (CTAB) under ultrasonication for 3h in tetrahydrofuran solution. Afterwards, the CTAB-modified CNT-containing PC masterbatch was prepared by solution mixing. The achieved masterbatch was then diluted with a pure PC by melt blending in a Haake mixer. Thus, it appears that the surface functionalization of CNT or the intrinsic properties of CNT could significantly affect the thermal stability of PC. Aside from the influence of fillers, the processing conditions [177], testing conditions (with or without the presence of oxygen, heating rate of TGA, etc.) [178,179], molecular weight of PC [180] as well as the additives incorporated in host polymers such as thermal stabilizers [181] or compatibilizers will also play a significant role in determining the thermal stability of resultant composites.

Furthermore, a parallel comparison was drawn with respect to the above thermal analysis data (i.e. T_d, T_{max} and R_{800}) obtained from the PC/CNT composites and the thick section of corresponding microparts. A slight reduction of corresponding values was detected for the thick section of microparts when compared with pure PC or PC/CNT blends, suggesting that the typical thermomechanical history (extreme shear rates and high thermal gradients) present in µIM may have an influence on the chain structure of PC. For example, chain scission effect of PC has been reported after experiencing multiple melt processing processes [299] or higher shearing and elongational flow conditions [300].

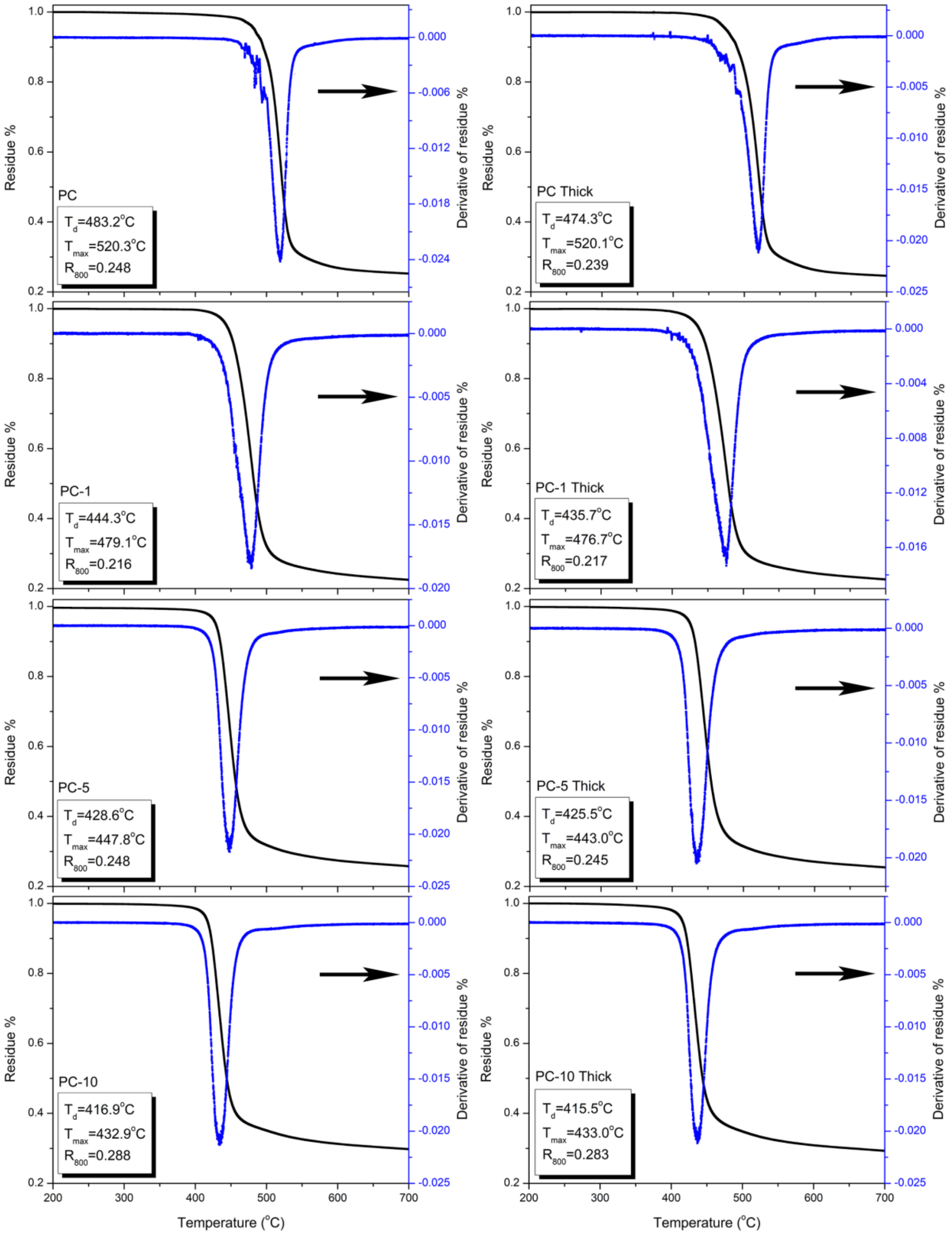

Figure 5.31 TGA graphs and derivative of weight loss thermograms of pure PC, PC/CNT blends and thick section of corresponding microparts.

5.2.4.2 Thermal stability of PP/CNT composites and subsequent moldings

The thermal decomposition behavior for PP/CNT composites and the thick section of corresponding microparts as a function of temperature is depicted in Figure 5.32. The representative thermal analysis data of all samples (including the middle and thin sections of respective microparts) are listed in Table 5.7.

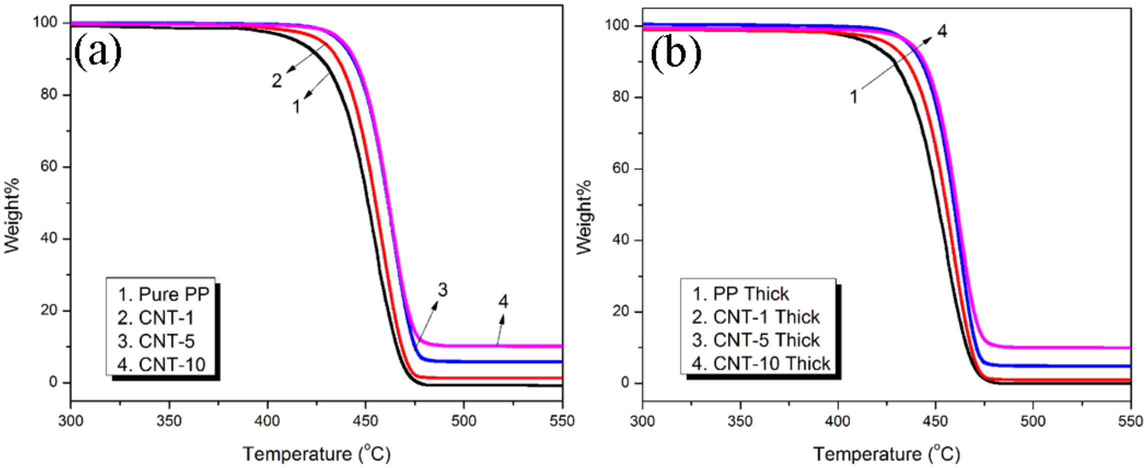

Figure 5.32 TGA graphs of (a) PP/CNT composites; (b) the thick section of corresponding microparts.

Figure 5.32 exhibits that there is only one decomposition stage during the heating process and both the T_d and T_{max} increase with the loading fraction of CNT (see Table 5.7). These results indicate that the thermal stability of diluted samples and corresponding microparts improves with the presence of CNT, which is consistent with previous studies [301,302]. The improved thermal stability of CNT-containing polymer composites is attributed to the intrinsically higher thermal stability of CNT when compared with PP and the barrier effect induced by the added fillers which could hinder the volatilization of PP segments during the monotonically heating process [303]. In addition, it has been reported that the activation energy of decomposition for PP/CNT composites is significantly enhanced with the presence of CNT [302]. For example, there is about 12°C increase for PP/CNT 1 wt% composite (CNT-1) when compared with pure PP with respect to T_d, whereas shifts of over 22°C to higher temperature regions are observed for CNT-5 and CNT-10, respectively. As discussed in *Section 5.4.1.1*, the loading of 1 wt% CNT is insufficient for the construction of 3D conductive pathways within PP whereas 5 wt% loading of CNT is well above the p_c. Therefore, both the addition of CNT and the formation of 3D interconnected pathways contribute to the enhancement of thermal stability of PP/CNT composites.

Table 5.7 The TGA decomposition temperature (T_d), the maximum decomposition temperature (T_{max}) and char residue at 650ºC (R_{650}) for pure PP, PP/CNT blends and each section of corresponding microparts.

Sample ID	T_d (ºC)	T_{max} (ºC)	R_{650} (%)
Pure PP	415.1	457.0	~0
CNT-1	427.4	460.0	1.28
CNT-5	437.1	464.7	5.70
CNT-10	437.6	465.8	10.3
PP Thick section	416.7	456.6	~0
CNT-1 Thick section	425.9	460.1	0.896
CNT-5 Thick section	436.4	463.9	4.63
CNT-10 Thick section	437.0	463.9	10.1
PP Middle section	396.1	453.6	~0
CNT-1 Middle section	429.6	457.5	1.52
CNT-5 Middle section	433.8	461.2	4.36
CNT-10 Middle section	437.3	460.3	9.66
PP Thin section	387.3	456.3	~0
CNT-1 Thin section	427.5	459.2	0.836
CNT-5 Thin section	434.9	461.9	4.64
CNT-10 Thin section	437.1	462.3	9.72

By comparing the values of T_d, T_{max} and R_{650} of diluted PP/CNT composites with the thick section of corresponding microparts, there is no significant difference between each characteristic value. However, a general trend is that a slight decrease of T_d or T_{max} is recorded for the thick section of microparts when compared with their PP/CNT counterparts. This might be explained by traces of smaller molecular fragments of PP chains that induced by the two-stage melt processing methods, i.e. melt dilution and subsequent µIM. Similarly, the middle and thin sections taken from the microparts showed one step decomposition process (not shown). However, there was a significant decrease of T_d for the middle and thin sections of PP microparts when compared with that of PP and their thick section counterpart, whereas the difference for T_{max} among these samples does not vary substantially, hinting that more and shorter fragments of PP chains might be yielded with increasing shearing intensity along the melt flow direction. In addition, the T_d and T_{max} for the middle and thin sections of PP/CNT microparts exhibited the same trend as that observed for PP/CNT blends and the thick section of corresponding microparts with an incremental loading fraction of CNT, which is attributed to the influence of CNT, as elaborated previously.

Results of *Section 5.2.4.2* were taken from the journal International Polymer Processing, 33(4), 514-524 (2018), by S. Zhou, A.N. Hrymak, Musa R. Kamal, © Carl Hanser Verlag GmbH & Co.KG, Muenchen. As per the permission obtained from the publisher.

5.2.5 Raman analysis

5.2.5.1 Raman analysis for PS/CNT microparts

The Raman spectroscopy technique is an effective method to investigate the orientation of CNT within the polymeric composites and the position of Raman peak is typical of certain chemical groups [12]. The Raman spectra for different sections of the injection molded PS/CNT microparts are illustrated in Figure 5.33. According to references [304,305], the characteristic peaks observed in the vicinity of 1000 cm^{-1} can be attributed to the vibration of phenyl groups or macromolecular chains of PS.

As shown in Figure 5.33, the distinct peaks observed in the vicinity of 1330 cm^{-1} and 1600 cm^{-1} are attributed to the D band (disordered band) and G band (graphite band or tangential band) of CNT, respectively. Abbasi et al. [12] proposed that the differences between the intensities of characteristic CNT peaks are helpful to study the CNT orientation within the polymer matrices. Therefore, the intensity ratios of the D_{FD}/D_{TD} and G_{FD}/G_{TD} (i.e. parallel/perpendicular to the flow direction) were analyzed to evaluate the degree of CNT orientation within the polymer matrix. All measurements were conducted under the same conditions, as Raman shifts of the CNT bands can be affected by external factors such as temperature, pressure, and excitation wavelength [306] as well as the intensity of laser power. The ratios of D_{FD}/D_{TD} and G_{FD}/G_{TD} as per sections are summarized in Table 5.8. It is noticeable that the resultant values of D_{FD}/D_{TD} and G_{FD}/G_{TD} for the microparts have a deviation from the unity which is indicative of the orientation of CNT along flow direction [12,307]. The corresponding values for the middle section of the microparts are higher than those of the thick section, suggesting that a higher degree of CNT orientation is present in the middle section with the step decrease of the thickness of the injection molded part. This is ascribed to the higher shearing effect that is rendered in middle section.

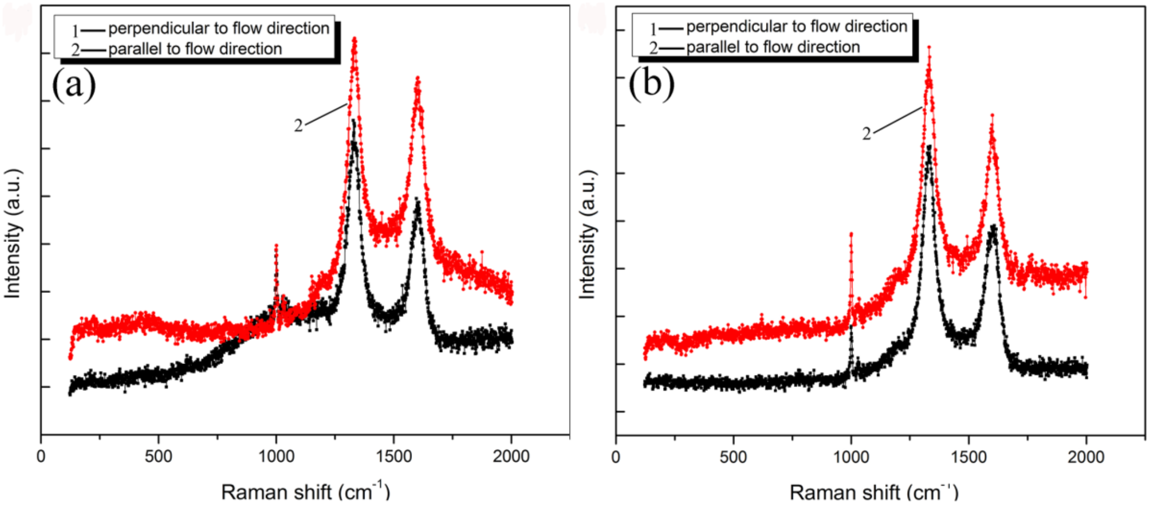

Figure 5.33 Raman spectra of (a) thick and (b) middle sections of microinjection molded PS/CNT 5 wt% composites with respect to flow direction.

Typically, the D/G ratio is used as a useful analytical tool for reflecting the degree of perfection of CNT or the crystallinity in the nanotubes structure [12]. Endo and co-workers [308] proposed that a constant value of D/G in both parallel and perpendicular geometry is a sign that no structural change is present in CNT. Therefore, the value of $(D/G)_{FD}/(D/G)_{TD}$

was applied to check the changes of perfection or crystalline structure of CNT [12]. It can thus be deduced from Table 5.8 that the ratios of both the thick and middle sections of the microparts showed mild deviation from unity, indicating that the structure of CNT was slightly changed and a shortening effect of CNT [309] might have occurred due to the high shearing conditions in µIM process.

Table 5.8 Raman intensity ratios of parallel/perpendicular to the flow direction of PS/CNT 5 wt% microparts with respect to investigated sections.

Designation	D_{FD}/D_{TD}	G_{FD}/G_{TD}	$(D/G)_{FD}/(D/G)_{TD}$
Thick section	1.27	1.51	0.842
Middle section	1.37	1.63	0.844

5.2.5.2 Raman analysis for PC/CNT microparts

Raman analysis is a non-destructive spectroscopy technique, which depends on inelastic scattering of incident visible or infrared light by molecules, and the position of Raman peaks is characteristic of certain chemical groups or structures [310]. For example, Dybal et al. [311] and Litchfield and Baird [312] studied the conformational change or orientation of polymer chains in PC and poly(ethylene terephthalate) (PET), respectively, with the help of Raman spectroscopy. In addition, this technique has been proposed to determine the diameter of nanotubes (for example, SWCNT), the structural properties and the orientation of nanotubes in polymer composites [12,310,313]

The representative Raman spectra of the thick section of pure PC and PC/CNT 5 wt% (PC-5) microparts are depicted in Figure 5.34. Figure 5.34(a) reveals that pure PC shows multiple peaks and the assignment of the position of Raman peaks is elaborated in literature [314]. In addition, Figure 5.34(b) indicates that CNT shows resonance-enhanced Raman scattering effects [310] and the multiple Raman peaks of unfilled PC almost vanish upon the incorporation of CNT. Given the large differences in peak intensities between CNT and those arising from pure PC, the Raman spectroscopy seems to be an ideal characterization technique for the orientation of nanotubes. According to Brown et al. [315], the prominent peak of CNT designating as the D-band, which is observed between 1250 and 1450 cm^{-1}

is attributed to the presence of disorders or defects in the carbon structures, as revealed in Figure 5.34(b). The authors also reported that there is a dependence of D-band frequency (i.e. Raman shift) of SWCNT on the energy of applied excitation laser light (*E*). To put it simply, the higher the *E*, the higher the peak frequency of D-band. The peak (tangential band or G-band), which centers in the vicinity of 1600 cm^{-1}, is ascribed to the existence of graphitic or crystalline structure in the carbon materials [12,313]. The G' band (2700 cm^{-1}) is the second-order overtone of the D-band which is attributed to strong coupling between the phonons and electrons [316]. Furthermore, the peaks observed beyond 2800 cm^{-1} in Figure 5.34(b) might be attributed to the influence of polymer matrix, PC, since some characteristic peaks are reflected in the spectroscopy of pure PC, as displayed in Figure 5.34(a). Therefore, Raman spectroscopy has been utilized to study the properties of various carbon structures [179] and carbon filler loaded polymer composites [310] as well as the orientation or perfection of CNT in bundles or polymer composites [313,314,317].

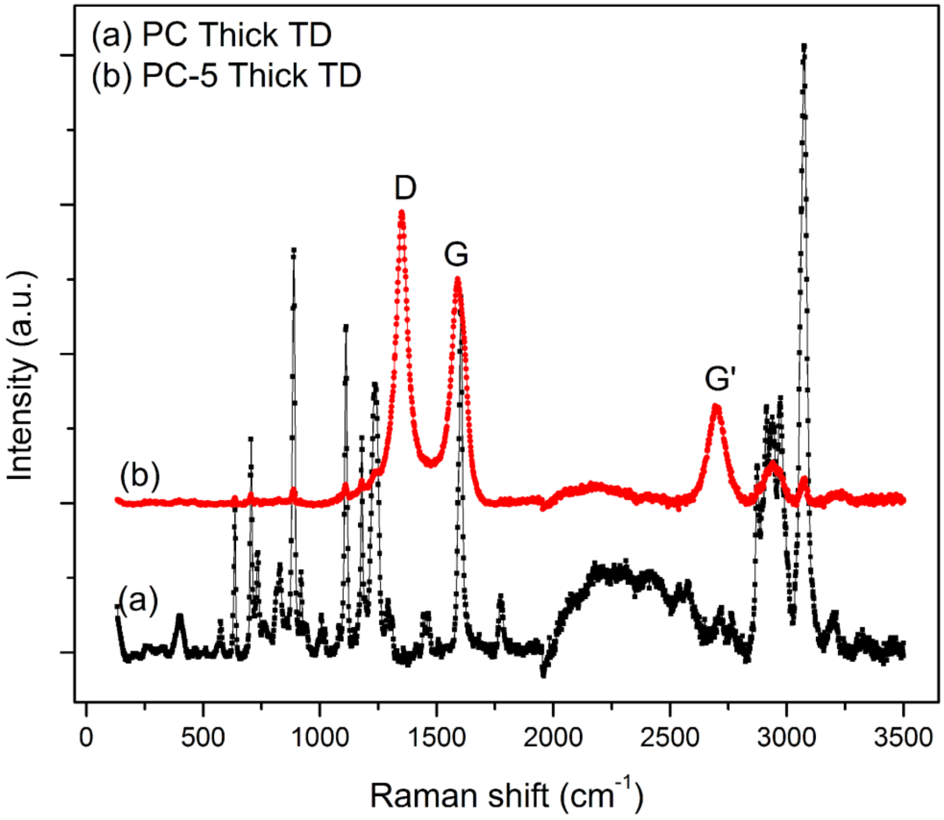

Figure 5.34 Raman spectra of the thick section of (a) pure PC and (b) PC-5 microparts, respectively. TD-perpendicular to predominant flow direction.

The Raman spectra of thick and middle sections regarding the measurement directions of PC-5 microparts are depicted in Figure 5.35(A). It is obvious that all samples followed a similar pattern in the obtained spectrum, signifying that CNT exhibited dominating Raman scattering effects. Interestingly, the response of the peak which is observed near 3100 cm^{-1} is stronger along the FD when compared with that observed across the TD, independent of targeted sections. According to Goyal et al. [314], the peak detected at 3075 cm^{-1} (P_{3075}) of the PC is attributed to the vibrations of C-H stretching. Therefore, these differences in peak intensity of P_{3075} in PC-5 microparts with respect to sampling directions might suggest a flow-induced alignment of polymer chains in µIM. However, such differences seem to be diminished with an increase of CNT loading concentrations, as given in Figure 5.35(B). This is undoubtedly attributed to the strong resonance-enhanced scattering effect of CNT. Furthermore, the nanotubes might interfere with or disrupt the orientation of PC chains along the flow direction. Thus, the response of PC from Raman spectra diminishes with the increasing loading fraction of nanotubes.

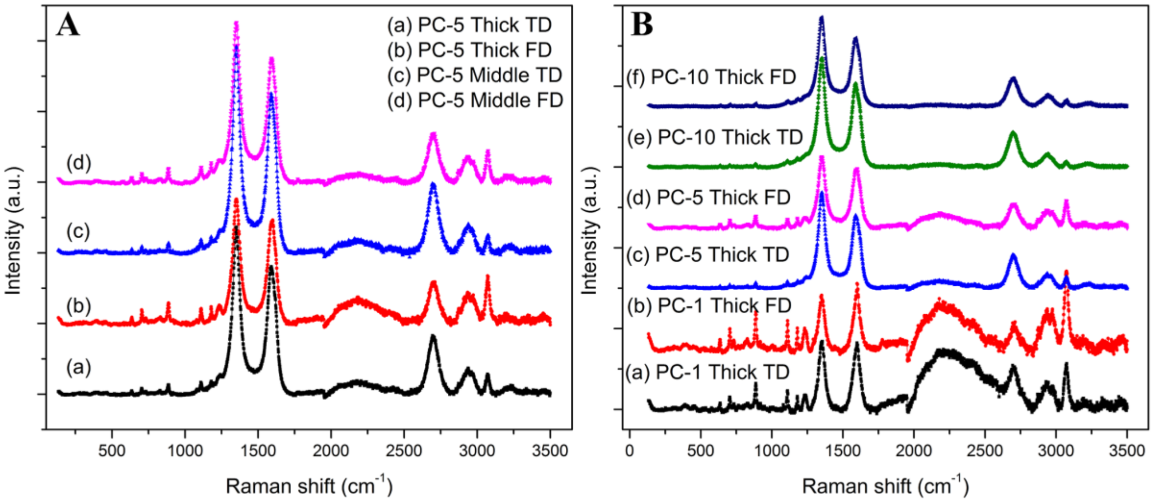

Figure 5.35 Raman spectra of (A) the thick and middle sections of PC-5 micropart; (B) the thick section of PC/CNT microparts with various filler concentrations as per measurement directions. FD-parallel to the predominant flow direction.

The integrated intensity ratio of the D-band and G-band, I_D/I_G, has been used as a measure to study the degree of CNT orientation [317] or the perfection of CNT [318]. For example, a smaller value of I_D/I_G ratio is indicative of a higher degree of CNT alignment [317] or more perfection in CNT structures [318]. Therefore, the values of I_D/I_G as per measuring directions, i.e. TD and FD, of each sample are given in Table 5.9. In addition, a constant value of I_D/I_G in both parallel and perpendicular geometry is proposed as a sign that no or insignificant structural change is present in CNT [12]. Therefore, the parameter of $(I_D/I_G)_{TD}/(I_D/I_G)_{FD}$ was applied to determine the possible structural changes or perfection of CNT [12]. Moreover, it has been reported that the value of I_D/I_G is proportional to the crystallite size, L_a, of nanographite [319]. A general formula (see below) which is proposed for the determination of L_a for nanographitic materials could, therefore, be used to calculate the L_a in nanotubes [316] and corresponding values are also listed in Table 5.9.

$$L_a = \frac{560}{E^4}\left(\frac{I_D}{I_G}\right)^{-1}$$

where the laser excitation energy E of the incident light (514 nm) is 2.41 eV [316].

The results reported in Table 5.9 are an average of three measurements, although there is no obvious statistical difference with respect to measurement directions of each section or between each section of microparts. Table 5.9 shows that the calculated value of I_D/I_G ratio for each sample measured along the FD is invariably lower than that obtained in the TD, suggesting a preferential alignment of CNT along the flow direction arising from very high shearing and extensional effects in µIM. In addition, it increases simultaneously with an incremental loading fraction of CNT, indicating that the degree of CNT orientation becomes less severe, despite the measurement directions. The tentative explanations for this phenomenon could be: on the one hand, the state of CNT distribution is not favored at higher CNT concentrations due to the steric hindrance effect that is exerted by adjacent CNTs; on the other hand, the presence of CNT aggregates could not be precluded even if the dispersion of CNT is improved after µIM. Although very high shearing and extensional force fields prevail in µIM, the probability of forming a more perfect or higher degree of CNT orientation along the flow direction could, to a certain extent, be impaired. Moreover, the intensity ratio of I_D/I_G across the TD for the middle section of PC-5 microparts is slightly higher than that of thick section counterpart, indicating more defects could be detected in the middle section. This might be attributed to a slightly structural change of CNT in the middle section arising from more severe shearing conditions. For example, a length reduction of CNT has been observed in samples prepared by µIM (see following section). Furthermore, the value of $(I_D/I_G)_{TD}/(I_D/I_G)_{FD}$ for each sample showed a mild deviation from unity, indicating that the structural change of CNT was insignificant [12] and a possible shortening effect of CNT might have occurred due to the very high shearing conditions in µIM process. Moreover, there is also a general downward trend of the Raman shifts for both the D-band and G-band of PC/CNT microparts with an increase of filler concentration, as shown in Table 5.9, which might be ascribed to increased interactions between adjacent CNTs.

Table 5.9 The peak positions of the D-band and G-band, the intensity ratios between the D-band and G-band (I_D/I_G), and the crystallite size (L_a) in CNT of the PC/CNT microparts with respect to CNT concentrations and measurement directions, respectively.

Samples		Peak position (cm^{-1})		I_D/I_G	$(I_D/I_G)_{TD}/(I_D/I_G)_{FD}$	L_a (nm)
		D-band	G-band			
PC-1 thick section	TD	1353	1597	1.022	1.116	16.24
	FD	1352	1598	0.916		18.12
PC-5 thick section	TD	1351	1595	1.102	1.012	15.06
	FD	1352	1596	1.089		15.24
PC-5 middle section	TD	1351	1595	1.142	1.049	14.54
	FD	1351	1596	1.089		15.24
PC-10 thick section	TD	1351	1594	1.124	1.010	14.77
	FD	1351	1595	1.113		14.92

5.2.6 Dissolving experiments and TEM

To qualitatively observe the dispersion of CNT in PA6/CNT 20 wt% masterbatch, diluted composites and corresponding microparts, the dissolving experiments were carried out with respect to each sample. The observation of dissolved samples in formic acid for PA6/CNT samples is presented in Figure 5.36.

Figure 5.36 shows that solutions of CNT5 extrudates and sections taken from subsequent microparts appear as homogeneous black solutions, indicating relatively homogeneous distribution of individual nanotubes or very small CNT aggregates [251]. However, a black sediment coupling with nearly transparent solution is visible for PA6/CNT masterbatch (sample 1), corresponding to the existence of remnants of CNT agglomerates. Therefore, the dispersion of CNT is improved after melt dilution and subsequent µIM processes.

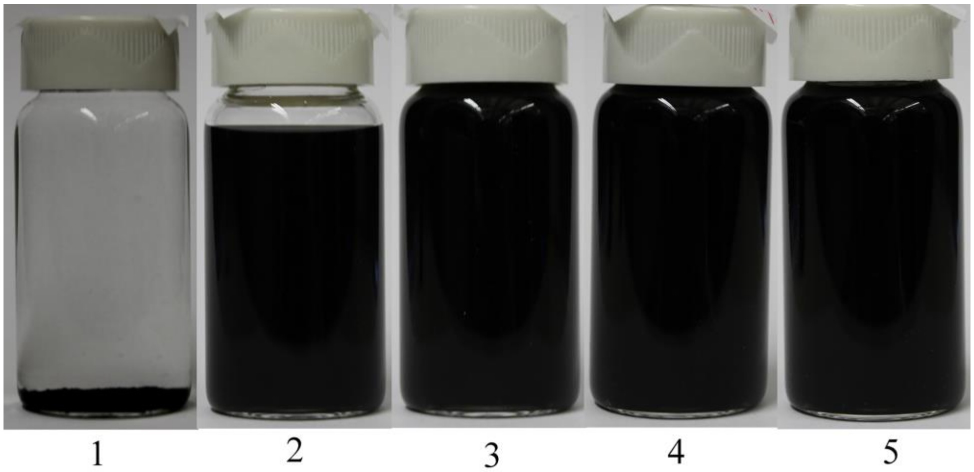

Figure 5.36 Digital photos of PA6/CNT/formic acid solutions after 2 months: 1. PA6/CNT 20 wt% masterbatch; 2. CNT5 extrudate; from 3 to 5 are the thick, middle and thin sections of CNT5 microparts, respectively.

Characterization of the nanostructure of CNT in respective samples was carried out by TEM. The CNTs have a hollow structure, which can be clearly observed in Figures 5.37(c), (d) and (f). The measured diameter of CNT ranges from 5 to 10 nm, which is consistent with the technical data provided by manufacturer. However, Figure 5.37(f) indicated that the length of CNT is significantly reduced when compared with their original length (over 10 µm) [289], suggesting that the melt blending and subsequent molding processes have a significant effect on the length reduction of CNT. Although the CNT5 extrudate has a homogeneous dispersion in formic acid (Figure 5.36, sample 2), Figures 5.37(a) and (b) suggest the presence of small size CNT bundles, implying that the CNT agglomerates that existed in the original masterbatch could be significantly reduced after subjecting to melt dilution process. Figures 5.37(c) and (d) reveal that there is a thin layer of PA6 matrix surrounding individual CNT, which suggests a good interfacial interaction between CNT and the host polymer. Thus, the adhesion of a thin layer of PA6 to the CNT explained well dispersion of corresponding materials in the formic acid solution.

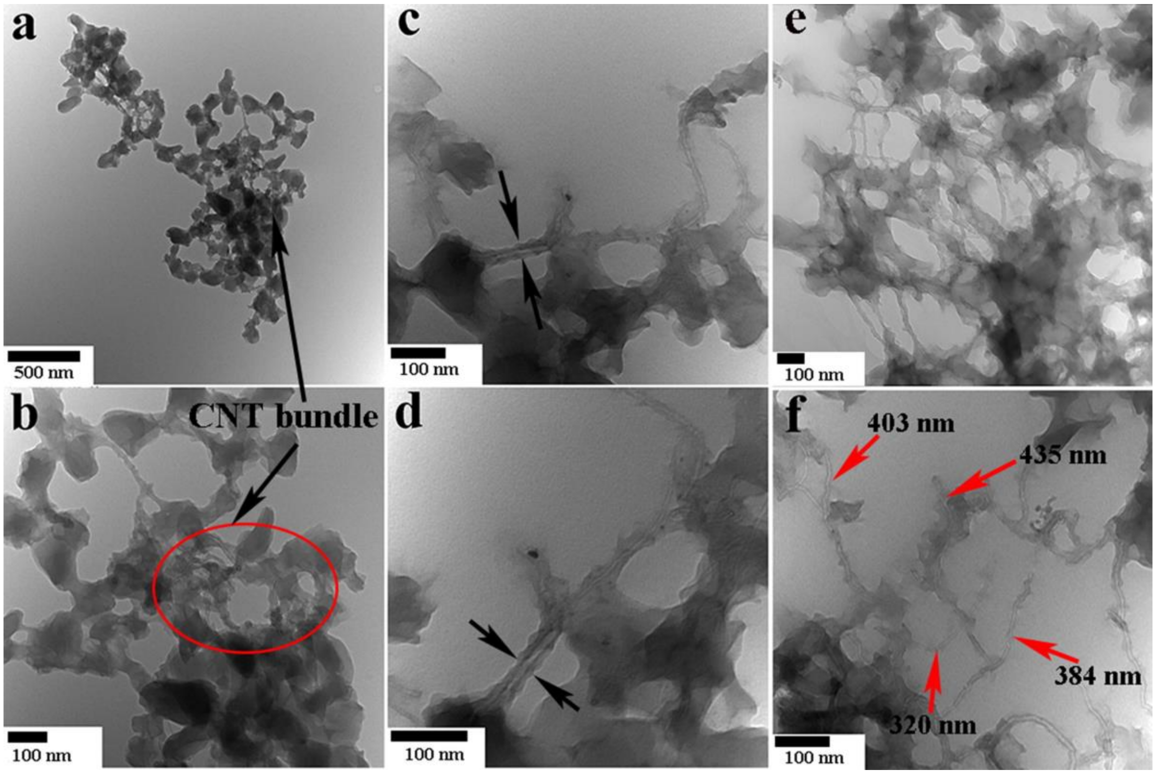

Figure 5.37 TEM images of (a, b) extruded CNT5, (c, d) CNT5 thick section and (e, f) CNT5 middle section.

5.2.7 Summary

In summary, a series of polymer/CNT composites were prepared via masterbatch dilution. Nanocomposite preparation was followed by compression molding or µIM processes. The three-stepped microparts were sectioned at transition regions to facilitate characterization and the volume electrical conductivity measurement was conducted with respect to the melt flow direction, which are along the flow direction (FD) and perpendicular to the flow direction (TD), respectively. The comparison of electrical conductivity values suggested a preferential alignment of CNT along the flow direction, which could be further confirmed by Raman analysis. The selection of host polymer matrices had an influence on the development of microstructure in subsequent microparts, which was corroborated by SEM observations. For example, microparts molded from PP/CNT 10 wt% composites exhibited the highest electrical conductivity when compared with that of PC/CNT, PS/CNT and PA6/CNT counterparts. The presence of CNT agglomerates in PP is thought to be crucial to the enhancement of electrical conductivity, regardless of measurement directions. The melting and crystallization behavior of PA6/CNT and PP/CNT composites and each section of subsequent microparts was characterized by DSC. Results from PA6/CNT samples indicated that the addition of CNT had little influence on the melting behavior of PA6/CNT composites and subsequent microparts. However, the crystallization behavior of nanotubes-containing samples was significantly altered with the appearance of a double crystallization peak. Based on the DSC data from PP/CNT samples, the incorporation of CNT and typical thermomechanical history experienced by the polymer melts during different molding processes had an influence on the melting and crystallization behavior of resultant samples. The thermal stability of PC/CNT and PP/CNT composites and subsequent microparts were characterized using TGA. The thermal stability of PC/CNT composites and thick section of corresponding microparts deteriorated upon the addition of CNT, which was attributed to the influence of surface or intrinsic properties of CNT. In the case of PP-related moldings, both the incorporation of CNT and the formation of 3D interconnected pathways contributed to the enhancement of thermal stability of PP/CNT composites and subsequent moldings. In addition, the dispersion of CNT improved in PA6 after melt blending and subsequent µIM. The thermomechanical history experienced by polymer melts in µIM might have a chain scission effect on polymer chains and shortening effect on the incorporated CNT due to the prevailing high shearing and extensional force fields.

5.3 The influence of selective localization of CNT by adopting immiscible polymer blend as host matrix

The morphological, thermal and electrical properties of microinjection molded CNT filled PLA and PLA/PBSA immiscible blend were studied systematically. The PLA/PBSA/CNT immiscible blends were prepared by melt blending of PLA, PBSA and CNT in a Brabender batch mixer. Four different types of compounding procedure were employed to study the influence of compounding sequence of various components on the electrical conductivity of subsequent microparts. Results revealed that regardless of the compounding sequence, the electrical conductivity of PLA/PBSA/CNT microparts is always higher than that of CNT filled mono-PLA counterparts and the selective localization of CNT in PBSA is thought to be the contributing factor. Furthermore, the prevailing high shearing conditions in μIM could lead to the coalescence of CNT-enriched PBSA domains, thereby favoring the formation of conductive pathways along the melt flow direction, as confirmed by SEM observations. The χ_c of PLA/PBSA immiscible blends is higher than that of mono-PLA system and a further increase of χ_c after μIM suggested flow-induced crystallization. Moreover, TGA analysis suggested that the prevailing high shear rates in μIM might have a chain scission effect on PLA and PBSA.

5.3.1 Morphology

The very high shearing conditions in μIM can affect the development of microstructure in subsequent moldings. Therefore, the morphology of both the shear and core layers of the thick and middle sections of PLA/CNT microparts is displayed in Figure 5.38. Figure 5.38 indicates that despite the existence of individually dispersed CNT agglomerates in both layers, CNT achieves a relatively uniform distribution in both the shear and core layers of the microparts. In addition, several fibril-like structures which are likely to be designated as the dispersed individual CNT are observed in the shear layer of the thick section, as displayed in Figure 5.38(f). The fibrillar CNT could function as a ‘bridge’ which spans between individual CNTs and discretely dispersed CNT agglomerates, thereby facilitating the enhancement of σ. Thus, the development of such microstructure could be attributed to the influence of strong shearing conditions that prevail in the shear layer of subsequent moldings. For example, Abbasi et al. [12] reported that the effective shear rate in μIM is several orders of magnitude higher than that present in CIM and compression molding. In addition, the existing shearing effect in the shear layer is significantly higher than that in the core layer of corresponding microparts, which may possibly lead to the appearance of fibril-like structure in the shear layer when compared with that of the core layer.

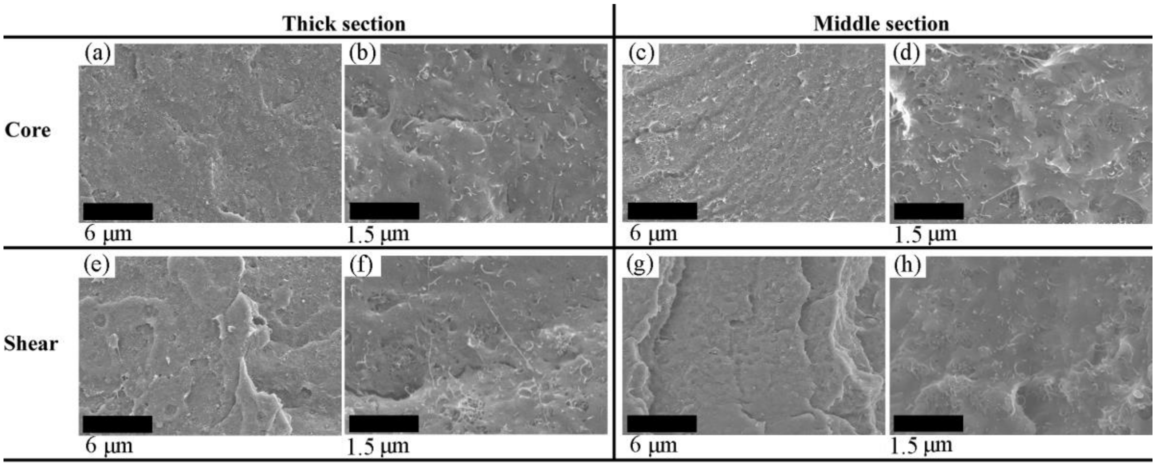

Figure 5.38 SEM images of the thick and middle sections of PLA/CNT 5 wt% microparts taken from the core and shear layers, respectively.

The microstructure for each layer of the thick and middle sections of PLA/PBSA/CNT microparts molded from *Sample 3* is given in Figure 5.39. According to Ojijo et al. [320], and Eslami and Kamal [321], PBSA was primarily distributed in a droplet form in the PLA matrix when blended in a mass ratio of 70/30 (PLA/PBSA). The morphology taken from the thick section reveals that CNT was not uniformly distributed in the host matrix, i.e. PLA/PBSA blend. The CNT was mainly dispersed in the PBSA domains, which leads to the presence of discretely distributed CNT aggregates in the core layer of thick section. Moreover, a typical layer of CNT aggregates could be observed in the shear layer of thick section, as displayed in Figure 5.39(f). This could be ascribed to the influence of higher shearing effect that prevails in the shear layer when compared with that of core region. For example, Jiang et al. [13] reported that shear rates as high as 10^6/s are not rare in μIM. Although Nofar et al. [322] proposed that the selective localization of nano-fillers could effectively prevent the droplet coalescence of dispersed phase under steady shear, very low shear rates (0.01 and 0.05/s) were involved in their study. Moreover, they found that the dispersed droplets could be further stretched and elongated along the shearing direction when the shear rate is increased to 0.05/s. Therefore, the prevailing high shear rates in µIM might overcome the barrier effect between dispersed PBSA droplets and the coalescence of CNT-containing PBSA domains leads to the formation of CNT-enriched layer in the shear layer. As a result, both the existence of CNT aggregates and CNT-enriched layer in the shear layer favor the construction of conductive pathways, resulting in a higher σ of subsequent moldings along the melt flow direction.

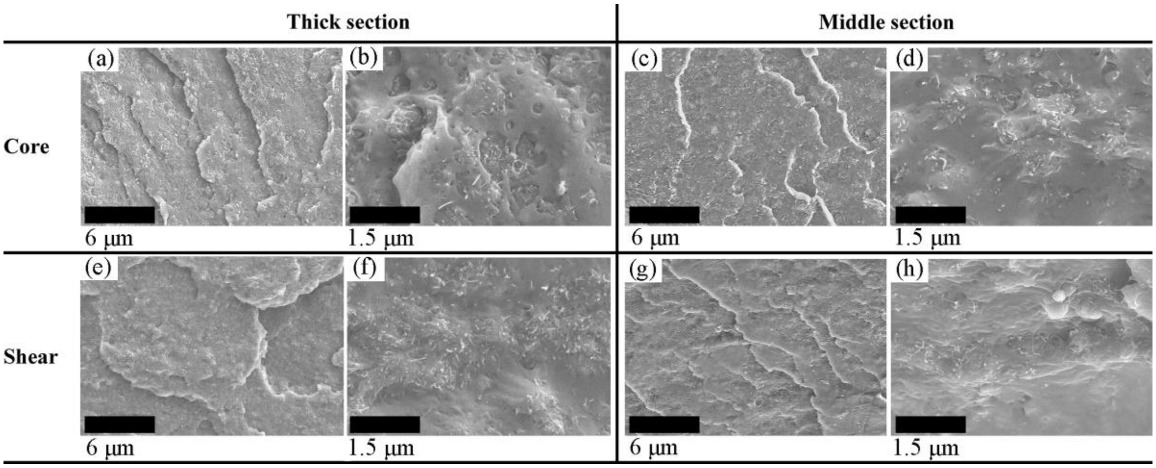

Figure 5.39 SEM images of the thick and middle sections of *Sample 3* microparts taken from the core and shear layers, respectively.

5.3.2 Differential scanning calorimetry (DSC)

As per *Section 4.5.4*, the melting and crystallization behavior of PLA/PBSA blend and CNT loaded polymer composites as well as sections taken from subsequent microparts was analyzed using DSC. The DSC heating traces of each sample are shown in Figures 5.40(a) and (b), respectively. As displayed in Figure 5.40(a), PBSA and PBSA/CNT blends have identical melting behavior, and both exhibit multiple melting endotherms. According to Ray et al. [323], the appearance of multiple melting peaks for PBSA and filler-containing PBSA blends was associated with the melting, re-crystallization and re-melting phenomenon. Simply put, the first step is the melting and re-crystallization of low melting crystallites, which are more susceptible to heat. Afterwards, the re-melting of as-developed crystallites during the DSC heating scans contributes to the melting peaks at higher temperatures.

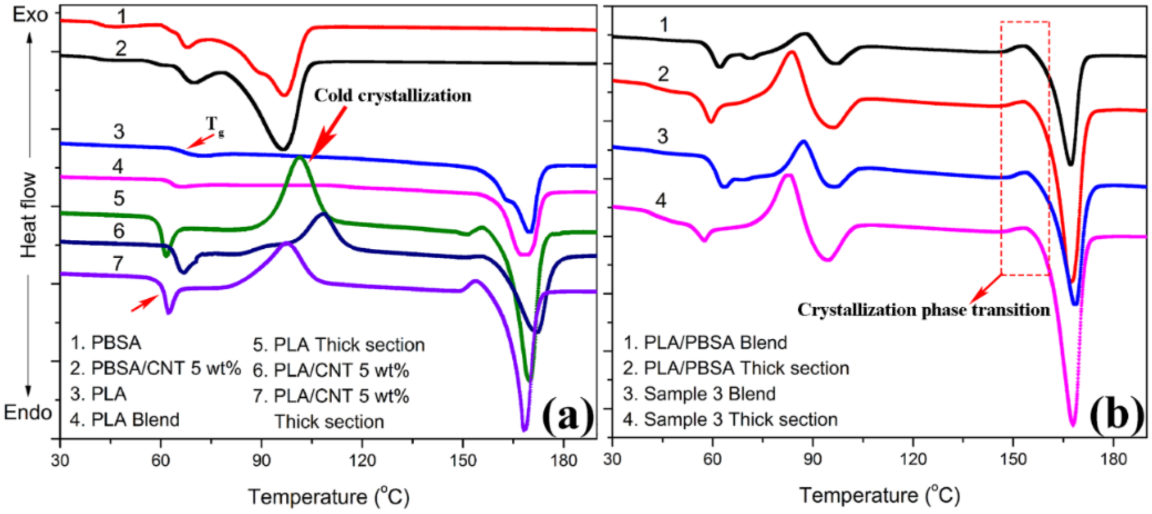

Figure 5.40 DSC curves of the 1st heating process of each sample.

The characteristic thermal analysis data, which were obtained from PLA-related heating curves, are tabulated in Table 5.10. Figure 5.40(a) indicates that a main melting peak which centers in the vicinity of 170°C is typically observed for all samples, is associated with the melting of PLA crystallites. However, a shoulder peak which was located at around 165°C for PLA pellet could be related to the possible presence of imperfect crystals. Interestingly, the shoulder peak disappeared for PLA blend after melt blending of original PLA pellets and a broad melting peak region which spans a range of 167-170°C was detected, suggesting that the melt processing might facilitate the crystallization of PLA chains. Consequently, the χ_c of subsequent melt processed PLA was slightly higher than that of the original PLA pellets. However, an enthalpy relaxation peak (62°C, associated with T_g) [14] and a typical cold crystallization exothermal peak (ca. 100°C) were observed in the melting behavior of the thick section of PLA microparts, indicating that the thermomechanical history experienced by the polymer melts has a significant effect on the microstructure of subsequent moldings. As very high cooling rates are typically involved in µIM, there would not be enough time for polymeric chains to form ordered or perfect crystals during the molding process. The constant heating rate during DSC measurements may promote the mobility and re-organization of polymer chains, thereby leading to the appearance of cold crystallization process. Thus, the cold crystallization peak in turn reflects the capability of polymer chains to mobilize or re-arrange themselves into ordered crystals. Additionally, a small exothermic peak at 155.5^{o}C which translates the crystal phase transition behavior is attributed to the phase transition from less thermally stable ά form crystals to the standard α-form crystals [324]. For PLA/CNT blends, T_g, T_{cc} and T_m shifted to higher temperatures when compared with those of other samples, as revealed by Figure 5.40(a) and Table 5.10. In such a case, it could be conjectured that the presence of large numbers of CNT particles could restrict the free motion of polymer chains. Therefore, more energy is required for polymer chains to overcome the steric hindrance that is imposed by the incorporated CNTs. Furthermore, the thick section of PLA/CNT microparts showed a similar melting behavior as that observed for PLA thick section. However, a shift of corresponding thermal analysis data such as T_g, T_{cc} and T_m to lower temperatures of thick section of PLA/CNT microparts might be indicative of a slight degradation effect on the polymer chains after melt blending and µIM processes. Moreover, the increased χ_c for the thick section of PLA microparts and PLA/CNT microparts suggests flow-induced crystallization in µIM.

Table 5.10 The characteristic data obtained from the DSC heating curves of PLA and PLA/CNT blends as well as thick section of corresponding microparts.

Sample	T_g (^{o}C)	T_{cc} (^{o}C)	T_m (^{o}C)	ΔH_m (J/g)	χ_c (%)
PLA	63.61	N/A	169.84	49.22	52.5
PLA Blend	61.34	N/A	167-170	49.75	53.1
PLA Thick	61.60	101.32	169.85	10.14	10.8
PLA/CNT Blend	63.32	108.47	172.07	4.1	4.6
PLA/CNT Thick	60.01	97.95	168.25	10.8	12.1

Figure 5.40(b) displays the DSC heating curves of unfilled PLA/PBSA, PLA/PBSA/CNT immiscible blends and the thick section of corresponding microparts. In combination with Figure 5.40(a), it could be deduced from Figure 5.40(b) that the small endothermic peak which was observed in the vicinity of 60^{o}C could be ascribed to the melting of less stable PBSA crystals and glass transition of PLA polymer chains. In addition, the melting peaks which are located at about 94^{o}C and 168^{o}C are the main melting peaks of PBSA and PLA,

respectively. Figure 5.40(b) shows that the cold crystallization process of PLA component in the PLA/PBSA, PLA/PBSA/CNT blends and thick section of corresponding microparts was negligible, which was contradictory to the results reported by Lee and Lee [325]. The authors found that the addition of PBSA could promote the cold crystallization process of PLA and they proposed that the PBSA could be treated as an efficient plasticizer of PLA. However, Liu et al. [14] found that µIM has a suppression effect on the cold crystallization process of PLA. In addition, the χ_c of PLA/PBSA immiscible blends is invariably higher than that of PLA microparts and PLA/CNT blends, as depicted in Tables 5.10 and 5.11. Herein, the absence of cold crystallization behavior of PLA in the immiscible blends might be ascribed to the overlap of the melting endotherm for PBSA and the re-crystallization exotherm for PLA. However, further investigations into the microstructure of subsequent moldings might be helpful to elucidate this phenomenon. Furthermore, in comparison with the PLA/PBSA and PLA/PBSA/CNT immiscible blends, the enhanced χ_c for thick section of corresponding microparts further confirmed the flow-induced crystallization of PLA in µIM.

Table 5.11 The melting enthalpy (ΔH_m) and χ_c of PLA component in PLA/PBSA blend, PLA/PBSA/CNT blend and thick section of corresponding microparts.

Sample	ΔH_m (J/g)	χ_c (%)
PLA/PBSA Blend	28.63	43.6
PLA/PBSA Thick	29.75	45.4
Sample 3	25.98	41.7
Sample 3 Thick	29.08	46.7

5.3.3 Thermogravimetric analysis (TGA)

Figure 5.41(a) indicates that pure PLA undergoes a one-step decomposition process and the thermal stability of PLA remains unchanged after melt blending, as revealed by their similar thermal decomposition behavior of original PLA pellets and PLA blends. However, thermal decomposition of the thick section of PLA microparts and corresponding T_{max} (i.e.

the peak value of derivative weight loss thermograms) shifted to lower temperature regions when compared with those of original PLA pellets and PLA blends, indicating that the prevailing higher shearing effect in µIM has a chain scission effect on PLA matrix [195]. Similarly, such effects could be observed in the Figures 5.41(b)-(d). Furthermore, Figure 5.41(b) reveals that the thick section of PBSA/CNT microparts demonstrated a two-step decomposition behavior which could be treated as an evidence that the prevailing shearing conditions in µIM also have a shortening effect on PBSA chains. Therefore, the fragments with lower molecular weights degrade first at a relatively lower temperature which is about 320^{o}C. Figure 5.41(c) reveals that the PLA/PBSA blends and thick section of corresponding microparts experienced a two-step decomposition behavior which was mainly ascribed to the fact that two different polymer components are involved during the thermal decomposition process. The occurrence of a two-stage degradation process is characteristic of the thermal degradation of a binary immiscible system [26]. Regarding the derivative weight loss thermograms (DTG), the peak which centers in the vicinity of 360^{o}C is associated with the degradation of PLA, whereas the peak around 400^{o}C corresponds to the degradation of PBSA. Figure 5.41(d) shows that although the maximum degradation temperature does not deviate significantly among PLA, PLA/CNT composite and the thick section of PLA/CNT microparts, the degradation of PLA/CNT composite and thick section of corresponding microparts deteriorated when compared with pure PLA, suggesting that the incorporation of CNT and the different thermomechanical history of corresponding polymer blends, which was reflected in the thermal degradation process, play an important role in determining the microstructure. Moreover, according to Table 5.10, the differences in χ_c of the three different polymer systems could be a contributing factor. Figure 5.41(e) shows the decomposition behavior of *Sample 3* and the thick section of corresponding microparts. Results indicate that all samples decompose in a two-stage process and the T_{max} is about 10^{o}C lower than that of PLA/PBSA immiscible blend. Despite the immiscibility of components of PLA and PBSA, a tentative explanation for this phenomenon is that the higher thermal conductivity of CNT-containing polymer composites [32] may facilitate heat conduction into internal regions of PLA/PBSA/CNT composites, and therefore, thermal degradation could occur simultaneously inside and outside of the composites [34].

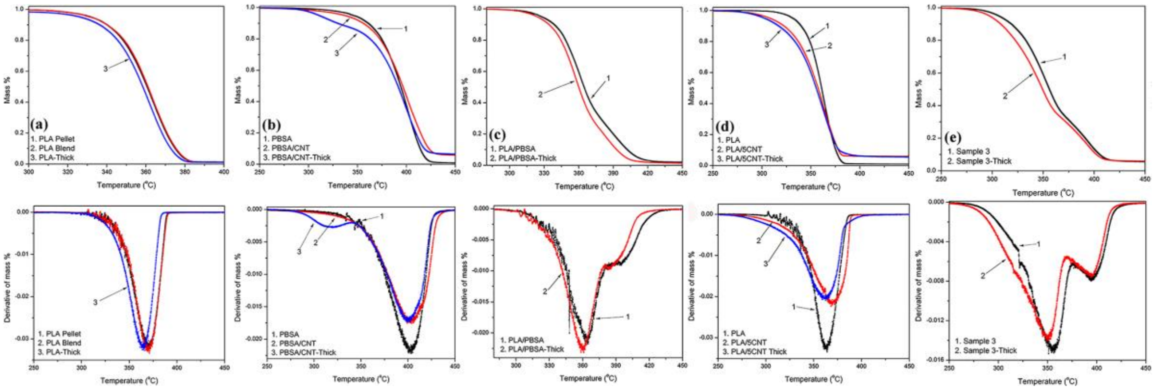

Figure 5.41 TGA and DTG curves of (a) PLA, (b) PBSA and PBSA/CNT, (c) PLA/PBSA, (d) PLA/CNT and (e) *Sample 3* as well as the thick section of corresponding microparts.

5.3.4 Electrical conductivity

The values of σ for each section of corresponding microparts are plotted as a function of measurement directions in Figure 5.42. Figure 5.42(a) shows that the FD σ is invariably higher than the TD σ with respect to each section of microparts. It is indicative of a role for orientation of CNT along the flow direction. Moreover, regardless of the compounding procedure, the σ of CNT filled PLA/PBSA systems is invariably superior to that of mono-PLA system when compared with respective sections in the same measurement direction, which could be attributed to the more effectively construction of conductive network by the dispersed CNT. It is thus suggested that the presence of the second polymer matrix, i.e. PBSA, could alter the distribution of CNT in subsequent blends. For example, Zhou et al. reported that the selective localization of flake graphite in PA6 phase is essential to the enhancement of thermal conductivity of PA6/PC [26] and PA6/PP [162] immiscible blends when compared with that of mono-PA6 system. Moreover, the TD σ for the thin section follows a similar trend as that observed for the thick and middle sections of microparts, which is displayed in Figure 5.42(b). Although there is no significant difference of σ value between each section of PLA/PBSA/CNT microparts at a specific measurement direction, the average values of σ for *Sample 3* are the highest when compared with respective sections taken from the microparts molded from the other PLA/PBSA/CNT immiscible blends and PLA/CNT composites. Therefore, the results indicated that the compounding sequence of various components during the preparation of PLA/PBSA/CNT immiscible blends might influence the distribution of CNT, thereby affecting the σ for different sections of resulting microparts.

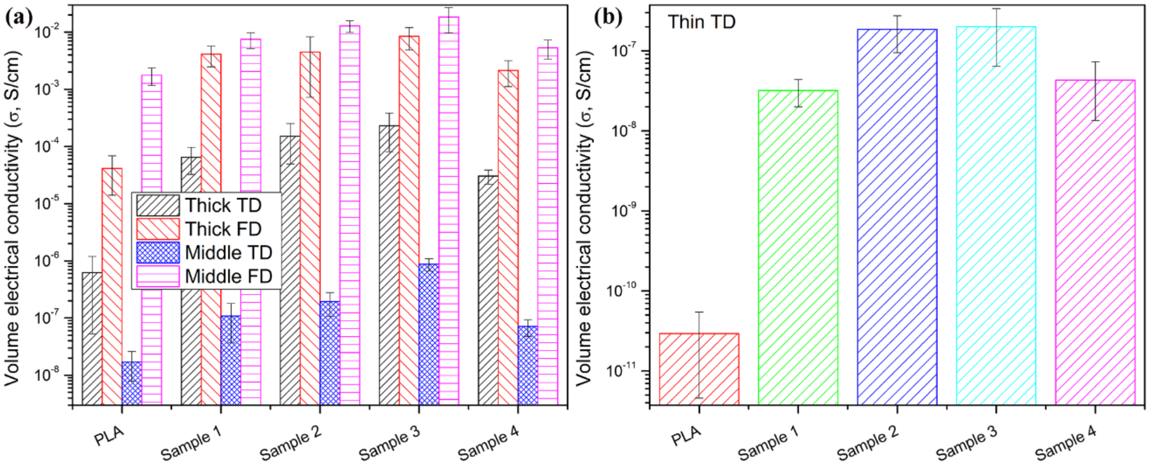

Figure 5.42 (a) The σ of the thick and middle sections of PLA/CNT and PLA/PBSA/CNT microparts with respect to the measurement directions; (b) the TD σ for the thin section of each sample. The concentration of CNT in all samples is 5 wt%.

Tu et al. [326] reported that selective localization of fillers in immiscible polymer blends is primarily dominated by the interfacial interactions with the polymer components and thermodynamic driving forces. According to Young's equation, the selective localization of filler in a ternary system could be evaluated by estimating the wetting coefficient, ω_a. The w_a could be calculated as follows:

$$\omega_a = \frac{\gamma_{B-filler} - \gamma_{A-filler}}{\gamma_{A-B}}$$

where $\gamma_{A-filler}$ and $\gamma_{B-filler}$ are the interfacial energy between the filler and component A, and the filler and component B, respectively. γ_{A-B} is the interfacial energy between component A and component B. If ω_a is higher than 1, the filler is distributed in phase A. If w_a is lower than -1, the filler will be mostly located in phase B. Otherwise, the filler is preferentially located at the interface of the two polymer components [327]. Based on the geometric-mean equation [328], the interfacial energy between two components could be calculated as follows:

$$\gamma_{A-B} = \gamma_A + \gamma_B - 2(\sqrt{\gamma_A^d \times \gamma_B^d} + \sqrt{\gamma_A^p \times \gamma_B^p})$$

where γ_A and γ_B are surface energy of component A and B, respectively. γ_A^d and γ_A^p are the dispersive and polar portions of surface energy for component A. The literature values of surface energy for PLA, PBSA and CNT used for calculation of the interfacial energy for pairs of PLA/PBSA, PLA/CNT and PBSA/CNT are summarized in Table 5.12. The geometric-mean equation is used and subsequent results are applied for Young's equation to calculate w_a. The calculated w_a for PLA/PBSA/CNT ternary blend is -1.52, which means that CNT is primarily dispersed in one phase, i.e. PBSA. The result is consistent with the morphology observation for thick section of microparts which were molded from *Sample 3*, as evidenced by SEM.

Table 5.12 Surface energy for PLA, PBSA, CNT, and the calculated interfacial energy for PLA/PBSA, PLA/CNT and PBSA/CNT pairs by using the geometric-mean equation.

Sample	Surface energy (mJ/m^2)			Sample A	Sample B	Interfacial energy, γ_{A-B} (mJ/m^2)
	γ^d	γ^p	γ			
PLA [328]	37	13	50	PLA	PBSA	-0.756
PBSA [328]	43	14	56	PLA	CNT	3.73
CNT [273]	17.6	10.2	27.8	PBSA	CNT	4.88

5.3.5 Summary

A series of PLA/PBSA/CNT immiscible blends were prepared by systematically altering the compounding sequence of components of PLA, PBSA and CNT in a laboratory scale batch mixer. The obtained polymer blends were subsequently used for µIM and results indicated that the addition of PBSA to PLA can alter the state of distribution of CNT in subsequent moldings. SEM observations revealed that CNT is primarily localized in the discretely distributed PBSA droplets in PLA, and the existence of CNT aggregates in subsequent blends is beneficial to the enhancement of electrical conductivity. Furthermore, a CNT-enriched layer which was typically observed in the shear layer of PLA/PBSA/CNT microparts could be attributed to the prevailing high shear fields in µIM. In this scenario, the very high shearing effect causes the shape deformation of CNT-containing phases and subsequent combination of these deformed structure leads to the appearance of CNT-enriched layer. TGA results indicated that the thermal stability of microinjection molded samples deteriorated when compared with that of corresponding polymer blends, suggesting that the presence of very high shear rates in µIM may have a severe degradation effect on PLA and PBSA chains, respectively.

5.4 The influence of the types of carbon fillers

A series of different types of carbon fillers (i.e. CB, CNT, GNP and graphite) loaded PP composites were prepared by melt blending, followed by compression molding or µIM. Direct current electrical conductivity measurements and melt rheology tests were utilized to detect the percolated structure for compression molded PP/carbon composites. For µIM, a rectangular mold insert which has three consecutive zones with decreasing thickness along the melt flow direction was adopted to study the influence of abrupt changes in mold geometry on the electrical and morphological properties of microparts. Results indicated that microparts demonstrated a higher p_c when compared with their compression molded counterparts. This is largely due to the severe shearing conditions that prevail in µIM. The morphology of microparts containing different types of carbon fillers was examined using SEM. The development of corresponding microstructure is found to be strongly dependent on the types of carbon fillers used in µIM, which is crucial to the enhancement of electrical conductivity for the resulting microparts. For example, the high structure CB and CNT are more effective in building conductive pathways within the microparts when compared with that of GNP. In addition, *in situ* expansion of LTEG is crucial to form conductive pathways within the host matrix, which is essential to the enhancement of electrical conductivity.

5.4.1 Properties of compression molded PP/carbon composites

5.4.1.1 Electrical and morphological properties of CNT, CB and GNP filled PP composites

Figure 5.43 shows the values of σ of compression molded PP/carbon composites, which was measured across the transverse direction (TD), as a function of filler content. The σ of different carbon filler containing systems is enhanced with increasing loading fractions in PP. It could be deduced from Figure 5.43 that CNT is effective in enhancing the σ of PP-based composites at lower filler concentrations (< 2 wt%), which could be attributed to the fact that CNT has a high aspect ratio and this is beneficial to the formation of conductive pathways, thereby enhancing the σ of corresponding composites [89]. A rapid increase of σ is observed at the CNT concentration of 2 wt%, resulting from the formation of conductive pathways within PP. Similarly, with further increasing filler content, the σ of CB filled system increases remarkably in the range of 1 to 2 wt%, which is due to the formation of a conductive network. Lin and Chung [329] reported that the addition of high structure CB is favorable for the formation of conductive pathways, thereby contributing to the enhancement of σ of resultant polymer composites. The σ of PP/GNP composites follows a linear trend with increasing addition of GNP until the filler concentration reaches 7 wt%. Afterwards, a significant increase of σ is observed, which is a result of the formation of conductive network within PP. Thus, the p_c for PP/GNP systems falls in the range of 7 to 10 wt%. Above all, the foregoing results indicate that CB and CNT are more effective in improving the conductive properties of PP composites when compared with GNP. The evolution of σ is correlated with the development of microstructure in PP with an increase of filler loading fractions which is detailed in the following part.

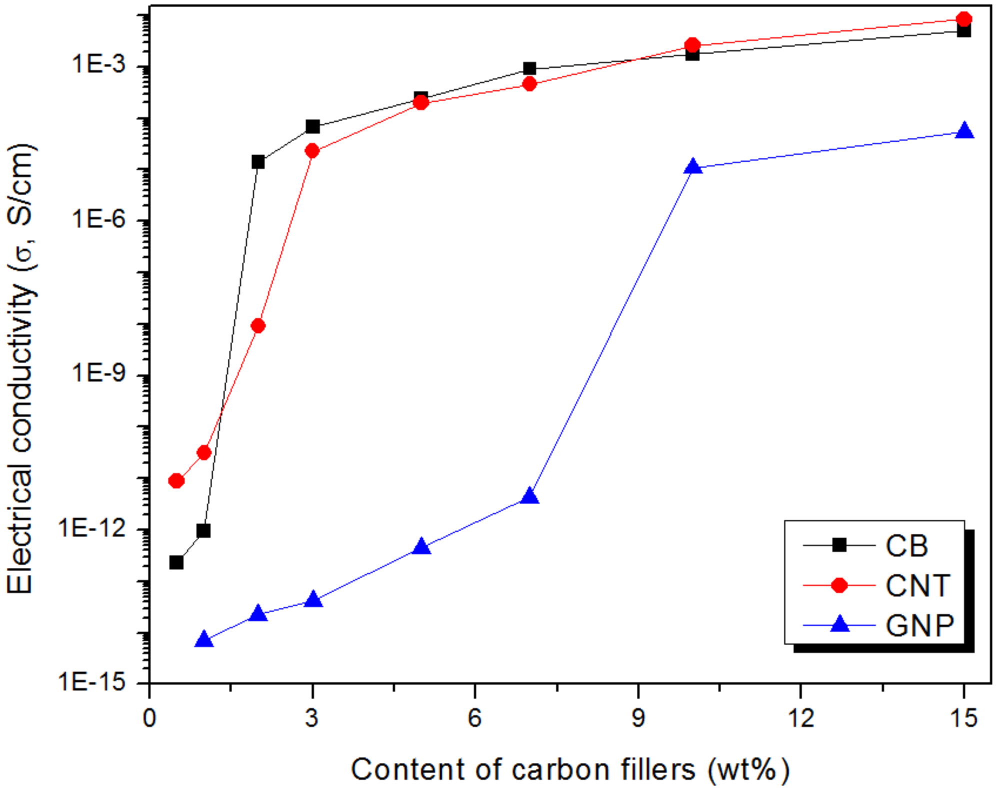

Figure 5.43 The TD σ of compression molded PP/carbon samples as a function of filler content.

The morphology of compression molded PP/CNT, PP/CB and PP/GNP composites with various filler concentrations was characterized by SEM. Prior to observations, all samples were fractured in liquid nitrogen and then coated with a thin layer of platinum to enhance surface conductivity. Figure 5.44 shows that CNTs are mainly dispersed in the form of small aggregates within the PP matrix, and corresponding CNT aggregates have a relatively uniform distribution. As can be seen from Figures 5.44(a)-(c), the size of CNT aggregates increased from several hundred nm to nearly one μm and the distance between different CNT aggregates was lowered simultaneously with increasing loading fraction of CNT, which contributed to the enhancement of σ.

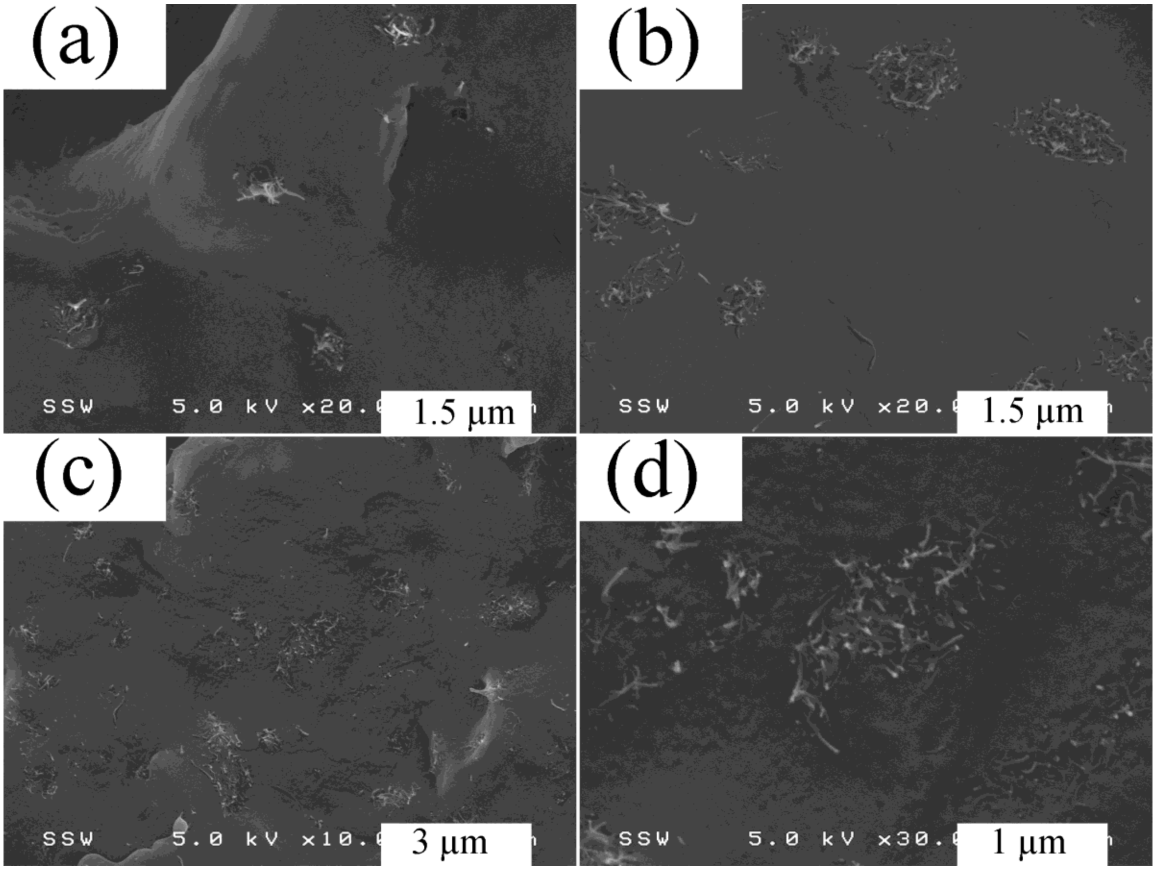

Figure 5.44 The morphology of PP/CNT composites with various filler concentrations: (a) 1 wt%; (b) 3 wt%; (c) and (d) 5 wt% at different magnifications.

Figure 5.45 shows the morphology of PP/CB composites with an increase of CB loading concentration. Figures 5.45(a)-(c) reveal that the distribution of primary CB particles is not uniform as the small aggregates could be observed within the PP matrix regardless of CB concentration. However, CB aggregates seemed to achieve an improved distribution with an increase of CB loading fraction, thereby facilitating the construction of 3D conductive network within PP. Compared with CNT filled PP composites, CB demonstrated a higher efficiency to build conductive pathways, thereby leading to a higher σ of corresponding composites than CNT loaded systems. It has been illustrated in Figure 5.43 that the σ of PP/CB composites is nearly three orders of magnitude higher than the value obtained from PP/CNT composites at 2 wt%.

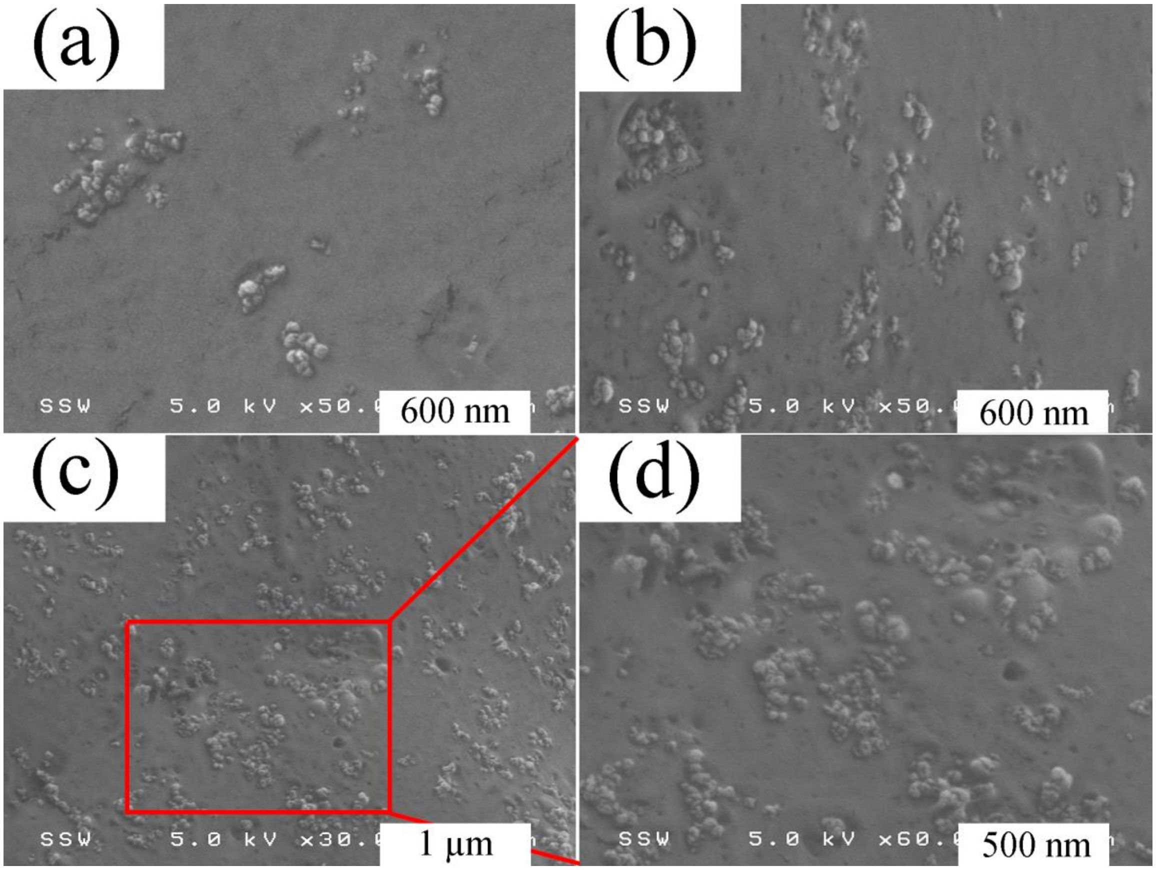

Figure 5.45 The morphology of PP/CB composites with various filler concentrations: (a) 1 wt%; (b) 3 wt%; (c) and (d) 5 wt% at different magnifications.

Figure 5.46 exhibits the distribution of GNP in PP at various filler concentrations. The presence of GNP fillers is indicated by red arrows. Results indicate that the plate-like GNP particles dispersed uniformly and discretely within PP. As shown in Figures 5.46(a) and (c), it is unlikely for GNP to form 3D conductive pathways at lower filler loading fractions. Moreover, an intact conductive network is hardly observed within the PP even at a 10 wt% GNP, as indicated by Figures 5.46(e) and (f). As shown in Figure 5.43, the σ of PP/GNP

10 wt% composite is comparable to corresponding value of PP/CB 2 wt% and PP/CNT 3 wt%, respectively. This further confirmed that GNP is not as efficient as the other carbon fillers, i.e. CB and CNT, in constructing conductive pathways within PP, which is corroborated by melt rheology analysis (as described in *Section 5.4.2.1*).

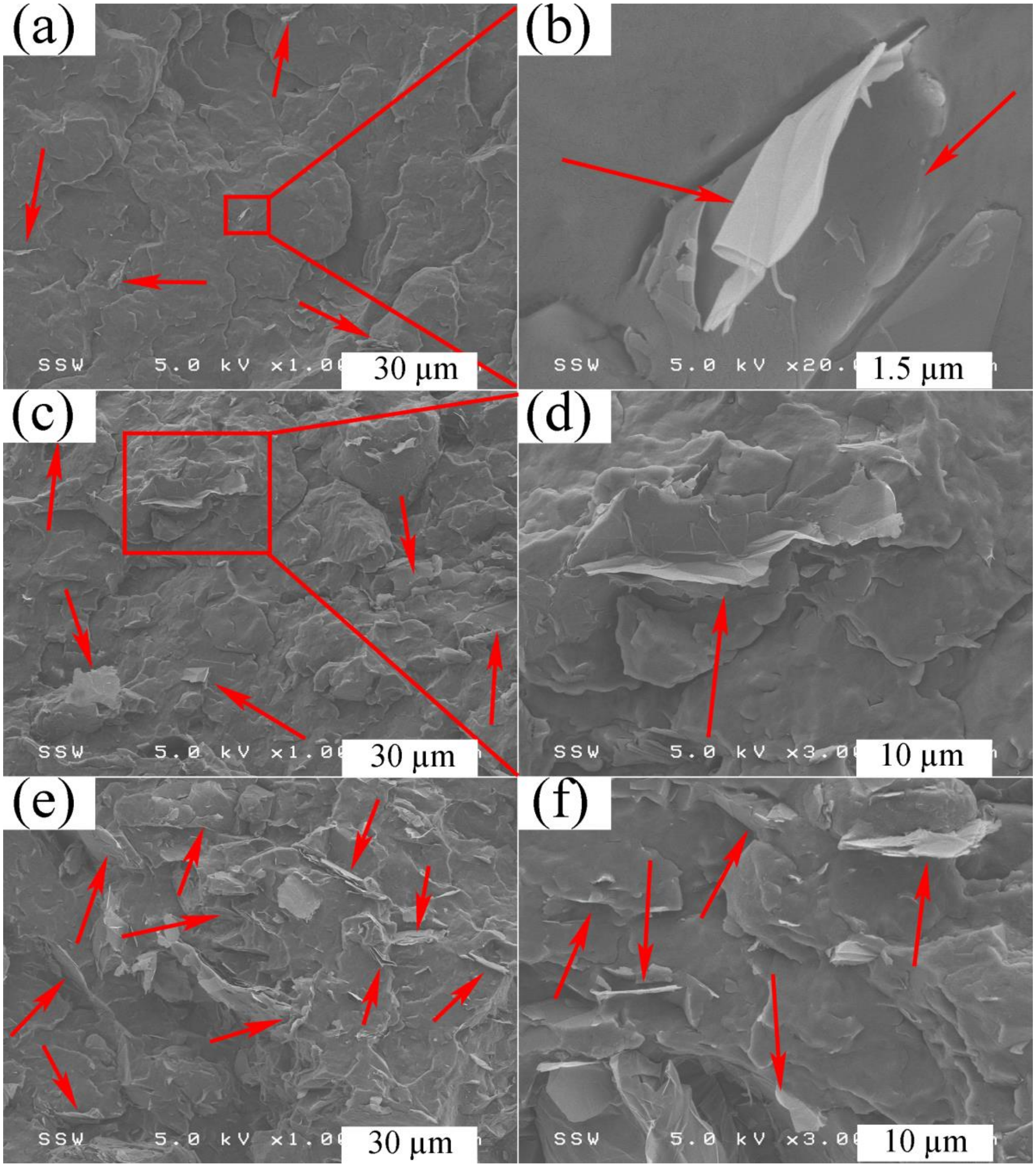

Figure 5.46 The morphology of PP/GNP composites with various filler concentrations at different magnifications: (a)-(b) 1 wt%; (c)-(d) 5 wt%; (e)-(f) 10 wt%.

5.4.1.2 Electrical and morphological properties of SG filled PP composites

The values of σ for compression molded PP/SG composites, which were determined across the TD are plotted as a function of filler content, as displayed in Figure 5.47. The values of σ for PP/SG samples with lower filler concentrations (< 20 wt%) are not detectable since their resistance is beyond the lower limit of the measurement scale of the testing equipment (Keithley 6514, USA) due to a lack of sufficient conductive pathways. With an incremental loading fraction of SG, a large increase of σ for PP/SG composites is observed at a filler content of 30 wt%, which is attributed to the formation of a conductive network through filler-filler interactions.

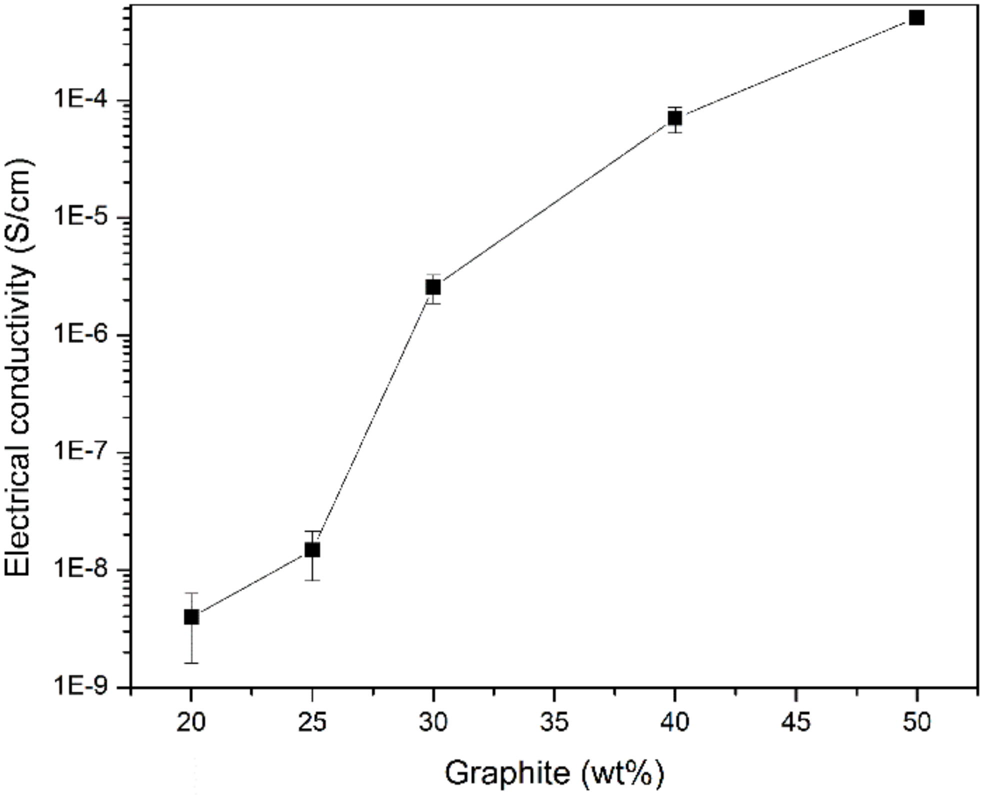

Figure 5.47 The TD σ for compression molded PP/SG composites as a function of filler content.

The morphology of SG particles is shown in Figure 5.48. The SG particles mainly assume a plate- or flake-like structure [330]. In addition, the microstructure of cryo-fractured surface of compression molded PP/SG composites is given in Figure 5.49. It is illustrated that the SG particles have a relatively uniform distribution in PP, as indicated by black arrows. Figure 5.49(a) indicates that the SG has a high tendency to form interconnected conductive pathways within PP, which is consistent with the rapid increase of σ for PP/SG composites at 30 wt%, as displayed in Figure 5.47. Furthermore, it is shown in Figure 5.49(b) that the SG particles have already constructed an intact conductive network within PP, which is essential to the enhancement of σ for subsequent polymer composites.

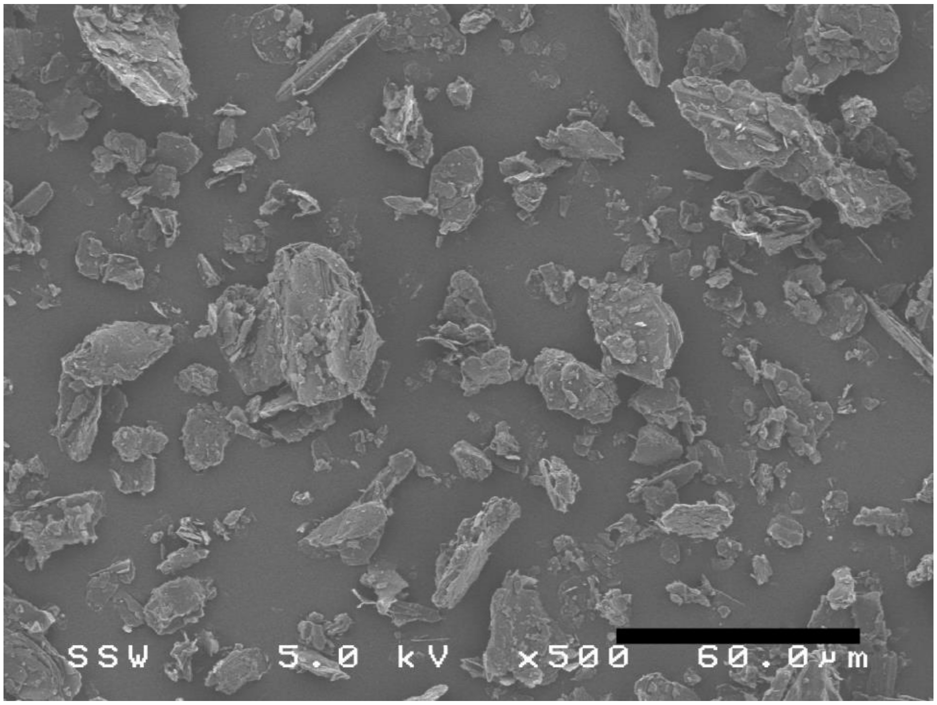

Figure 5.48 The morphology of synthetic graphite (SG).

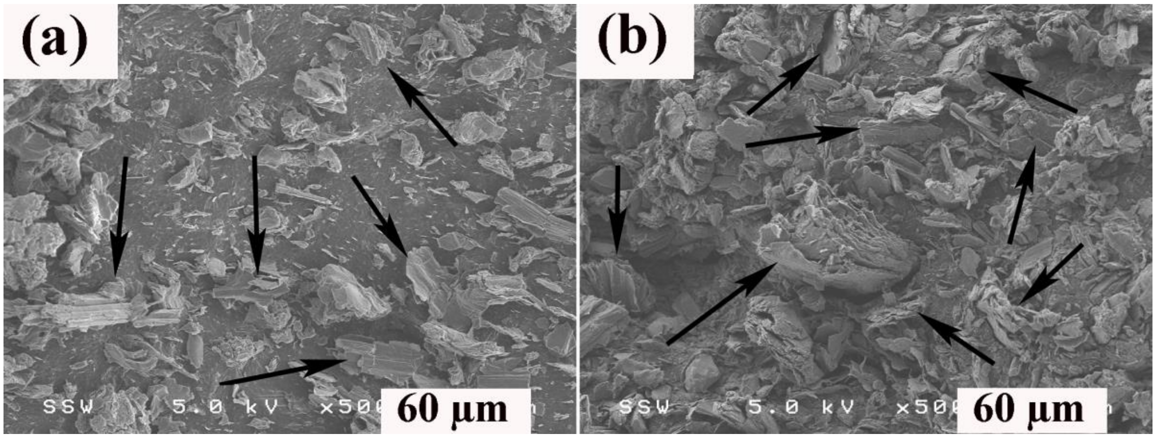

Figure 5.49 SEM images of compression molded (a) SG30 and (b) SG50 composites.

5.4.2 Melt rheology

5.4.2.1 Melt rheology of CNT, CB and GNP filled PP composites

Melt rheology is sensitive to the microstructure change in polymer composites resulting from the addition of fillers. Figures 5.50(a)-(c) are the plots of storage modulus (G') versus loss modulus (G") as a function of frequency and weight fraction of CB, CNT and GNP, respectively. Taking Figure 5.50(a) as an example, G' increases with increasing CB content in PP. Starting from 2 wt% CB, there is an apparent deviation of the slope of G' versus G" with increasing CB content. Pötschke et al. [252] reported that the shift and change in the slope of G' versus G" indicate a significant change in microstructure of filler-containing polymer composites. Therefore, in combination with Figure 5.43, it could be deduced from Figure 5.50 that the change of microstructure is related to the formation of conductive pathways within PP. Similarly, a microstructure change of PP/CNT composites is found to occur in the vicinity of 3 wt%. However, as shown in Figure 5.50(c), there is only a slight deviation of the slope of G' versus G" when the GNP concentration is lower than 15 wt%, revealing that this plot is not sensitive for PP/GNP composites to probe the microstructure change with increasing GNP content. This may be due to the geometrical effect of different types of carbon fillers. Figure 4.1(b) shows that GNP has a plate-like structure and therefore they are more susceptible to the shearing effect. In addition, the lower surface area of GNP particles (see Table 4.3) may be another contributing factor since a stable physical network is hardly formed at lower filler loading concentrations. In combination with the results given in Figure 5.43, it could be concluded that plate-like GNP is not as efficient as CB and CNT in constructing 3D interconnected pathways within PP.

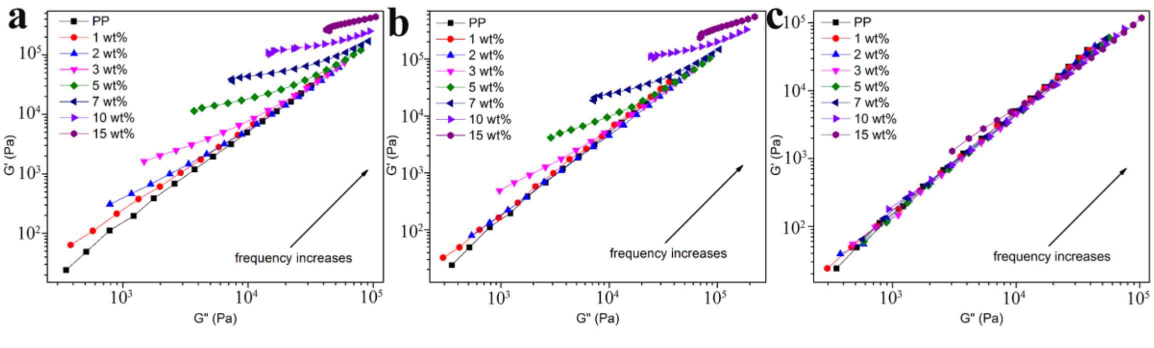

Figure 5.50 G' as function of G" of (a) CB, (b) CNT and (c) GNP loaded PP at 190^{o}C.

5.4.2.2 Melt rheology of SG filled PP composites

Data on the dependence of G', G", tan δ and complex viscosity (η*) on angular frequency for PP/SG composites are shown in log-log plots in Figure 5.51, respectively. In general, both the values of G' and G" increase with increasing SG content in the entire range of frequency employed. Taking G' versus frequency as an example, the magnitude of G' increases and the slope of these curves decreases in the low frequency region with increasing filler content. Starting from 30 wt% SG, there is an obvious deviation of the slopes for PP/SG composites when compared with that of unfilled PP or PP/SG composites with lower filler concentrations. Simultaneously, shear thinning behavior is noticeable in η*, which is mainly attributed to the formation of a physical network in the polymer matrix due to the added fillers [26]. Thus, the rheology results are consistent with the results given in Figure 5.45, i.e. the p_c is around 30 wt% SG.

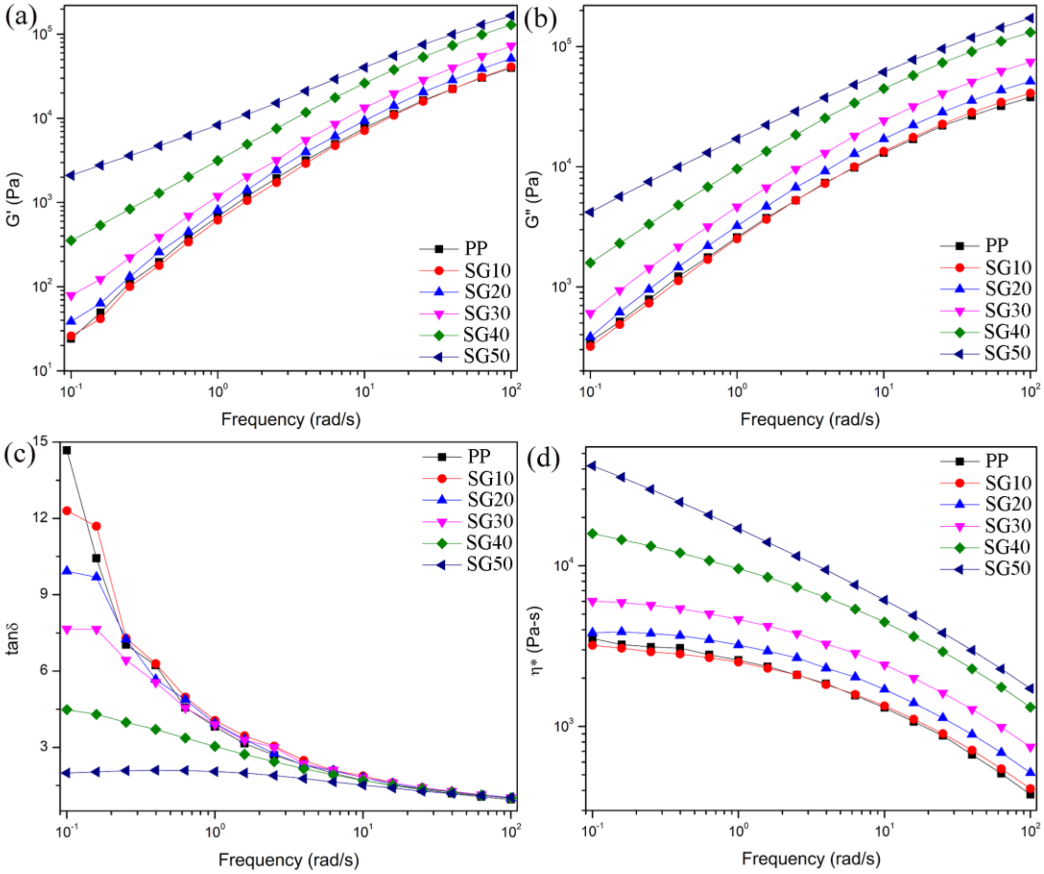

Figure 5.51 (a) G', (b) G", (c) tan δ, and (d) η* as a function of frequency for different filler concentrations of PP/SG composites at 190°C, respectively.

5.4.3 Properties of microinjection molded PP/carbon composites

The σ and microstructure development of different carbon fillers loaded PP microparts are given as follows. *Section 5.4.3.1* discusses the effect of CNT, CB and GNP content on the σ of microinjection molded three-stepped microparts, which is correlated with morphology observations. *Section 5.4.3.2* focuses on the properties of PP/graphite composites in µIM, with an emphasis on the influence of different types of graphite fillers (i.e. SG and LTEG) on the σ and development of microstructure in subsequent moldings.

5.4.3.1 CNT, CB and GNP filled PP microparts

5.4.3.1.1 Microinjection molding of PP/CB composites

The log σ of each section of the PP/CB microparts measured in the FD and TD is reported in Figure 5.52. Figure 5.52 reveals that the σ measurements for each section of microparts were only carried out with samples containing higher filler concentrations (> 3 wt%). The obtained σ for the thin section is invariably lower than those achieved for their thick and middle section counterparts at identical CB concentrations as per measurement directions. Simulation results (Moldflow) show that shear rates in the thin section are the highest when compared with those of the thick and middle sections (see *Section 5.4.4*), which is thought to be unfavorable for the network formation by the spherical CB particles. For example, Chodák et al. [172] reported that the p_c depends strongly on the processing method and the p_c for compression molded PP/CB samples is much lower than that of injection molded counterparts, which could be attributed to the influence of shearing differences. Similar to CNT filled PS systems (see *Section 5.2.2.1*), the σ measured along the FD (Figure 5.52b) is several orders of magnitude higher than that across the TD (Figure 5.52a), indicating a preferential network formation along the flow direction.

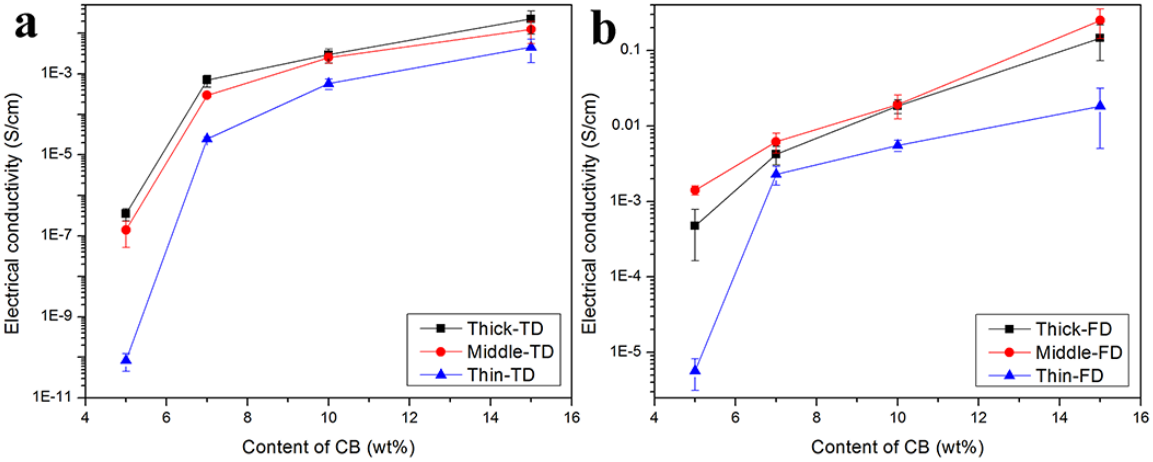

Figure 5.52 DC electrical conductivity of each section of the microparts measured across the (a) TD and (b) FD as a function of CB concentration.

The improvement of σ for PP/carbon composites is strongly related to the evolution of microstructure within the microparts. Thus, the microstructure of subsequent PP/carbon microparts is observed with respect to each cut section. The examined surfaces were sectioned across the TD by using a microtome, followed by chemical etching treatment for at least 8 h by using a mixture of sulfuric acid/phosphoric acid/potassium permanganate ($H_2SO_4/H_3PO_4/KMnO_4$), as per Park et al. [246]. The development of microstructure for different sections of subsequent microparts with respect to the core layer and shear layer (close to the mold wall) are presented in Figure 5.53.

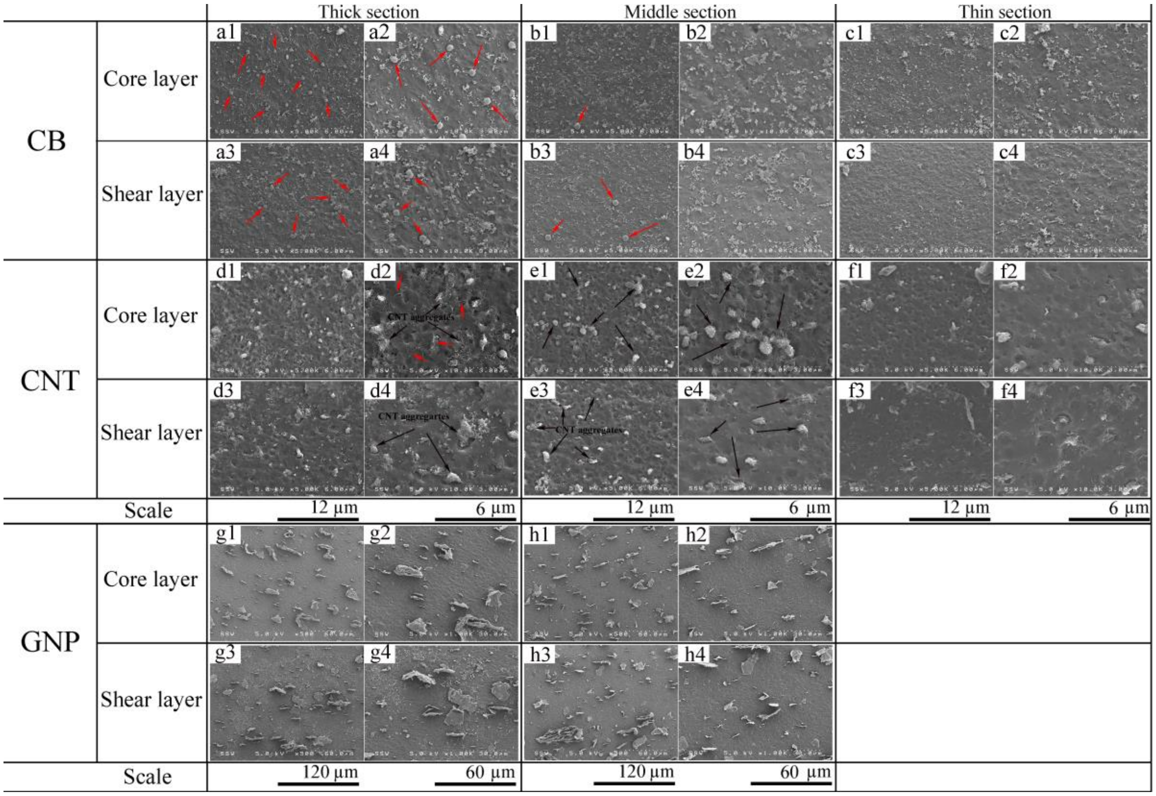

Figure 5.53 The morphology (TD) taken from the core and shear layers of the thick, middle and thin sections of different PP/carbon microparts. The filler concentration for all samples is fixed at 2 wt%.

Figures 5.53(a)-(c) demonstrate the morphology of the core layer and shear layer of CB2 microparts observed across the TD. The presence of CB agglomerates is indicated by red arrows. As shown in Figures 5.53(a1) and (a3), a larger number of CB agglomerates are found in the core layer than the shear layer. In addition, the high structure CB could form a typical ‘grape’ like structure (labeled in Figure 5.54), which facilitates the construction of conductive pathways in PP. In general, the distribution of CB aggregates is quite uniform in both the shear layer and core layer of the thick section, albeit the presence of discretely dispersed spherical CB agglomerates.

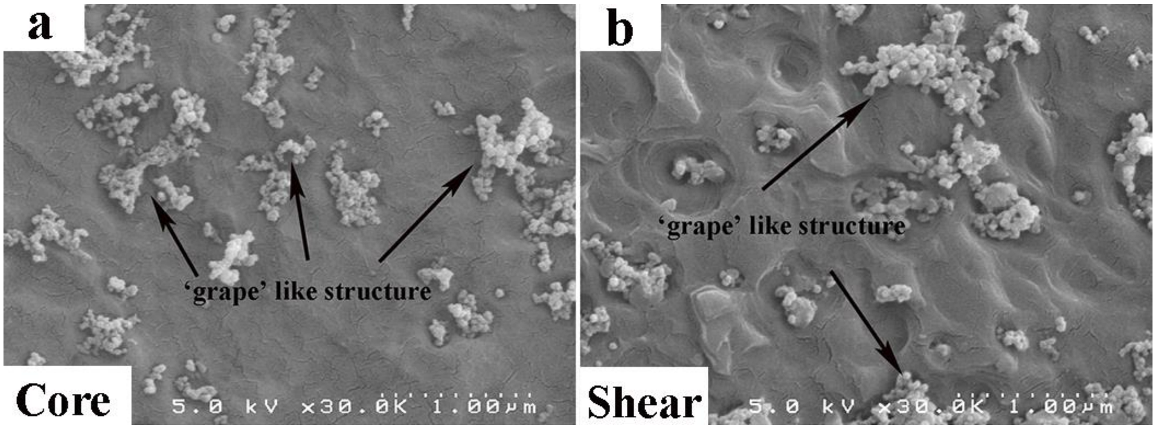

Figure 5.54 The high magnification images of the (a) core layer and (b) shear layer of thick section of CB2 microparts.

Similar to the morphology of the thick section (Figure 5.53a), Figure 5.53(b) reveals that CB aggregates are uniformly distributed within the middle section. The major difference is that there is an obvious reduction of the number of spherical CB agglomerates present in the middle section when compared with that of thick section, which could be attributed to the significant increase of the shearing conditions with a sharp reduction of mold cavity thickness from 0.85 (thick section) to 0.5 mm (middle section). In addition, the extensional force fields are quite significant near the contraction regions amid the thick and middle sections. Therefore, both the shearing and extensional force fields contribute to the microstructural changes in different sections of the PP/CB microparts.

The distribution of CB aggregates in the thin section of CB2 microparts is given in Figure 5.53(c). It can be deduced from Figure 5.53(c) that the distribution of CB aggregates is not uniform between the shear layer and core layer. It is evident that there is a larger fraction of CB particles present in the core layer (Figure 5.53c1) when compared with that of the shear layer (Figure 5.53c3). This could be attributed to the filler migration effect which is commonly observed in high shear conditions, like injection molding process [331]. As a result, the σ for the thin section is invariably lower than that obtained from both the thick and middle sections due to a lack of sufficient conductive pathways. Notably, by comparing Figure 5.43 with Figure 5.52(b), one can easily note that the σ measured along the FD for all sections of microparts is higher than that of compression molded counterparts at higher filler concentrations (> 5 wt%), implying that the dispersion of CB is greatly improved with an increase of shearing effect.

5.4.3.1.2 Microinjection molding of PP/CNT composites

Figure 5.55 shows the log σ of each section of PP/CNT microparts as a function of filler content measured across the TD and FD, respectively. As shown in Figure 5.55, the σ measurements for the thin section of microparts were only carried out with samples containing higher filler concentrations (> 3 wt%). The σ measured along the FD of PP/CNT microparts is always higher than that obtained across the TD, indicating a role for the orientation of CNT along the flow direction [332]. Figure 5.55(a) suggests that the p_c for both the thick and middle sections measured across the TD falls in the range from 3 to 5 wt% whereas the p_c obtained from both sections of the microparts in FD is in the vicinity of 3 wt%, as illustrated in Figure 5.55(b). Moreover, our results are comparable to that reported by Abbasi et al. [101] as they found that the p_c for PP/CNT microparts is about 4 wt%. The p_c for PP/CNT microparts is higher than that observed for compression molded counterparts, as illustrated in Figure 5.43. This could be ascribed to the influence of shearing conditions, which is quite significant in µIM and nearly negligible for compression molding process [12]. Thus, the presence of very high shear rates favors the preferential orientation of CNT in the FD and therefore, impairs the formation of random conductive pathways within subsequent microparts which could, to some extent, restrict the enhancement of σ across the TD and increase it in the FD, respectively. Additionally, possible length reduction of CNT after experiencing high shearing conditions could be an influencing factor. For example, Andrews et al. [136] observed a significant shortening effect of CNT in a laboratory mixer with increasing shearing conditions. Similar reduction effect has also been reported by Fu et al. [333] where the authors adopted a high shearing three-roll calendering technique to fabricate epoxy/CNT composites. Therefore, the p_c of subsequent moldings would shift to higher filler concentrations as per Bauhofer and Kovacs [38].

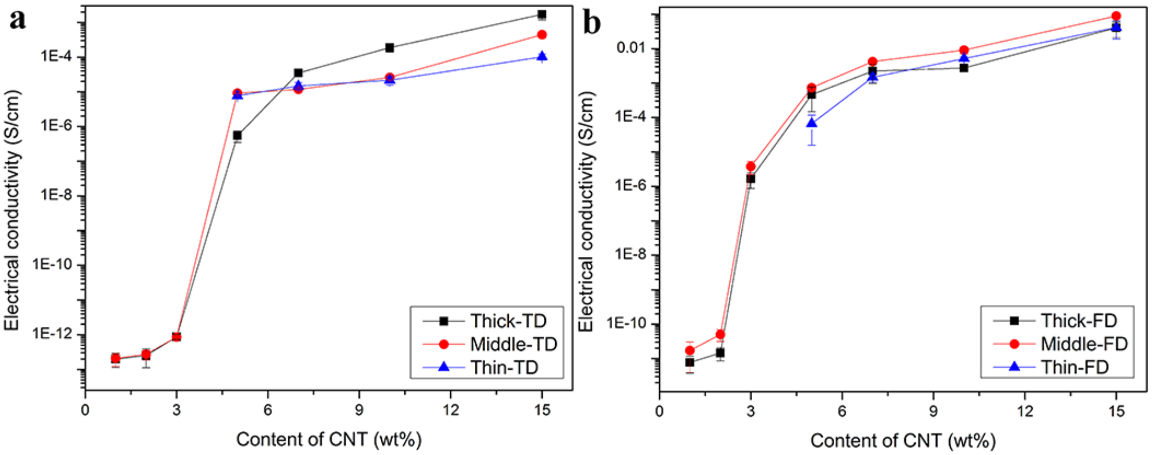

Figure 5.55 DC electrical conductivity of each section of the PP/CNT microparts measured across the (a) TD and (b) FD as a function of filler concentration.

The microstructure of PP/CNT 2 wt% (CNT2) microparts was characterized with each cut section. Figure 5.53(d) reveals the microstructure of the thick section. In Figures 5.53(d2) and (d4), the presence of CNT agglomerates has been pointed out by black arrows and the individually dispersed CNT is highlighted by red arrows. It could be deduced from Figure 5.53(d) that a larger fraction of CNT agglomerates is observed in the core layer (Figure 5.53d1) than shear layer (Figure 5.53d3). In addition, the individually dispersed CNT functions as connecting ‘bridge’ among discretely distributed CNT agglomerates, which is favorable for the transport of electrons.

Similar to that observed in the thick section (Figure 5.53d), the morphology of the middle section (Figure 5.53e) shows that there is a larger fraction of CNT agglomerates in the core layer (Figure 5.53e2) when compared with that of shear layer (Figure 5.53e4). In addition, the size of CNT agglomerates presents in the shear layer of the middle section (Figure 5.53e4) is somewhat smaller than that of thick section counterpart (Figure 5.53d4), indicating that the shearing conditions present in the middle section are more severe than those in thick section. This will be further confirmed by numerical simulation in *Section 5.4.4*. According to Xu et al. [332], the rigid CNT network would be deformed under high shear rates in the host polymers when CNT loading fraction is in the vicinity of p_c, thereby influencing the properties of corresponding blends.

Figure 5.53(f) exhibits the morphology observed for the core layer and shear layer of thin section of CNT2 microparts across the TD, respectively. When compared with the thick and middle sections of CNT2 microparts, a distinct difference is that very few CNT agglomerates could be observed in the thin section. The distribution of CNT aggregates is not as uniform as that observed for previous sections (i.e. thick and middle sections) and this well explains why there is a difficulty in determining the σ of thin section with lower CNT loading concentrations (< 5 wt%).

The morphology of the thick section of CNT2 microparts observed in the FD is displayed in Figure 5.56. Figures 5.56(a) and (c) indicate that a portion of CNT agglomerates are deformed to assume an elongated morphology in one specific direction, i.e. flow direction. This is associated with the strong shear force field that prevails in the melt filling direction, which is characteristic of injection molding process [13,334]. In addition, it seems that the individually dispersed CNT is likely to form a 3D conductive network, which is essential to the enhancement of σ.

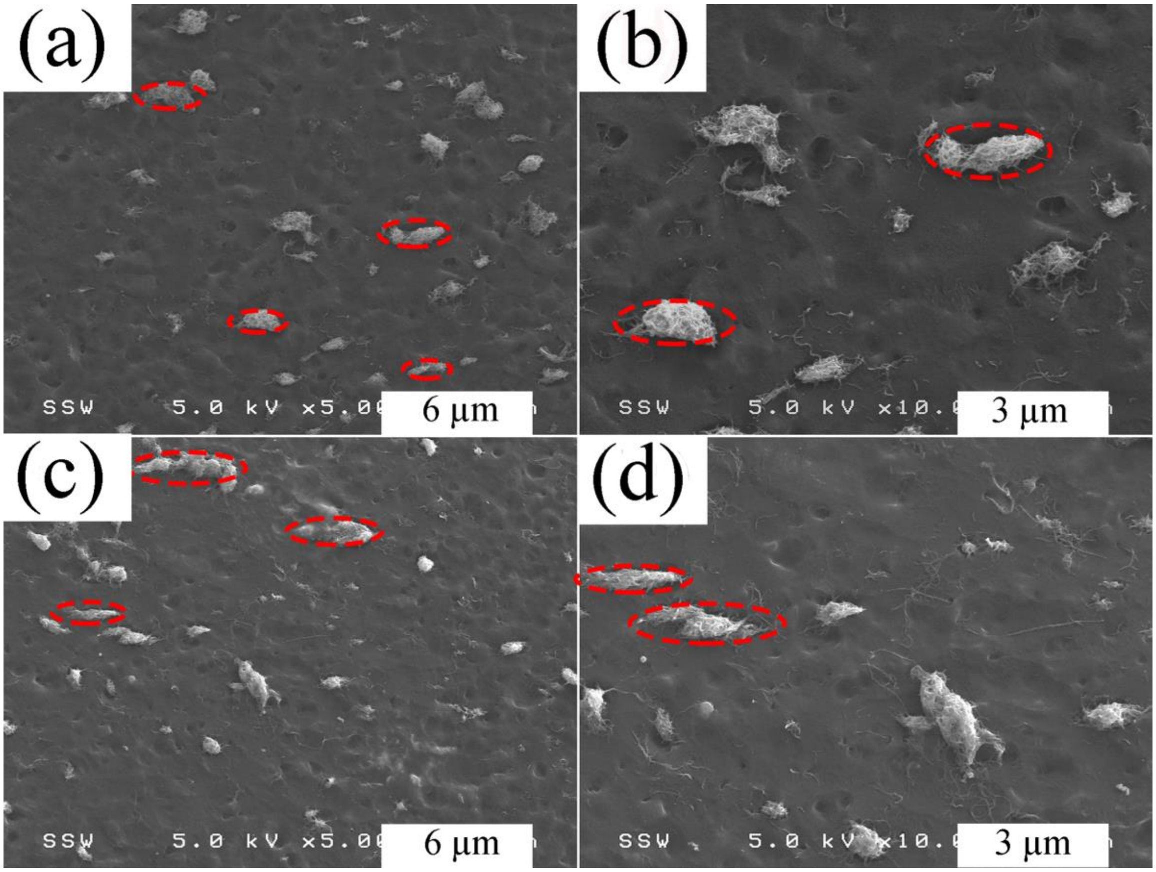

Figure 5.56 The morphology (FD) of thick section in the core layer (a, b) and shear layer (c, d) of CNT2 microparts

Figure 5.57 indicates that the CNT aggregates are further stretched by the higher shearing conditions that prevail in the middle section of microparts when compared with those of thick section, which results from the step reduction of mold cavity thickness. In addition, the extensional force fields are quite significant at these contraction areas amid different sections of the microparts. Moreover, an increase of the shearing effect leads to improved distribution of individual CNTs and CNT aggregates, yielding a relatively higher σ for the middle section when compared with that of the thick section along the FD, as displayed in Figure 5.55(b).

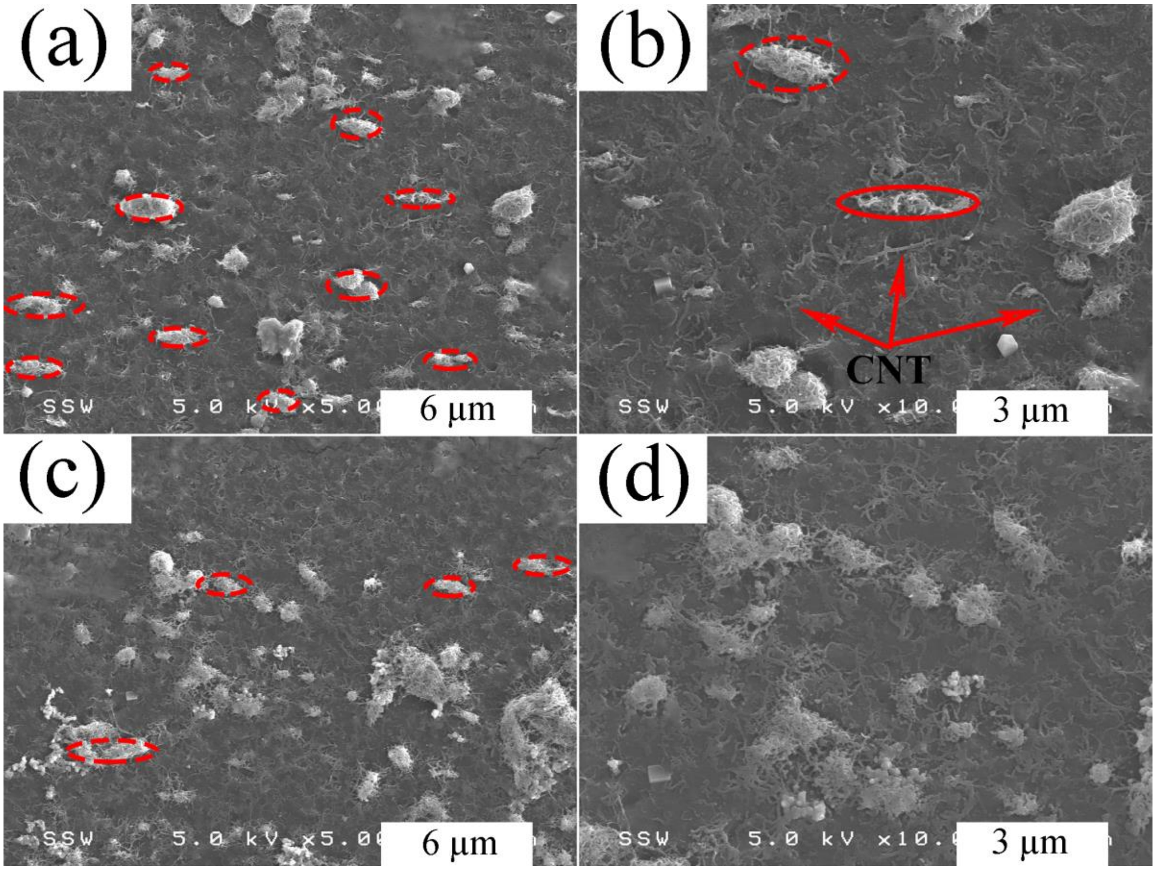

Figure 5.57 The morphology (FD) of the middle section in the core layer (a, b) and shear layer (c, d) of CNT2 microparts

Similar to Figure 5.53, Figure 5.58 shows that fewer CNT agglomerates could be observed from the thin section when compared with previous observations from both the thick and middle section counterparts, especially in the shear layer. In addition, the distribution of CNT aggregates is not as uniform as that observed for previous sections. The evolution of maximum shear rates present in different sections of microparts was simulated via Moldflow (Autodesk). Results suggested that the distribution of maximum shear rates obeys an order of thin section > middle section > thick section (see *Section 5.4.4*). Thus, the development of microstructure in different sections of the microparts is primarily associated with the difference of shearing conditions.

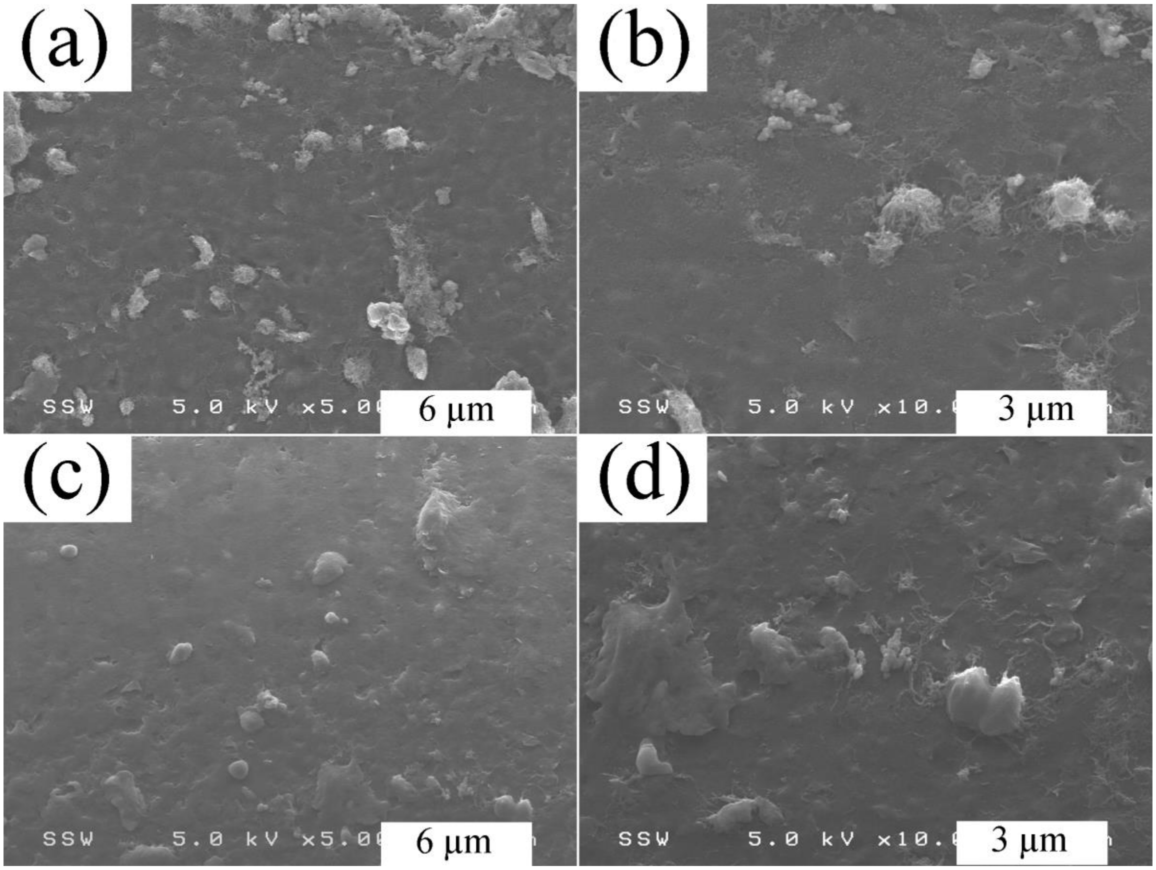

Figure 5.58 The morphology (FD) of the thin section in the core layer (a, b) and shear layer (c, d) of CNT2 microparts.

The microstructure at the transition area from the middle section to thin section of CNT2 microparts is given in Figure 5.59. It reveals that CNT aggregates and the individually dispersed CNT tend to preferentially align in the melt flow direction which is a result of ‘converging flow’ arising from the sharp reduction of mold cavity thickness from the middle section (0.5 mm) to thin section (0.2 mm), thereby leading to a rapid increase of shear rates. Obrzut et al. [335] reported that the applied shear fields would greatly affect the CNT network within the host polymer matrix and the p_c is dependent on the applied shear rate, i.e. the p_c increases with the applied shear rate. This could be ascribed to the preferential orientation of CNT along the shearing direction and subsequent shear induced deformation of CNT network. Therefore, the remarkable increase of shear rates along the FD is expected to affect the microstructure within different sections of PP/CNT microparts.

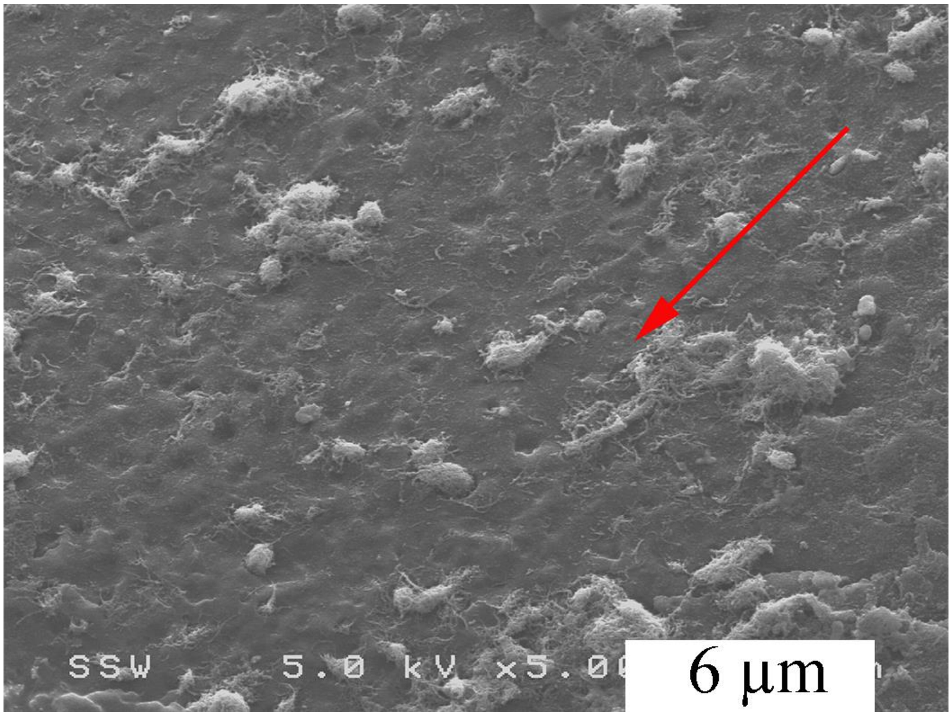

Figure 5.59 The morphology observed at the transition region from the middle section to the thin section of CNT2 microparts. Red arrow indicates the melt flow direction.

Figures 5.56 to 5.58 were taken from the journal International Polymer Processing, 33(4), 514-524 (2018), by S. Zhou, A.N. Hrymak, Musa R. Kamal, © Carl Hanser Verlag GmbH & Co.KG, Muenchen. As per the permission obtained from the publisher.

5.4.3.1.3 Microinjection molding of PP/GNP composites

As reported in the Figure 5.43, the p_c for compression molded PP/GNP composites falls in the range of 7 to 10 wt%. The plate-like structure of GNP particles makes it easier to align in the flow direction due to the high shear rates in μIM, which is unfavorable for random construction of 3D conductive network within PP, thereby affecting the σ of microparts. Table 5.13 shows that the σ for the thin section is out of the lower limit for the measurement range for the Keithley electrometer even at a filler concentration of 15 wt%, indicating that the formation of 3D conductive pathways within the PP is unlikely for GNP under severe shearing conditions. Normally, a higher loading concentration of GNP is required to achieve sufficient conductive pathways within PP. Kalaitzidou et al. [130] reported that the p_c for injection molded PP/GNP composites is near 7 vol%, namely 14.3 wt%. Moreover, the σ measured in the FD is always higher than that achieved in TD as per cut sections from the microparts, suggesting the preferential alignment of GNP along the melt flow direction. This will be further corroborated by following morphology observations.

Table 5.13 DC σ of both the thick and middle sections of GNP15 microparts measured across the TD and FD, respectively. At least five specimens were tested and StDev denotes standard deviation of the values of σ.

GNP15 microparts	TD (S/cm)	StDev (S/cm)	FD (S/cm)	StDev (S/cm)
Thick section	6.8E-8	2.9E-8	7.7E-6	4.1E-6
Middle section	1.2E-5	9.1E-6	2.6E-5	1.7E-5

Unlike the morphology observed for PP/CB and PP/CNT microparts, Figure 5.53(g) indicates that most of the GNP particles are discretely distributed, with possible stacking, within the thick section of PP/GNP counterparts. The distribution of GNP is quite uniform and there is no significant difference of the observed microstructure between the shear layer and core layer. Thus, a relatively higher GNP loading fraction is required to attain sufficient conductive pathways within the injection molded articles.

The microstructure of the middle section of GNP2 microparts is given in Figure 5.53(h). It seems that there is a larger fraction of GNP in the middle section when compared with that observed for the thick section counterpart (Figure 5.53g). In addition, the mean distance among the individually dispersed GNP is slightly shortened in the middle section, yielding a higher σ in the middle section than the thick section (Table 5.12). Thus, it is proposed that prevailing higher shearing effect in the middle section may cause a reduction of the particle size or disruption of GNP aggregates into smaller ones, which is advantageous to the enhancement of σ. For example, the obtained σ for the middle section across the TD is at least two orders of magnitudes higher than that of the thick section.

The morphology obtained along the FD for both the thick and middle sections of GNP2 microparts is shown in Figure 5.60. It can be seen from both Figures 5.60(a) and (b) that there is an obvious orientation of GNP particles in the shear layer when compared with that of core layer, reflecting the marked difference of shear rates present between the shear layer and core layer of injection molded articles. Moreover, the preferential orientation of GNP increases the probability of creating conductive pathways along melt flow direction, albeit the random distribution of GNP particles in the core layer. This could accordingly explain that the σ achieved in the FD is always higher than that in TD, as displayed in Table 5.12.

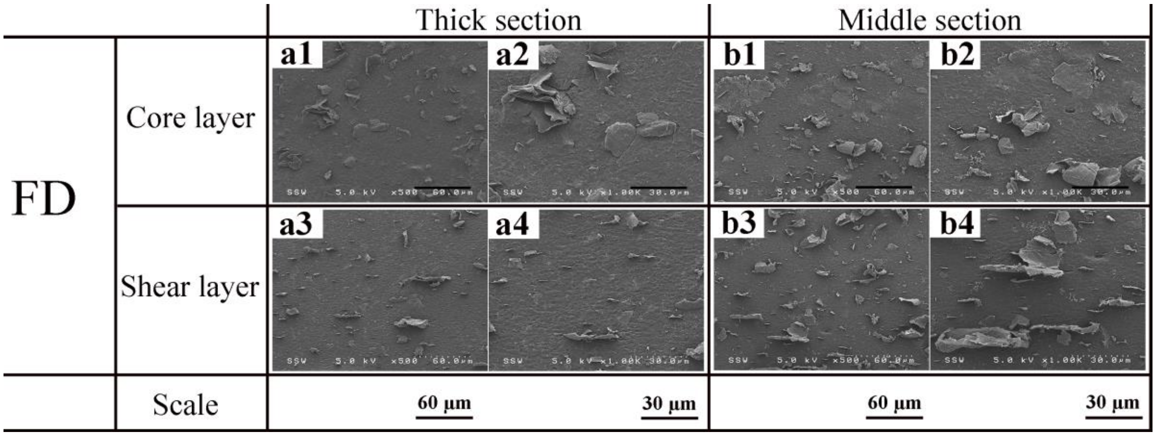

Figure 5.60 The morphology (FD) of the (a) thick and (b) middle sections observed in the core and shear layers of GNP2 microparts.

Figure 5.61 shows the microstructure of the thick section of the GNP5 microparts observed across the TD. Similarly, GNP has a uniform distribution within the host matrix. Although the mean distance between individually dispersed GNP decreases with an increase of filler content, a continuous 3D conductive network is hardly observed in the thick section, indicating that a higher GNP loading concentration is required for subsequent microparts when compared with that of CB or CNT filled systems. This is consistent with the σ measurements obtained from compression molded samples, as given in Figure 5.43.

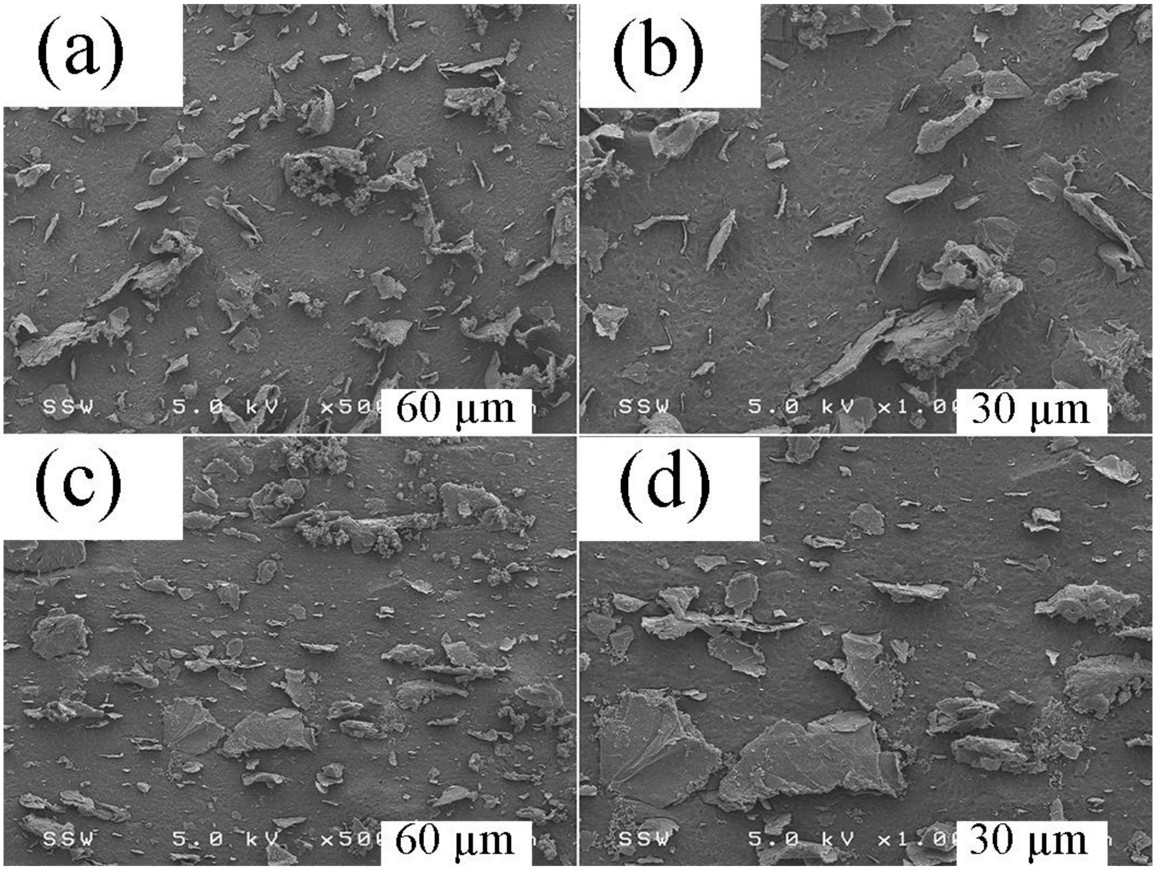

Figure 5.61 The morphology (TD) of the thick section in the core layer (a, b) and shear layer (c, d) of GNP5 microparts.

5.4.3.2 Microinjection molding of PP/graphite composites

The DC σ for each section of graphite filled PP microparts was determined with respect to measurement directions, which is displayed in Figure 5.62. The FD σ for the thin section is not measured because it was not feasible to place this section properly between the copper electrodes for the two-probe method. The FD σ for both the thick and middle sections of microparts is invariably higher than the TD σ of corresponding counterparts, indicating a role for the orientation of conductive fillers along the FD. A similar trend has been observed for their CNT-containing PP counterparts, as reported in *Section 5.1*.

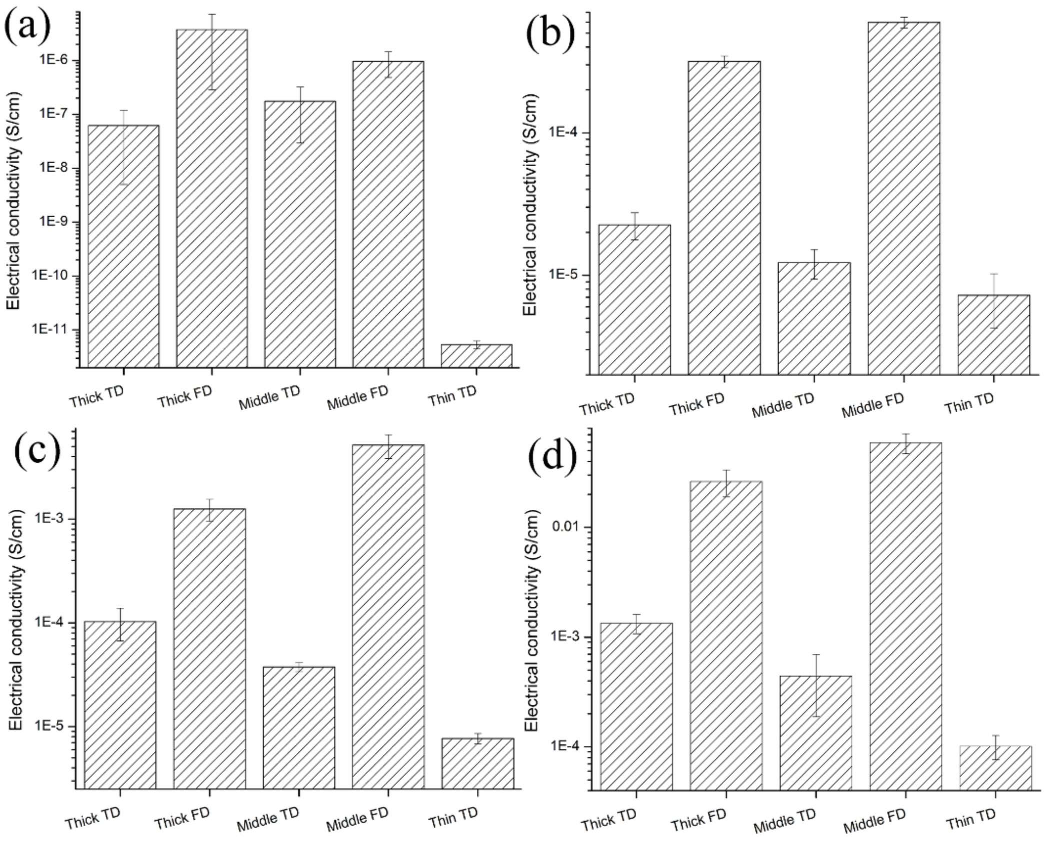

Figure 5.62 The σ for different sections of corresponding microparts with respect to the measurement directions, i.e. across the TD and along the FD, respectively. (a) SG30, (b) SG40, (c) SG50 and (d) LTEG30.

Generally, the values of σ increase with an incremental loading concentration of SG in PP, suggesting that the σ of subsequent moldings is related to the construction of conductive pathways within the host matrix. Interestingly, the trend of σ for each section of the SG30 microparts is different from that of high concentration (> 30 wt%) SG-loaded or LTEG30 counterparts, which could be related to the development of microstructure in each section of subsequent moldings. For example, the average TD σ for the middle section of the SG30 microparts, i.e. SG30 Middle, (1.75×10^{-7} S/cm) is slightly higher than that of SG30 Thick (6.23×10^{-8} S/cm); the average FD σ for SG30 Thick (3.74×10^{-6} S/cm), however, is relatively higher than that of SG30 Middle (9.67×10^{-7} S/cm). As per Figure 5.47, the p_c for compression molded PP/SG composites is about 30 wt%. It has been reported that the p_c for microinjection molded samples normally shifted to higher filler concentrations when compared with the samples prepared under less shearing effect, like compression molding

[101]. For example, Abbasi et al. [101] reported that the p_c for compression molded PP/CNT and PC/CNT composites is about 1 and 3 wt%, respectively. However, corresponding values for PP/CNT and PC/CNT microparts increased to 4 and 6 wt%, respectively. Thus, it could be inferred that the SG particles within PP would be insufficient to form conductive pathways when the filler concentration is 30 wt%. Moreover, Li and Shimizu [236] found that there would be an improved dispersion of fillers in the polymer matrix when they were processed under elevated shearing conditions. In this scenario, although direct contact among the added fillers is limited, the improved distribution of SG particles might facilitate the transport of electrons through the 'hopping' or 'tunneling' mechanism.

Enough conductive pathways could be formed with further increasing concentration of SG. Moreover, the preferential alignment of conductive particles would be beneficial to the enhancement of σ along the melt flow direction. For example, the FD σ for the SG50 Thick (1.25×10^{-3} S/cm) is approximately 2.5 times higher than that obtained from its compression molded counterpart (5.06×10^{-4} S/cm). In addition, the FD σ for SG50 Middle is about 4.2 times higher than the FD σ for the SG-50 Thick. The above observation could be attributed to the combined influence of the higher shearing conditions in μIM [12] and 'convergence' of the adopted mold cavities along the flow direction. Thus, there should be a sharp increase of maximum shear rates amid the stepped transition regions. As a result, it is likely to obtain a higher degree of filler orientation in the thinner section of the microparts arising from the increasing shearing conditions.

Moreover, there is a concurrent reduction of the TD σ along the melt flow direction of the stepped microparts, which could be related to the orientation of SG particles. It would be anticipated that there is a higher possibility of filler-filler interaction along the FD, whereas their ability to form an intact conductive network across the TD would be, to some degree, impaired, as given in Figures 5.62(b) and (c). A similar trend was also observed for LTEG-containing microparts, as shown in Figure 5.62(d). This indicates that sufficient conductive pathways could be constructed within the microparts when the LTEG concentration is 30 wt%, suggesting that less amount of LTEG is needed to attain sufficient conductive pathways within the molded samples. According to recent studies [47,102,109], the *in-situ* exfoliation of LTEG during melt blending process is essential to the formation of conductive network in subsequent blends. In addition, the average particle size for LTEG (about 180 μm) is larger than that of SG (nearly 20 μm). Therefore, less contact resistance would be expected in order to generate enough conductive pathways by physical connection between adjacent fillers. As a result, the addition of LTEG would significantly enhance the σ of subsequent moldings. Furthermore, the achieved σ for each section, with respect to measurement directions, of LTEG30 microparts is higher than that obtained from SG50 counterparts, implying that LTEG has a higher efficiency to create intact conductive pathways when compared with SG. Moreover, the higher σ for LTEG30 microparts could adequately fulfill requirements in certain applications, such as sensors, thermal and electrostatic dissipation [336].

Figure 5.62 shows that the TD σ for the thin section is invariably lower than that of their thick and middle section counterparts, signifying that the typical shearing conditions and thermomechanical history in the thin section is less favorable for the construction of 3D conductive pathways. Similarly, the TD σ for the thin section of CNT and CB filled PP microparts was lower than respective value of their thick and middle section counterparts. Additionally, Pan et al. [194] reported that the cooling time drops substantially with a reduction of the mold cavity thickness. Thus, it would be anticipated that the generated structure in the thin section (0.2 mm) would instantly ‘freeze’ and have little chance of returning to a random orientation. In this scenario, the TD σ for the thin section of subsequent microparts could be significantly reduced due to lack of sufficient conductive pathways.

The high shearing conditions and large thermal gradients present in μIM would determine the development of microstructure in microparts, which is crucial to the enhancement of σ. Therefore, the microstructure of corresponding microparts was characterized using a high-resolution SEM. Figure 5.63 shows the morphology for both the thick and middle sections of SG-containing microparts. The presence of SG particles within the host polymer is pointed out by black arrows. Figures 5.63(a) and (b) exhibit the microstructure of the thick and middle sections of SG30 microparts, respectively. Figure 5.63(a) shows that the SG particles are somewhat randomly dispersed in the thick section whereas SG particles have a higher tendency to align in one specific direction, i.e. along flow direction, in the middle section, as displayed in Figure 5.63(b). This could be attributed to the plate-like structure of SG particles and the difference of maximum shear rate that prevails in different sections of the stepped microparts. For SG50 microparts, SG particles have a relatively uniform distribution in either the thick section (Figure 5.63c) or middle section (Figure 5.63d). In addition, sufficient conductive pathways could be constructed at such a high concentration, i.e. 50 wt% SG. Besides, the shear induced orientation of SG particles in μIM is favorable for the enhancement of σ along the FD. For example, the FD σ for SG50 Thick (1.25×10^{-3} S/cm) is approximately 2.5 times higher than that of compression molded counterparts. Meanwhile, the preferred alignment of SG particles along the FD would, to some extent, limit or impair the network formation across TD. It has been reported that the maximum shear rate present in μIM is a few orders of magnitude higher than that in compression molding process [12]. Thus, the σ for compression molded SG50 (5.06×10^{-4} S/cm) samples is higher than that of the TD σ for SG50 Thick (1.03×10^{-4} S/cm).

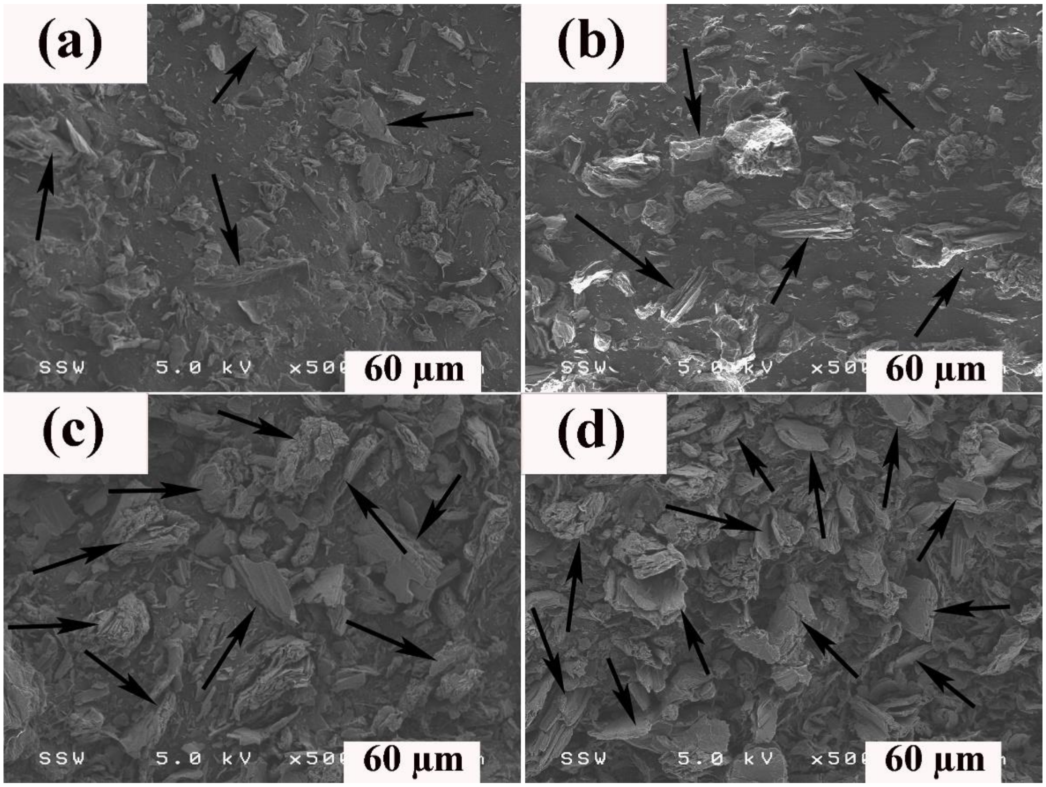

Figure 5.63 SEM images of the (a) SG30 Thick, (b) SG30 Middle, (c) SG50 Thick and (d) SG50 Middle.

The characterization of LTEG is given in Figure 5.64. Figure 5.64(b) displays the expanded volume of 0.5 g LTEG after a thermal treatment at 190°C for 10 min using a conventional oven (Binder, ED 115, Germany). The expanded volume measured by a graduated cylinder was about 7 mL/g, indicating that the intercalated agents could easily escape from stacked graphite flakes of LTEG. In addition, the *in situ* expansion of LTEG during processing has been reported to be crucial to the enhancement of thermal conductivity for HDPE [102] and PA6 [47].

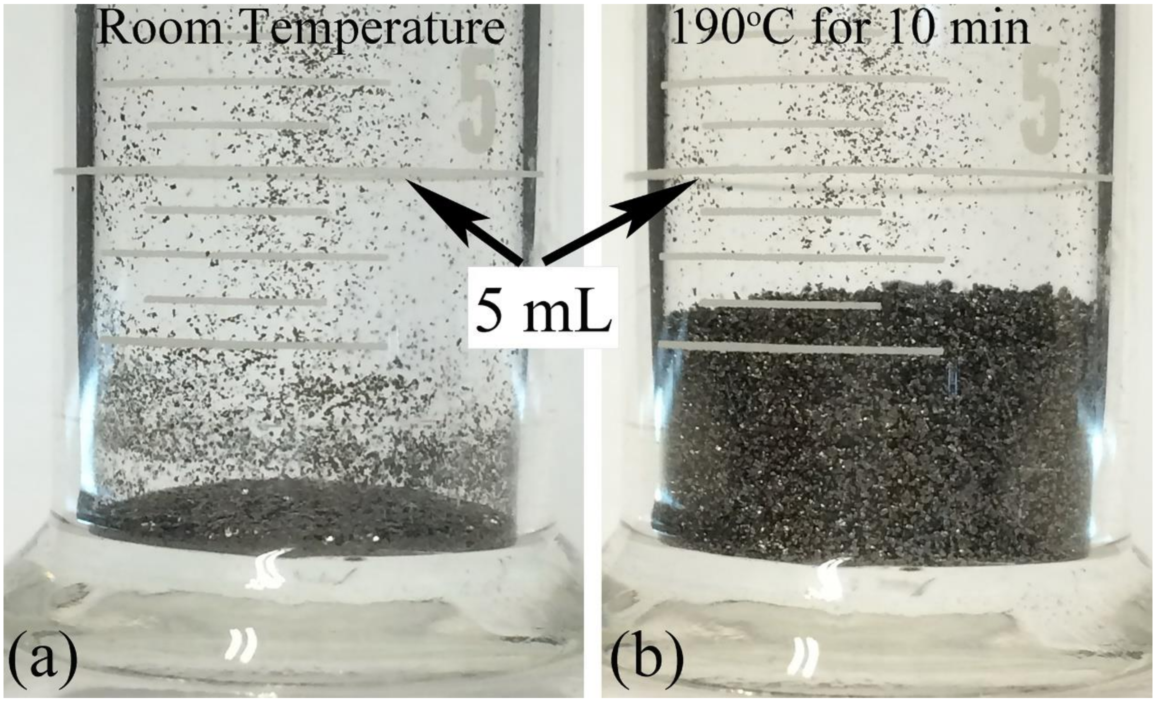

Figure 5.64 The images of 0.5 g (a) pristine LTEG, and (b) expanded LTEG after thermal shock at 190°C for 10 min.

The development of microstructure in different sections of LTEG30 microparts is given in Figure 5.65. Sufficient conductive pathways would be formed within the microparts due to the large particle size and *in situ* expansion of LTEG during melt processing.

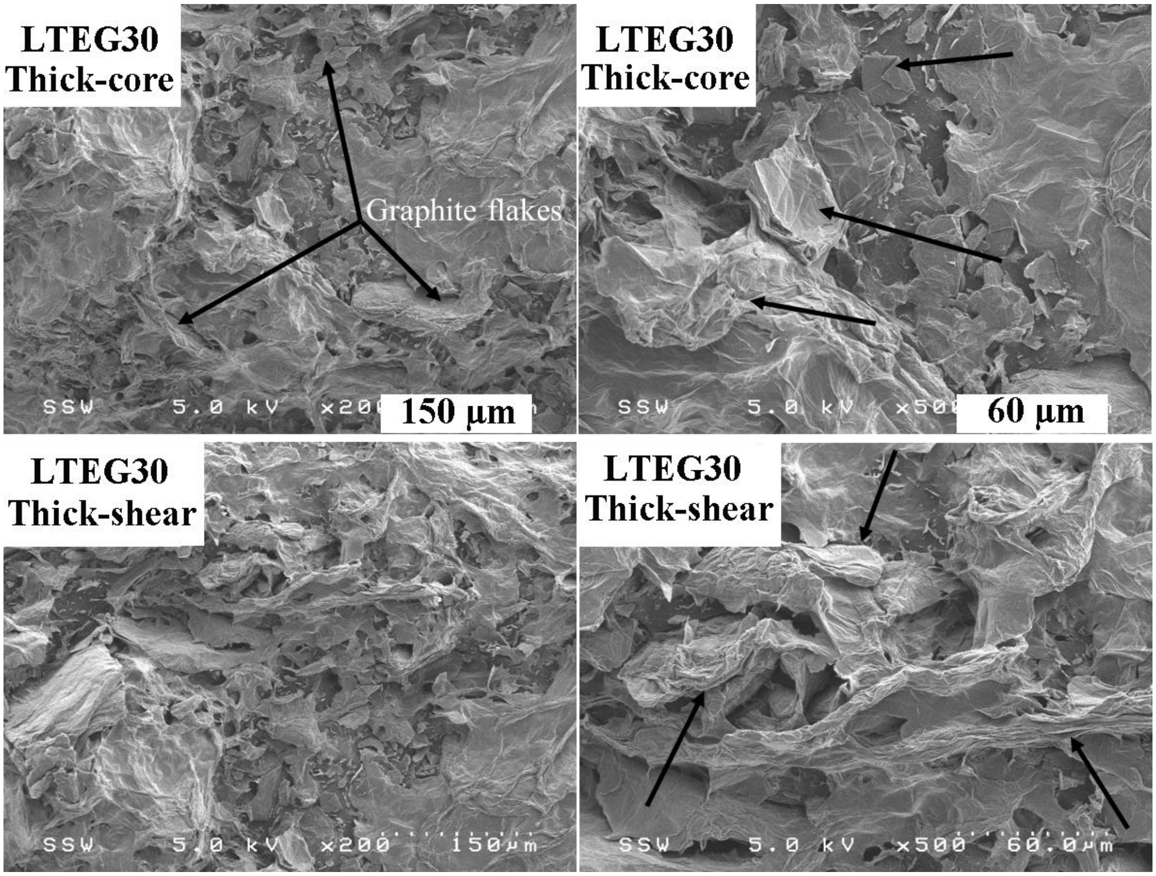

Figure 5.65 The microstructure of the thick section of LTEG30 microparts.

5.4.4 Simulation (Moldflow)

As per *Section 4.5.6*, the simulation software package, Autodesk Moldflow Synergy 2016, was used to assess the maximum shear rates in µIM of PP/carbon microparts. Figures 5.66(a) and (b) exhibit that the distribution of shear rates follows an increasing trend along the melt flow direction, from the thick section to thin section, of microparts. This could be attributed to, on one hand, the step reduction of mold cavity thickness; on the other hand, the applied process parameters such as melt temperature, mold temperature and injection velocity are always set at higher values when compared with those of CIM process. The distribution of maximum shear rates as a function of distance across the TD with respect to each section of resultant microparts is shown in Figure 5.66(b). It is apparent that the highest shear rates for each section occur near the shear layer of subsequent microparts.

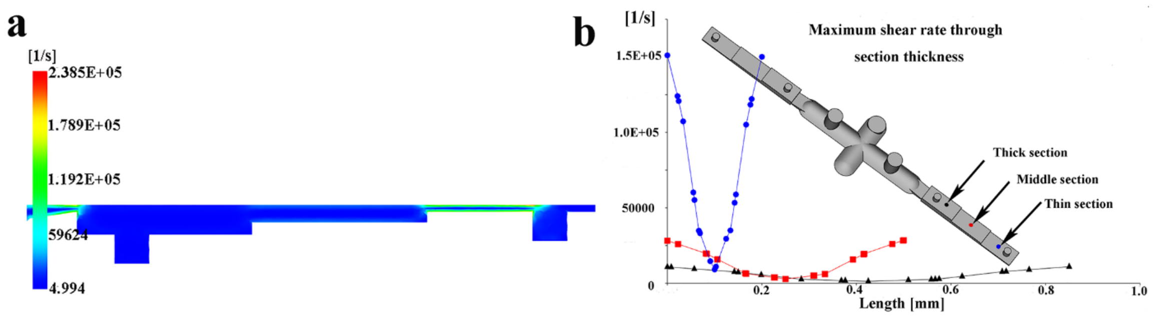

Figure 5.66 The distribution of maximum shear rates (Moldflow) along the flow direction and (b) the probe plot of maximum shear rate as a function of distance across the TD.

5.4.5 Summary

A series of PP composites containing different types of carbon fillers (CB, CNT, GNP and graphite) were prepared by melt blending. Nanocomposite preparation was followed by compression molding and μIM processes, respectively. The volume electrical conductivity of resultant moldings was determined using a two-probe method. Results indicated that the percolation threshold for the microparts is invariably higher than their compression molded counterparts, which is largely attributed to the severe shearing conditions that prevail in μIM process. The development of microstructure in PP is strongly dependent on the applied shearing conditions and the types of carbon fillers. We found that CB and CNT are more effective in enhancing the electrical conductivity of microparts when compared with GNP filled systems. The enhancement of electrical conductivity for microparts is closely related to the development of internal microstructure. A ‘grape’ like structure was observed in the PP/CB microparts which is advantageous to the formation of conductive pathways, thereby yielding higher electrical conductivity. In addition, a conductive network could be constructed in the PP/CNT microparts since individually dispersed CNT functions as a ‘bridge’ between discretely distributed CNT aggregates, thereby facilitating the transport of electrons. However, such morphology is hardly observed in compression molded PP/GNP samples or subsequent microparts. As a result, very high GNP concentrations are generally required to attain sufficient conductive pathways within GNP-containing moldings. Moreover, LTEG is superior to SG in terms of enhancing the electrical conductivity of PP which is attributed to its large particle size and *in situ* expansion nature.

To conclude, the morphology and intrinsic properties of different carbonaceous fillers significantly influence the electrical and morphological properties of subsequent moldings.

5.5 The influence of hybrid carbon filler loading

The effect of hybrid carbon fillers of CNT and CB on the electrical and morphological properties of PS composites were systematically studied in μIM. The polymer composites with three different filler concentrations (i.e. 3, 5 and 10 wt%) at various weight ratios of CNT/CB (100/0, 30/70, 50/50, 70/30, 0/100) were fabricated by melt blending, followed by μIM under a defined set of processing conditions. A rectangular mold insert which has three consecutive zones with decreasing thickness along the flow direction was adopted to evaluate the abrupt changes in mold geometry on the properties of subsequent microparts. The distribution of carbon fillers within microparts was investigated by morphology observations, which was correlated with the electrical conductivity measurements. Results suggested that there is a flow-induced orientation of incorporated carbon fillers and this orientation increased with increasing shearing effect along the melt flow direction. High structure CB is found to be more effective than CNT in terms of enhancing the electrical conductivity, which was attributed to the good distribution of CB in PS and their ability to form conductive networks via self-assembly. Morphology observations indicated that there is a shear-induced depletion of CB particles in the shear layer, which is due to the marked difference of shear rates between the shear and core layers of the microparts. Moreover, an annealing treatment is beneficial to enhance the electrical conductivity of CNT-containing microparts.

5.5.1 Electrical conductivity

The DC σ for both the thick and middle sections of corresponding microparts with respect to the measurement directions is displayed in Figure 5.67. The FD σ for each section of the microparts is higher than that measured across the TD, which is indicative of preferred orientation of carbon fillers along the FD, arising from the predominant shearing effect that prevails in the injection molding process [334]. Furthermore, it should be kept in mind that in addition to the stepped decrease in thickness of the mold cavities along the FD, the adopted molding parameters, such as melt and mold temperatures as well as injection velocity, are higher than those encountered in CIM. As a result, the shear rate generated in μIM is at least two orders of magnitude higher than that in CIM [13], which is accountable for preferential alignment of carbon fillers in microparts [12]. For instance, Abbasi et al.

[12] reported that the p_c for PC/CNT microparts shifted to higher filler concentrations when compared with that of compression molded or CIM macroparts. Meanwhile, the preferred orientation of carbon fillers along the FD would be detrimental to the random formation of conductive pathways across the TD within host matrix. Therefore, the TD σ for the middle section of microparts is lower than their thick section counterparts, at a specific filler concentration. For instance, the TD σ for the middle section of PS/CB 3 wt% microparts is beyond the lower limit of the measurement scale for Keithley 6514 electrometer, whereas the TD σ for their thick section counterparts is about 5.12×10^{-11} S/cm.

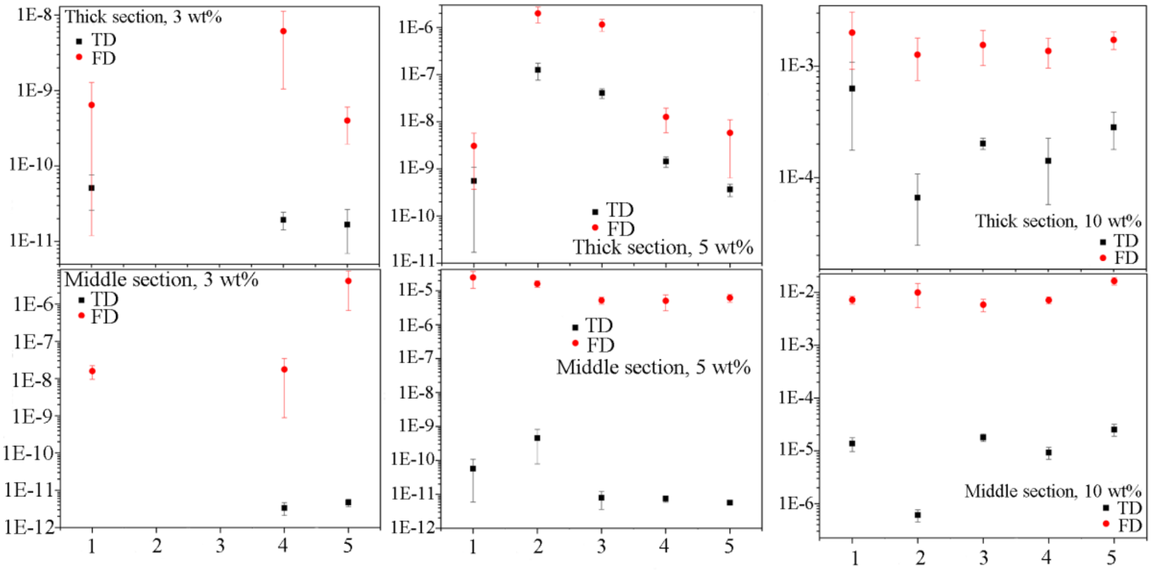

Figure 5.67 The electrical conductivity for each section of the microparts molded from hybrid carbon filled PS composites. All measurements were conducted with respect to the TD and FD, respectively. Where, 1-PS/CB; 2-PS/CNT; 3-PS/CB(30)/CNT(70); 4-PS/CB(50)/CNT(50); 5-PS/CB(70)/CNT(30).

In addition, it is worth mentioning that the σ for either the thick section or middle section of PS/CNT 3 wt% microparts is beyond the lower limit of the measurement scale for Keithley 6514 electrometer, indicating a lack of conductive pathways. The finding is consistent with the results reported by Arjmand et al. [281] where the authors reported that the p_c for PS/CNT composites is about 5 wt% in CIM. Thus, the prevailing shearing effect in µIM would largely limit the possibility of CNT-CNT contact in the microparts. However, the values of σ for both sections of PS/CB 3 wt% microparts are measurable except that the TD σ for the middle section is out of the lower limit of the measurement scale for Keithley 6514 electrometer. Thus, the above description indicated that despite the high aspect ratio and intrinsically high electrical conductivity of CNT [89], the state of distribution of the added fillers plays a significant role in determining the σ of subsequent polymer composites [337], Additionally, the ratio of FD σ to TD σ, i.e. $(FD/TD)_{\sigma}$, for the middle section of microparts is invariably higher than that of the thick section counterparts (see Table 5.14), confirming that the increasing shearing effect would facilitate filler orientation along the flow direction. Therefore, the values of $(FD/TD)_{\sigma}$ can be used as an indicator to assess the degree of filler orientation in the injection molded CPCs.

Moreover, the values of $(FD/TD)_{\sigma}$ decrease with an incremental loading concentration of added fillers, indicating that the difference between the TD σ and FD σ is reduced with increasing filler concentrations. According to this scenario, there would be a higher possibility to form sufficient conductive pathways within subsequent moldings at higher filler concentrations, regardless of the shear-induced orientation of incorporated fillers along the predominant flow direction. Besides, the trend of decreasing ratio of $(FD/TD)_{\sigma}$ with an increase of filler concentration is generally applicable to either only CNT or hybrid carbon fillers (regardless of the weight ratio of CNT/CB) loaded PS microparts.

Table 5.14 The ratio of $(FD/TD)_{\sigma}$ for both the thick and middle sections of PS/CB microparts.

Sample	$(FD/TD)_{\sigma}$	
	Thick section	Middle section
PS/CB 3 wt%	12.6	N/A
PS/CB 5 wt%	5.6	4.3×10^{5}
PS/CB 10 wt%	3.2	527

Similar to PS/CNT 3 wt% microparts, the values of σ for both the thick and middle sections of 3 wt%-PS/CNT70/CB30 microparts cannot be detected using the Keithley electrometer due to insufficient conductive pathways, however, corresponding values could be detected for the other combinations of hybrid carbon fillers loaded PS systems (at the same total filler concentration, i.e. 3 wt%) where CB occupies a relatively higher weight fraction, suggesting that high structure CB is more effective than CNT in enhancing the σ of subsequent moldings. In this scenario, the polymer-filler interfacial interaction might be an influencing factor. According to Clingerman et al. [338], a lower interfacial tension between polymer matrix and fillers promotes better wettability of polymer chains with the added fillers, thereby leading to an improved dispersion of carbon fillers in the host matrix. Consequently, the improved dispersion of conductive fillers would, in turn, increase the p_c of CPCs [339].

The values of surface tension of PS, CB and CNT, and the interfacial tension between PS and different carbon fillers at 260°C are tabulated in Table 5.15. The interfacial tension between the polymer-filler pair was calculated using the following Wu's harmonic mean average equation [340].

$$\gamma_{12} = \gamma_1 + \gamma_2 - 4\left(\frac{\gamma_1^d \gamma_2^d}{\gamma_1^d + \gamma_2^d} - \frac{\gamma_1^p \gamma_2^p}{\gamma_1^p + \gamma_2^p} \right)$$

where, γ_{12} is the interfacial tension between component 1 and component 2; γ_i is the value of surface tension of component *i*, which equals to $\gamma_i^d + \gamma_i^p$. Moreover, γ_i^d and γ_i^p are the dispersion part and the polar part of surface tension of the *i*th component, respectively.

Table 5.15 reveals that the interfacial tension of PS/CB pair is lower than that of PS/CNT pair, indicating that the polymer chains could easily wet the surface of CB particles, which leads to an improved distribution of CB in PS. The improved distribution of CB particles explains the fact that although a direct contact of conductive fillers is unlikely at a lower total filler concentration (e.g. 3 wt%) [281], it allows free passage of electrons though the 'tunneling' or 'hopping' mechanism in the host matrix. It is thus not surprising that the values of σ for both the thick and middle sections of microparts molded from 3 wt%-PS/CNT70/CB30 and PS/CNT 3 wt% composites are not detectable due to a lack of sufficient conductive pathways, regardless of the measurement directions. Additionally, a typical synergistic effect of hybrid carbon fillers on the σ for both the thick and middle sections of 3 wt%-PS/CNT50/CB50 microparts is discernible since the values of σ for 3 wt%-PS/CNT50/CB50 microparts are generally superior to those of PS/CNT 3 wt% or PS/CB 3 wt% counterparts. In this scenario, it could be deduced that the co-existence of CB particles with CNT facilitates the formation of conductive network within PS.

Table 5.15 Surface tension of pure components and interfacial tension of PS/filler pair.

	γ	γ_i^d	γ_i^p	γ_{12}
	mN/m	mN/m	mN/m	mN/m
PS[a)]	23.44	23.272	0.168	
CB[b)]	21.77	19.59	2.18	
CNT[c)]	27.8	17.6	10.2	
PS/CB				3.29
PS/CNT				11.82

[a)] From reference [270]; [b)] From reference [338]; [c)] From reference [273].

When the total carbon filler concentration is increased to 5 wt%, it is expected that enough conductive pathways could be constructed by CNT in PS because the σ for PS/CNT 5 wt% microparts is always higher than that of PS/CB 5 wt% counterparts, as shown in Figure 5.67. However, no synergistic effect of CNT and CB on the σ of subsequent microparts is detected since the σ for the thick section of hybrid filler-containing microparts is normally within the range of PS/CB 5 wt% (lower bound) and PS/CNT 5 wt% (upper bound) counterparts, whereas the σ for the middle section is invariably lower than that of PS/CB 5 wt% or PS/CNT 5 wt% counterparts, regardless of the measurement directions. Moreover, the σ for either section of the PS/CNT/CB microparts increases with an incremental loading fraction of CNT, revealing that the presence of CNT is favorable for the formation of conductive pathways. For example, the FD σ and TD σ for the thick section increase from 5.81×10^{-9} (5 wt%-PS/CNT30/CB70) to 1.16×10^{-6} S/cm (5 wt%-PS/CNT70/CB30) and from 3.66×10^{-10} (5 wt%-PS/CNT30/CB70) to 4.05×10^{-8} S/cm (5 wt%-PS/CNT70/CB30), respectively. A monotonic increase of FD σ for the thick section is attributed to the favored alignment of CNT along the FD since more conductive pathways could be constructed with an increasing weight fraction of nanotubes. Also, a concurrent increase of the TD σ for the thick section is ascribed to the spatial distribution of CNT across the TD, thereby facilitating the formation of conductive pathways, albeit the favored orientation of CNT along FD. Furthermore, more filler orientation in the middle section is expected with an increase of shear rates, arising from a sharp reduction of mold cavity thickness, from 0.85 (thick section) to 0.50 mm (middle section). As a result, the FD σ for the middle section is higher than that of its thick section counterpart whereas the TD σ for the thick section is invariably higher than that of the middle section. Similarly, such trend also applies to microparts which have a total carbon filler concentration of 10 wt%, in which cases sufficient conductive pathways can be constructed. In addition, Table 5.16 shows that the presence of CB is beneficial to the enhancement of σ for subsequent microparts, which could be ascribed to the uniform distribution of CB within the host polymer.

Table 5.16 The σ for the thick section of 10 wt% carbon fillers loaded PS microparts.

Sample	Thick-TD ($\times10^{-5}$ S/cm)	Thick-FD ($\times10^{-5}$ S/cm)
PS/CNT 10 wt%	6.59	127
10 wt%-PS/CNT70/CB30	20.2	155
10 wt%-PS/CNT50/CB50	14.1	137
10 wt%-PS/CNT30/CB70	28.2	172
PS/CB 10 wt%	62.9	201

Based on the range of total carbon filler concentrations studied, no obvious synergistic effect of hybrid loading of CNT and CB on the enhancement of σ for PS microparts was detected. According to a review by Szeluga et al. [341], hybrid carbon fillers loading of CNT and CB does not always guarantee a synergy in enhancing the σ of subsequent polymer composites. On the one hand, the weight ratio of carbon nanofillers in the hybrid mixture is crucial to determining the properties of subsequent polymer composites, such as the mechanical properties, thermal and electrical conductivities [341]. On the other hand, the interaction between polymer matrix and carbon nanofillers or the quality of dispersion of conductive particles may play a role in constructing co-supportive conductive pathways since a synergistic enhancement of σ was typically observed for semi-crystalline polymer, e.g. PP [342] and epoxy-based composites [89,343,344]. As reported in *Section 5.2*, the intrinsic properties of polymer matrix can determine the state of distribution of added CNTs, thereby affecting the σ of subsequent moldings. Thus, a thorough investigation on the influence of intrinsic properties of the host polymers on the properties of hybrid carbon nanofillers (i.e. CNT/CB) loaded systems would be helpful to elucidate this phenomenon.

Overall, the synergistic enhancement of σ could be achieved in PS microparts when the total carbon fillers concentration is 3 wt% wherein the CB and CNT have equivalent weight fractions. In addition, the middle section of both 3-PS-NT30 and 10-PS-NT30 microparts showed a synergy in terms of enhancing the σ when compared with other filler-containing counterparts. However, such synergistic effect was absent at higher filler concentrations and the σ of subsequent microparts tends to increase with increasing weight fractions of CNT and CB when the total filler concentration is 5 and 10 wt%, respectively.

5.5.2 The effect of annealing treatment

To study the effect of annealing on the σ of subsequent micromoldings, microparts molded from 10 wt% carbon filled composites were subjected to a thermal treatment at 100°C for 2h under vacuum. Figure 5.68 indicates that the TD σ for the thick section of PS/CB 10 wt% microparts decreased significantly after the annealing treatment. Two possible mechanisms are proposed to explain the annealing-induced decrease of σ for only CB-containing PS microparts: *(1)* the very high shear rate and large temperature gradients during μIM could largely induce a preferred orientation of polymer chains and the added fillers along the flow direction. Thus, the rapid solidification of generated structure has little chance of returning to a random orientation. The mobility of polymer chains could be greatly enhanced during the annealing treatment, which leads to a relaxation of orientated polymer chains to random coils [345]. In addition, since the adopted CB has a relatively high surface area (about 1400 m^2/g), the dispersed CB particles have a greater tendency to form segregated aggregates, which could disrupt conductive pathways within the polymer matrix. *(2)* Since the mobility of polymer chains can be greatly improved at higher temperatures, more macromolecular chains are likely to migrate to the surface of CB due to the good wettability of PS with CB. Moreover, the high surface area of CB could be a contributing factor because a certain amount of polymer chains is required to wet the outer surface of CB particles. A similar downward trend of σ with temperature was reported by Liang and Tjong [345] in a carbon nanofiber (CNF) filled PS system. The authors proposed that increased mobility of polymer chains at higher temperatures would interrupt the formation of conductive network, thereby increasing the resistivity of samples [345]. As a result, the annealing treatment is detrimental to only CB-containing samples.

Unlike PS/CB 10 wt% microparts, the TD σ for the thick section of only CNT or hybrid carbon fillers loaded PS counterparts increased after the annealing treatment. For example, the TD σ for thick section of 10 wt%-PS/CNT50/CB50 microparts increased from 1.41×10^{-4} to 4.86×10^{-4} S/cm after the annealing treatment. The annealing-induced enhancement of σ can be explained as follows: as described previously, there would be a preferential orientation of carbon fillers along the melt flow direction arising from the predominant shearing effect and rapid solidification of products in μIM. As a result, the residual stress and strain will exist in the interfacial polymer phases amid the added fillers [235]. However, this is not a thermodynamically-favored state, and the frozen-in polymer chains as well as orientated structure have a great tendency to reorder or rearrange themselves to a random orientation, provided that the polymer chains gain a certain degree of mobility. In addition, the presence of surrounding insulating polymers would increase the contact resistance and limit the possibility to construct conductive pathways through direct connection of carbon fillers, thereby impairing the enhancement of σ. Li et al. [262] proposed the annealing treatment could relieve the residual stress and strain that exists in the interfacial polymers between the added fillers thanks to the increased mobility of polymer chains. As a result, the mean distance between adjacent CNTs decreased slightly with an increase of the annealing temperature [262], which in turn leads to a reduction of the ‘tunneling’ resistance, thereby contributing to the enhancement of σ. Moreover, the increased mobility of polymer chains promotes secondary agglomeration of CNT (e.g. loosely packed CNT network) [150,346], which is advantageous to the enhancement of σ for subsequent moldings. Interestingly, a significant increase of the TD σ was observed for the thick section of 10 wt%-PS/CNT50/CB50 microparts where the CB and CNT have equivalent weight fraction in PS, i.e. 5 wt%, respectively. As mentioned previously, conductive pathways could be formed in either only CB- or CNT-containing PS microparts at 5 wt%. Thus, it is reasonable to suggest that the synergistic effect of hybrid carbon fillers on the enhancement of σ arises from the formation of CB aggregates and the restoration of loosely packed CNT network within host matrix after the annealing treatment.

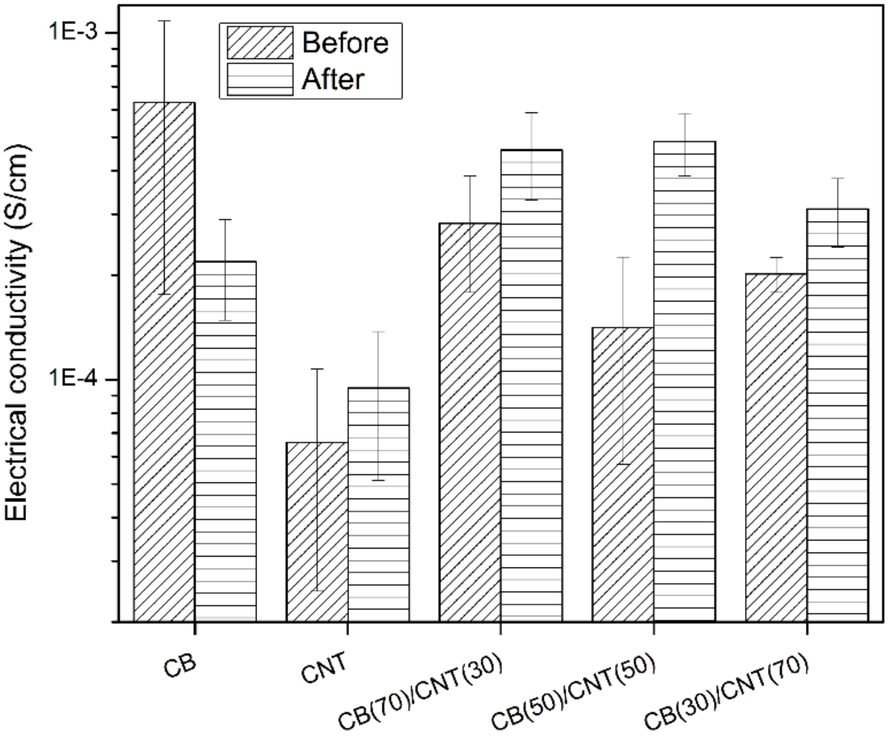

Figure 5.68 The TD electrical conductivity for the thick section of different combinations of carbon fillers (i.e. CB/CNT) loaded PS microparts. Results were collected from samples before and after annealing treatment at 100°C for 2h.

5.5.3 Morphology

The cross-section microstructure of the thick section of PS/CB 5 wt% microparts is given in Figure 5.69. Figures 5.69(a) and (b) indicate that the CB particles have a relatively uniform distribution in the core layer of the thick section, in the form of small aggregates or chain-like structure, suggesting that high structure CB particles could form a random conductive network via self-assembly even under very high shearing conditions, which is beneficial to the enhancement of σ. A similar phenomenon was observed by Yui et al. [347]

in CIM PP/HDPE/CB macroparts. However, despite the uniform distribution of CB aggregates in the shear layer, there are some regions devoid of CB particles and shear-induced depletion of CB particles could be the contributing factor. For example, Jana [348] reported that the loss of surface and volume σ in conductive polymer composites could be ascribed to the shear-induced migration of conductive fillers during mold filling process in injection molding. In addition, Hong et al. [280] reported that the migration of conductive fillers became severe with an increase of shearing conditions. Jiang et al. [13] pointed out that shear rates as high as 10^6/s are not rare in μIM. Moreover, the shear layer exhibits a higher shear rate relative to that of the core layer (as shown in *Section 5.4.4*). Thus, shear-induced migration of CB particles would become more significant in the shear layer, as shown in Figure 5.69(d).

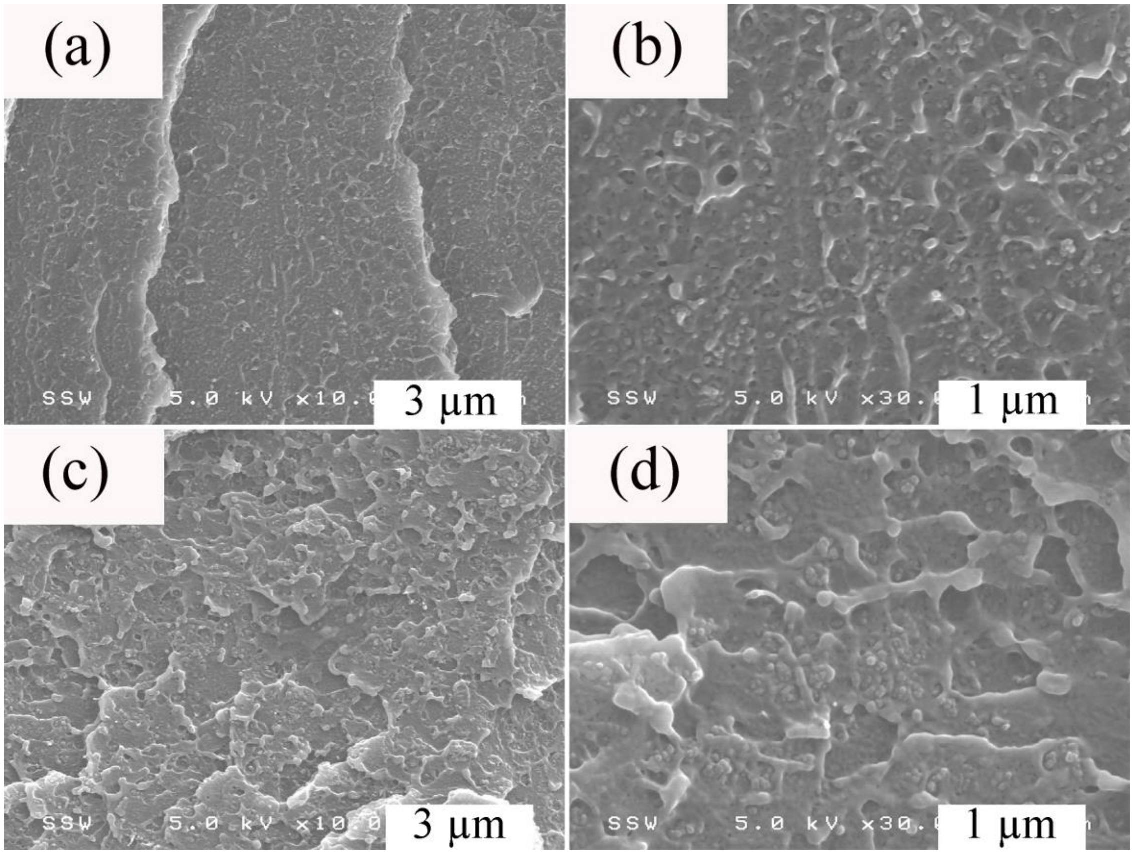

Figure 5.69 The morphology (TD) taken from the (a, b) core layer and (c, d) shear layer of the thick section of PS/CB 5 wt% microparts.

The cross-section morphology of the thick section of PS/CNT 5 wt% microparts is given in Figure 5.70. Figure 5.70 indicates that CNT has a relatively uniform distribution across the TD of the thick section. Moreover, CNT agglomerates seem to be absent from the thick section across the TD and no obvious shear-induced depletion effect on CNT-containing counterparts is observed in the shear layer. This suggests that there exists a good wettability between PS macromolecular chains and the surface of nanotubes, which leads to a good distribution of CNT in the host matrix [274]. In addition, the particle size may play a role when it comes to shear-induced migration phenomenon. For example, unlike CB particles, the adopted CNT has a very high aspect ratio (>1000). Thus, the shear-induced depletion effect would be insignificant in terms of the particle size of CNT and rapid mold filling process in μIM.

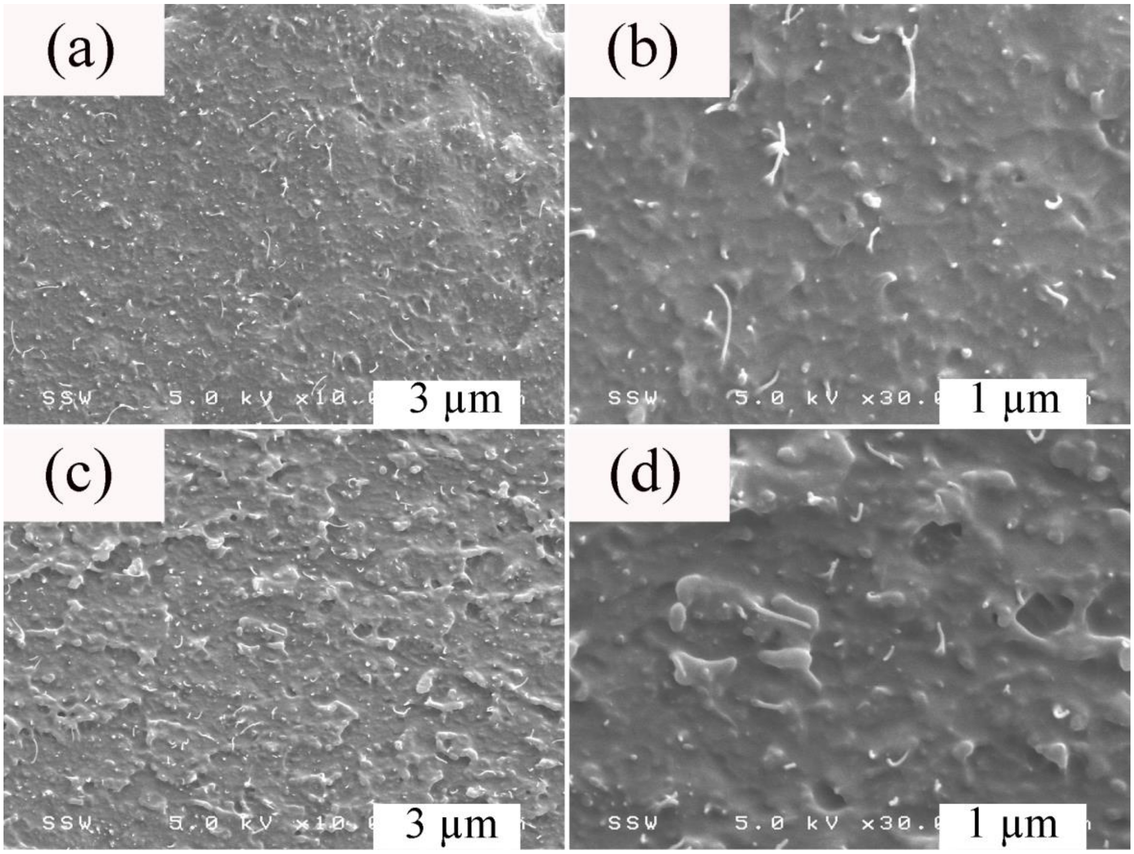

Figure 5.70 The morphology (TD) taken from the (a, b) core layer and (c, d) shear layer of the thick section of PS/CNT 5 wt% microparts.

The cross-section morphology for the thick section of 5 wt%-PS/CNT50/CB50 microparts prior to annealing treatment is displayed in Figure 5.71. Figure 5.71 indicates that both the CNT and CB have a relatively uniform distribution across the TD. The existence of CNT agglomerates could be detected in the core layer of the microparts, which have been labeled in black contours, as shown in Figure 5.71(a). However, discretely dispersed CB and CNT would be unfavorable for effective construction of conductive pathways within subsequent microparts [349]. For example, Wu et al. [349] proposed that the co-existence of two independent phases, namely the main particle phase (i.e. CB aggregates) and the bridge phase (individually dispersed CNT or CNT agglomerates) is unfavorable for the overall enhancement of σ. As a result, the σ for 5 wt%-PS/CNT50/CB50 microparts is somewhat lower than that of the only CNT-containing counterparts, as displayed in Figure 5.67.

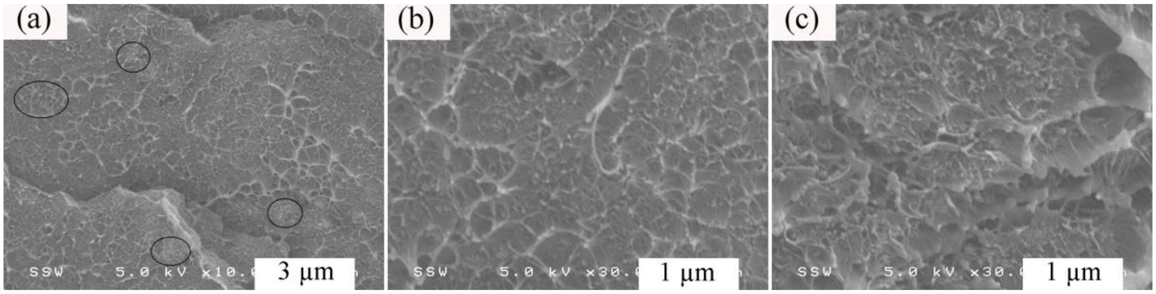

Figure 5.71 The morphology (TD) taken from the (a, b) core and (c) shear layers of the thick section of 5 wt%-PS/CNT50/CB50 microparts prior to the annealing treatment.

The cross-section morphology for the thick section of 5 wt%-PS/CNT50/CB50 microparts after the annealing treatment is given in Figure 5.72. Similar to Figure 5.71, both CB and CNT have a relatively uniform distribution in the PS. In addition, despite the presence of individually dispersed CB and CNT, it seems that the annealing treatment could promote secondary agglomeration of CNT [150] and the formation of CB aggregates in the host matrix [350], which are responsible for the enhancement of σ [147]. As a result, the TD σ for the thick section of 10 wt%-PS/CNT50/CB50 microparts after the annealing treatment is 3.45 times higher than that obtained from their counterparts prior to annealing treatment, as displayed in Figure 5.68.

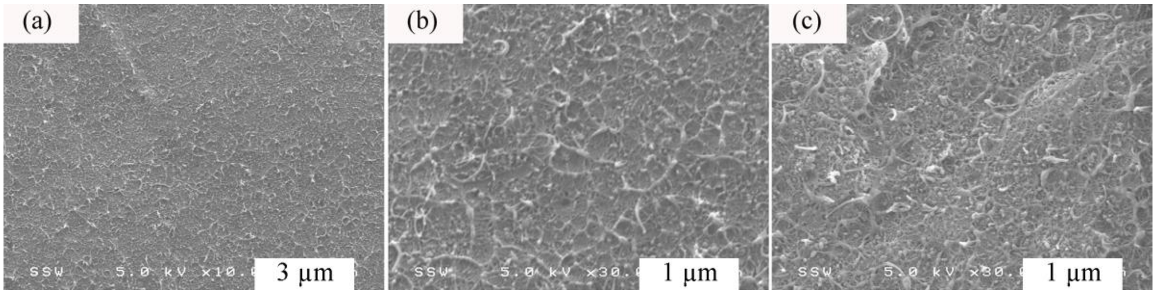

Figure 5.72 The morphology (TD) taken from the (a, b) core and (c) shear layers of the thick section of 5 wt%-PS/CNT50/CB50 microparts after the annealing treatment.

5.5.4 Summary

A series of hybrid fillers of CNT and CB loaded PS composites were prepared by melt blending. The weight ratio of CNT/CB was systematically altered at the same total filler concentrations, i.e. 3, 5 and 10 wt%. Afterwards, the obtained blends were subjected to μIM under a defined set of molding conditions. The distribution of carbon fillers within the microparts was evaluated by a combination of electrical conductivity measurements and SEM observations. Results indicated that both the CB and CNT have a relatively uniform distribution within PS. Although there is a shear-induced depletion effect in the shear layer of CB-containing microparts, the electrical conductivity measurements suggested that high structure CB has a greater tendency to form conductive pathways within the microparts via self-assembly even under very high shearing conditions of μIM. In this study, however, no obvious synergistic effect of hybrid fillers on the construction of conductive pathways is detected, which is thought to be crucial to the enhancement of electrical conductivity for conductive polymer composites [351]. Further studies regarding the effect of intrinsic properties of polymer matrices on hybrid carbon fillers (i.e. CNT/CB) loaded composites might be helpful to elucidate this phenomenon. Furthermore, the influence of annealing treatment on the electrical and morphological properties of as-molded microparts which have identical total filler concentration, i.e. 10 wt%, at various weight ratio of CNT/CB combinations was investigated as well. Results revealed that the electrical conductivity for CNT-containing samples increased after the thermal treatment whereas corresponding values for only CB-containing counterparts decreased. In this scenario, the occurrence of secondary agglomeration of CNT and the formation of CB aggregates are thought to be contributing factors thanks to the increased mobility of polymer chains during annealing treatment. For example, a flow-induced orientation of CNT in microparts is expected due to the combined effects of high shearing and cooling in μIM. Thus, the reorganization of orientated CNT and the occurrence of secondary agglomeration of CNT facilitate the construction of conductive pathways. Besides, the formation of CB aggregates further promotes the formation of conductive pathways within the host polymer matrix. However, the aggregation of CB particles in only CB-containing samples might break down the continuum of conductive pathways, thereby leading to a reduction of electrical conductivity after the thermal treatment.

Chapter 6

6 Conclusions

The research was carried out in a manner to fully explore and understand the influence of process parameters and molding materials on the electrical and morphological properties of carbon filled thermoplastic polymers in microinjection molding. A micropart which has three-consecutive zones with decreasing thickness along the flow direction was fabricated. To facilitate characterizations, all microparts were cut into three different sections based on part thickness, namely thick section, middle section and thin section, respectively. The electrical conductivity for each section of microparts was characterized relative to the melt flow direction, i.e. parallel to the flow direction (FD) and perpendicular to flow direction (TD), by a two-probe method. Results from the electrical conductivity measurements were correlated with the development of microstructure in microparts. The following conclusion could be drawn from this work:

The state of distribution and degree of orientation of CNT are influenced by the process parameters in microinjection molding. It was found that an increase of backpressure does not significantly contribute to enhancing the electrical conductivity, but it has an important influence on the dimensional stability of the microparts. High melt temperature and mold temperature are advantageous to the formation of conductive pathways within microparts. Higher injection velocity reduces the electrical conductivity values measured across the TD, whereas the values of electrical conductivity increases along the FD of the microparts, which was correlated with the orientation of CNT.

As expected, simulation (Moldflow) results revealed that the distribution of maximum shear rates within the three-step microparts obeys the following order: thick section < middle section < thin section. The microstructure development along the FD was correlated with the simulation results. For example, the number of CNT agglomerates in each section of PP/CNT microparts decreased along the predominant flow direction, which could be related to the variation of shearing effect. The crystallization of unfilled PP microparts is shear rate (temperature) dependent along the FD, i.e. the peak crystallization temperature follows a similar trend as the simulation results. However, this phenomenon is absent in

CNT-containing systems, indicating that the presence of CNT can alter the crystallization process of polymer chains.

The selection of host polymer matrices for CNT has an influence on the microstructure of microparts, which was corroborated by SEM observations. The interfacial interactions between CNT and the host matrix can determine the state of filler distribution. For example, the microparts molded from CNT-containing PP composites demonstrated higher electrical conductivity when compared with those of PC/CNT, PS/CNT and PA6/CNT counterparts, which was attributed to the presence of CNT agglomerates in PP.

The crystallization process of carbon filled semi-crystalline polymers such as PA6 and PP was significantly accelerated with the filler acting as a nucleation agent. For example, the crystallization behavior of PA6/CNT composites and subsequent moldings was greatly altered with the appearance of a typical double crystallization peak whereas only a single crystallization peak was observed for their pure PA6 counterparts. Additionally, the peak crystallization temperature of CNT-containing PP composites and subsequent moldings shifted to higher temperature regions with a monotonic increase of CNT concentration, up to 10 wt%.

The effect of CNT filled polymers on the thermal stability varied with respect to the types of host polymer matrix employed. For example, the thermal stability of PC/CNT composites and thick section of subsequent microparts deteriorated upon the addition of CNT, whereas the thermal stability of PP/CNT composites and subsequent moldings increased with increasing filler concentration, which was ascribed to the intrinsic properties of CNT and the state of filler distribution within corresponding micropart.

The distribution of CNT was significantly improved in PA6 after the melt blending and subsequent microinjection molding processes. The typical thermomechanical history experienced by polymer melts during melt processing could have a chain scission effect on the polymer chains and a shortening effect on the added CNT due to the prevailing high shearing and extensional force fields.

Raman spectroscopy analysis was found useful to characterize the orientation of carbon fillers and qualitatively check the properties of carbon fillers in microparts.

The adoption of immiscible polymer blends could enhance the electrical conductivity of subsequent moldings by the concept of selective localization of conductive fillers in the dispersed phase of immiscible blends. Moreover, the high shearing effect in microinjection molding favors the coalescence of dispersed filler-enriched phase, which is advantageous to the formation of conductive pathways.

The development of microstructure in carbon filled PP microparts is influenced by the intrinsic properties of adopted fillers. We found that the high structure CB and CNT are more effective in enhancing the electrical conductivity of microparts, when compared with GNP-containing counterparts. Besides, the adoption of LTEG can effectively enhance the electrical conductivity of microparts, which is attributed to the *in situ* exfoliation of conductive fillers during melt processing. In addition, the percolation threshold for carbon filled microparts is invariably higher than their compression molded counterparts, which is attributed to the severe shearing conditions that prevail in microinjection molding process. Therefore, the morphology and intrinsic properties of carbon fillers significantly influence the electrical and morphological properties of subsequent moldings.

Based on the range of total carbon filler concentrations studied, no obvious synergistic effects of hybrid loading of CNT and CB on the enhancement of σ for PS microparts was detected. An annealing treatment could effectively enhance the electrical conductivity of CNT-containing microparts, which can be related to the restoration of conductive network due to the increased mobility of polymer chains, whereas a negative effect on the electrical conductivity was observed for only CB-loaded counterparts.

Chapter 7

7 Recommendations for future research

The following issues could be addressed in the future to extend our understanding of microinjection molding of filler loaded polymer composites.

1. Process characterization:
    - Understanding of the microinjection molding process for filler-containing polymer composites by collecting the in-line process data via proper sensors installation.
    - Flow visualization with the aid of high speed camera or other techniques.
2. Improve the interfacial interaction between fillers and host polymer matrices:
    - Surface modification of inorganic fillers is essential to improve the dispersion of functionalized fillers in the host polymers by enhancing the interfacial interactions between fillers and host polymers. Thus, the efficacy of filler modification is worth investigating from the viewpoints of research and application.
    - The other approach is to introduce compatibilizers or other additives such as ionic liquids and other dispersive agents. These aspects have been studied in conventional injection molding and/or compression molding processes, but are rarely investigated in terms of microinjection molding process.
3. Optimize the filler distribution by *in situ* foaming process:
    - The foaming process could be introduced by directly applying the inert gas during the molding process. However, this process may be quite challenging due to the very short cycle times, high injection pressure and limited space of the mold cavities. Thus, proper mixing of chemical foaming reagents with

polymer composites will be a viable way to study the influence of foaming on the properties of foamed articles.

4. Conduct a thorough study of the mechanical properties of carbon filler-containing microparts and make a comparison of mechanical properties between conventional injection molded counterparts or microparts with various part thickness. By doing this, one may correlate the mechanical properties, such as tensile strength, Young's modulus and elasticity with the size of injection molded products.

5. Investigate the development of crystal morphologies with or without the presence of fillers by using optical microscopy analysis. A comprehensive understanding of the microstructure would be helpful to correlate the microstructure development with the mechanical performance of molded microparts.

6. Quantify thermal conductivity of carbon-containing microparts. The evaluation of thermal conductivity is of equivalent importance as the determination of electrical conductivity, which may shed light on their potential applications in the areas of heat dissipation, etc.

7. Develop suitable toolkits for characterizing the rheological behavior of polymers and polymer composites at high shearing conditions. Proper acquisition of rheology data under extreme shearing conditions would be essential to develop suitable packages/toolkits for accurate simulation of the microinjection molding process.

8. Study the effect of annealing and thermal aging on the electrical and morphological properties of carbon-containing microparts. This may provide some insights into the correlation between microstructure development and performance of microparts in the frame of time series.

9. The occurrence of shear-induced coalescence of CNT-enriched PBSA domains in the shear layer of PLA/PBSA/CNT microparts is quite interesting. Therefore, future work may focus on the influence of filler geometry (such as spherical, plate-like and other fibrous particles) on the microstructure development of filler-containing immiscible blends in microinjection molding.

References

[1] Yang C, Yin X-H, Cheng G-M. Microinjection molding of microsystem components: new aspects in improving performance. J Micromech Microeng 2013;23:093001.

[2] Heckele M, Schomburg WK. Review on micro molding of thermoplastic polymers. J Micromech Microeng 2004;14:R1–14.

[3] Attia UM, Marson S, Alcock JR. Micro-injection moulding of polymer microfluidic devices. Microfluid Nanofluidics 2009;7:1–28.

[4] Whiteside BR, Martyn MT, Coates PD, Allan PS, Hornsby PR, Greenway G. Micromoulding: process characteristics and product properties. Plast Rubber Compos 2003;32:231–9.

[5] Zhao Z, Yang Q, Gong P, Sun H, Wu P, Huang Y, et al. Effects of process temperatures on the flow-induced crystallization of isotactic polypropylene/poly(ethylene terephthalate) blends in microinjection molding. Ind Eng Chem Res 2017;56:9467–77.

[6] Uppuluri CT, Devineni J, Han T, Nayak A, Nair KJ, Whiteside BR, et al. Microneedle-assisted transdermal delivery of Zolmitriptan: effect of microneedle geometry, *in vitro* permeation experiments, scaling analyses and numerical simulations. Drug Dev Ind Pharm 2017;43:1292–303.

[7] Chu J, Kamal MR, Derdouri S, Hrymak A. Characterization of the microinjection molding process. Polym Eng Sci 2010;50:1214–25.

[8] Zhang N, Chu JS, Byrne CJ, Browne DJ, Gilchrist MD. Replication of micro/nano-scale features by micro injection molding with a bulk metallic glass mold insert. J Micromech Microeng 2012;22:065019.

[9] Giboz J, Spoelstra AB, Portale G, Copponnex T, Meijer HEH, Peters GWM, et al. On the origin of the “core-free” morphology in microinjection-molded HDPE. J Polym Sci Part B Polym Phys 2011;49:1470–8.

[10] Giboz J, Copponnex T, Mélé P. Microinjection molding of thermoplastic polymers: morphological comparison with conventional injection molding. J Micromech Microeng 2009;19:025023.

[11] Heinrich M, Decker R, Schaufuss J, Troeltzsch J, Mehner J, Kroll L. Electrical contact properties of micro-injection molded polypropylene/CNT/CB-composites on metallic electrodes. Adv Mater Res 2015;1103:77–83.

[12] Abbasi S, Carreau PJ, Derdouri A. Flow induced orientation of multiwalled carbon nanotubes in polycarbonate nanocomposites: Rheology, conductivity and mechanical properties. Polymer 2010;51:922–35.

[13] Jiang Z, Chen Y, Liu Z. The morphology, crystallization and conductive performance of a polyoxymethylene/carbon nanotube nanocomposite prepared under microinjection molding conditions. J Polym Res 2014;21:451.

[14] Liu Z, Chen Y, Ding W, Zhang C. Filling behavior, morphology evolution and crystallization behavior of microinjection molded poly(lactic acid)/hydroxyapatite nanocomposites. Compos Part A Appl Sci Manuf 2015;72:85–95.

[15] Abdelhamid ME, O'Mullane AP, Snook GA. Storing energy in plastics: a review on conducting polymers & their role in electrochemical energy storage. RSC Adv 2015;5:11611–26.

[16] Al-Saleh MH, Sundararaj U. A review of vapor grown carbon nanofiber/polymer conductive composites. Carbon 2009;47:2–22.

[17] Ramasubramaniam R, Chen J, Liu H. Homogeneous carbon nanotube/polymer composites for electrical applications. Appl Phys Lett 2003;83:2928–30.

[18] Shi Y, Ma C, Peng L, Yu G. Conductive "smart" hybrid hydrogels with PNIPAM and nanostructured conductive polymers. Adv Funct Mater 2015;25:1219–25.

[19] Kaur G, Adhikari R, Cass P, Bown M, Gunatillake P. Electrically conductive polymers and composites for biomedical applications. RSC Adv 2015;5:37553–67.

[20] Wang Y, Jing X. Intrinsically conducting polymers for electromagnetic interference shielding. Polym Adv Technol 2005;16:344–51.

[21] Balint R, Cassidy NJ, Cartmell SH. Conductive polymers: Towards a smart biomaterial for tissue engineering. Acta Biomater 2014;10:2341–53.

[22] Mantione D, del Agua I, Sanchez-Sanchez A, Mecerreyes D. Poly(3,4-ethylenedioxythiophene) (PEDOT) derivatives: Innovative conductive polymers for bioelectronics. Polymers 2017;9:354.

[23] AL-Oqla FM, Sapuan SM, Anwer T, Jawaid M, Hoque ME. Natural fiber reinforced conductive polymer composites as functional materials: A review. Synth Met 2015;206:42–54.

[24] Jiang X, Yan D-X, Bao Y, Pang H, Ji X, Li Z-M. Facile, green and affordable strategy for structuring natural graphite/polymer composite with efficient electromagnetic interference shielding. RSC Adv 2015;5:22587–92.

[25] Wang M, Zhang K, Dai X-X, Li Y, Guo J, Liu H, et al. Enhanced electrical conductivity and piezoresistive sensing in multi-wall carbon nanotubes/polydimethylsiloxane nanocomposites via the construction of a self-segregated structure. Nanoscale 2017;9:11017–26.

[26] Zhou S, Chen Y, Zou H, Liang M. Thermally conductive composites obtained by flake graphite filling immiscible Polyamide 6/Polycarbonate blends. Thermochim Acta 2013;566:84–91.

[27] Weber M, Kamal MR. Microstructure and volume resistivity of composites of isotactic polypropylene reinforced with electrically conductive fibers. Polym Compos 1997;18:726–40.

[28] Mamunya YP, Davydenko VV, Pissis P, Lebedev EV. Electrical and thermal conductivity of polymers filled with metal powders. Eur Polym J 2002;38:1887–97.

[29] Bishay IK, Abd-El-Messieh SL, Mansour SH. Electrical, mechanical and thermal

properties of polyvinyl chloride composites filled with aluminum powder. Mater Des 2011;32:62–8.

[30] Ramezani Kakroodi A, Kazemi Y, Rodrigue D. Effect of conductive particles on the mechanical, electrical, and thermal properties of maleated polyethylene. Polym Adv Technol 2015;26:362–8.

[31] Burmistrov I, Gorshkov N, Ilinykh I, Muratov D, Kolesnikov E, Anshin S, et al. Improvement of carbon black based polymer composite electrical conductivity with additions of MWCNT. Compos Sci Technol 2016;129:79–85.

[32] Han Z, Fina A. Thermal conductivity of carbon nanotubes and their polymer nanocomposites: A review. Prog Polym Sci 2011;36:914–44.

[33] Motlagh GH, Hrymak AN, Thompson MR. Improved through-plane electrical conductivity in a carbon-filled thermoplastic via foaming. Polym Eng Sci 2008;48:687–96.

[34] Zhou S, Yu L, Song X, Chang J, Zou H, Liang M. Preparation of highly thermally conducting polyamide 6/graphite composites via low-temperature *in situ* expansion. J Appl Polym Sci 2014;131:39596.

[35] Gulrez SKH, Ali Mohsin ME, Shaikh H, Anis A, Pulose AM, Yadav MK, et al. A review on electrically conductive polypropylene and polyethylene. Polym Compos 2014;35:900–14.

[36] Dicks AL. The role of carbon in fuel cells. J Power Sources 2006;156:128–41.

[37] Sengupta R, Bhattacharya M, Bandyopadhyay S, Bhowmick AK. A review on the mechanical and electrical properties of graphite and modified graphite reinforced polymer composites. Prog Polym Sci 2011;36:638–70.

[38] Bauhofer W, Kovacs JZ. A review and analysis of electrical percolation in carbon nanotube polymer composites. Compos Sci Technol 2009;69:1486–98.

[39] Tang W, Santare MH, Advani SG. Melt processing and mechanical property characterization of multi-walled carbon nanotube/high density polyethylene (MWNT/HDPE) composite films. Carbon 2003;41:2779–85.

[40] Ren Z, Lan Y, Wang Y. Introduction to Carbon. In book: Aligned Carbon Nanotubues: Physics, Concepts, Fabrication and Devices, Springer, Berlin, Heidelberg; 2012, p. 1–5.

[41] Falcao EH, Wudl F. Review carbon allotropes: beyond graphite and diamond. J Chem Technol Biotechnol 2007;82:524–31.

[42] Pierson HO. Handbook of Carbon, Graphite, Diamond, and Fullerenes: Properties, Processing, and Applications. Noyes Publications; 1993.

[43] Wu Z-S, Ren W, Gao L, Zhao J, Chen Z, Liu B, et al. Synthesis of graphene sheets with high electrical conductivity and good thermal stability by hydrogen arc discharge exfoliation. ACS Nano 2009;3:411–7.

[44] Kim KS, Zhao Y, Jang H, Lee SY, Kim JM, Kim KS, et al. Large-scale pattern growth of graphene films for stretchable transparent electrodes. Nature

2009;457:706–10.

[45] Balandin AA, Ghosh S, Bao W, Calizo I, Teweldebrhan D, Miao F, et al. Superior thermal conductivity of single-layer graphene. Nano Lett 2008;8:902–7.

[46] Ghosh S, Calizo I, Teweldebrhan D, Pokatilov EP, Nika DL, Balandin AA, et al. Extremely high thermal conductivity of graphene: Prospects for thermal management applications in nanoelectronic circuits. Appl Phys Lett 2008;92:151911.

[47] Zhou S, Lei Y, Zou H, Liang M. High thermally conducting composites obtained via in situ exfoliation process of expandable graphite filled polyamide 6. Polym Compos 2013;34:1816–23.

[48] Huang J-C. Carbon black filled conducting polymers and polymer blends. Adv Polym Technol 2002;21:299–313.

[49] Donnet J-B, Bansal RC, Wang M-J. Carbon Black: Science and Technology. CRC Press; 1993.

[50] Rigbi Z. Reinforcement of Rubber by Carbon Black. Part of Advances in Polymer Science book series. Springer, Berlin, Heidelberg; 1980, p. 21–68.

[51] Sau KP, Chaki TK, Khastgir D. Electrical and mechanical properties of conducting carbon black filled composites based on rubber and rubber blends. J Appl Polym Sci 1999;71:887–95.

[52] Roy N, Sengupta R, Bhowmick AK. Modifications of carbon for polymer composites and nanocomposites. Prog Polym Sci 2012;37:781–819.

[53] Allen NS, Edge M, Corrales T, Childs A, Liauw CM, Catalina F, et al. Ageing and stabilisation of filled polymers: an overview. Polym Degrad Stab 1998;61:183–99.

[54] Edge M, Allen NS, Gonzalez-Sanchez R, Liauw CM, Read SJ, Whitehouse RB. The influence of cure and carbon black on the high temperature oxidation of natural rubber I. Correlation of physico-chemical changes. Polym Degrad Stab 1999;64:197–205.

[55] Kumar AP, Depan D, Singh Tomer N, Singh RP. Nanoscale particles for polymer degradation and stabilization-Trends and future perspectives. Prog Polym Sci 2009;34:479–515.

[56] Yousif E, Haddad R. Photodegradation and photostabilization of polymers, especially polystyrene: review. Springerplus 2013;2:398.

[57] Azuma Y, Takeda H, Watanabe S, Nakatani H. Outdoor and accelerated weathering tests for polypropylene and polypropylene/talc composites: A comparative study of their weathering behavior. Polym Degrad Stab 2009;94:2267–74.

[58] Balberg I. A comprehensive picture of the electrical phenomena in carbon black–polymer composites. Carbon 2002;40:139–43.

[59] Novoselov KS, Geim AK, Morozov S V, Jiang D, Zhang Y, Dubonos S V, et al. Electric field effect in atomically thin carbon films. Science 2004;306:666–9.

[60] Kuilla T, Bhadra S, Yao D, Kim NH, Bose S, Lee JH. Recent advances in graphene

based polymer composites. Prog Polym Sci 2010;35:1350–75.

[61] Stankovich S, Dikin DA, Dommett GHB, Kohlhaas KM, Zimney EJ, Stach EA, et al. Graphene-based composite materials. Nature 2006;442:282–6.

[62] Novoselov KS, Falʹko VI, Colombo L, Gellert PR, Schwab MG, Kim K. A roadmap for graphene. Nature 2012;490:192–200.

[63] Hu K, Kulkarni DD, Choi I, Tsukruk VV. Graphene-polymer nanocomposites for structural and functional applications. Prog Polym Sci 2014;39:1934–72.

[64] Geim AK, Novoselov KS. The rise of graphene. Nat Mater 2007;6:183–91.

[65] Ramanathan T, Abdala AA, Stankovich S, Dikin DA, Herrera-Alonso M, Piner RD, et al. Functionalized graphene sheets for polymer nanocomposites. Nat Nanotechnol 2008;3:327–31.

[66] Fang M, Wang K, Lu H, Yang Y, Nutt S. Covalent polymer functionalization of graphene nanosheets and mechanical properties of composites. J Mater Chem 2009;19:7098.

[67] Yu J, Huang X, Wu C, Jiang P. Permittivity, thermal conductivity and thermal stability of poly(vinylidene fluoride)/graphene nanocomposites. IEEE Trans Dielectr Electr Insul 2011;18:478–84.

[68] Kim H, Abdala AA, Macosko CW. Graphene/polymer nanocomposites. Macromolecules 2010;43:6515–30.

[69] Hernandez Y, Nicolosi V, Lotya M, Blighe FM, Sun Z, De S, et al. High-yield production of graphene by liquid-phase exfoliation of graphite. Nat Nanotechnol 2008;3:563–8.

[70] Li D, Müller MB, Gilje S, Kaner RB, Wallace GG. Processable aqueous dispersions of graphene nanosheets. Nat Nanotechnol 2008;3:101–5.

[71] Potts JR, Dreyer DR, Bielawski CW, Ruoff RS. Graphene-based polymer nanocomposites. Polymer 2011;52:5–25.

[72] Verdejo R, Bernal MM, Romasanta LJ, Lopez-Manchado MA. Graphene filled polymer nanocomposites. J Mater Chem 2011;21:3301–10.

[73] Gaikwad S, Tate J, Theodoropoulou N, Koo J. Electrical and mechanical properties of PA11 blended with nanographene platelets using industrial twin-screw extruder for selective laser sintering. J Compos Mater 2013;47:2973–86.

[74] Iijima S. Helical microtubules of graphitic carbon. Nature 1991;354:56–8.

[75] Grobert N. Carbon nanotubes – becoming clean. Mater Today 2007;10:28–35.

[76] Harris PJF. Carbon nanotube composites. Int Mater Rev 2004;49:31–43.

[77] Baughman RH, Zakhidov AA, de Heer WA. Carbon nanotubes--the route toward applications. Science 2002;297:787–92.

[78] Dorri Moghadam A, Omrani E, Menezes PL, Rohatgi PK. Mechanical and tribological properties of self-lubricating metal matrix nanocomposites reinforced by carbon nanotubes (CNTs) and graphene – A review. Compos Part B Eng

2015;77:402–20.

[79] Bakshi SR, Lahiri D, Agarwal A. Carbon nanotube reinforced metal matrix composites - a review. Int Mater Rev 2010;55:41–64.

[80] Yang Y, Liang X, Chen W, Cao L, Li M, Sheldon BW, et al. Quantification and promotion of interfacial interactions between carbon nanotubes and polymer derived ceramics. Carbon 2015;95:964–71.

[81] Baishya P, Maji TK. Functionalization of MWCNT and their application in properties development of green wood nanocomposite. Carbohydr Polym 2016;149:332–9.

[82] Bokobza L. Multiwall carbon nanotube elastomeric composites: A review. Polymer 2007;48:4907–20.

[83] Thostenson ET, Ren Z, Chou T-W. Advances in the science and technology of carbon nanotubes and their composites: a review. Compos Sci Technol 2001;61:1899–912.

[84] Coleman JN, Khan U, Blau WJ, Gun’ko YK. Small but strong: A review of the mechanical properties of carbon nanotube–polymer composites. Carbon 2006;44:1624–52.

[85] Breuer O, Sundararaj U. Big returns from small fibers: A review of polymer/carbon nanotube composites. Polym Compos 2004;25:630–45.

[86] Treacy MMJ, Ebbesen TW, Gibson JM. Exceptionally high Young’s modulus observed for individual carbon nanotubes. Nature 1996;381:678–80.

[87] Versavaud S, Régnier G, Gouadec G, Vincent M. Influence of injection molding on the electrical properties of polyamide 12 filled with multi-walled carbon nanotubes. Polymer 2014;55:6811–8.

[88] Villmow T, Pegel S, Pötschke P, Wagenknecht U. Influence of injection molding parameters on the electrical resistivity of polycarbonate filled with multi-walled carbon nanotubes. Compos Sci Technol 2008;68:777–89.

[89] Ma P-C, Liu M-Y, Zhang H, Wang S-Q, Wang R, Wang K, et al. Enhanced electrical conductivity of nanocomposites containing hybrid fillers of carbon nanotubes and carbon black. ACS Appl Mater Interfaces 2009;1:1090–6.

[90] Liu T, Phang IY, Shen L, Chow SY, Zhang WD. Morphology and mechanical properties of multiwalled carbon nanotubes reinforced nylon-6 composites. Macromolecules 2004;37:7214–22.

[91] Spitalsky Z, Tasis D, Papagelis K, Galiotis C. Carbon nanotube–polymer composites: Chemistry, processing, mechanical and electrical properties. Prog Polym Sci 2010;35:357–401.

[92] Rahmat M, Hubert P. Carbon nanotube–polymer interactions in nanocomposites: A review. Compos Sci Technol 2011;72:72–84.

[93] Eitan A, Jiang K, Dukes D, Andrews R, Schadler LS. Surface modification of multiwalled carbon nanotubes: Toward the tailoring of the interface in polymer

composites. Chem Mater 2003;15:3198–201.

[94] Velasco-Santos C, Martínez-Hernández AL, Fisher FT, Ruoff R, Castaño VM. Improvement of thermal and mechanical properties of carbon nanotube composites through chemical functionalization. Chem Mater 2003;15:4470–5.

[95] Ferreira T, Paiva MC, Pontes AJ. Dispersion of carbon nanotubes in polyamide 6 for microinjection moulding. J Polym Res 2013;20:301.

[96] Gojny FH, Wichmann MHG, Fiedler B, Bauhofer W, Schulte K. Influence of nano-modification on the mechanical and electrical properties of conventional fibre-reinforced composites. Compos Part A Appl Sci Manuf 2005;36:1525–35.

[97] Gojny FH, Wichmann MHG, Fiedler B, Kinloch IA, Bauhofer W, Windle AH, et al. Evaluation and identification of electrical and thermal conduction mechanisms in carbon nanotube/epoxy composites. Polymer 2006;47:2036–45.

[98] Li J, Ma PC, Chow WS, To CK, Tang BZ, Kim J-K. Correlations between percolation threshold, dispersion state, and aspect ratio of carbon nanotubes. Adv Funct Mater 2007;17:3207–15.

[99] Du F, Fischer JE, Winey KI. Effect of nanotube alignment on percolation conductivity in carbon nanotube/polymer composites. Phys Rev B 2005;72:121404.

[100] Torres-Giner S, Chiva-Flor A, Feijoo JL. Injection-molded parts of polypropylene/multi-wall carbon nanotubes composites with an electrically conductive tridimensional network. Polym Compos 2016;37:488–96.

[101] Abbasi S, Derdouri A, Carreau PJ. Properties of microinjection molding of polymer multiwalled carbon nanotube conducting composites. Polym Eng Sci 2011;51:992–1003.

[102] Luo W, Cheng C, Zhou S, Zou H, Liang M. Thermal, electrical and rheological behavior of high-density polyethylene/graphite composites. Iran Polym J 2015;24:573–81.

[103] Ravindran P, Manisekar K, Narayanasamy R, Narayanasamy P. Tribological behaviour of powder metallurgy-processed aluminium hybrid composites with the addition of graphite solid lubricant. Ceram Int 2013;39:1169–82.

[104] Liu YB, Lim SC, Ray S, Rohatgi PK. Friction and wear of aluminium-graphite composites: the smearing process of graphite during sliding. Wear 1992;159:201–5.

[105] Kato H, Takama M, Iwai Y, Washida K, Sasaki Y. Wear and mechanical properties of sintered copper–tin composites containing graphite or molybdenum disulfide. Wear 2003;255:573–8.

[106] Li J, Feng L, Jia Z. Preparation of expanded graphite with 160 μm mesh of fine flake graphite. Mater Lett 2006;60:746–9.

[107] Dresselhaus MS, Dresselhaus G. Intercalation compounds of graphite. Adv Phys 1981;30:139–326.

[108] Zheng W, Wong S-C. Electrical conductivity and dielectric properties of PMMA/expanded graphite composites. Compos Sci Technol 2003;63:225–35.

[109] Wu H, Lu C, Zhang W, Zhang X. Preparation of low-density polyethylene/low-temperature expandable graphite composites with high thermal conductivity by an in situ expansion melt blending process. Mater Des 2013;52:621–9.

[110] Sinha Ray S, Okamoto M. Polymer/layered silicate nanocomposites: a review from preparation to processing. Prog Polym Sci 2003;28:1539–641.

[111] Meng H, Li G. A review of stimuli-responsive shape memory polymer composites. Polymer 2013;54:2199–221.

[112] Xanthos M. Polymers and Polymer Composites. In book: Functional Fillers for Plastics, Wiley-Blackwell; 2005, p. 1–16.

[113] Tibbetts GG, Lake ML, Strong KL, Rice BP. A review of the fabrication and properties of vapor-grown carbon nanofiber/polymer composites. Compos Sci Technol 2007;67:1709–18.

[114] Buck F, Brylka B, Müller V, Müller T, Weidenmann KA, Hrymak AN, et al. Two-scale structural mechanical modeling of long fiber reinforced thermoplastics. Compos Sci Technol 2015;117:159–67.

[115] Saheb DN, Jog JP. Natural fiber polymer composites: A review. Adv Polym Technol 1999;18:351–63.

[116] Miao C, Hamad WY. Cellulose reinforced polymer composites and nanocomposites: a critical review. Cellulose 2013;20:2221–62.

[117] Fabbri P, Bassoli E, Bon SB, Valentini L. Preparation and characterization of poly (butylene terephthalate)/graphene composites by in-situ polymerization of cyclic butylene terephthalate. Polymer 2012;53:897–902.

[118] Park C, Ounaies Z, Watson KA, Crooks RE, Smith J, Lowther SE, et al. Dispersion of single wall carbon nanotubes by in situ polymerization under sonication. Chem Phys Lett 2002;364:303–8.

[119] Jiang X, Bin Y, Matsuo M. Electrical and mechanical properties of polyimide-carbon nanotubes composites fabricated by in situ polymerization. Polymer 2005;46:7418–24.

[120] Barkoula NM, Alcock B, Cabrera NO, Peijs T. Fatigue properties of highly oriented polypropylene tapes and all-polypropylene composites. Polym Polym Compos 2008;16:101–13.

[121] Zheng G, Wu J, Wang W, Pan C. Characterizations of expanded graphite/polymer composites prepared by in situ polymerization. Carbon 2004;42:2839–47.

[122] Xu Z, Gao C. *In situ* polymerization approach to graphene-reinforced nylon-6 composites. Macromolecules 2010;43:6716–23.

[123] Fim F de C, Guterres JM, Basso NRS, Galland GB. Polyethylene/graphite nanocomposites obtained by *in situ* polymerization. J Polym Sci Part A Polym Chem 2010;48:692–8.

[124] Roghani-Mamaqani H, Haddadi-Asl V, Salami-Kalajahi M. In situ controlled radical polymerization: A review on synthesis of well-defined nanocomposites.

Polym Rev 2012;52:142–88.

[125] López-Manchado M, Herrero B, Arroyo M. Organoclay–natural rubber nanocomposites synthesized by mechanical and solution mixing methods. Polym Int 2004;53:1766–72.

[126] Li N, Huang Y, Du F, He X, Lin X, Gao H, et al. Electromagnetic interference (EMI) shielding of single-walled carbon nanotube epoxy composites. Nano Lett 2006;6:1141–5.

[127] Gelves GA, Al-Saleh MH, Sundararaj U. Highly electrically conductive and high performance EMI shielding nanowire/polymer nanocomposites by miscible mixing and precipitation. J Mater Chem 2011;21:829–36.

[128] Kuila T, Bose S, Hong CE, Uddin ME, Khanra P, Kim NH, et al. Preparation of functionalized graphene/linear low density polyethylene composites by a solution mixing method. Carbon 2011;49:1033–7.

[129] Ren J, Silva AS, Krishnamoorti R. Linear viscoelasticity of disordered polystyrene−polyisoprene block copolymer based layered-silicate nanocomposites. Macromolecules 2000;33:3739–46.

[130] Kalaitzidou K, Fukushima H, Drzal LT. A new compounding method for exfoliated graphite–polypropylene nanocomposites with enhanced flexural properties and lower percolation threshold. Compos Sci Technol 2007;67:2045–51.

[131] Hu H, Zhang G, Xiao L, Wang H, Zhang Q, Zhao Z. Preparation and electrical conductivity of graphene/ultrahigh molecular weight polyethylene composites with a segregated structure. Carbon 2012;50:4596–9.

[132] Du J, Zhao L, Zeng Y, Zhang L, Li F, Liu P, et al. Comparison of electrical properties between multi-walled carbon nanotube and graphene nanosheet/high density polyethylene composites with a segregated network structure. Carbon 2011;49:1094–100.

[133] Pang H, Chen T, Zhang G, Zeng B, Li Z-M. An electrically conducting polymer/graphene composite with a very low percolation threshold. Mater Lett 2010;64:2226–9.

[134] Müller MT, Krause B, Kretzschmar B, Pötschke P. Influence of feeding conditions in twin-screw extrusion of PP/MWCNT composites on electrical and mechanical properties. Compos Sci Technol 2011;71:1535–42.

[135] Pötschke P, Dudkin SM, Alig I. Dielectric spectroscopy on melt processed polycarbonate-multiwalled carbon nanotube composites. Polymer 2003;44:5023–30.

[136] Andrews R, Jacques D, Minot M, Rantell T. Fabrication of carbon multiwall nanotube/polymer composites by shear mixing. Macromol Mater Eng 2002;287:395.

[137] Pötschke P, Villmow T, Krause B. Melt mixed PCL/MWCNT composites prepared at different rotation speeds: Characterization of rheological, thermal, and electrical properties, molecular weight, MWCNT macrodispersion, and MWCNT length

distribution. Polymer 2013;54:3071–8.

[138] Alig I, Lellinger D, Engel M, Skipa T, Pötschke P. Destruction and formation of a conductive carbon nanotube network in polymer melts: In-line experiments. Polymer 2008;49:1902–9.

[139] Jollands M, Gupta RK. Effect of mixing conditions on mechanical properties of polylactide/montmorillonite clay nanocomposites. J Appl Polym Sci 2010;118:1489-1493.

[140] Pujari S, Ramanathan T, Kasimatis K, Masuda J, Andrews R, Torkelson JM, et al. Preparation and characterization of multiwalled carbon nanotube dispersions in polypropylene: Melt mixing versus solid-state shear pulverization. J Polym Sci Part B Polym Phys 2009;47:1426–36.

[141] Baiardo M, Zini E, Scandola M. Flax fibre–polyester composites. Compos Part A Appl Sci Manuf 2004;35:703–10.

[142] Ryman-Rasmussen JP, Cesta MF, Brody AR, Shipley-Phillips JK, Everitt JI, Tewksbury EW, et al. Inhaled carbon nanotubes reach the subpleural tissue in mice. Nat Nanotechnol 2009;4:747–51.

[143] Muller J, Huaux F, Lison D. Respiratory toxicity of carbon nanotubes: How worried should we be? Carbon 2006;44:1048–56.

[144] Prashantha K, Soulestin J, Lacrampe MF, Krawczak P, Dupin G, Claes M. Masterbatch-based multi-walled carbon nanotube filled polypropylene nanocomposites: Assessment of rheological and mechanical properties. Compos Sci Technol 2009;69:1756–63.

[145] Mahmoodi M, Arjmand M, Sundararaj U, Park S. The electrical conductivity and electromagnetic interference shielding of injection molded multi-walled carbon nanotube/polystyrene composites. Carbon 2012;50:1455–64.

[146] Thostenson ET, Chou T-W. Carbon nanotube networks: Sensing of distributed srain and damage for life prediction and self healing. Adv Mater 2006;18:2837–41.

[147] Tiusanen J, Vlasveld D, Vuorinen J. Review on the effects of injection moulding parameters on the electrical resistivity of carbon nanotube filled polymer parts. Compos Sci Technol 2012;72:1741–52.

[148] Kanbur Y, Küçükyavuz Z. Electrical and mechanical properties of polypropylene/carbon black composites. J Reinf Plast Compos 2009;28:2251–60.

[149] Wegrzyn M, Juan S, Benedito A, Giménez E. The influence of injection molding parameters on electrical properties of PC/ABS-MWCNT nanocomposites. J Appl Polym Sci 2013;130:2152–8.

[150] Alig I, Pötschke P, Lellinger D, Skipa T, Pegel S, Kasaliwal GR, et al. Establishment, morphology and properties of carbon nanotube networks in polymer melts. Polymer 2012;53:4–28.

[151] Mahmoodi M, Mostofa MG, Jun M, Park SS. Characterization and micromilling of flow induced aligned carbon nanotube nanocomposites. J Micro Nano-

Manufacturing 2013;1:011009.

[152] Clingerman ML, King JA, Schulz KH, Meyers JD. Evaluation of electrical conductivity models for conductive polymer composites. J Appl Polym Sci 2002;83:1341–56.

[153] Socher R, Krause B, Müller MT, Boldt R, Pötschke P. The influence of matrix viscosity on MWCNT dispersion and electrical properties in different thermoplastic nanocomposites. Polymer 2012;53:495–504.

[154] Jing X, Zhao W, Lan L. The effect of particle size on electric conducting percolation threshold in polymer/conducting particle composites. J Mater Sci Lett 2000;19:377–9.

[155] Sohi NJS, Bhadra S, Khastgir D. The effect of different carbon fillers on the electrical conductivity of ethylene vinyl acetate copolymer-based composites and the applicability of different conductivity models. Carbon 2011;49:1349–61.

[156] Huang C-L, Wang Y-J, Fan Y-C, Hung C-L, Liu Y-C. The effect of geometric factor of carbon nanofillers on the electrical conductivity and electromagnetic interference shielding properties of poly(trimethylene terephthalate) composites: a comparative study. J Mater Sci 2017;52:2560–80.

[157] Yi JY, Choi GM. Percolation behavior of conductor-insulator composites with varying aspect ratio of conductive fiber. J Electroceramics 1999;3:361–9.

[158] Arjmand M, Mahmoodi M, Gelves GA, Park S, Sundararaj U. Electrical and electromagnetic interference shielding properties of flow-induced oriented carbon nanotubes in polycarbonate. Carbon 2011;49:3430–40.

[159] Du F, Fischer JE, Winey KI. Coagulation method for preparing single-walled carbon nanotube/poly(methyl methacrylate) composites and their modulus, electrical conductivity, and thermal stability. J Polym Sci Part B Polym Phys 2003;41:3333–8.

[160] Enomoto K, Yasuhara T, Ohtake N, Kato K. Injection molding of polystyrene matrix composites filled with vapor grown carbon fiber. JSME Int J Ser A 2003;46:353–8.

[161] Wu H, Drzal LT. High thermally conductive graphite nanoplatelet/polyetherimide composite by precoating: Effect of percolation and particle size. Polym Compos 2013;34:2148–53.

[162] Zhou S, Luo W, Zou H, Liang M, Li S. Enhanced thermal conductivity of polyamide 6/polypropylene (PA6/PP) immiscible blends with high loadings of graphite. J Compos Mater 2016;50:327–37.

[163] Wang X, Jiang Q, Xu W, Cai W, Inoue Y, Zhu Y. Effect of carbon nanotube length on thermal, electrical and mechanical properties of CNT/bismaleimide composites. Carbon 2013;53:145–52.

[164] Mahmoodi M, Lee YH, Mohamad A, Park SS. Effect of flow induced alignment on the thermal conductivity of injection molded carbon nanotube-filled polystyrene nanocomposites. Polym Eng Sci 2015;55:753–62.

[165] Ha SM, Lee HL, Lee S-G, Kim BG, Kim YS, Won JC, et al. Thermal conductivity of graphite filled liquid crystal polymer composites and theoretical predictions. Compos Sci Technol 2013;88:113–9.

[166] Bukkinakere KC, Manjunatha HR, Bambore LSK, Srinivasan D. Highly thermally-conductive moldable thermoplastic composites and compositions. US8299159B2, 2010.

[167] Hofmann D, Keinath M, Thomann R, Mülhaupt R. Thermoplastic carbon/polyamide 12 composites containing functionalized graphene, expanded graphite, and carbon nanofillers. Macromol Mater Eng 2014;299:1329–42.

[168] Du J, Cheng H-M. The fabrication, properties, and uses of graphene/polymer composites. Macromol Chem Phys 2012;213:1060–77.

[169] Stan F, Sandu LI, Fetecau C. Effect of processing parameters and strain rate on mechanical properties of carbon nanotube–filled polypropylene nanocomposites. Compos Part B Eng 2014;59:109–22.

[170] Bhuiyan MA, Pucha RV, Karevan M, Kalaitzidou K. Tensile modulus of carbon nanotube/polypropylene composites – A computational study based on experimental characterization. Comput Mater Sci 2011;50:2347–53.

[171] Murariu M, Dechief AL, Bonnaud L, Paint Y, Gallos A, Fontaine G, et al. The production and properties of polylactide composites filled with expanded graphite. Polym Degrad Stab 2010;95:889–900.

[172] Chodák I, Omastová M, Pionteck J. Relation between electrical and mechanical properties of conducting polymer composites. J Appl Polym Sci 2001;82:1903–6.

[173] Karsli NG, Aytac A. Effects of maleated polypropylene on the morphology, thermal and mechanical properties of short carbon fiber reinforced polypropylene composites. Mater Des 2011;32:4069–73.

[174] Xu J-Z, Zhong G-J, Hsiao BS, Fu Q, Li Z-M. Low-dimensional carbonaceous nanofiller induced polymer crystallization. Prog Polym Sci 2014;39:555–93.

[175] Kazemi Y, Kakroodi AR, Wang S, Ameli A, Filleter T, Pötschke P, et al. Conductive network formation and destruction in polypropylene/carbon nanotube composites via crystal control using supercritical carbon dioxide. Polymer 2017;129:179–88.

[176] Xia H, Wang Q, Li K, Hu G-H. Preparation of polypropylene/carbon nanotube composite powder with a solid-state mechanochemical pulverization process. J Appl Polym Sci 2004;93:378–86.

[177] Abbås KB. Degradational effects on bisphenol A polycarbonate extruded at high shear stresses. Polymer 1981;22:836–41.

[178] Jang BN, Wilkie CA. The thermal degradation of bisphenol A polycarbonate in air. Thermochim Acta 2005;426:73–84.

[179] Peng Z, Kong LX. A thermal degradation mechanism of polyvinyl alcohol/silica nanocomposites. Polym Degrad Stab 2007;92:1061–71.

[180] Adam GA, Hay JN, Parsons IW, Haward RN. Effect of molecular weight on the

thermal properties of polycarbonates. Polymer 1976;17:51–7.

[181] Jang BN, Wilkie CA. The effects of triphenylphosphate and recorcinolbis(diphenylphosphate) on the thermal degradation of polycarbonate in air. Thermochim Acta 2005;433:1–12.

[182] Schartel B, Braun U, Knoll U, Bartholmai M, Goering H, Neubert D, et al. Mechanical, thermal, and fire behavior of bisphenol a polycarbonate/multiwall carbon nanotube nanocomposites. Polym Eng Sci 2008;48:149–58.

[183] Wang M, Li B, Wang J, Bai P. Preparation and properties of polysiloxane grafting multi-walled carbon nanotubes/polycarbonate nanocomposites. Polym Adv Technol 2011;22:1738–46.

[184] Wu T-M, Chen E-C, Lin Y-W, Chiang M-F, Chang G-Y. Preparation and characterization of melt-processed polycarbonate/multiwalled carbon nanotube composites. Polym Eng Sci 2008;48:1369–75.

[185] Jakab E, Omastová M. Thermal decomposition of polyolefin/carbon black composites. J Anal Appl Pyrolysis 2005;74:204–14.

[186] Kashiwagi T, Du F, Douglas JF, Winey KI, Harris RH, Shields JR. Nanoparticle networks reduce the flammability of polymer nanocomposites. Nat Mater 2005;4:928–33.

[187] Giboz J, Copponnex T, Mélé P. Microinjection molding of thermoplastic polymers: a review. J Micromech Microeng 2007;17:R96–109.

[188] Heckele M, Bacher W, Müller KD. Hot embossing - The molding technique for plastic microstructures. Microsyst Technol 1998;4:122–4.

[189] Piotter V, Mueller K, Plewa K, Ruprecht R, Hausselt J. Performance and simulation of thermoplastic micro injection molding. Microsyst Technol 2002;8:387–90.

[190] Michaeli W, Spennemann A, Gärtner R. New plastification concepts for micro injection moulding. Microsyst Technol 2002;8:55–7.

[191] Zhang N, Gilchrist MD. Characterization of microinjection molding process for milligram polymer microparts. Polym Eng Sci 2014;54:1458–70.

[192] Whiteside BR, Martyn MT, Coates PD, Greenway G, Allen P, Hornsby P. Micromoulding: process measurements, product morphology and properties. Plast Rubber Compos 2004;33:11–7.

[193] Zhang N, Choi SY, Gilchrist MD. Flow induced crystallization of poly(ether-block-amide) from the microinjection molding process and its effect on mechanical properties. Macromol Mater Eng 2014;299:1362–83.

[194] Pan Y, Shi S, Xu W, Zheng G, Dai K, Liu C, et al. Wide distribution of shish-kebab structure and tensile property of micro-injection-molded isotactic polypropylene microparts: a comparative study with injection-molded macroparts. J Mater Sci 2014;49:1041–8.

[195] Ding W, Chen Y, Liu Z, Yang S. In situ nano-fibrillation of microinjection molded poly(lactic acid)/poly(ε-caprolactone) blends and comparison with conventional

injection molding. RSC Adv 2015;5:92905–17.

[196] Benzler T, Piotter V, Hanemann T, Mueller K, Norajitra P, Ruprecht R, et al. Innovations in molding technologies for microfabrication. In: Smith JH, Karam JM, editors. vol. 3874, International Society for Optics and Photonics; 1999, p. 53–60.

[197] Su Q, Zhang N, Gilchrist MD. The use of variotherm systems for microinjection molding. J Appl Polym Sci 2016;133:42962.

[198] Xie L, Ziegmann G. A visual mold with variotherm system for weld line study in micro injection molding. Microsyst Technol 2008;14:809–14.

[199] Gornik C. Injection moulding of parts with microstructured surfaces for medical applications. Macromol Symp 2004;217:365–74.

[200] Chen SC, Tsai RI, Chien RD, Lin TK. Preliminary study of polymer melt rheological behavior flowing through micro-channels. Int Commun Heat Mass Transf 2005;32:501–10.

[201] Yao D, Kim B. Simulation of the filling process in micro channels for polymeric materials. J Micromechanics Microengineering 2002;12:314.

[202] Chien R-D, Jong W-R, Chen S-C. Study on rheological behavior of polymer melt flowing through micro-channels considering the wall-slip effect. J Micromech Microeng 2005;15:1389–96.

[203] Vasco JC, Maia JM, Pouzada AS. Thermo-rheological behaviour of polymer melts in microinjection moulding. J Micromech Microeng 2009;19:105012.

[204] Xie L, Ziegmann G. Effect of gate dimension on micro injection molded weld line strength with polypropylene (PP) and high-density polyethylene (HDPE). Int J Adv Manuf Technol 2010;48:71–81.

[205] Su Y-C, Shah J, Lin L. Implementation and analysis of polymeric microstructure replication by micro injection molding. J Micromech Microeng 2004;14:415–22.

[206] Su Q, Zhang N, Symms N, Gilchrist MD. Accurate validation of micro injection moulding process for manufacturing a thin-wall micro part based on Moldex3D. 4M/IWMF2016 Glob. Conf. Micro Manuf. Inc. 11th Int. Conf. Multi-Material Micro Manuf. 10th Int. Work. Microfactories in Kgs. Lyngby, Denmark. Research Publishing Services; 2016, p. 159–62.

[207] Sieber I, Li L, Gengenbach U, Beckert E, Steinkopf R, Yi AY. Optical performance simulation of free-form optics for an eye implant based on a measurement data enhanced model. Appl Opt 2016;55:6671.

[208] Metwally K, Barriere T, Khan-Malek C. Replication of micrometric and sub-micrometric structured surfaces using micro-injection and micro-injection compression moulding. Int J Adv Manuf Technol 2016;83:779–89.

[209] El Otmani R, Kandoussi K, Kamal MR, Derdouri S, Boutaous M. Morphology and flow effect of microinjection-molded plastic microgears. Polym Adv Technol 2017;28:511–5.

[210] Gheisari R, Bártolo PJ, Goddard N. Analysis for microstructure of micro-cantilevers

arrays in micro-injection molding by using numerical simulations. AIP Conf. Proc., vol. 1779, AIP Publishing LLC; 2016, p. 050016.

[211] Zhang N, Su Q, Choi SY, Gilchrist MD. Effects of gate design and cavity thickness on filling, morphology and mechanical properties of microinjection mouldings. Mater Des 2015;83:835–47.

[212] Kamal MR, Chu J, Derdouri S, Hrymak A. Morphology of microinjection moulded polyoxymethylene. Plast Rubber Compos 2010;39:332–41.

[213] Grellmann W, Seidler S. Polymer Testing. Carl Hanser Verlag GmbH & Co. KG; 2013.

[214] Tekce HS, Kumlutas D, Tavman IH. Effect of particle shape on thermal conductivity of copper reinforced polymer composites. J Reinf Plast Compos 2007;26:113–21.

[215] Lee E-S, Lee S-M, Shanefield DJ, Cannon WR. Enhanced thermal conductivity of polymer matrix composite via high solids loading of aluminum nitride in epoxy resin. J Am Ceram Soc 2008;91:1169–74.

[216] Teng C-C, Ma C-CM, Lu C-H, Yang S-Y, Lee S-H, Hsiao M-C, et al. Thermal conductivity and structure of non-covalent functionalized graphene/epoxy composites. Carbon 2011;49:5107–16.

[217] Kalaprasad G, Pradeep P, Mathew G, Pavithran C, Thomas S. Thermal conductivity and thermal diffusivity analyses of low-density polyethylene composites reinforced with sisal, glass and intimately mixed sisal/glass fibres. Compos Sci Technol 2000;60:2967–77.

[218] Yang S-Y, Lin W-N, Huang Y-L, Tien H-W, Wang J-Y, Ma C-CM, et al. Synergetic effects of graphene platelets and carbon nanotubes on the mechanical and thermal properties of epoxy composites. Carbon 2011;49:793–803.

[219] Xu Y, Ray G, Abdel-Magid B. Thermal behavior of single-walled carbon nanotube polymer–matrix composites. Compos Part A Appl Sci Manuf 2006;37:114–21.

[220] Xu Y, Chung DDL. Increasing the thermal conductivity of boron nitride and aluminum nitride particle epoxy-matrix composites by particle surface treatments. Compos Interfaces 2000;7:243–56.

[221] Xu Y, Chung DDL, Mroz C. Thermally conducting aluminum nitride polymer-matrix composites. Compos Part A Appl Sci Manuf 2001;32:1749–57.

[222] Iguchi CY, dos Santos WN, Gregorio R. Determination of thermal properties of pyroelectric polymers, copolymers and blends by the laser flash technique. Polym Test 2007;26:788–92.

[223] dos Santos WN, Mummery P, Wallwork A. Thermal diffusivity of polymers by the laser flash technique. Polym Test 2005;24:628–34.

[224] Lee G-W, Park M, Kim J, Lee JI, Yoon HG. Enhanced thermal conductivity of polymer composites filled with hybrid filler. Compos Part A Appl Sci Manuf 2006;37:727–34.

[225] Sarı A, Karaipekli A. Thermal conductivity and latent heat thermal energy storage

characteristics of paraffin/expanded graphite composite as phase change material. Appl Therm Eng 2007;27:1271–7.

[226] Franco A. An apparatus for the routine measurement of thermal conductivity of materials for building application based on a transient hot-wire method. Appl Therm Eng 2007;27:2495–504.

[227] Assael MJ, Antoniadis KD, Tzetzis D. The use of the transient hot-wire technique for measurement of the thermal conductivity of an epoxy-resin reinforced with glass fibres and/or carbon multi-walled nanotubes. Compos Sci Technol 2008;68:3178–83.

[228] Zhou Z, Wang S, Zhang Y, Zhang Y. Effect of different carbon fillers on the properties of PP composites: Comparison of carbon black with multiwalled carbon nanotubes. J Appl Polym Sci 2006;102:4823–30.

[229] Santos R, Mould S, Formánek P, Paiva M, Covas J. Effects of particle size and surface chemistry on the dispersion of graphite nanoplates in polypropylene composites. Polymers 2018;10:222.

[230] Paiva MC, Simon F, Novais RM, Ferreira T, Proença MF, Xu W, et al. Controlled functionalization of carbon nanotubes by a solvent-free multicomponent approach. ACS Nano 2010;4:7379–86.

[231] Bose S, Bhattacharyya AR, Bondre AP, Kulkarni AR, Pötschke P. Rheology, electrical conductivity, and the phase behavior of cocontinuous PA6/ABS blends with MWNT: Correlating the aspect ratio of MWNT with the percolation threshold. J Polym Sci Part B Polym Phys 2008;46:1619–31.

[232] Zhao J, Mayes RH, Chen G, Xie H, Chan PS. Effects of process parameters on the micro molding process. Polym Eng Sci 2003;43:1542–54.

[233] Song MC, Liu Z, Wang MJ, Yu TM, Zhao DY. Research on effects of injection process parameters on the molding process for ultra-thin wall plastic parts. J Mater Process Technol 2007;187–188:668–71.

[234] Sha B, Dimov S, Griffiths C, Packianather MS. Investigation of micro-injection moulding: Factors affecting the replication quality. J Mater Process Technol 2007;183:284–96.

[235] Fei G, Tuinea-Bobe C, Li D, Li G, Whiteside B, Coates P, et al. Electro-activated surface micropattern tuning for microinjection molded electrically conductive shape memory polyurethane composites. RSC Adv 2013;3:24132.

[236] Li Y, Shimizu H. High-shear processing induced homogenous dispersion of pristine multiwalled carbon nanotubes in a thermoplastic elastomer. Polymer 2007;48:2203–7.

[237] Heinrich M, Sichting F, Kroll L. Microinjection molding of polypropylene (PP) filled with MWCNT: Influence of processing parameters on the mechanical properties. 2012 IEEE Nanotechnol. Mater. Devices Conf., IEEE; 2012, p. 111–5.

[238] Wang B, Li Y, Weng G, Jiang Z, Chen P, Wang Z, et al. Reduced graphene oxide enhances the crystallization and orientation of poly(ε-caprolactone). Compos Sci

Technol 2014;96:63–70.

[239] Zhong J, Isayev AI. Properties of polyetherimide/graphite composites prepared using ultrasonic twin-screw extrusion. J Appl Polym Sci 2015;132:41397.

[240] Liou GL, Young WB. The filling behavior of reinforcing glass fiber in micro injection molding. Int Polym Process 2010;25:264–9.

[241] Shaffer MSP, Windle AH. Fabrication and characterization of carbon nanotube/poly(vinyl alcohol) composites. Adv Mater 1999;11:937–41.

[242] Inoue S, Ichikuni N, Suzuki T, Uematsu T, Kaneko K. Capillary condensation of N_2 on multiwall carbon nanotubes. J Phys Chem B 1998;102:4689–92.

[243] Mirzadeh A, Ghasemi H, Mahrous F, Kamal MR. Reactive extrusion effects on rheological and mechanical properties of poly(lactic acid)/poly[(butylene succinate)-co-adipate]/epoxy chain extender blends and clay nanocomposites. J Appl Polym Sci 2015;132:42664.

[244] Rew Y, Baranikumar A, Tamashausky A V., El-Tawil S, Park P. Electrical and mechanical properties of asphaltic composites containing carbon based fillers. Constr Build Mater 2017;135:394–404.

[245] Kamal MR, El Otmani R, Derdouri A, Chu J-S. Flow and thermal history effects on morphology and tensile behavior of poly(oxymethylene) micro injection molded parts. Int Polym Process 2017;32:590–605.

[246] Park J, Eom K, Kwon O, Woo S. Chemical etching technique for the investigation of melt-crystallized isotactic polypropylene spherulite and lamellar morphology by scanning electron microscopy. Microsc Microanal 2001;7:276–86.

[247] Arvidson SA, Khan SA, Gorga RE. Mesomorphic-α-monoclinic phase transition in isotactic polypropylene: A study of processing effects on structure and mechanical properties. Macromolecules 2010;43:2916–24.

[248] Harris AM, Lee EC. Improving mechanical performance of injection molded PLA by controlling crystallinity. J Appl Polym Sci 2008;107:2246–55.

[249] Cheng S, Liu T, Zhao Y, Lam P-M, Yin Y. Mechanical and thermal properties of chicken feather fiber/PLA green composites. Compos Part B Eng 2009;40:650–4.

[250] Fang L, Wei M, Shang Y, Jimenez, Lady, Kazmer D, Barry C, et al. Surface morphology alignment of block copolymers induced by injection molding. Polymer 2009;50:5837–45.

[251] Pötschke P, Bhattacharyya AR, Janke A, Goering H. Melt mixing of polycarbonate/multi-wall carbon nanotube composites. Compos Interfaces 2003;10:389–404.

[252] Pötschke P, Fornes TD, Paul DR. Rheological behavior of multiwalled carbon nanotube/polycarbonate composites. Polymer 2002;43:3247–55.

[253] Meister S, Drummer D. Influence of mold temperature on mold filling behavior and part properties in micro injection molding. Int Polym Process 2013;28:550–7.

[254] Alig I, Skipa T, Engel M, Lellinger D, Pegel S, Pötschke P. Electrical conductivity

recovery in carbon nanotube–polymer composites after transient shear. Phys Status Solidi 2007;244:4223–6.

[255] Kharchenko SB, Douglas JF, Obrzut J, Grulke EA, Migler KB. Flow-induced properties of nanotube-filled polymer materials. Nat Mater 2004;3:564–8.

[256] Eken AE, Tozzi EJ, Klingenberg DJ, Bauhofer W. A simulation study on the effects of shear flow on the microstructure and electrical properties of carbon nanotube/polymer composites. Polymer 2011;52:5178–85.

[257] Gerard P, Raine J, Pabiot J. Characterization of fiber and molecular orientations and their interaction in composite injection molding. J Reinf Plast Compos 1998;17:922–34.

[258] Jinsong Chu. Characterization of the Micro Injection Molding Process and Its Products. PhD Thesis, McGill University, 2009.

[259] Jansen KMB, Pantani R, Titomanlio G. As-molded shrinkage measurements on polystyrene injection molded products. Polym Eng Sci 1998;38:254–64.

[260] Shelesh-Nezhad K, Taghizadeh A. Shrinkage behavior and mechanical performances of injection molded polypropylene/talc composites. Polym Eng Sci 2007;47:2124–8.

[261] Radhakrishnan S, Ramanujam BTS, Adhikari A, Sivaram S. High-temperature, polymer–graphite hybrid composites for bipolar plates: Effect of processing conditions on electrical properties. J Power Sources 2007;163:702–7.

[262] Li D, Fei G, Xia H, Spencer PE, Coates PD. Micro-contact reconstruction of adjacent carbon nanotubes in polymer matrix through annealing-induced relaxation of interfacial residual stress and strain. J Appl Polym Sci 2015;132:1–11.

[263] Papageorgiou DG, Bikiaris DN, Chrissafis K. Effect of crystalline structure of polypropylene random copolymers on mechanical properties and thermal degradation kinetics. Thermochim Acta 2012;543:288–94.

[264] Liu F, Guo C, Wu X, Qian X, Liu H, Zhang J. Morphological comparison of isotactic polypropylene parts prepared by micro-injection molding and conventional injection molding. Polym Adv Technol 2012;23:686–94.

[265] Phulkerd P, Arayachukeat S, Huang T, Inoue T, Nobukawa S, Yamaguchi M. Melting point elevation of isotactic polypropylene. J Macromol Sci Part B 2014;53:1222–30.

[266] Logakis E, Pollatos E, Pandis C, Peoglos V, Zuburtikudis I, Delides CG, et al. Structure–property relationships in isotactic polypropylene/multi-walled carbon nanotubes nanocomposites. Compos Sci Technol 2010;70:328–35.

[267] Bikiaris D, Vassiliou A, Chrissafis K, Paraskevopoulos KM, Jannakoudakis A, Docoslis A. Effect of acid treated multi-walled carbon nanotubes on the mechanical, permeability, thermal properties and thermo-oxidative stability of isotactic polypropylene. Polym Degrad Stab 2008;93:952–67.

[268] Nuriel S, Liu L, Barber AH, Wagner HD. Direct measurement of multiwall nanotube

surface tension. Chem Phys Lett 2005;404:263–6.

[269] Steinmann S, Gronski W, Friedrich C. Influence of selective filling on rheological properties and phase inversion of two-phase polymer blends. Polymer 2002;43:4467–77.

[270] Omonov TS, Harrats C, Groeninckx G. Co-continuous and encapsulated three phase morphologies in uncompatibilized and reactively compatibilized polyamide 6/polypropylene/polystyrene ternary blends using two reactive precursors. Polymer 2005;46:12322–36.

[271] Solid surface energy data (SFE) for common polymers. http://www.surface-tension.de/solid-surface-energy.htm (accessed April 21, 2018).

[272] Pötschke P, Pegel S, Claes M, Bonduel D. A novel strategy to incorporate carbon nanotubes into thermoplastic matrices. Macromol Rapid Commun 2008;29:244–51.

[273] Barber AH, Cohen SR, Wagner HD. Static and dynamic wetting measurements of single carbon nanotubes. Phys Rev Lett 2004;92:186103.

[274] Navas IO, Arjmand M, Sundararaj U. Effect of carbon nanotubes on morphology evolution of polypropylene/polystyrene blends: Understanding molecular interactions and carbon nanotube migration mechanisms. RSC Adv 2017;7:54222–34.

[275] Alig I, Skipa T, Lellinger D, Pötschke P. Destruction and formation of a carbon nanotube network in polymer melts: Rheology and conductivity spectroscopy. Polymer 2008;49:3524–32.

[276] Pegel S, Pötschke P, Petzold G, Alig I, Dudkin SM, Lellinger D. Dispersion, agglomeration, and network formation of multiwalled carbon nanotubes in polycarbonate melts. Polymer 2008;49:974–84.

[277] Prusty RK, Rathore DK, Ray BC. CNT/polymer interface in polymeric composites and its sensitivity study at different environments. Adv Colloid Interface Sci 2017;240:77–106.

[278] Lellinger D, Xu D, Ohneiser A, Skipa T, Alig I. Influence of the injection moulding conditions on the in-line measured electrical conductivity of polymer-carbon nanotube composites. Phys Status Solidi 2008;245:2268–71.

[279] Joseph R, Martyn MT, Tanner KE, Coates PD, Bonfield W. Rheological characterisation of hydroxyapatite filled polyethylene composites. Part 2 - Isothermal compressibility and wall slip. Plast Rubber Compos 2001;30:205–12.

[280] Hong C-M, Kim J, Jana SC. Shear-induced migration of conductive fillers in injection molding. Polym Eng Sci 2004;44:2101–9.

[281] Arjmand M, Apperley T, Okoniewski M, Sundararaj U. Comparative study of electromagnetic interference shielding properties of injection molded versus compression molded multi-walled carbon nanotube/polystyrene composites. Carbon 2012;50:5126–34.

[282] Slobodian P, Králová D, Lengálová A, Novotný R, Sáha P. Adaptation of

polystyrene/multi-wall carbon nanotube composite properties in respect of its thermal stability. Polym Compos 2009;31:452–8.

[283] Wang L, Dang Z-M. Carbon nanotube composites with high dielectric constant at low percolation threshold. Appl Phys Lett 2005;87:042903.

[284] Min C, Shen X, Shi Z, Chen L, Xu Z. The electrical properties and conducting mechanisms of carbon nanotube/polymer nanocomposites: A review. Polym Plast Technol Eng 2010;49:1172–81.

[285] Psarras GC. Charge transport properties in carbon black/polymer composites. J Polym Sci Part B Polym Phys 2007;45:2535–45.

[286] Chen G-X, Li Y, Shimizu H. Ultrahigh-shear processing for the preparation of polymer/carbon nanotube composites. Carbon 2007;45:2334–40.

[287] Krause B, Mende M, Petzold G, Boldt R, Pötschke P. Characterization of dispersability of industrial nanotube materials and their length distribution before and after melt processing. In book: Carbon Nanotubube-Polymer Composites, Royal Society of Chemistry Cambridge, UK; 2013, p. 212–33.

[288] Via MD, King JA, Keith JM, Bogucki GR. Electrical conductivity modeling of carbon black/polycarbonate, carbon nanotube/polycarbonate, and exfoliated graphite nanoplatelet/polycarbonate composites. J Appl Polym Sci 2012;124:182–9.

[289] Logakis E, Pandis C, Peoglos V, Pissis P, Stergiou C, Pionteck J, et al. Structure-property relationships in polyamide 6/multi-walled carbon nanotubes nanocomposites. J Polym Sci Part B Polym Phys 2009;47:764–74.

[290] Krause B, Pötschke P, Häußler L. Influence of small scale melt mixing conditions on electrical resistivity of carbon nanotube-polyamide composites. Compos Sci Technol 2009;69:1505–15.

[291] Phang IY, Ma J, Shen L, Liu T, Zhang W-D. Crystallization and melting behavior of multi-walled carbon nanotube-reinforced nylon-6 composites. Polym Int 2006;55:71–9.

[292] Ferreira T, Lopes PE, Pontes AJ, Paiva MC. Microinjection molding of polyamide 6. Polym Adv Technol 2014;25:891–5.

[293] Bikiaris D, Dimitrios. Microstructure and Properties of Polypropylene/Carbon Nanotube Nanocomposites. Materials 2010;3:2884–946.

[294] Seo M-K, Lee J-R, Park S-J. Crystallization kinetics and interfacial behaviors of polypropylene composites reinforced with multi-walled carbon nanotubes. Mater Sci Eng A 2005;404:79–84.

[295] Yang B-X, Shi J-H, Pramoda KP, Goh SH. Enhancement of the mechanical properties of polypropylene using polypropylene-grafted multiwalled carbon nanotubes. Compos Sci Technol 2008;68:2490–7.

[296] Bao SP, Tjong SC. Mechanical behaviors of polypropylene/carbon nanotube nanocomposites: The effects of loading rate and temperature. Mater Sci Eng A

2008;485:508–16.

[297] Davis A, Golden JH. Degradation of polycarbonates. III. Viscometric study of thermally-induced chain scission. Die Makromol Chemie 1964;78:16–23.

[298] Guo J, Liu Y, Prada-Silvy R, Tan Y, Azad S, Krause B, et al. Aspect ratio effects of multi-walled carbon nanotubes on electrical, mechanical, and thermal properties of polycarbonate/MWCNT composites. J Polym Sci Part B Polym Phys 2014;52:73–83.

[299] González-González VA, Neira-Velázquez G, Angulo-Sánchez JL. Polypropylene chain scissions and molecular weight changes in multiple extrusion. Polym Degrad Stab 1998;60:33–42.

[300] Buchholz BA, Zahn JM, Kenward M, Slater GW, Barron AE. Flow-induced chain scission as a physical route to narrowly distributed, high molar mass polymers. Polymer 2004;45:1223–34.

[301] Wen X, Tian N, Gong J, Chen Q, Qi Y, Liu Z, et al. Effect of nanosized carbon black on thermal stability and flame retardancy of polypropylene/carbon nanotubes nanocomposites. Polym Adv Technol 2013;24:971–7.

[302] Cheng HKF, Chong MF, Liu E, Zhou K, Li L. Thermal decomposition kinetics of multiwalled carbon nanotube/polypropylene nanocomposites. J Therm Anal Calorim 2014;117:63–71.

[303] Nurul M, Mariatti M. Effect of thermal conductive fillers on the properties of polypropylene composites. J Thermoplast Compos Mater 2013;26:627–39.

[304] Yuan C, Chen G, Yang J. Orientation structures in injection-molded pellets of polystyrene/carbon nanotube nanocomposites. Ind Eng Chem Res 2012;51:11695–9.

[305] Chipara DM, Macossay J, Ybarra AVR, Chipara AC, Eubanks TM. Raman spectroscopy of polystyrene nanofibers-Multiwalled carbon nanotubes composites. Appl Surf Sci 2013;275:23–7.

[306] Yan X, Itoh T, Kitahama Y, Suzuki T, Sato H, Miyake T, et al. A Raman spectroscopy study on single-wall carbon nanotube/polystyrene nanocomposites: Mechanical compression transferred from the polymer to single-wall carbon nanotubes. J Phys Chem C 2012;116:17897–903.

[307] Bliznyuk VN, Singamaneni S, Sanford RL, Chiappetta D, Crooker B, Shibaev PV. Matrix mediated alignment of single wall carbon nanotubes in polymer composite films. Polymer 2006;47:3915–21.

[308] Endo M, Kim YA, Fukai Y, Hayashi T, Terrones M, Terrones H, et al. Comparison study of semi-crystalline and highly crystalline multiwalled carbon nanotubes. Appl Phys Lett 2001;79:1531–3.

[309] Wegrzyn M, Sahuquillo O, Benedito A, Gimenez E. Morphology, mechanical performance, and nanoindentation behavior of injection molded PC/ABS-MWCNT nanocomposites. J Appl Polym Sci 2015;132:42014.

[310] Zhao Q, Wagner HD. Raman spectroscopy of carbon-nanotube-based composites. Philos Trans A Math Phys Eng Sci 2004;362:2407–24.

[311] Dybal J, Schmidt P, Baldrian J, Kratochvil J. Ordered structures in polycarbonate studied by infrared and Raman spectroscopy, wide-angle X-ray scattering, and differential scanning calorimetry. Macromolecules 1998;31:6611–9.

[312] Litchfield DW, Baird DG. The role of nanoclay in the generation of poly(ethylene terephthalate) fibers with improved modulus and tenacity. Polymer 2008;49:5027–36.

[313] Pötschke P, Brünig H, Janke A, Fischer D, Jehnichen D. Orientation of multiwalled carbon nanotubes in composites with polycarbonate by melt spinning. Polymer 2005;46:10355–63.

[314] Goyal PK, Kumar V, Gupta R, Mahendia S, Anita, Kumar S. Modification of polycarbonate surface by Ar^+ ion implantation for various opto-electronic applications. Vacuum 2012;86:1087–91.

[315] Brown SDM, Jorio A, Dresselhaus MS, Dresselhaus G. Observations of the *D*-band feature in the Raman spectra of carbon nanotubes. Phys Rev B 2001;64:073403.

[316] Soin N, Roy SS, Ray SC, McLaughlin JA. Excitation energy dependence of Raman bands in multiwalled carbon nanotubes. J Raman Spectrosc 2010;41:1227–33.

[317] Heise HM, Kuckuk R, Ojha AK, Srivastava A, Srivastava V, Asthana BP. Characterisation of carbonaceous materials using Raman spectroscopy: a comparison of carbon nanotube filters, single- and multi-walled nanotubes, graphitised porous carbon and graphite. J Raman Spectrosc 2009;40:344–53.

[318] Bulusheva LG, Okotrub A V., Kinloch IA, Asanov IP, Kurenya AG, Kudashov AG, et al. Effect of nitrogen doping on Raman spectra of multi-walled carbon nanotubes. Phys Status Solidi 2008;245:1971–4.

[319] Pimenta MA, Gomes AP, Fantini C, Cançado LG, Araujo PT, Maciel IO, et al. Optical studies of carbon nanotubes and nanographites. Phys E Low-Dimensional Syst Nanostructures 2007;37:88–92.

[320] Ojijo V, Sinha Ray S, Sadiku R. Role of specific interfacial area in controlling properties of immiscible blends of biodegradable polylactide and poly[(butylene succinate)-co-adipate]. ACS Appl Mater Interfaces 2012;4:6690–701.

[321] Eslami H, Kamal MR. Effect of a chain extender on the rheological and mechanical properties of biodegradable poly(lactic acid)/poly[(butylene succinate)-*co*-adipate] blends. J Appl Polym Sci 2013;129:2418–28.

[322] Nofar M, Heuzey M-C, Carreau PJ, Kamal MR. Effects of nanoclay and its localization on the morphology stabilization of PLA/PBAT blends under shear flow. Polymer 2016;98:353–64.

[323] Ray SS, Bandyopadhyay J, Bousmina M. Thermal and thermomechanical properties of poly[(butylene succinate)-co-adipate] nanocomposite. Polym Degrad Stab 2007;92:802–12.

[324] Zhang J, Duan X, Sato H, Tsuji H. Noda I, Yan S, et al. Crystal modifications and thermal behavior of poly(l-lactic acid) revealed by infrared spectroscopy. Macromolecules 2005;38:8012–21.

[325] Lee S, Lee JW. Characterization and processing of biodegradable polymer blends of poly (lactic acid) with poly (butylene succinate adipate). Korea-Australia Rheol J 2005;17:71–7.

[326] Tu C, Nagata K, Yan S. Influence of melt-mixing processing sequence on electrical conductivity of polyethylene/polypropylene blends filled with graphene. Polym Bull 2017;74:1237–52.

[327] Wu D, Lin D, Zhang J, Zhou W, Zhang M, Zhang Y, et al. Selective localization of nanofillers: Effect on morphology and crystallization of PLA/PCL blends. Macromol Chem Phys 2011;212:613–26.

[328] Eslami H, Kamal MR. Elongational rheology of biodegradable poly(lactic acid)/poly[(butylene succinate)-*co*-adipate] binary blends and poly(lactic acid)/poly[(butylene succinate)-*co*-adipate]/clay ternary nanocomposites. J Appl Polym Sci 2013;127:2290–306.

[329] Lin C, Chung DDL. Effect of carbon black structure on the effectiveness of carbon black thermal interface pastes. Carbon 2007;45:2922–31.

[330] Zakaria MY, Sulong AB, Sahari J, Suherman H. Effect of the addition of milled carbon fiber as a secondary filler on the electrical conductivity of graphite/epoxy composites for electrical conductive material. Compos Part B Eng 2015;83:75–80.

[331] Drubetski M, Siegmann A, Narkis M. Hybrid particulate and fibrous injection molded composites: Carbon black/carbon fiber/polypropylene systems. Polym Compos 2005;26:454–64.

[332] Xu DH, Wang ZG, Douglas JF. Influence of carbon nanotube aspect ratio on normal stress differences in isotactic polypropylene nanocomposite melts. Macromolecules 2008;41:815–25.

[333] Fu S-Y, Chen Z-K, Hong S, Han CC. The reduction of carbon nanotube (CNT) length during the manufacture of CNT/polymer composites and a method to simultaneously determine the resulting CNT and interfacial strengths. Carbon 2009;47:3192–200.

[334] Mavridis H, Hrymak AN, Vlachopoulos J. The effect of fountain flow on molecular orientation in injection molding. J Rheol 1988;32:639–63.

[335] Obrzut J, Douglas JF, Kharchenko SB, Migler KB. Shear-induced conductor-insulator transition in melt-mixed polypropylene-carbon nanotube dispersions. Phys Rev B 2007;76:195420.

[336] Pang H, Xu L, Yan D-X, Li Z-M. Conductive polymer composites with segregated structures. Prog Polym Sci 2014;39:1908–33.

[337] Dang ZM, Shehzad K, Zha JW, Mujahid A, Hussain T, Nie J, et al. Complementary percolation characteristics of carbon fillers based electrically percolative thermoplastic elastomer composites. Compos Sci Technol 2011;72:28–35.

[338] Clingerman ML, Weber EH, King JA, Schulz KH. Development of an additive equation for predicting the electrical conductivity of carbon-filled composites. J Appl Polym Sci 2003;88:2280–99.

[339] Mamunya EP, Davidenko VV, Lebedev EV. Effect of polymer-filler interface interactions on percolation conductivity of thermoplastics filled with carbon black. Compos Interfaces 1997;4:169–76.

[340] Al-Saleh MH, Sundararaj U. Electromagnetic interference (EMI) shielding effectiveness of PP/PS polymer blends containing high structure carbon black. Macromol Mater Eng 2008;293:621–30.

[341] Szeluga U, Kumanek B, Trzebicka B. Synergy in hybrid polymer/nanocarbon composites. A review. Compos Part A Appl Sci Manuf 2015;73:204–31.

[342] Zhang SM, Lin L, Deng H, Gao X, Bilotti E, Peijs T, et al. Synergistic effect in conductive networks constructed with carbon nanofillers in different dimensions. Express Polym Lett 2012;6:159–68.

[343] Sumfleth J, Adroher XC, Schulte K. Synergistic effects in network formation and electrical properties of hybrid epoxy nanocomposites containing multi-wall carbon nanotubes and carbon black. J Mater Sci 2009;44:3241–7.

[344] Wei T, Song L, Zheng C, Wang K, Yan J, Shao B, et al. The synergy of a three filler combination in the conductivity of epoxy composites. Mater Lett 2010;64:2376–9.

[345] Liang GD, Tjong SC. Electrical properties of percolative polystyrene/carbon nanofiber composites. IEEE Trans Dielectr Electr Insul 2008;15:214–20.

[346] Pan Y, Cheng HKF, Li L, Chan SH, Zhao J, Juay YK. Annealing induced electrical conductivity jump of multi-walled carbon nanotube/polypropylene composites and influence of molecular weight of polypropylene. J Polym Sci Part B Polym Phys 2010;48:2238–47.

[347] Yui H, Wu G, Sano H, Sumita M, Kino K. Morphology and electrical conductivity of injection-molded polypropylene/carbon black composites with addition of high-density polyethylene. Polymer 2006;47:3599–608.

[348] Jana SC. Loss of surface and volume electrical conductivities in polymer compounds due to shear-induced migration of conductive particles. Polym Eng Sci 2003;43:570–9.

[349] Wu D, Lv Q, Feng S, Chen J, Chen Y, Qiu Y, et al. Polylactide composite foams containing carbon nanotubes and carbon black: Synergistic effect of filler on electrical conductivity. Carbon N Y 2015;95:380–7.

[350] Reidy RF, Simkovich G. Anomalous electrical behaviour of polymer-carbon composites as a function of temperature. J Mater Sci 1993;28:799–804.

[351] Shen L, Wang FQ, Yang H, Meng QR. The combined effects of carbon black and carbon fiber on the electrical properties of composites based on polyethylene or polyethylene/polypropylene blend. Polym Test 2011;30:442–8.

[352] Lew CY, Dewaghe C, Claes M. Injection moulding of polymer–carbon nanotube

composites. In book: Polymer-Carbon Nanotube Composites, Elsevier; 2011, p. 155–92.

Appendices

8 The influence of mold geometry on the electrical and morphological properties of PP/CNT microparts

8.1 Background

As reported in Chapter 1 *Section 1.4.1.4*, the adoption of different types of gate design or configurations of mold inserts would affect the thermomechanical history that prevails in the samples prepared by injection molding process. For example, Zhang et al. [211] studied the mold filling, morphological and mechanical properties of poly(ether-block-amide) dumbbell microparts by systematically changing gate design (i.e. opening and thickness) and cavity thickness (100-500 µm). They reported that a reduction of the gate size has two conflicting effects, i.e. reducing the gate size increases the shear heating, which leads to increased flow length; however, a simultaneously increased cooling effect reduces the flow length. In addition, the mold filling increases significantly with an increase of mold cavity thickness whereas the skin ratio decreases from 70 to 10% when the mold cavity thickness increases from 100 to 500 µm, which significantly determines the mechanical properties of subsequent moldings. Enomoto et al. [160] reported that the σ of PS/VGCF composites increased with increasing mold geometry thickness, which is due to the difference between the degree of filler orientation.

In our previous studies which were reported in *Chapter 5*, we found that prevalent shearing and cooling effects in different sections of three-step microparts would significantly affect the distribution and orientation of the incorporated fillers, thereby determining the properties of the microparts. To attempt to study the effect of mold geometry on the properties of PP/CNT microparts, a series of plaque mold inserts which have different cavity thickness were fabricated. A 3D view of the plaque microparts is displayed in Figure 8.1. The plaque microparts have a thickness of 0.85 mm, a width of 2.4 mm and a length of 14.8mm. The PP/CNT composites were prepared by melt dilution of masterbatches (see *Chapter 4*). The plaque microparts were fabricated under the same conditions as those of the three-step counterparts, i.e. melt temperature (260^{o}C), mold temperature (100^{o}C) and injection velocity (300 mm/s). Afterwards, the electrical conductivity and morphological properties of PP/CNT microparts were compared with those of three-stepped counterparts.

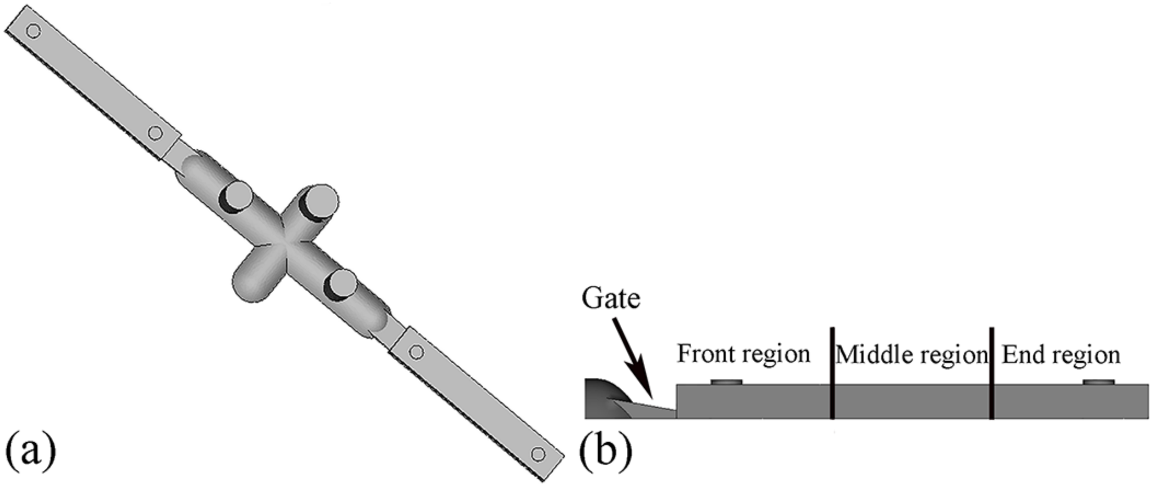

Figure 8.1 (a) The 3D view of a plaque micropart; (b) the micropart was divided into three sections for morphology observations.

8.2 Electrical conductivity and morphology

The σ for the plaque microparts was compared with the values of each section of the three-stepped microparts. For the plaque microparts, the σ was measured along the flow direction (FD) by using a two-probe method. Figure 8.2(a) shows the comparison of σ obtained from the plaque microparts with corresponding values determined across the transverse direction (TD) for each section of the three-step microparts. Results revealed that the FD σ for plaque microparts was lower than the TD σ obtained from each section of the three-step microparts when the CNT concentration is less than 7 wt%, whereas it becomes higher when the filler concentration exceeds 7 wt%. This suggested that the preferential alignment of nanotubes along the FD facilitates the formation of conductive pathways at higher CNT concentration. However, the FD σ for plaque microparts was much lower when compared with the TD σ for each section of three-step microparts at 5 wt% CNT, provided a preferential orientation of CNT along the flow direction. Thus, it could be deduced that the length of the flow path may affect the continuous construction of conductive pathways, thereby affecting the σ of subsequent moldings. For example, Villmow et al. [88] reported that both the volume and surface σ of injection molded PC/CNT plates varied locally along the flow direction, which could be correlated with the changes of nanotubes network arising from the network orientation, network disruption, orientation of separated nanotubes and cluster formation. Therefore, the formation of conductive pathways is not consistent within injection molded plates, which could be related to the combined shearing and cooling effects involved during the molding process. In addition, Eken et al. [256] reported that an increase of shear rate causes alignment of nanotubes along the flow direction. Thus, the orientation of individual nanotubes or nanotubes network might become more severe in the case of μIM when compared with that of CIM counterparts. As a result, the development of internal microstructure for subsequent moldings could be significantly affected by the mold geometry employed in μIM.

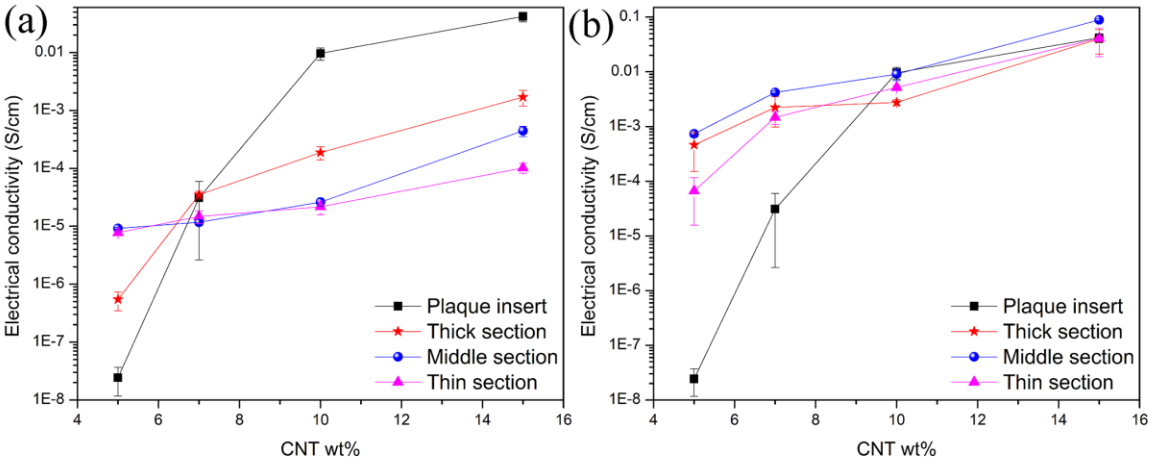

Figure 8.2 Comparison of the σ between the plaque microparts and each section of three-step microparts as a function of CNT content. The thickness of the plaque microparts is 0.85 mm. For the three-step microparts, σ was determined (a) across the TD and (b) along the FD, respectively.

Similarly, the FD σ for the plaque microparts was much lower than corresponding values of each section of the three-step microparts whereas such difference was minimized when CNT concentration is higher than 7 wt%, as depicted in Figure 8.2(b). This further indicates that the geometry of employed mold inserts has a significant influence on the development of microstructure within corresponding microparts. The flow path and thermomechanical history experienced by polymer melts would be significantly different in the two different mold inserts employed. For example, the length of the plaque microparts is 14.8 mm which is nearly 3 times longer than that of each section of the three-step microparts (Table 4.5). Since μIM is characteristic of high shearing and large cooling effects, the development of microstructure in PP/CNT microparts could be greatly affected by the thermomechanical history that endured by the polymer melts. For example, Kamal et al. [212] found that there is an increase of melt temperature along the flow direction which was attributed to the shear heating, as validated by Moldflow simulation. As a result, the prevailing thermomechanical history would be different between both mold cavities, i.e. the plaque mold insert and the three-step mold insert. For example, there is a significant increase of shear rates along the FD in the three-step microparts (Figure 5.66) whereas the changes of shear rates along the FD is insignificant in different locations of plaque microparts (see *Section 8.3, Figure 8.6*), leading to the formation of different microstructure within subsequent microparts, thereby affecting σ.

The development of microstructure in PP/CNT 2 wt% plaque microparts, which was taken from different regions, is given in Figure 8.3. As shown in Figure 8.1(b), the plaque microparts were divided into three sections along the FD, i.e. front region, middle region and end region, respectively. Each section of the microparts was fractured in liquid nitrogen across the TD and the morphology was taken from either the core layer or shear layer of each section. The fractured surface was chemically etched to remove the amorphous phase of PP [246]. It could be observed that the microstructure was different in various locations of the microparts, which could significantly affect the σ of resultant moldings. Although sufficient conductive pathways could be observed from the end region (Figure 8.3c), an intact conductive network was hardly observed in the middle region (Figure 8.3b), indicating that higher CNT concentration is needed to form continuous conductive pathways within the plaque microparts. A similar trend was also reported by Wegrzyn et al. [149] in conventional injection molded PC/ABS-CNT composites. In their study, the distribution and content of CNT in each part of the injection molded PC/ABS-CNT samples was evaluated using TGA. They reported that the distribution of CNT was inhomogeneous and the region farthest from the gate showed higher filler content, as displayed in Figure 8.4.

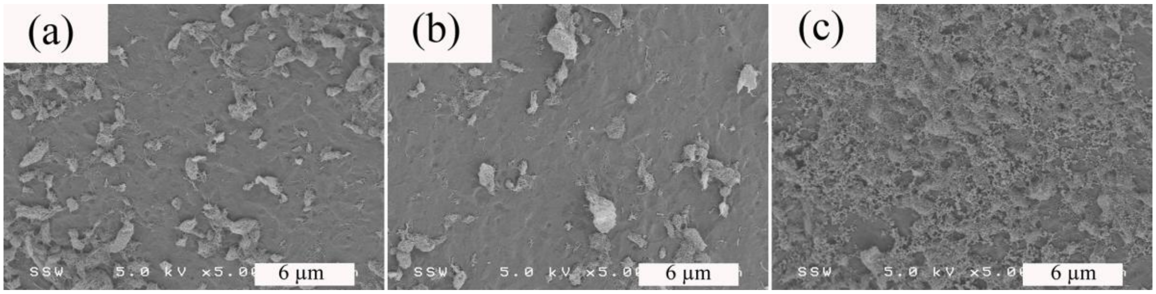

Figure 8.3 The morphology of PP/CNT 2 wt% plaque microparts. Images were taken from the core layer of (a) front region, close to gate, (b) middle region and (c) end region, opposite to gate.

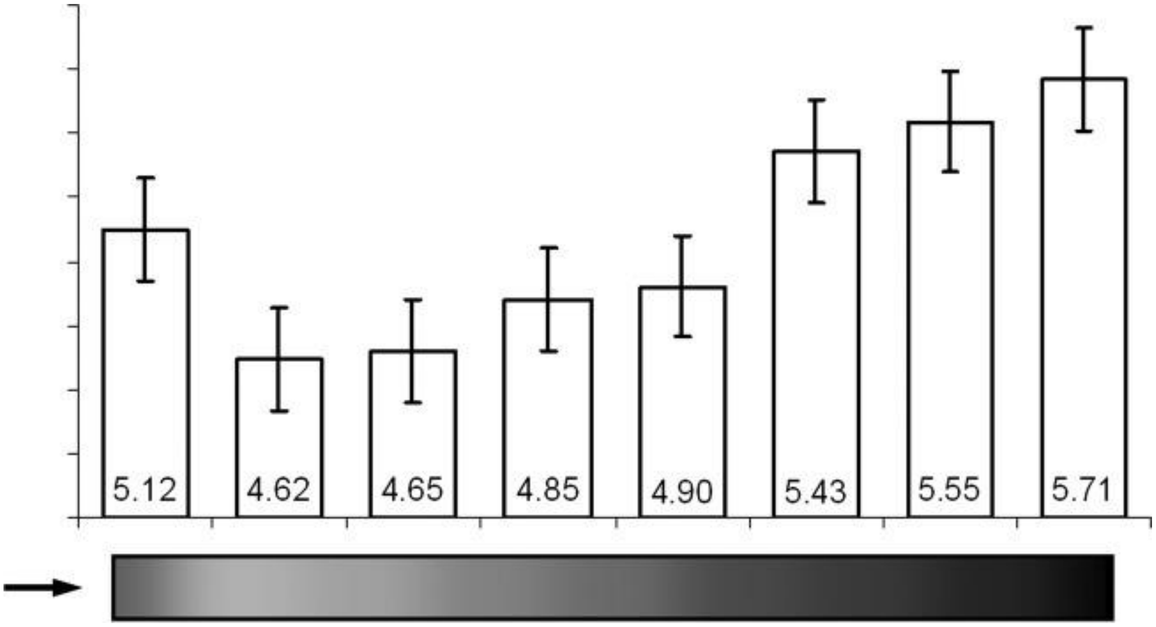

Figure 8.4 The distribution and content of CNT in injection molded PC/ABS-CNT 5.0 wt% samples. Rectangular specimen was cut into pieces and analyzed with respect to the distance from gate, marked by the black arrow [149].

In addition, the microstructure of PP/CNT 5 wt% plaque microparts taken from the shear and core layers of the middle region is displayed in Figure 8.5. Results revealed that an intact conductive network could be well constructed in both layers of the microparts. However, a distinct difference in microstructure between both layers was discerned. For example, Figure 8.5(d) shows some areas where are devoid of CNT, which might be related to shear-induced migration of CNT, as often reported in injection molding process [352].

Thus, a detailed analysis by TEM through the transverse direction of the microparts might be helpful to further elucidate this phenomenon.

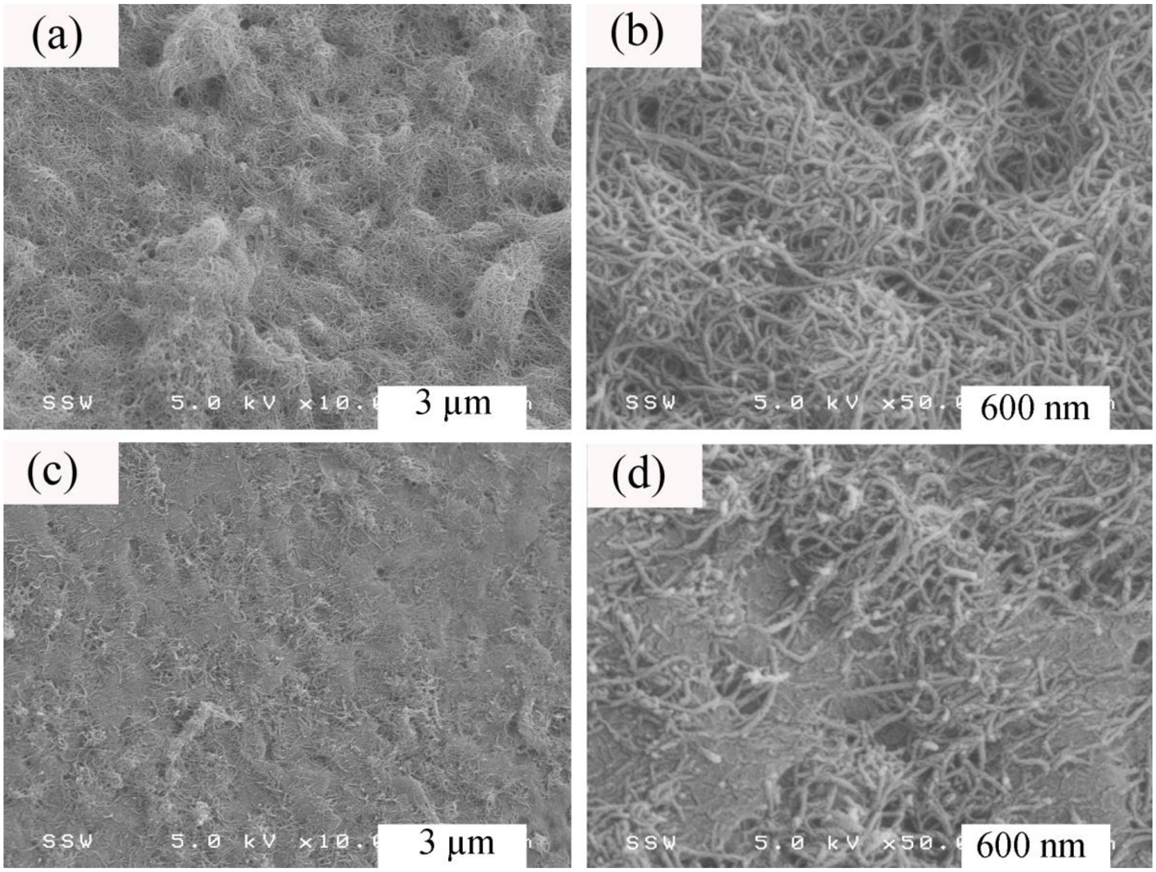

Figure 8.5 The morphology of PP/CNT 5 wt% plaque microparts. (a) and (b) were taken from the core layer whereas (c) and (d) were taken from the shear layer.

8.3 Simulation (Moldflow)

As per *Section 4.5.6*, the simulation software package, Autodesk Moldflow Synergy 2016, was used to evaluate the maximum shear rates in PP/CNT plaque microparts. Figure 8.6(a) shows the distribution of maximum shear rates within the microparts from the gate region to the end region of the plaque microparts. The change of shear rates is significant between the runner and mold cavity, which could lead to an orientation of polymer chains and CNT.

The distribution of maximum shear rates as a function of distance across the TD with respect to each section of the microparts is displayed in Figure 8.6(b). It is apparent that the highest shear rates for each region (see Figure 8.1b) occur near the shear layer of the microparts, however, the difference of maximum shear rates exist in each section of the microparts is insignificant. Therefore, the state of filler orientation along the flow direction of plaque microparts will be different when compared with each section of the three-step microparts, thereby affecting the σ of subsequent moldings.

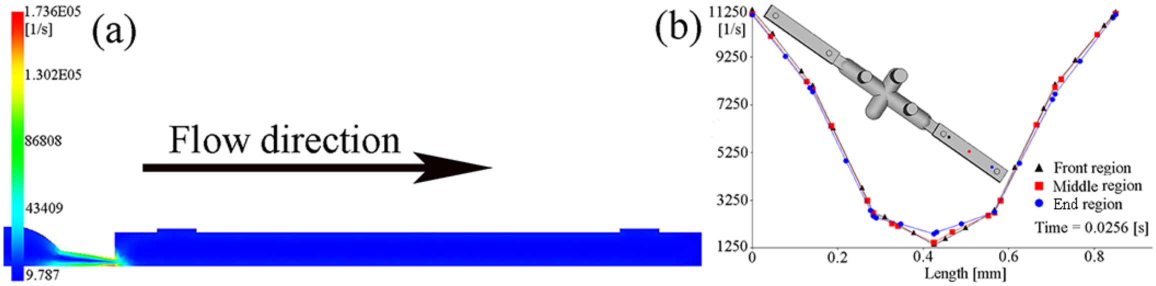

Figure 8.6 (a) Distribution of maximum shear rates (Moldflow) along the flow direction and (b) the probe plot of maximum shear rates as a function of distance across the thickness of the plaque microparts.

8.4 Summary

In summary, the morphology of PP/CNT microparts can be affected by the mold geometry employed, which could determine the electrical conductivity of subsequent moldings. For example, the FD σ for PP/CNT plaque microparts was invariably lower than either the FD σ or the TD σ of each section of the three-stepped counterparts when the filler concentration is less than 7 wt%, suggesting that the flowing path of the polymer melts could affect the development of microstructure. For example, morphology observations revealed that the development of microstructure in PP/CNT plaque microparts varied locally along the flow direction, which could be attributed to the influence of prevailing shearing and cooling effects in μIM. This observation is consistent with the results reported by Wegrzyn et al. [149]. In addition, there is likely a shear-induced migration of CNT in the shear layer of the microparts. Overall, a higher filler concentration of CNT is typically required to acquire intact conductive pathways in μIM and the variations of mold inserts could influence the mold filling, thereby affecting the development of microstructure. Therefore, the influence of mold cavity thickness on the electrical and morphological properties of CNT-containing plaque microparts is currently under investigation.

Curriculum Vitae

Name:	Shengtai Zhou
Post-secondary Education and Degrees:	Qingdao University (青岛大学) Qingdao, Shandong, China 2007-2011 B.Sc.
	Sichuan University (四川大学) Chengdu, Sichuan, China 2011-2014 M.Sc.
	The University of Western Ontario London, Ontario, Canada 2014-2018 Ph.D.
Honours and Awards:	Outstanding Volunteer of Qingdao University 05/2010
	Excellent Graduate Student of Sichuan University 10/2013
	National Scholarship 10/2013
	Scholarship from China Scholarship Council 2014-2018
	PPS-34 Conference Graduate Travel Award 05/2018
Related Work Experience	Research Assistant State Key Laboratory of Polymer Materials Engineering, Polymer Research Institute of Sichuan University, Chengdu, Sichuan, China 2013-2014
	Teaching Assistant Department of Chemical and Biochemical Engineering, The University of Western Ontario, London, Ontario, Canada 2015-2018

Publications

Journal papers:

1. **S. Zhou**, A.N. Hrymak, and M.R. Kamal (2016). Electrical and morphological properties of microinjection molded polystyrene/multi-walled carbon nanotubes nanocomposites. *Polym Eng Sci*, 56(10), 1182-1190 (one of the journal's top 20 most downloaded papers published between 2016-2017).
2. **S. Zhou**, A.N. Hrymak, and M.R. Kamal (2017). Electrical and morphological properties of microinjection molded polypropylene/carbon nanocomposites. *J Appl Polym Sci*, 134, 45462.
3. **S. Zhou**, A.N. Hrymak, and M.R. Kamal (2017). Electrical, morphological and thermal properties of polyamide 6/multi-walled carbon nanotubes nanocomposites. *Compos Part A-Appl Sci Manuf*, 103, 84-95.
4. **S. Zhou**, A.N. Hrymak, and M.R. Kamal (2018). Microinjection molding of polypropylene/multi-walled carbon nanotube nanocomposites: The influence of process parameters. *Polym Eng Sci*, 58(S1), E226-E234.
5. **S. Zhou**, A.N. Hrymak, and M.R. Kamal (2018). Microinjection molding of multi-walled carbon nanotubes (CNT)-filled polycarbonate nanocomposites and comparison with electrical and morphological properties of various other CNT filled thermoplastic micromoldings. *Polym Adv Technol*, 29(6), 1753-1764.
6. **S. Zhou**, A.N. Hrymak, and M.R. Kamal (2018). Properties of microinjection-molded multi-walled carbon nanotubes-filled poly(lactic acid)/poly[(butylene succinate)-co-adipate] blend nanocomposites. *J Mater Sci*, 53(12): 9013-9025.
7. **S. Zhou**, A.N. Hrymak, and M.R. Kamal (2018). Electrical, morphological and thermal properties of microinjection molded polypropylene/multi-walled carbon nanotubes nanocomposites. *Int Polym Proc*, 33(4), 514-524.
8. **S. Zhou**, A.N. Hrymak, and M.R. Kamal (2018). Effect of hybrid carbon fillers on the electrical and morphological properties of polystyrene nanocomposites in microinjection molding, submitted.

Conference Proceeding:

1. **S. Zhou**, A.N. Hrymak, and M.R. Kamal (2016). Microinjection molding: Influence of the molding parameters on the electrical conductivity of polypropylene filled with multi-walled carbon nanotubes. SPE ANTEC®-Indianapolis (USA), 1167-1171.
2. **S. Zhou**, A.N. Hrymak, and M.R. Kamal (2018). Microinjection molding of polypropylene/graphite composites. SPE ANTEC®-Orlando (USA).

Book Chapter:

1. **S. Zhou**, A.N. Hrymak, and M.R. Kamal (2018). Book chapter of "Microinjection molding of filler loaded polymer nanocomposites" in the book '*Processing of Nanocomposite Polymers*' edited by Professor Samuel Kenig (Israel).